Enhanced Modulation Dynamic Performance of Optically-Injected Widely-Tunable Semiconductor Lasers

Onur Duzgol

A thesis submitted for the degree of Doctor of Philosophy

School of Computer Science and Electronic Engineering

University of Essex

Supervisor: Dr. Nick Zakhleniuk

January 2017

SUMMARY

This dissertation is devoted to a comprehensive theoretical and modelling study of dynamic modulation characteristics of semiconductor wide-wavelength tunable laser diodes (TLDs). The two major goals were to investigate how modulation properties of a TLD depend on the wavelength tuning, and how the modulation performance of a TLD can be enhanced in terms of the achievable speed and improved frequency chirping behaviour under the direct modulation regimes using external light for optical injection-locking (OIL).

It is demonstrated that modulation performance of free running (FR) widely tunable lasers strongly depends on the tuned lasing wavelength. The relaxation oscillation frequency (ROF) of FR TLD increases from 2.2 GHz to 5.5 GHz with tuning.

The main results of investigation of modulation dynamics of OIL TLDs include demonstration of substantial (up to an order of magnitude) increase of the ROF and the modulation bandwidth in comparison with the FR regime and investigation of dependence of ROF on the wavelength tuning. The ROF increases to 24 GHz. We prove that the ROF of the OIL TLD is defined by the difference between the injected master laser's light frequency and the cavity shifted mode frequency. The latter non-lasing mode has been identified as corresponding to the amplified spontaneous emission and was clearly reproduced in CW spectra of a steady-state OIL TLD. This finding has important practical implications as it allows to directly relating the CW lasing spectra fine features with dynamic performance of the OIL TLDs.

Important results were obtained for case of large-signal modulation of the OIL TLD and for a large frequency detuning for side-mode optical injection regime when the master laser's light is injected near the side-mode of FR TLD with large SMSR. Direct large-signal modulation of the OIL TLD using pseudo-random bit sequence shows superior performance in terms of enhanced modulation speed.

ACKNOWLEDGEMENTS

I am grateful to my supervisor Dr Nick Zakhleniuk for his great encouragement to complete this thesis. During the last four years of research, I was impressed by his great analytical skills and deep knowledge. Our long discussions on laser physics motivated me to do my best. I also want to thank my colleague Dr Georgios Kyritsis for his great collaboration.

This project was mainly sponsored by the Turkish Ministry of Education. I want to thank to them for their support.

I want to thank my parents for their endless patience during these or the last four years. It would have been impossible to complete this thesis without their unconditional love and support.

I would especially like to thank my fiancé Dr Ioanna Pavlaki for her real understanding during my PhD. I have always felt much stronger and happier with her. Also, my dear friends Dr Nikos Vastardis, Dr Anil Yilmaz-Vastardis, Dr Laura Carrea, Dr Chathura Sarathchandra, Dr Ozgul Bilici, Mr Manolis Theofilos, Dr Andreas Bontozoglou and Dr Celia Antoniou were always with me during my PhD. I am really grateful for their real friendship and support.

Lastly, I wish like to dedicate this thesis to my dear sister Fatma Duzgol who has the most innocent and lovely soul I have ever seen.

Thanks.

LIST OF PUBLICATIONS

Papers

1. O. Duzgol, G. Kyritsis and N. Zakhleniuk: 'Modulation dynamic response of optical-injection-locked wavelength-tunable semiconductor laser diodes', IET Optoelectronics, 2016, DOI: 10.1049/iet-opt.2016.0075

2. O. Duzgol, G. Kyritsis and N. Zakhleniuk, "Travelling-Wave Modelling of the Modulation Dynamic Performance of Wavelength-Tunable Laser Diodes Using the Integrated VPI and PICS3D Software", IEToptoelectronics. (Accepted)

Conferences

1. O. Duzgol, G. Kyritsis and N. Zakhleniuk, "Travelling-wave modelling of dynamic performance of wavelength-tunable laser diodes using the integrated VPI and PICS3D software", 2016 Semiconductor and Integrated OptoElectronics Conf. Cardiff, UK

2. O. Duzgol, G. Kyritsis and N. Zakhleniuk, "Simulation of small-signal modulation response of optical injection-locked wavelength-tunable laser diodes", 2016 Semiconductor and Integrated OptoElectronics Conf. Cardiff, UK

3. O. Duzgol, G. Kyritsis and N. Zakhleniuk, "Enhanced dynamic response and spectral characteristics improvement of optically-injected widely-tunable laser diodes," 2016 International Semiconductor Laser Conference (ISLC), Kobe, Japan, 2016

Published papers which are not included in thesis:

1. G. Kyritsis, O. Duzgol and N. Zakhleniuk, "Power and wavelength tuning performance of multi-quantum-well and bulk tunable laser diodes and main limiting factors," 2016 International Semiconductor Laser Conference (ISLC), Kobe, Japan, 2016

Papers in preparation:

1. O. Duzgol and N. Zakhleniuk, "Large-Signal Performance of Optically Injection-Locked Widely Tunable Semiconductor Diodes with Enhanced Dynamic Characteristics" (in preparation, to be submitted to IEEE Journal of Quantum Electronics, 2017)

2. O. Duzgol and N. Zakhleniuk, "Side-Mode Optical Injection Locking of Tunable Semiconductor Diode Lasers" (in preparation, to be submitted to IEEE Photonics Technology Letters, 2017)

LIST OF ACRONYMS

TLD	Tunable Laser Diodes
OIL	Optically-Injection Locked
FR	Free Running
ROF	Relaxation Oscillation Frequency
SMSR	Side Mode Suppression Ratio
CW	Continuous Wave
TLLM	Transmission Line Laser Model
IM	Intensity Modulation
ASE	Amplified Spontaneous Emission
PRBS	Pseudo-Random Bit Sequence
BL	Bit Rate-Distance Product
MASER	Microwave Amplification by Stimulated Emission of Radiation
LASER	Light Amplification By Stimulated Emission Of Radiation
LED	Light-Emitting Diodes
TDM	Time Division Multiplexing
WDM	Wavelength Division Multiplexing
EDFA	Erbium Doped Optical-Fibre Amplifiers
DFB	Distributed Feedback Laser
DBR	Distributed Bragg Reflectors
RIN	Relative Intensity Noise
REM	Rate Equations Model
TWM	Travelling Wave Model

FP	Fabry-Perot
VCSEL	Vertical Cavity Surface Emitting Lasers
BER	Bit Error Rate
DSM	Dynamics Signal Mode
CIP	Corrugated Pitch-Modulation
PPR	Photon-Photon Resonance
QD	Quantum-Dot
QWR	Quantum-Wire
SGDBR	Sampled Grating Distributed Bragg Reflector
FC	Free Carrier
IVBA	Intervalence Band Absorption
FM	Frequency Modulation
CPR	Chirp to Power Ratio
TCAD	Technology Computer-Aided Design
MQW	Multi-Quantum Well
AR	Active Region
SL	Slave Laser
ML	Master Laser
SRH	Shockley-Read-Hall

BRIEF DESCRIPTION OF THE DISSERTATION SCOPE AND THE RESULTS

In this dissertation a comprehensive theoretical and modelling study of dynamic modulation characteristics of semiconductor wide-wavelength tunable laser diodes (TLDs) is carried out. The two major goals were to investigate how modulation properties of a TLD depend on the wavelength tuning, and how the modulation performance of a TLD can be enhanced in terms of the achievable speed and improved frequency chirping behaviour under the direct modulation regimes using external light for optical injection-locking (OIL).

For this purpose we have developed an integrated simulation model based on utilisation of two powerful physic-based Technology Computer Aided Design (TCAD) tools VPI (from VPIphotonocs GmbH) and PICS3D (from CrossLight) which were carefully calibrated in order to ensure mutual self-consistently of the modelled devices by both embodiments. The VPI allows to simulate various optical components with composite design, like multi-section lasers using a spatio-temporal travelling-wave approach which is implemented within the transmission-line laser model (TLLM). This approach is crucial for our simulation of 3-section TLDs since the alternative approach based on the rate equations is not suitable for such devices due to composite design of the cavity which includes section with different functionality. For such devices it is difficult or impossible to introduce average parameters which depend on time only, as required in the rate equation models.

We demonstrate that modulation performance of free running (FR) widely tunable lasers strongly depends on the tuned lasing wavelength. The relaxation oscillation frequency (ROF) of FR TLD increases from 2.2 GHz to 5.5 GHz with tuning. This effect is explained by dispersion of the differential gain which varies (increases) more that 4-times over a 21-nm tuning range near the 1550 nm lasing wavelength. Because of this, we also show physical importance of using correct shape of the gain spectra. Our gain spectrum was imported into the VPI model from the PICS3D where it was calculated taking into account linewidth broadening effects. As a by-product of this analysis, we also suggest a simplified fitted parabolic gain spectra model which can satisfactory reproduce correct laser modulation dynamics.

In order to achieve enhanced modulation behaviour of a TLD, we investigate direct intensity modulation (IM) response of the OIL TLD. The necessary dynamic maps for different tuned lasing wavelengths of the OIL TLD have been obtained. These maps allow to define the stable locking regions in terms of the frequency detuning between the master and slave laser and the injection power ratio of these lasers. Various OIL regimes have been investigated with the front and back mirror injection, and positive and negative frequency detuning.

The main results of investigation of modulation dynamics of OIL TLDs include demonstration of substantial (up to an order of magnitude) increase of the ROF and the modulation bandwidth in comparison with the FR regime and investigation of dependence of ROF on the wavelength tuning. The ROF increases to 24 GHz. We prove that the ROF of the OIL TLD is defined by the difference between the injected master laser's light frequency and the cavity shifted mode frequency. The latter non-lasing mode has been identified as corresponding to the amplified spontaneous emission (ASE) and was clearly reproduced in CW spectra of a steady-state OIL TLD. This finding has important practical implications as it allows to directly relate the CW lasing spectra fine features with dynamic performance of the OIL TLDs.

Important original results have been obtained for case of large-signal modulation of the OIL TLD and for a large frequency detuning within the side-mode optical injection regime when the master laser's light is injected near the side-mode of FR TLD with large SMSR. Direct large-signal modulation of the OIL TLD using pseudo-random bit sequence (PRBS) shows superior performance in terms of enhanced modulation speed, increased eye diagram openings, and improved frequency chirping characteristics. For a side-mode optical injection, we show that OIL slave lase lases at the master laser frequency and the ROF is defined by the difference between the master laser frequency and the shifted side-mode frequency corresponding to the ASE.

The original findings in the thesis have practical importance for utilisation of TLDs as high-speed transmitters for optical-fibre communication applications.

TABLE OF CONTENTS

CHAPTER 1

INTRODUCTION

The first long haul optical communication system, called the 'Optical Telegraph', was invented by Chappe in 1792 [1]. Since then great advances have been made in telecom systems technology. At the beginning of the 1830s, electrical based telegraph systems were designed and used in long haul communication systems. Telegraphy allowed continents to be connected via telegraph lines and by utilizing the development of the Morse coding a transmission speed approximately of 10 b/s was achieved.

In 1876, the telephone was invented by Graham Bell [2] and this radically changed the course of communication systems evolution. The main challenge of setting up a worldwide telephone network laid within the transmission capabilities of the telecom components. Initially, coaxial cable was used to overcome this problem, but it had limitations too, mainly due to its high loss characteristics. To increase the transmission speed as well as the number of channels that could be transmitted, it was important to design new transmission elements. The introduction of microwave technology to telecom systems in 1948 increased the transmission speed to 100 Mb/s and this was further enhanced to 274Mb/s by the use of advanced coaxial cables. These new elements did not come without problems; cost-effectivity became an issue as it was shown that in order to transmit data over long distances many repeaters should be introduced in long-haul systems.

A popular characteristics which is used to estimate figure of merit of communication systems is the relation between transmission bit rate and distance, and it is termed as the 'bit rate-distance product – BL'. The evolution of BL product since mid-19^{th} century is illustrated in Fig. 1.1, where it is clearly demonstrated that progress in telecom systems technologies has resulted in an increase over many orders of magnitude of the BL products.

Firstly, it became evident that shifting the carrier frequency to the optical range led to faster transmission with reduced losses [1]. Following that, the invention of microwave amplification

by stimulated emission of radiation (Maser) by Maiman in 1959 [3] changed technological direction in developing novel component for telecommunication systems. It quickly became clear that in order to provide proper medium for light transmission, new research and development work was necessary to introduce disruptive technologies into practice. Research on optical fibre cables became crucial. Before this, optical fibre cables were only used in medical imaging systems because of the fact of high losses which were too extensive for utilisation of the fibres for long haul communication. Fundamental contribution to development of the optical fibres capable of long-haul transmission was achieved in 1966 by Charles Kao at Standard Telecom Labs in Harlow (Essex). Their group has concluded [4] that fundamental limitation for light attenuation in silica-based optical fibres is well below 20 db/km (this value was considered at that time as a key threshold with the actual typical values of ~1000 dB/km being achieved in practice). They have identified that the main loss mechanism in optical fibres was due to present impurities rather than due to fundamental physical effects, and have unambiguously demonstrated that practical low-loss optical fibres were possible with the ideal medium candidate of silica (SiO_2) being suggested. Subsequently, Kao has been recognised as a "Father of Optical-Fibre Communication" and won 2009 Nobel Prize in Physics. In 1970, Kapron et al. [5] managed to obtain a transmission loss of 20 dB/km, and finally this was reduced even further to 0.2 dB/km by Miya et al. in 1979 [6].

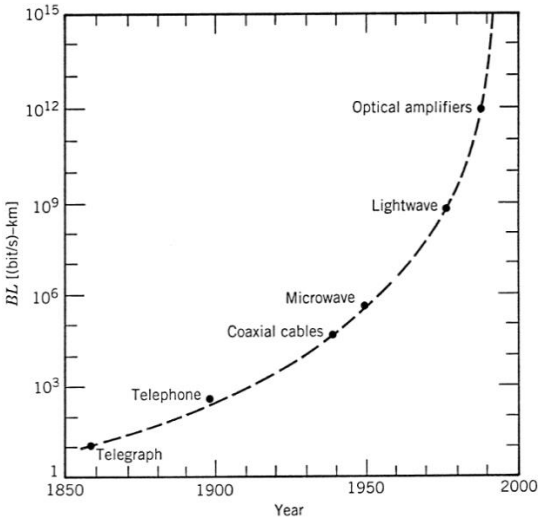

Fig. 1.1 The evolution of BL products since 1850 [1].

The improvements in optical network technologies are illustrated in Fig. 1.2 [7]. The first generation of optical networks used the semiconductor Light-Emitting Diodes (LEDs) or multimode lasers operating at 0.82 μm wavelengths as optical transmitters. The multimode fibre cables were used as waveguides [8]. Due to the high loss characteristics of multimode fibres, the electrical based regenerators were frequently placed (every 10-km of the fibre span) to reconstruct the signal. Later, in the second generation of the optical networks, it was discovered that fibre losses could be dropped significantly (below of 1 dB/km) at 1.3 μm operation wavelength where the optical dispersion was also minimal. The latter property became especially important since after managing the optical loss problem in the fibres, it was necessary to overcome the optical chromatic dispersion issue which limits the bitrate [9] because the optical waves with different wavelengths have different phase and group velocity which in turn are defined by the dispersion of the refractive index of the fibre. In multimode fibres different modes have different wavelengths and travel at different speed, which results in an intermodal dispersion. Following the development of single mode fibres resolved the problem of the intermodal dispersion and the repeater distance was considerably increased allowing also to achieve a higher transmission speed. For transmission of the beams which have wavelength

away from the zero-dispersion 1.3 μm point, new technological solutions have been proposed with use of dispersion-shifted fibres which allow to compensate positive material dispersion with the correspondingly engineered negative waveguide dispersion [1].

The discovery of the minimum loss characteristics of fibres at 1.55 μm wavelength changed the direction of development of the optical network systems. This led to provide even higher repeater distance and had substantially reduced the costs. It was also necessary to provide single mode lasers working at 1.55 μ wavelength rather than multimode ones. In order to overcome the optical dispersion problem at this wavelength, the dispersion managed fibres were proposed and this was another way of solution to compensate the dispersion related signal degradations. The optical networks operating at 1.55 m with single mode lasers was the fundamental improvements of the third generation networks.

In the fourth generation networks, the number of channels which were transmitted over fibre cables was increased by introducing the wavelength multiplexing (WDM) or time division multiplexing (TDM) techniques, as demonstrated in Fig. 1.2.d and in Fig. 1.3. In order to realise these techniques in practice, optical multiplexers and demultiplexers were developed and introduced in the optical-fibre networks. Additionally, the electrical based regenerators were replaced by Erbium doped optical-fibre amplifiers (EDFA) at the beginning of 1990s [10], and the demonstration of intercontinental fibre installation with optical amplifiers was achieved [11].

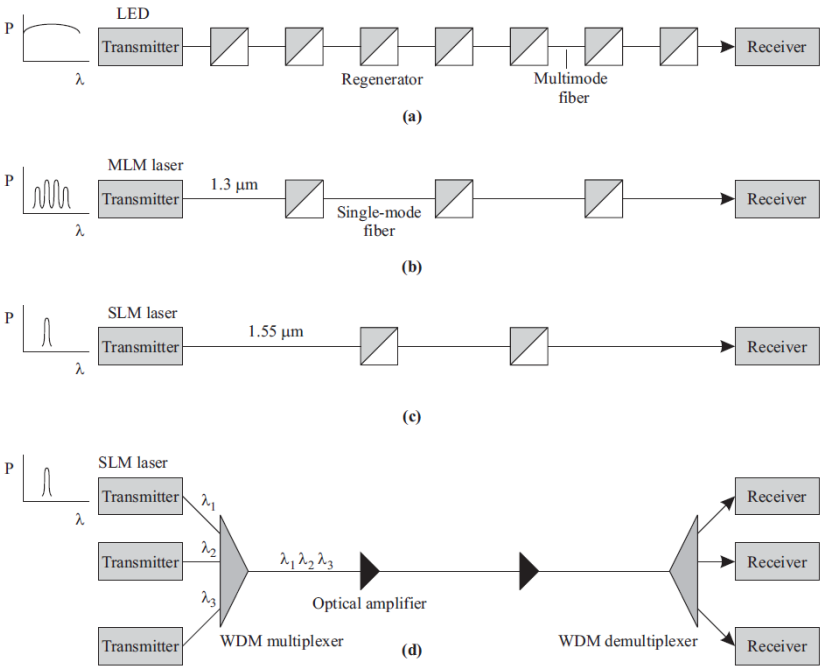

Fig. 1.2 The evolution of optical networks [7].

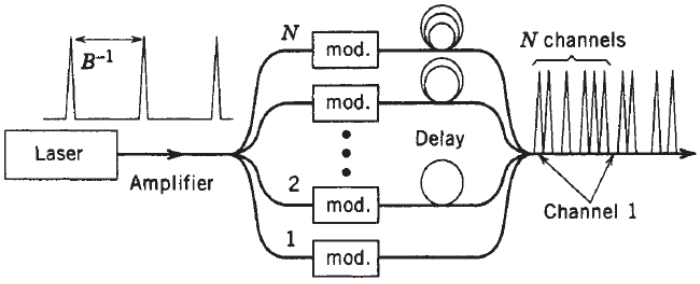

Fig. 1.3 Demonstration of the optical TDM design [1].

The evolution of optical networks shows the importance of single mode semiconductor lasers for high-speed long-haul optical telecommunication systems. In 1970 the first semiconductor laser, operating at room temperature, was developed by Hayashi [12]. The early examples of semiconductor lasers had multimode emission. However, in order to resolve the need for a single mode operation at 1.55 μm, many different single-mode laser designs were proposed. In single mode lasers, the wavelength-dependent mirror loss mechanism was introduced to the laser design for one of the cavity modes to be selected for lasing. There are different single mode laser concepts such as distributed feedback (DFB) lasers or distributed Bragg reflectors (DBR) lasers.

DFB laser consists of a periodically changing refractive index along the cavity and the wavelength selection is carried out by this grating. On the other hand, in DBR lasers, the same mode selection is achieved by mirrors in an external region of the cavity. In Fig. 1.4.a DFB laser structure with periodical gratings inside of the active section is illustrated. The DBR laser structure with external region mirrors is shown in Fig. 1.4.b.

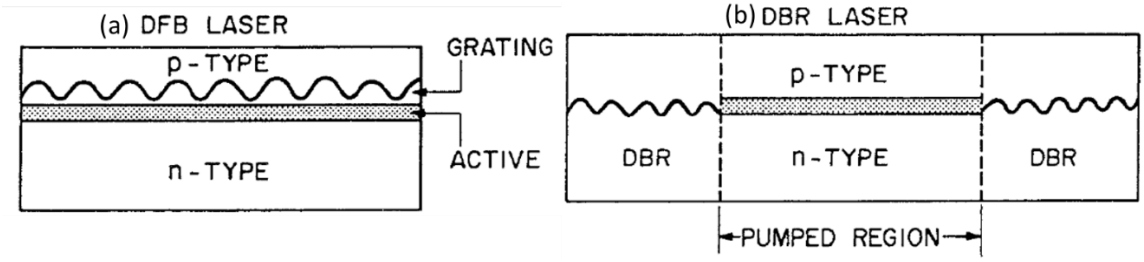

Fig.

Fig 1.4 Single mode laser structures of (a) DFB and (b) DBR lasers [1].

There are two main differences between the DFB laser and DBR lasers. The first is that in the DFB lasers the active photon-generating region overlaps with the optical-filter grating region, while in the DBR lases these regions are separated. The second point is that the optical properties of the DBR section (e.g. its refractive index) can in principle be modified by injecting electrical current if the additional contacts are introduced to the DBR section. The injected current increases the carrier density in DBR section and the refractive index and Bragg wavelength are changed accordingly. This in turn allows to modify (tune) the lasing wavelength of such DBR-based laser, as will be explained later. This feature of such wavelength-tunable lasers makes them very desirable optical component for WDM applications. In addition to various novel technological possibilities of such component in optical-fibre networks, this also gives a cost-effective alternative to using many different DFB lasers is the introduction of tunable laser diodes (TLDs) into the optical networks.

Optical communication requires transmission of signals with imprinted data information. This is achieved via optical signal modulation techniques. The modulation technique of the laser is an

important factor in fibre optic networks. Direct laser modulation (when the output optical signal is changed by changing the current injected into the laser) is a desired technique since it requires less complexity and it is cheaper in comparison with the external modulation (when the laser operates in a continuous wave (CW) regime, and the transmitter output is modulated using an additional device, called an optical modulator). However, the direct modulation technique has its drawbacks due to the laser's fundamental limitations, such as limited speed of response due to turn-on delay and relaxation oscillation effects (which reduce the modulation bandwidth), frequency chirping (which destroys spectral purity of the signal), and the relative intensity noise (RIN) (which affects stability of the output optical power), all of which restrict the direct modulation response of the laser.

During the last decade or so, scientists and telecom engineers were looking for possible technological solutions which would allow mitigation the above limitations of the directly-modulated semiconductor lasers. The corresponding research works in solving this problem are generally divided into two different groups. Within the first group, the scientist and engineers were looking for novel designs of the lasers with enhanced dynamic characteristics by optimising the active region design in such high-speed lasers, e.g. using low-dimensional quantum heterostructures (quantum wells, wires, and dots) [13] The other direction is focussed on the search for novel operation regimes of the lasers, the prominent example of which is optical injection of the signal from external laser into the modulated laser. It was found since the pioneering work of Lang and Kobayashi on optically-injected semiconductor lasers [14, 15] that laser operation under optical has a very rich physics with various regimes [16]. In this thesis our main interest will be focussed on the optical injection locking (OIL) regime which allows us to drastically enhance performance of semiconductor laser as optical transmitters. OIL is an extremely efficient technique to improve laser's modulation response by improving its internal dynamics. According to embodiment of the OIL model, in order to improve the stability and

modulation dynamic the modulated laser (slave laser) is connected to another external laser (master laser) via an isolator. A stable locking is provided by the light injection from the master laser into the slave laser. It has been shown by many studies that fundamental characteristics of laser such as bandwidth [17], chirping [18], RIN [19] can be improved by OIL.

OIL lasers have been investigated by different groups, and each of them focusing on different aspects [16]. Some studies have covered the response of the laser to light injection and various dynamic regimes have been reported [20]. On the other hand, several groups studied the enhancement of laser characteristics by using the OIL technique. There are generally two main theoretical models which are used to analyse OIL lasers; the rate equation (RE) model and the travelling wave (TW) model. The conventional RE model for OIL was developed by Lang-Kobayashi [15] in 1980. This model is useful for the analysis of free running (FR) and OIL lasers; however it has the caveat that the change in carrier density and photon density are calculated only as an average value, while all spatial cavity effects are omitted, which are of particular importance in TLDs, as was shown in [21]. On the contrary, TW model divides the cavity in subsections and calculates all relevant quantity by taking the variations in the cavity. Due to mathematical and computational complexity of the TW model, the majority of the research publications on OIL semiconductor lasers use the RE model. The RE approach still gives good theoretical results which have been supported by experimental data as was first demonstrated in [22] This was the case of the fixed wavelength lasers where the cavity is typically a single section region, like in Fabry-Perot (FP) lasers, or DFB, DBR lasers. A very detailed direct comparison between the RE theory and experiment for the OIL vertical cavity surface emitting lasers (VCSELs) is presented in a recent work [23]. The problem of investigating the laser behaviour under optical injection becomes, however, considerably more complex in case of the laser with composite cavity, like for example in multi-section TLDs. In this case the total cavity consists of various sections with very different electrical and optical

properties which also operate in different regimes. As a result, it is questionable whether the RE model can justifiably be applied to such lasers under optical injection conditions. The main problem here is that the optical field in the slave laser (TLD) varies spatially along the cavity as well as it varies in time. The interaction between the injected light and the free-running laser is also spatio-temporal dependent. More than this, it is not even clear how to assign the average photon and carrier density in such lasers with so different properties of multi-section regions. It seems, in such cases of composite laser cavities the use of the TW model should be preferred to the RE model. To the best of our knowledge, the dynamic response of OIL TLDs using the TW model have been theoretically analysed by Labukhin et al. [21] and Stolz et al. [24]. In the latter work the authors have also presented a direct comparison of the RE, TW, and the FP model [25]. They found that TW model provides more accurate results than the RE model. These works were focussed on various chaotic operation regimes of TLD under optical injection in line with the corresponding analysis for a fixed wavelength lasers [26]. On the other hand, the problem of modulation dynamics and modulation bandwidth enhancement and improved modulation characteristics of semiconductor TLDs under the OIL conditions have not been addressed or investigated previously.

The main focus of the study presented in this thesis is on investigation of the modulation performance of the OIL TLD under various injection conditions and under wide range of the wavelength tuning. To carry out this investigation we have developed an integrated physics-based computational model which is capable to solve the spatio-temporal problem for laser field under external optical injection. Two technology computer aided design (TCAD) programs have been used, the VPIphotonics [27] and the PICS3D [28] to achieve an adequate description of the key physical processes in composite laser cavity and to solve small- and large-signal modulation dynamics problems with the required accuracy. A three-section TLD which is designed using the PICS3D software with advanced gain models is implemented in the VPI for solution of the

spatio-temporal TW model with the transmission-line model (TLM) approach [29]. The integrated hybrid model includes an embedded gain spectrum which is produced in PICS3D instead of a simplified parabolic shape spectrum available in the VPI. Additionally, the DBR tuning is carried out by considering both fundamental contributions to the electronic refractive index change under the current injection: (i) due to the Kramers-Kronig contribution, and (ii) due to the free carrier plasma effect (the effect of temperature on refractive index change is neglected as it could be prevented with cooler). Although the VPI model takes only plasma effect into account, we have developed a special fitting procedure in order to correctly represent tuning behaviour of the TLD when the both above effects are included. The change in the refractive index under the current injection into the DBR section is first analysed using the PICS3D model, and then the corresponding required change in the differential refractive index is introduced in the VPI model at every small step of the current injection in order to include both effects.

The main obtained original results of the investigation include:

1) An accurate demonstration of the TLD in VPI is increased by importing a realistic gain spectrum which is calculated in PICS3D.
2) The ROF of the FR TLD increases 3-4 times with tuning as a result of the dramatic change in the differential gain.
3) The OIL TLD provides a substantial amount of bandwidth enhancement. The ROF of TLD is enhanced to 24 GHz with injection locking.
4) The results prove that the change in the bandwidth enhancement is observable in the optical frequency spectrum under CW regime. The difference between the locking frequency and the shifted cavity resonance frequency is equal to the ROF of the OIL TLD.

5) As a result of the increase in differential gain with blue wavelength tuning, the ROF enhancement for constant detuning frequency is increasing with shorter lasing wavelengths.
6) We have observed that there is a limitation in bandwidth enhancement. The carrier density of OIL TLD drops sharply when the detuning frequency is at around half side-mode distance and the laser stops responding to any change in the electrical injection. This behaviour continues until detuning frequency is increased up to side-mode distance.
7) We demonstrated that it is possible to achieve bandwidth enhancement if the locking is applied to the side mode of the laser. The shifted side mode cavity resonance frequency is visible on frequency spectrum with the locking frequency. The difference between them gives the new ROF of the TLD.
8) Finally, we investigate the large signal modulation response of OIL TLD. The results show that the OIL TLD has good response to the higher modulation bit rates than the fundamental limitations of the FR TLD. It is also demonstrated that there is a sharp decrease in the transient chirp from 20 GHz to less than 4 GHz.

The overall structure of the thesis is as follows.

A detailed literature review on semiconductor lasers, TLDs, and OIL is carried out in Chapter 2. The recent studies on laser technologies and the fundamental improvements of OIL lasers are discussed in this chapter.

Chapter 3 includes a brief theoretical discussion on relevant physics of semiconductor materials. Different semiconductor materials are discussed according to their fundamental characteristics. Later, the theory of the gain-loss mechanisms in semiconductor lasers are explained and the basics of single-mode DBR lasers are also presented. The operation of the OIL

lasers as well as the effect of the optical injection on modulation bandwidth enhancement are discussed within the RE model. The last part of this chapter includes the demonstration of TLD with transmission line model (TLM) approach.

The main TCAD program which is used in the simulation of laser modulation dynamics, the VPI, is reviewed and explained in detail, and the corresponding simulation techniques are given in Chapter 4.

The first original analysis is presented in Chapter 5. It covers the small-signal analysis of TLD by using the developed model. The analysis of the improved TLD model is completed using a gain spectrum which was imported from another simulation program, PICS3D, using available interface in the VPI. Additionally, the DBR tuning is considered by taking different free-carrier contributions into account. Originally, the VPI is managing the wavelength tuning taking into consideration only the plasma effect. It is demonstrated that the Kramers-Kronig effect, which is simulated in PICS3D, must also be included, since it provides the main contribution to the tuning, particularly at high injected carrier densities. By correctly calculating the corresponding values of refractive index in PICS3D, larger tuning ranges are be obtained, which then are implemented in the VPI model. Additionally, the effect of the realistic material gain spectrum on the small signal response of the laser is analysed and compared with a simplistic parabolic gain spectrum which often used in laser modelling. We demonstrate the shortcomings of such approximations as well as suggest the recipe for how to correctly re-calibrate the obtained data.

The bandwidth enhancement of the OIL TLD is discussed and original results are given in Chapter 6. The small signal response of the OIL TLD, which is modelled with TLM, is analysed in this chapter. A substantial amount of bandwidth enhancement (>20 GHz) is achieved with light injection under various tuning regimes. Analysis is carried out for different tuning regimes

and also the effect of the optical injection parameters (frequency detuning and power injection ratio) on the modulation bandwidth enhancement is investigated.

The large signal modulation response of OIL TLD and the new discovered effect of side mode injection are presented in Chapter 7. The investigation of the side mode injection includes the detailed study of the effect of large frequency detuning on small signal response. We show that side mode injection can provide a large bandwidth enhancement. To compare the large signal response of the FR and OIL lasers, we focus on the improvement of the modulated pulse shape which indicates potential decrease of the bit error rate (BER), and on increase of the corresponding eye diagram openings. The frequency chirping of the OIL modulated laser is also investigated and its substantial decrease is demonstrated.

The final Chapter 8 presents the overall conclusions and the main results obtained in the project, as well as some possible interesting directions of the future work are briefly outlined.

CHAPTER 2

LITERATURE REVIEW

2.1 Overview

Due to the sharp increase in demand, telecom infrastructures have become more complicated than in their early times, and as a result of this it has become essential to design much faster and more reliable network components for modern optical fibre communication systems. To obtain such high transmission speeds, it was crucially important to produce fast and stable optical transmitters. Another essential requirement is that these transmitters must be cost-effective. The most straightforward way to achieve this goal is to use semiconductor laser diodes as optical transmitters operating under the direct modulation regime. For this reason we first present a brief overview of semiconductor laser technology evolution in application to telecommunications.

Long after the existence of the stimulated emission was discovered by Einstein in 1917 [30], MASERs (Microwave Amplification by Stimulated Emission of Radiation) were invented by Gordon to produce amplified electromagnetic waves in 1953 [31]. The first practical Maser operating in optical wavelength was demonstrated later in 1955 by Gordon, Zeiger and Townes [32].

A couple of years later after Maser, Schawlow and Townes introduced the ‘oscillator’ operating in optical range of electro-magnetic spectrum [33]. Soon after, the solid-state ruby and gas lasers working in visible spectra have also been demonstrated [3] [34]. In the beginning of 1960s the first semiconductor lasers based on GaP and GaAs substrates were invented [35] [36]. Since that time, telecom engineers have been working on designing lasers which can operate beyond the basic laser’s limitations, like multimode light emission and optical pumping. The next sections will give a brief description of single mode semiconductor injection lasers, tunable laser diodes, and optical injection locking which represent important steps in evolution of optical transmitters.

2.2 Single Mode Lasers

Semiconductor laser diodes are essential optical network elements which provide high speed modulation to improve the transmission speed. Compare to other light source like LEDs, laser diodes provide more stable and coherent light emission, and become the most important elements of the optical fibre systems for cost-effective long-haul transmission systems.

In 1962, the first observation of the coherent laser light emission was demonstrated by Hall [35]. In the same year, similar observations were published in [36] [37] [38]. It was shown that by biasing a GaAs p-n homojunction the output spectrum of the laser becomes narrower and sharper after passing the threshold level, and this was the proof of the stimulated emission in semiconductor material structures. The early laser designs were based on a homojunction structures which consisted of two layers of the same material (mainly GaAs) with n- and p-doping, respectively. In 1963 the first semiconductor laser with a single heterojunction structure was demonstrated by Kroemer which substantially improved the ability of the CW operation [39]. After these achievements, it was seen that a coherent light emission can be provided by electrical injection current pumping to a semiconductor (active) medium. As a result of this, the interest of the light emission devices has shifted to the semiconductor material heterostructures [40] rather than gas tube or solid-state lasers. Although, the gas and solid-state lasers played a crucial role in the early development stages of the optical fibre communications (particularly, for demonstration of waveguiding properties of silica fibres in 1960s), they have fundamental flaws which were detrimental for their unitisation in practical/commercial transmission systems which were capable to operate beyond research labs in the real world. The key problems were related to their size, cost, and availability of the required emission wavelengths, and the active medium pumping. The early lasers were bulky, expensive, with limited emission spectra options, and

relied on either electrical discharge or optical pumping. All this has been changed with invention of semiconductor heterojunction injection laser diodes.

The single heterojunction lasers diodes demonstrated substantial improvement in comparison with homojunction laser. They still have, however, too high threshold current and, as a result, limited life time. In 1970, a continuous wave (CW) double heterostructure AlAs-GaAs laser was developed with low threshold current level by Alferov et al. [41], and this was also the first demonstration of the operation of CW semiconductor laser at room temperature (RT). Practically simultaneously with this very important laser invention, the low-loss fibre cables were also further developed, following the pioneering work of Charles Kao [4] (2009 Nobel Prize in Physics). These two achievements brought a new opportunity to improve transmission speed dramatically [5] [40].

In Fig 2.1, the transmission loss spectrum is shown in silica optical waveguides [7]. It was found that 4 dB/km loss can be obtained between 0.8-0.85 μm wavelength window and at around 1.05 μm for long haul communication [42]. It was later shown in 1976 that the zero material dispersion transmission can also be achieved at around 1.3 um wavelength [43]. Three years later, finally in 1979, it was shown that the lowest loss (0.2 dB/km) transmission with a good dispersion level (17 ps/nm km) was achieved for 1.55 μm [6]. After these technological discoveries and optical fibre improvements, single mode lasers operating at 1.55 μm emission wavelength have become more popular and the investigations have shifted to this wavelength range. In Fig. 2.2 the range of suitable materials for compound semiconductor lasers are given with their melting point and knoop hardness level [44]. The hatched lines show the wavelength range of materials. After 1976, due to its superior material physical and technological features for production, GaInAsP-based active medium became more desirable since it was also technologically most suitable for industrial production [40].

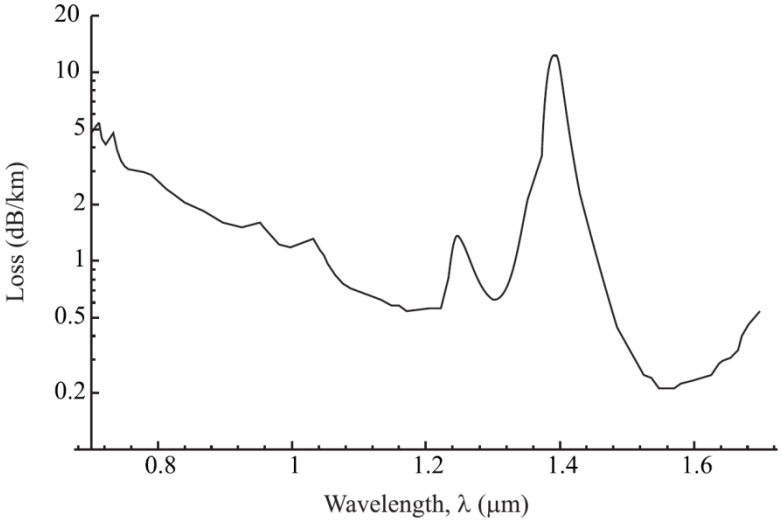

Fig. 2.1 Transmission loss spectrum vs wavelength in fibre optic cables [7].

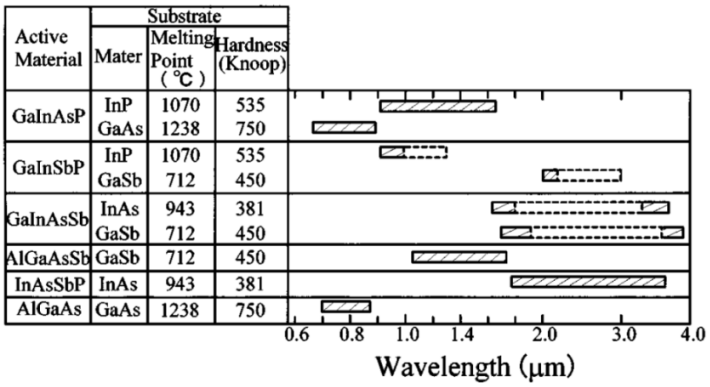

Fig. 2.2 Material specifications vs operation wavelength for semiconductor heterostructure [45].

Since the beginning of the 1970s, it has been aimed to produce semiconductor lasers with a steady operation for use in optical fibre communication. It was found that the first GaAlAs/GaAs multimode heterojunction lasers had unstable emission operation. In order to overcome this problem and also to improve utilisation of the optical fibre transmission bandwidth, Suematsu and Yamada have proposed in 1972 the first single mode laser operation [46]. These types of lasers were eventually branded as Dynamics Signal Mode (DSM) lasers. Until the end of 1970s, several studies on CW room temperature single mode laser diodes operating at 1.55 μm have been reported by Arai [47], Kawaguchi [48], and Kaminow [49]. Distributed feedback lasers

(DFBs) were theoretically proposed by Kogelnik and Shank in 1972 [50]. In the same year another single mode laser, Distributed Bragg Reflectors (DBR) laser with external selecting mirrors were demonstrated by Kaminow [49]. The first DFB laser emitting at 1.5 μm and operating at room temperature was announced in 1981 [51]. The two-mode lasing spectral feature of this laser made it difficult to be used for data transmission. To resolve the mode selectivity of DFB lasers, the first phase-shifted DFB lasers were fabricated in 1984 [52]. In Fig. 2.3 below, a few different types of DFB lasers are shown which were designed to overcome this problem [40].

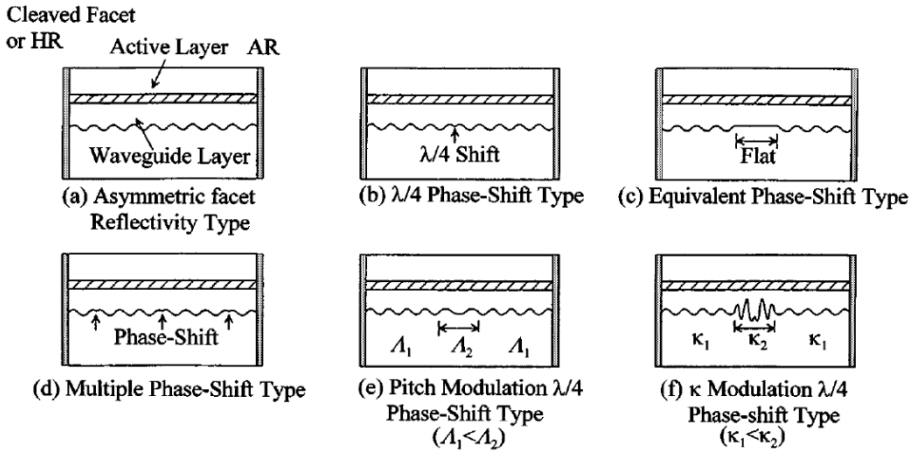

Fig. 2.3 Various types of DFB lasers [40].

In Fig 2.3.a, a DFB laser design is shown with a periodic reflection structure which was initially suggested by Kogelnik and Shank [50]. In this type of DFB laser two main adjacent modes have equal chance to emit and this was causing the emission stabilisation problems. As is seen in Fig. 2.3.b, to overcome this problem a phase shifted DFB laser was proposed and fabricated by Sekartedjo et al. in 1983 [52]. There are also other "phase-adjusted" DFB designs, as is shown in Fig. 2.3.c. The π/2-phase adjustment was achieved by connecting two distributed active reflectors with a waveguide inside the active section [53]. There are also DFB lasers with many phase shift regions, like shown in Fig. 2.3.d [54]. As a result of coupling of the two reflectors, the 5 times narrower linewidth (0.2 MHz) was achieved. In Fig. 2.3.e it is shown how

the mode selection can be improved with “corrugated pitch-modulation (CIP)”, and this resulted a 170-kHz narrow linewidth [55]. Later in 1993, a MQW CIP was introduced to DFB lasers, as is demonstrated in Fig.2.3.f, and this dramatically decreased the linewidth to 3.7 kHz [56].

DFB lasers are still the most popular semiconductor transmitters being used in long-haul communication systems and there is still great interest in investigating their design and operation [57] [58] [59] [60] [61]. In the recent studies, the directly or externally modulated DFB lasers demonstrating a 56 Gbps transmission speed and with good frequency stabilization have been demonstrated with InP membranes [62] and silicon waveguides to improve their integration with optical systems [63]. Considerable attention was paid to increasing the DFB lasers direct modulation bandwidth. This includes such techniques as optical injection and photon-photon resonance (PPR). Further discussion of injection-locked DFB lasers will be given in Section 2.4. Photon-photon resonance (PPR) is an effective technique that provides high resonance frequency enhancement in semiconductor lasers. The resonance frequency of the lasers is mainly restricted with the interaction between electrons and photons in the cavity. On the other hand in PPR technique, the adjacent cavity mode coupling is provided by a special laser design and photon-photon resonance between the dominant mode and first side mode is achieved. The frequency difference between the modes gives the new resonance frequency [64]. The first DFB laser with PPR was demonstrated by Radziunas et al. in 2007 [65] with around 40 GHz resonance frequency obtained. Recently it was shown by Dumitrescu et al. [66] that 37 GHz 3dB bandwidth is achievable, Fig. 2.4.

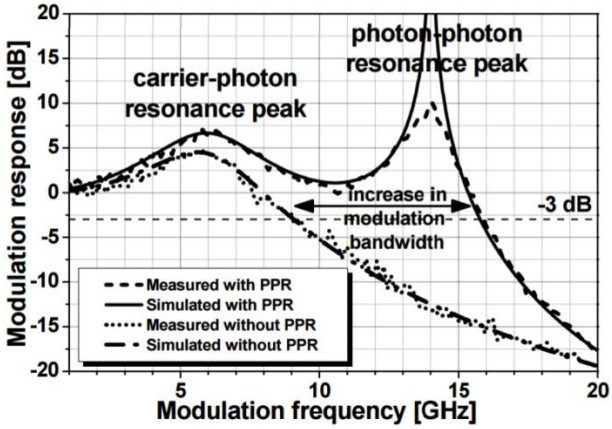

Fig 2.4. Small signal responses of the experimental and theoretical results with and without Photon-Photon Resonance [66].

Apart from DFB lasers, vertical cavity surface emitting lasers (VCSELs) were designed by Iga in 1977 to allow easily device fabrication and testing at various stages throughout the production process, which resulted in considerable increase of yield. Iga and his group has demonstrated the first GaInAsP/InP heterojunction VCSEL in 1979 [67]. VCSELs were designed to have perpendicular to the active region light emission rather than parallel to it as in conventional lasers, as is schematically shown in Fig. 2.5 [68].

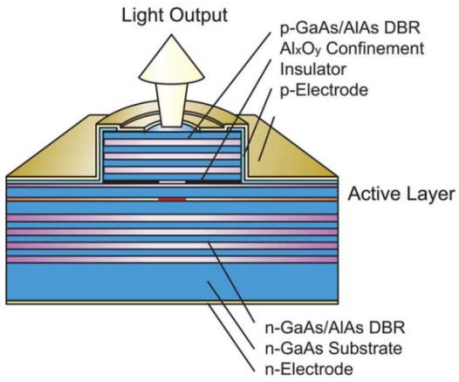

Fig. 2.5. Schematic representation of the VCSEL [41]

The only drawback of this first invented VCSEL was its high threshold current (at around 800 mA). The high threshold current problem was resolved in 1986 when a VCSELs with 6 mA threshold current was achieved by decreasing the active section thickness and using GaAs-based

material for the active section [69]. The first room temperature VCSELs were demonstrated in 1988 with 40 mA threshold current [70], and later in 1989 Lee et al. have reported a new design of VCSEL with 1-1.5 mA threshold current level [71]. Very soon after, Geels and Coldren demonstrated a VCSEL with super-low threshold current level (0.7 mA) [72]. As a result of all these studies VCSELs become a good source of optical emission for various applications. In 2007, Nishiyama demonstrated a low-power VCSEL which was stable for high temperature operation emitting at 1.3 and 1.5 μm wavelength [73] with subsequent 10-Gbps long-wavelength data transmission using this VCSEL. This was the first experimental demonstration of VCSELs utilisation for real telecom applications. There are recent studies on VCSELs to enhance its performance for fibre optical networks. On the other hand, VCSELs become very popular for other industrial applications (such as printers, video displays and recorders, optical sensors etc.) [74].

To improve fundamental characteristics of semiconductor lasers, different designs of active layers have been developed using advantages of novel growth technologies. In usual laser structures, the carriers are confined to bulk 3-dimensional (3D) regions, however in 1975 Van der Ziel has designed the first laser with quantum well (QW) active region **[75]** in which the carrier motion was 2D-confined. The double heterostructure single-QW and multi-QW CW injection lasers were soon developed and investigated by Dupuis et al. **[76, 77]** and by Rezek et al. **[78]**. Adding QWs in the active section resulted in a considerable reduction of the threshold current, increased frequency stability, and enhanced modulation bandwidth of the laser **[79]**. After developing the lasers with 2D QW quantised active regions, further enhancement of semiconductor laser performance was achieved by introducing the multi-dimensional confinement in active layers when the electrons are free to move only in one-dimension (1D), or using complete quantum confinement to zero dimension (0D) of free electron movement. The corresponding laser structures were called the quantum-wire (QWR) lasers or the quantum-dot

(QD) lasers, respectively, as was proposed by Arakawa et al. in 1982 **[80]**. The key advantages of the QWR and QD semiconductor lasers was that they were expected to exhibit very low threshold current, reduced temperature sensitivity, narrower spectral linewidth, and higher modulation bandwidth . All these improvements are of fundamental importance for development of novel high-performance optical transmitters for telecommunications.

2.3 Tunable Laser Diodes

There has been a great interest in wavelength tunable laser diodes since the beginning of the 1980s. Firstly, an integrated laser which consists of an active and a passive sections was demonstrated by Suematsu and his group in early 1980s [81] [82]. In these works, the effect of room temperature on the emission frequency of the single mode laser was investigated. After achieving the single mode operation with DBR reflectors, wavelength tuning was achieved by Tohmori at al. [83] [84]. The wavelength tuning was carried out by injecting electric current into the DBR passive section and changing the free-carrier contribution to the refractive index by increasing the injected carrier density. In these studies, the integrated monolithic laser was developed to keep the emission frequency as stable as possible under different conditions. The wavelength tuning in general can be achieved using various external effects on the refractive index change, like application of a strong external field, changing temperature, or injecting electric current. Each of these methods has advantages and disadvantages. The electric current injection is a particularly attractive tuning method due to its relatively low-insertion and technical simplicity. Still, even in the case of change of the DBR refractive index by current injection is necessary to use some additional design steps in order to keep temperature sensitive emission wavelength steady and to decrease mode hopping noise. The change in refractive index

under the current injection was initially explained only by the plasma effect, although it was shown later that the situation is more complex, as will be discussed later.

In addition to these efforts, Bell Labs worked on “etched groove” two active section devices to provide tuning [85] [86]. In this model the laser is consisted by only two active layers connected by an etched groove. The wavelength tuning was obtained by either changing the temperature or changing pre-bias level. In this model/design there is no DBR section to select emission wavelength.

There has been great improvement in the design of tunable laser diodes since 1985 [87] [84] [88] [89]. Suematsu and his group have demonstrated a stabilized high temperature single mode operation with DBR injection tuning in [84] and there was no phase section in this device. Additionally, the tuning range was severely restricted (0.91 nm). The tunable operation with phase and DBR tuning has been demonstrated by the same group later in [88]. In this study, the tuning range was increased to 5.8 nm. After this achievement, the tuning range was improved to 6.2 nm and with an additional waveguide improvement the 10-nm tuning has been demonstrated [89]. Also in [90] a two-section TLD with 11-nm tuning range is reported.

As can observed from the literature, two- or three-section TLDs could be tuned over only limited amount (11 nm maximum) during 1980s. The bandwidth of erbium doped fibres and gain spectrums of the semiconductor lasers were much bigger than the achieved tuning ranges [91] [92]. Investigations on the TLDs with wide tuning range and stable spectrum properties continued during 1990s due to the increasing importance of the WDM systems and high potential of the TLDs as key optical components of telecom systems. The tuning range $\Delta\lambda/\lambda$ was either equal or less than the obtained refractive index change $\Gamma\Delta\mu/\mu$ as it is discussed in literature [93] [94]. In [95], 38-nm tuning was achieved by using novel design with integrated interferometric section. Although this laser shows longer tuning range than in the previous

works, it had a poor SMSR (only 15-20 dB). To overcome the tuning range restriction in TLDs, a new TLD design with "sampled grating" was demonstrated in 1992 by Coldren's group [93]. As is seen in Fig. 2.6, a four-section device with two DBR sections, one active section and one phase section between them, were introduced to increase the tuning range to the 29.3 nm. In the concept demonstrated in the figure, by having two DBR mirrors with different periods, the aim was to get more stable high-performing tuning mechanism. In 1993 Larry Coldren and his group published theoretical framework of the novel Sampled Grating Distributed Bragg Reflector (SGDBR) laser [94]. In [96] and [97] a 57-nm and a 63-nm wide tuning ranges were demonstrated for the first time by improving the design concept.

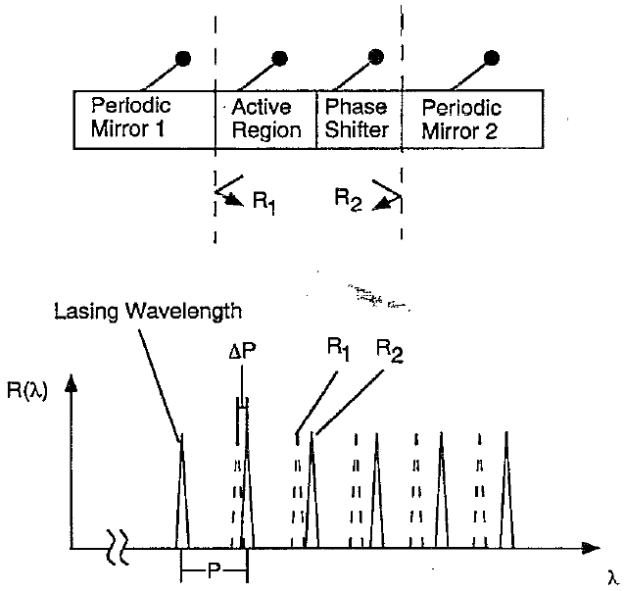

Fig. 2.6 Schematics of sampled grating tunable laser diode and its tuning concept [92].

There is at present a great interest in the operation of tunable lasers and enhancement of their performance. Tuning range and power performance (stability of power output under the wavelength tuning) are the most important challenges to achieve a cost effective and technologically advanced WDM transmission. Wavelength tuning of TLD is mostly achieved by changing the refractive index of DBR section with free carrier (FC) contributions as was demonstrated by Okuda in 1977 [98]. There are different models describing the refractive index

change via FC contributions. The Kramers-Kronig effect on refractive index change was investigated by Henry in 1981 [99] in connection with studies of the linewidth enhancement α-factor in the fixed wavelength lasers. The effect of free carrier contributions, band-filling effect, band-gap shrinkage and free-carrier absorption on the change of refractive index was theoretically investigated in [100]. It was shown that band-filling effect and free-carrier absorption effects is decreasing the refractive index, on the other hand the band-gap shrinkage is increasing it. There were also other important experimental and theoretical studies on the free carrier contributions [101] [102]. It is important that practically all these works were limited to investigation of the material refractive index change under the free carrier injection. In theoretical studies of sampled grating TLDs which demonstrate very wide tuning ranges, usually only plasma effect was considered [103] [104]. Recently, it was shown in the first self-consistent numerical analysis of widely-tunable TLD by Kyritsis and Zakhleniuk [105] that optimising the design of the DBR section, a large 30-nm tuning range can be achieved in a 3-section classic device design. Later in 2016, the main limiting factors which affect the wavelength tuning range and the output power performance of the same TLD were studied in [106]. According to the obtained results, it was demonstrated that the shape of the gain spectrum and DBR reflectivity spectrum, the intervalence band absorption (IVBA) coefficients in DBR section, and the physically different roles played by the IVBA loss in the DBR passive section and in the active section (where it defines the net gain (g_{net})) are directly affecting the wavelength tuning range and the output power change of the TLD under tuning.

2.4 Optically Injection-Locked Semiconductor Lasers

Directly modulated semiconductor lasers allows cost effective high-performance transmission in optical fibre networks. To improve the fundamental modulation characteristics of the laser transmitters, directly modulated (slave) laser is locked to another (master) laser through the light injection into the slave laser cavity. It has been shown that spectral purity can be dramatically improved and modulation bandwidth of the laser can be enhanced by the optical injection locking.

Injection locking is fundamentally based on a physical mechanism which was first discovered in 17^{th} century [107]. Huygens showed that the pendulums of clocks on the same wall will finally have the same frequency and lock each other [107]. This mechanism was later applied to radio communications and the properties of electrical injection locking were studied in 1946 by Adler [108]. After the invention of the lasers at the beginning of 1960s [35], Stover and Steier presented the first experimental demonstration of the injection locking in 1966 [109]. In this study, two HeNe lasers operating at 632.8 nm were locked by injecting light directly from the first laser to the second one. The investigations of the injection locked lasers later shifted to various new types of lasers that have been constructed, and CO_2 lasers were experimentally investigated in [110]. The main aim of injection locking investigations of these lasers was to stabilise the frequency and the phase of the optical oscillators [23].

The injection locking technique was applied to semiconductor lasers for the first time in 1980 by Kobayashi and Kimura [22]. The same group experimentally demonstrated in 1981 [111] the frequency modulation (FM) noise reduction under the injection locking. Also the modulation dynamic response improvement of the directly modulated injection-locked laser was investigated in 1982 [112]. The physical mechanism of injection-locked semiconductor laser operation was

studied using the rate equations in 1982 [15]. Since that time there have been many studies on the dynamics of the OIL lasers, and its effects on the laser operation in various regimes.

An optically injection-locked laser can exhibit different spectral dynamics due to the complex interaction between the injected light wave and the wave generated in the free running laser cavity. The nonlinear effects of optical injection locking have been demonstrated in different studies. There were different reported regimes of the laser operation under optical injection, like stable locking, four-wave mixing, period-one, and chaotic regime. Stable and unstable regimes were experimentally demonstrated by Kobayashi and Kimura in 1980 [22]. Theory of stable locked regimes was developed in [15] taking into account the carrier dependent refractive index change and its effect on the locking maps. This effect was explained using the Henry's alpha factor [99]. The observed asymmetric behaviour of the locking curve was shown to be a result of alpha factor effect. This result was also experimentally demonstrated in [113] where the locking bandwidth of injection locked laser is also investigated.

In Fig 2.7 locking bandwidth is plotted for different alpha factors in order to show its effect on locking [114]. In addition to this result, it was also shown that the spatio-temporal travelling wave model provides more accurate results than the rate equation model, in particular for cases of higher injection power ratio. There have also been later many subsequent studies on stable locking [25] [26] [115] [116] [117], period-one [118] [119], four-wave mixing [120] [121], and chaotic regimes [122] [123].

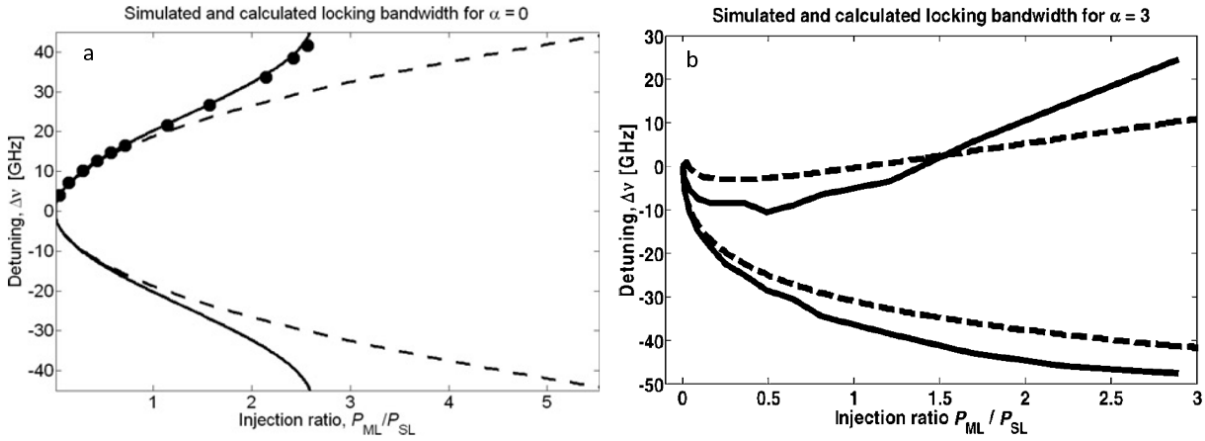

Fig. 2.7 Locking bandwidth of the optically injected laser for high injection ratio. (a) The locking bandwidth obtained for alpha = 0. The solid line shows the results produced with travelling wave model, and the dashed line shows the results from rate equation model. Simulation results are given with dots. (b) Asymmetric locking range calculated for alpha = 3 [114].

As was already mentioned, directly modulated semiconductor lasers are considerably more cost effective network elements compare to externally modulated lasers because of high cost of external modulators. There are however, fundamental laser characteristics which limit the capabilities of directly modulated lasers. The desirable change and enhancement of these characteristics, such as resonance frequency, turn-on delay, frequency chirping, and relative intensity noise, have been investigated with injection locking in different studies [107]. There has been great interest in the bandwidth enhancement of the optically-injection locked (OIL) semiconductor lasers since the first application of the injection locking in studies of semiconductor laser dynamics was achieved in 1982 [124] [125] [126] [127] [125] [128] and [129].

Various physical reasons for the bandwidth enhancement have been discussed in several studies. Wang et al. [126] indicated the increase of the photon number in a cavity as a reason of the enhancement, but it was not given as a major factor. The main reason of the bandwidth enhancement was explained as the effect of coupling of the phase and field amplitude of the

cavity's complex field. On the other hand, Yabre explained the reason of resonance frequency enhancement as the coherent addition of the injected light field to the slave laser's own field, rather than the increase of the photon number [127]. Another explanation, which is given in [128] and [130], shows that the bandwidth enhancement is depended on the frequency difference between the shifted lasing cavity mode of the slave laser and the injected light of the master laser. This case was theoretically investigated and explained in [17]. First of all, the effect of injection parameters (detuning frequency, injection power ratio) on bandwidth enhancement was studied at depth and it was shown that by keeping the detuning frequency constant, the resonance frequency can be increased dramatically by increasing the injection power ratio. Although the increase in the power ratio provides higher resonance frequency, the transfer function of the slave laser is decreasing. This result can be seen in Fig. 2.7.a. Another studied regime corresponds to the case when the power ratio is kept constant, but the frequency detuning (which is defined as the frequency difference between the master and slave lasers) is varied in order to show its effect on the modulation bandwidth enhancement. As can be clearly seen from Fig. 2.7.b, the positive detuning provides higher transfer function and higher resonance frequency than the negative detuning. The effect of positive and negative detuning on resonance enhancement was shown to be similar in [17]. This case was also investigated experimentally and theoretically for OIL DFB laser in [131].

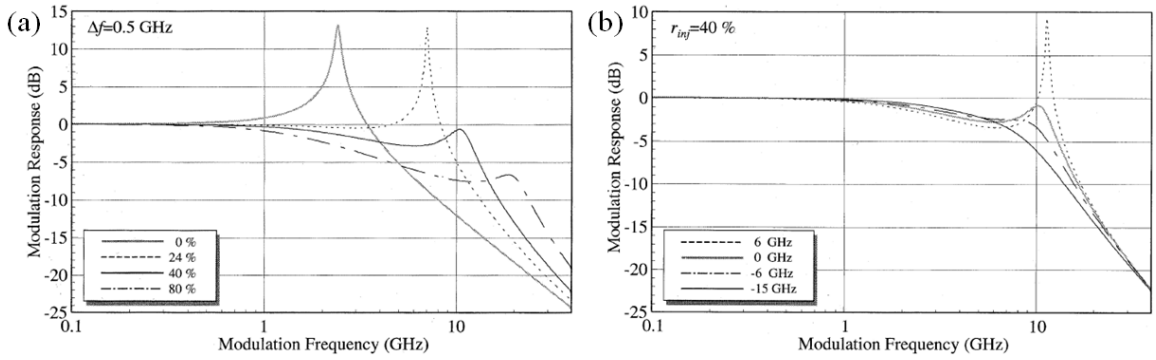

Fig. 2.7. Small signal modulation response of the OIL laser corresponding to: a) fixed detuning frequency (0.5 GHz) vs various injection ratios. b) fixed injection ratio (%40) vs various detuning frequencies [17].

Recently, Sung and Lau showed that it was possible to obtain 72-GHz resonance frequency and 44 GHz modulation bandwidth in directly modulated lasers which operated under injection locking [131]. Relationship between the alpha factor related to the cavity shift and the bandwidth enhancement was also experimentally shown. The upper limit on the bandwidth enhancement was directly related to the detuning frequency. It was explained that the detuning frequency is also limited by the inter-mode distance. In [132] Lau demonstrated the 100-GHz small signal response for OIL DFB and VCSEL lasers and the bandwidth enhancement was shown to be a function of the coupling quality factor (Q factor) [133].

The fundamentals of bandwidth enhancement effect by the optical injection are still under investigation in many studies. There are recent studies on the OIL ring lasers. In 2009 more than 40-GHz 3-dB modulation bandwidth was demonstrated with optical injection locking of semiconductor ring laser [134]. In 2011, Smolyakov et al. theoretically proposed a new monolithically integrated OIL ring laser scheme to obtain very high resonance frequency enhancement [135]. According to their numerical model, they predicted up to 160 GHz resonance frequency enhancement with OIL. On the other hand, the modulation response of the designed ring lasers did not show a good result for low modulation frequencies, and in 2015 a

cascaded model of ring laser was presented to overcome this problem. It was theoretically shown that 160 GHz modulation is possible with good low frequency modulation response [136].

Another important parameter of the directly modulated laser is the frequency chirping which strongly affects long haul transmission quality. It has been shown in several studies that frequency chirping can be dramatically reduced by injection locking [107] and [137]. The frequency chirping reduction with optical injection was first demonstrated experimentally by Piazzolla in 1986 [124]. The chirp to power ratio (CPR), which is an important parameter for directly modulated lasers, shows the lasing frequency deviation of the modulated laser with change in the output power. The small-signal analysis of the OIL laser showed that the CPR of directly modulated laser drops dramatically under the injection locking. Early studies on chirp reduction were showing 2 Gbps transmission speed by the directly modulated lasers with low chirping under moderate light injection [138] [18]. Mohrdiek [139] demonstrated that the moderate light injection is not sufficient in order to achieve small lasing frequency deviations for higher modulation speeds (around 10 Gbps), but on the other hand it was also shown that higher injection ratio (more than 0.1) would be useful to reduce the chirping. In 1996, Yabre theoretically demonstrated the CPR reduction in the OIL lasers using the rate equation model under strong injection locking regime [127]. Due to its strong effect on frequency stabilisation of directly modulated lasers, the injection locking is still under intensive investigation in various recent studies [140] [114].

It has been also demonstrated that the relative intensity noise (RIN) of the directly modulated laser can be dramatically reduced with injection locking [107]. In 1986, Schunk and Petermann published the first theoretical study of the analysis of RIN reduction in injection locked lasers [141]. By using the same equations, the RIN reduction was simulated in [129], [142], [143], and the results were confirming the considerable RIN improvement. Finally, in 2003, the first experimental investigation of the RIN reduction with the light injection were published by

Chrostowski et al. [19]. It was clearly shown that the RIN response is following the resonance frequency and important amount of RIN reduction can be observed in OIL lasers by positive frequency detuning.

Injection locking technique has also been applied to tunable laser diodes and different effects of light injection on laser operation have been investigated. Since the analysis of multi section lasers is more complicated than single section lasers, there is still more questions to answer about multi section OIL lasers. One of the early reports show, using the rate equation model, that the injection locking technique is applied to a three section TLD to achieve the CW lasing frequency stabilisation [144]. It is necessary to note, however, that this study did not investigate and did not address any questions related to modulation dynamics of TLD under the OIL conditions, or to mapping possible regimes of the lasers in these conditions. To obtain the dynamic map of the optically injected tunable laser diode, Labukhin et al. showed that the travelling wave model is more adequate and more accurate than the conventional rate equation model [114]. Later in 2010 Labukhin et al. published a detailed analysis of the nonlinear dynamics of optically injected TLD with various spectral behaviours (different locking regimes) [21].

The bandwidth enhancement of the OIL TLD was for the first time experimentally observed by Lee et al. in 2000 [145]. Later in 2010, experimental investigation on the modulation response of the OIL sampled grating (SG) TLD was published by Bhardwaj et al. [146]. In this study the resonance frequency enhancement from 1.05 GHz to 20 GHZ was demonstrated for different detuning frequencies. These results prove that the injection locking can dramatically increase TLD laser modulation and that the OIL technique could be applied to the other tunable lasers. The important question which needed to be answered is about the effect of tuning regimes and optical injection parameters on the tunable laser modulation characteristics. This question, however, was not investigated in [146]. This question has recently been discussed in one of our own studies using the travelling wave approach which is necessary to simulate the multi-section

lasers, where considerable modulation characteristics improvement of the OIL TLD have been demonstrated for various tuning regimes [147]. The adequate gain spectra were also calculated and taken into account in our integrated model to improve physical scope and the accuracy of the simulation. The effect of injection parameters, detuning frequency and injected power ratio on resonance frequency enhancement has been investigated, which will be later presented and discussed in this thesis.

CHAPTER 3

BASICS OF THEORY OF SEMICONDUCTOR MATERIALS AND SEMICONDUCTOR LASER DIODES

3.1 Review of Basic Properties of Semiconductor Materials and Devices

Semiconductor materials which are used in various components of telecom systems, such as optical transmitters (lasers), receivers, modulators, amplifiers, etc., have a crystal structure. Crystal structure is one of the most fundamental features of solids which directly define their physical properties and the key device parameters. The crystal structure consists of periodically repeating blocks or elementary units (cells) which can be either produced by nature or artificially engineered and manufactured. In order to obtain semiconductor materials with the required physical properties for various device applications, there have been many investigations on material chemistry and growth techniques which allow scientists and engineers to build novel crystal structures with novel elementary blocks.

It is essential for a quantitative analysis and description to define the lattice structure in terms of some basic parameters which allow to show how a crystal structure is constructed [148]. A lattice structure involves points which are periodically distributed in space. Each lattice point is attached to a basis to produce the crystal structure. In Eq. (3.1), it is show how two lattice points, $\vec{R}$ and $\vec{R}'$, are connected via the three vectors $\vec{a}_1$, $\vec{a}_2$, $\vec{a}_3$.

$$\vec{R}' = \vec{R} + m_1\vec{a}_1 + m_2\vec{a}_2 + m_3\vec{a}_3 \tag{3.1}$$

It shown in Eq. (3.1) that the $\vec{R}'$ point of the lattice can be derived by using the other lattice point $\vec{R}$ and three vectors with the integers m_1, m_2, m_3. The three vectors $\vec{a}_1$, $\vec{a}_2$, $\vec{a}_3$ define the crystal lattice basis. They define the smallest possible elementary unit which is called a primitive unit cell.

Each lattice structure possesses a certain symmetry which in general can be achieved by applying operations of rotation. To fill in a limited volume with unit cells, it is important to have rotations with 2π, 2π/2, 2π/3, 2π/4 and 2π/6 angles. Other rotations like 2π/5 or 2π/7 are not possible to fill in the volume [148]. The lattice structures can be defined using different primitive unit cells. Cubic lattices are one of the most common lattice structures, and three types of cubic lattices are shown in Fig. 3.1 below [148].

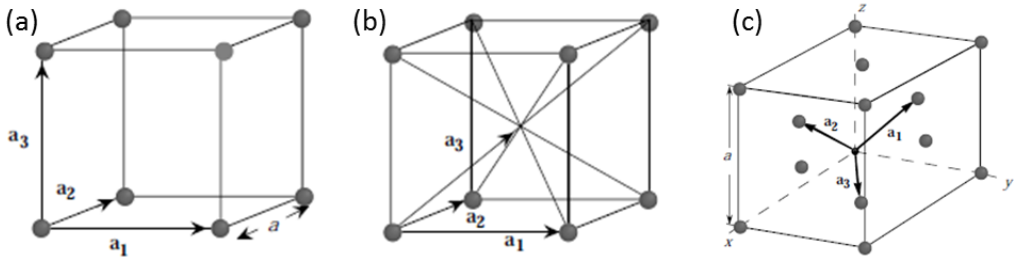

Fig. 3.1 Cubic lattice structures: (a) Simple cubic (b), Body-centred cubic, (c) Face-centred cubic [148].

In Fig. 3.1.a, a simplest cubic structure called Simple Cubic is illustrated. The primitive vectors of the Simple Cubic unit cell can be presented as [148]:

$$a\vec{x}, a\vec{y}, a\vec{z} \tag{3.2}$$

The cube edge has a length a, and $\vec{x}, \vec{y}, \vec{z}$ represent the basis unit vectors. This structure has not been found in any semiconductor material in nature. (The only material in nature which possesses the Simple Cubic structure is a conductor Polonium).

The other crystal lattice shown in Fig. 3.1.b represents the Body-Centred Cubic (bcc) structure. The difference between bcc and Simple Cubic lattice is that it has the point (atom) in the centre of the cube. As is illustrated in Fig 3.1.b, the distance between the lattice points is not the same as in the simple cubic lattice. As a result of this, the primitive vectors of the bcc structure can be presented as:

$$\vec{a}_1 = a\vec{x}, \quad \vec{a}_2 = a\vec{y}, \quad \vec{a}_3 = \frac{a}{2}(\vec{x} + \vec{y} + \vec{z}) \tag{3.3}$$

The last cubic lattice type of the crystal structure shown in Fig. 3.1.c, is called the Face-Centred Cubic (fcc) lattice. It is the most common lattice structure of semiconductor materials. The fcc can be produced by adding points to the centre of the each cube faces. The primitive vector of this model can be presented as:

$$\vec{a}_1 = \frac{a}{2}(\vec{y} + \vec{z}), \quad \vec{a}_2 = \frac{a}{2}(\vec{z} + \vec{x}), \quad \vec{a}_3 = \frac{a}{2}(\vec{x} + \vec{y}) \tag{3.4}$$

There are two types of semiconductor structures based on the fcc: Diamond and Zinc Blende structures [149]. The fcc structure has a two-atom basis (two atoms in elementary cell) and if these two atoms are the same, the structure is called the Diamond structure. On the other hand if the atoms are different, the structure is called the Zinc Blende structure. For example, Si and Ge are semiconductor materials which have Diamond structure. They are also called the elemental semiconductors. Such important semiconductors as GaAs, GaP, InAs, InP have Zinc Blende lattice structures. Because they consist of different chemical elements they are called the Compound Semiconductors. Compound semiconductors are classified according to the position of their elements in periodic table's groups. These classes are:

GaAs, AlAs, InP, etc. – III-V Semiconductors

CdS, HgTe, CdTe, etc. – II-VI Semiconductors

3.2 Electrons in Crystals

Free electrons in semiconductor materials play important role in operation of semiconductor devices based on these materials under the action of external forces. To understand how the

electrons behave according to quantum mechanics, it is essential to specify the energy, the position, and the momentum of these particles and their responses to internal and external fields. According to De Broglie, a moving particle's frequency and its wavelength can be calculated from its energy (E) and momentum (p) as follows [149]:

$$\nu = \frac{E}{h} \tag{3.5}$$

$$\lambda = \frac{h}{p} \tag{3.6}$$

Here h denotes Planck's constant (6.63×10^{-34} Js). The second De Broglie relationship can also be presented in another form using concept of wave vector, as is shown in Eq. (3.7):

$$p = \hbar k \qquad (\hbar = h/2\pi) \tag{3.7}$$

The wave vector k is defined by the electron wavelength:

$$k = \frac{2\pi}{\lambda} \tag{3.8}$$

After understanding the relation between the particle's energy and frequency and momentum (wave vector) and wavelength, it is also fundamentally important to establish the relationship between the energy and momentum – the so-called energy dispersion law. The energy dispersion law necessary in order to adequately describe electron dynamics in crystals under the action of external forces and the electron (hole) interaction with photons (electromagnetic field) or the other fields (e.g. collective lattice vibrations – phonons). In general, the dependence of the electron energy E on momentum $\vec{p} = \hbar\vec{k}$ is given by some function $E = E(\vec{p})$. For a classical particle the total energy is given by the sum of its kinetic energy $p^2 / 2m_0$ (where $\vec{p}$ is a true momentum of a particle, $\vec{p} = m_0\vec{v}$, $\vec{v}$ is a particle velocity) and potential energy $U(\vec{r})$, as

expressed in Eq. (3.9). The momentum $\vec{p}$ of the electron in a crystal becomes a quasi-momentum since it reflects both a particle-like and a wave-like properties of the electron and it becomes discrete-valued contrary to usual momentum of a classical particle which is continuous. In presence of external electric $\vec{F}$ and magnetic $\vec{H}$ fields, the electron momentum obeys a standard Newton's equation of motion explain the dependency between momentum and energy, and how momentum changes under the action of external like in Eq. (3.9) and Eq. (3.10) [149]:

$$E = \frac{p^2}{2m_0} + U(r) \tag{3.9}$$

$$\frac{d\vec{p}}{dt} = \vec{F}_{ext} = -e\left(\vec{F} + \frac{\vec{v}}{c} \times \vec{H}\right) \tag{3.10}$$

The electron motion in a crystal is described by the quantum-mechanical wave equation (or the Schrödinger equation) which is given in Eq. (3.11) (for simplicity we discuss here a one-dimensional case of x – coordinate dependence):

$$-\frac{\hbar^2}{2m_0}\frac{\partial^2 \Psi_k(x)}{\partial x^2} + U(x)\Psi_k(x) = E\Psi_k(x) \tag{3.11}$$

The quantum state of the electron is described by the wave function $\Psi_k(x)$. The potential energy of the electron is given with U(x) which includes all fields acting on the electron from the ions and the other electrons in a crystal, but does not include any external field. As a result, the electron behaviour in a semiconductor crystal structure becomes very different than in the free space. The potential energy U(x), which is constant or a zero for free electron, becomes non-zero coordinate-dependent quantity in a crystal due to its periodical atomic structure.

For zero potential energy, the stationary solution of the Schrödinger wave equation is given by Eq. (3.12):

$$\Psi(x,t) = e^{-i(\omega t)}\Psi_k(x) = Ae^{-i(\omega t - k\,x)} \tag{3.12}$$

where $\omega = 2\pi\nu$ and $E = \hbar\omega = \hbar^2 k^2 / 2m_0 = p^2 / 2m_0$ is the electron energy.

When the electrons are in crystals, their energies are restricted by the values which are consistent with the Schrödinger equation. To solve Schrödinger equations for these electrons, it is important to take the effect of the crystal structures fields into account. Potential energy due to the interaction between a given electron and the other electrons is an important phenomenon and should be added to Schrödinger equation. The periodical crystal structure is also another important feature to be considered in defining the electrons' behaviour. The spatially-periodic dependency of the potential energy change of electrons in periodic crystal is implied to the wave equation by the Bloch theorem:

$$\Psi(x + na) = e^{ikna}\Psi_k(x) \tag{3.13}$$

Here in Eq. (3.13), the lattice constant is presented with a and n is an integer number. On the other hand, if only the spatial dependence of the wave function $\Psi_k(x)$ is known, it is also possible to calculate the probability of the distributions of electrons in a crystal. An important outcome of the Bloch theorem as applied to the electrons in crystals, is that the allowed values of the electron's wave vector k (or the momentum $p = \hbar k$) are confined to a region of the inverse space given by the relationship $-\pi / a \le k \le \pi / a$. This region is called the Brillouin zone. As is seen in Fig. 3.2 below, the electron energy in the crystal structure has 2π/a long periodicity [150].

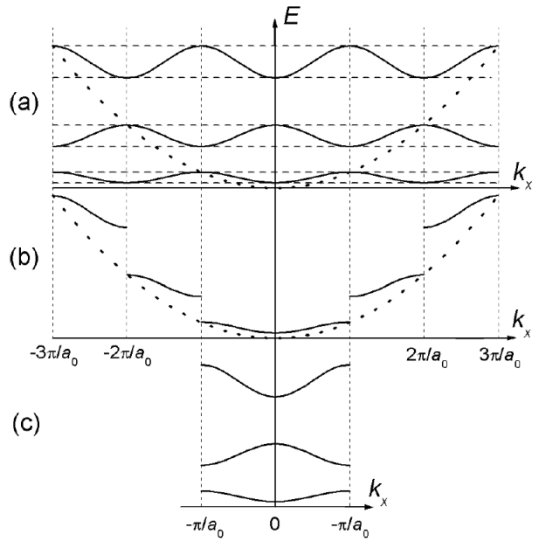

Fig. 3.2 Energy distributions demonstrations for different approaches [150].

In general, the Brillouin zones have complex 3-dimensional shape which reflects symmetry of a particular crystal structure. The electron energy dispersion $E(\vec{k})$ is obtained from the solution of the Schrödinger equation and it is in general quite a complex function which for practical semiconductors can be obtained by numerical solution. The free electron mass m_0 in Eq. (3.10) is needed to be adjusted for crystal structure. Instead of a free electron mass it becomes the effective mass which takes into account the crystal fields acting on the electron. Particular importance (but not the only one) of the effective mass is demonstrated in case if the electron energy is close to the energy bandgap. In this case the energy dispersion becomes a simple parabolic function $E(\vec{k}) = \hbar^2 k^2 / 2m^*$ in many semiconductors (particularly for III-V semiconductors, like GaAs). The effective mass of the electrons near the bandgap becomes constant and is in case of cubic structure is calculated as $1/m^* = (1/\hbar^2) \times \partial^2 E(k) / \partial k^2$. For direct bandgap semiconductors, this mass appears near k=0 point in the Brillouin zone. The effective mass is one of the key parameters which defines the electron dynamics in semiconductor crystals under the action of the external fields, electron transport properties (current), and the electron population in the conduction and valence energy bands under doping

or external injection of free carriers. The latter is of particular importance in semiconductor laser diodes, as will be discussed later.

3.3 Population Statistics and Fermi Distribution Function in Semiconductors

In semiconductor materials, there are different quasi-particles from point of view of their statistics: Fermions and Bosons. Electrons, neutrons and protons are classified as Fermions, and photons and phonons are classified as Bosons. The statistical distribution of particles over the energy states is an important matter for calculation of collective properties of the particle ensembles. This is because the contribution of each particle to the collective property (e.g. the electric current) depends on its energy as well as on the number of particles in each energy state. To explain how energy states are filled it is essential to take into account the spin of particles. While Fermions have half-integral spin ($\hbar/2$, $3\hbar/2$..), Bosons have either zero or an integral spin (0, $\hbar$, $2\hbar$..) [149]. Generally, one energy state is occupied by one Fermion with a given spin. Only if two Fermions which have different spins $\hbar/2$ and $-\hbar/2$ they can occupy the same energy state. This situation is different for Bosons. An energy state can be occupied by many Bosons and it is not possible to distinguish them.

A rigorous quantum-statistical theory gives the particle population probability of a state (with a given spin) as a function of the energy of this state. Such population probabilities are called the distribution functions of the particles. For electrons in crystals (such as metals, semiconductors, dielectrics) the distribution is given by the Fermi distribution function which can be presented as:

$$f(E) = \frac{1}{1 + \exp\left[\dfrac{E - E_F}{k_B T}\right]} \tag{3.14}$$

Here k_B is the Boltzmann constant, T is temperature in Kelvin, and E_F is a parameter of the distribution which is called the Fermi energy.

The occupied energy densities can be statistically analysed using Eq. (3.14) and the occupation probability of energy states for different temperatures are shown in Fig. 3.3. The probability drops to 0.5 at $E=E_F$ and this level is called as the Fermi level. This level is also the highest energy level the particles (electrons) occupy when T=0K. Additionally, when T=0K, the valence band is full of electrons and the conduction band is empty semiconductors or dielectrics (but not in metals where the valence and conduction bands overlap and there will always be electrons in the conduction band even at T=0K). Another important result from the Fig. 3.3 shows that the probability of particle occupation for energy states above E_F energy increases with higher temperatures.

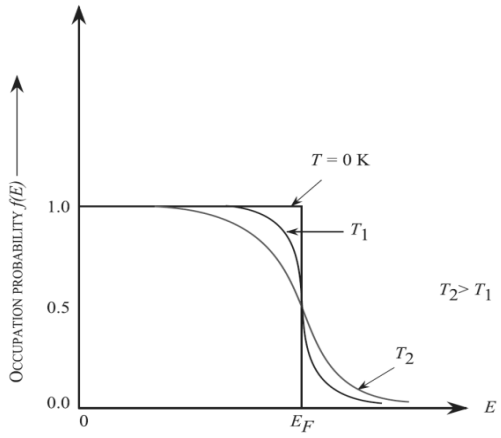

Fig. 3.3 Fermi Distribution Function for different temperatures [149].

By using Fermi distribution function and the electron density of states D(E), the electron and the hole densities within a small energy interval are found as [150]:

$$dn(E) = D_c(E)\, f(E) dE \tag{3.15}$$

$$dp(E) = D_v(E)\left[1 - f(E)\right] dE \tag{3.16}$$

For simple parabolic energy dispersion, the density of states in conduction and valence bands can be computed as:

$$D_c(E) = \frac{1}{2\pi^2}\left(\frac{2m_c}{\hbar^2}\right)^{3/2}\sqrt{E - E_c} \tag{3.17}$$

$$D_v(E) = \frac{1}{2\pi^2}\left(\frac{2m_v}{\hbar^2}\right)^{3/2}\left(\frac{2m_v}{\hbar^2}\right)^{3/2}\sqrt{E_v - E} \tag{3.18}$$

Where m_c and m_v represent the effective masses in conduction (electrons) and valence (holes) bands, respectively, and $E_{c(v)}$ is the conduction (valence) band edge. The Fermi distribution in Eq. (3.14) allows further simplification for particular cases of high or low temperatures and carrier densities. In the former case the exponent in the denominator can be neglected and $f(E) = 1$ for $0 < E < E_F$, and $f(E) = 0$ for $E > E_F$ where the exponent in the denominator becomes (infinitely) large. This case is called a completely degenerate state of the electron gas which takes place at high carrier densities and low temperatures (in heavily doped semiconductors or metals). In the latter case, at high temperatures and small carrier densities, the Fermi energy becomes negative and the exponent in the denominator of Eq. (3.14) becomes large, one can then neglect 1, and the Fermi distribution becomes $f(E) = \exp\left[-(E - E_F)/k_B T\right]$. This is the Boltzmann distribution function which is also applied to particles in a gas. This case corresponds to a non-degenerate electron gas in semiconductors which takes place at low carrier densities (lightly doped semiconductors) and high temperatures (in many practical cases at the room temperatures).

3.4 Energy Levels and Band Structures

The separated energy bands play an important role to transport carriers through semiconductor sample under the influence of the applied electric field (electric current). If the allowed energy band does not have available empty states to accept/move electrons, the electrical current cannot be transported. This type of materials is electrically insulated. On the other hand, metals which are highly conductive materials have plenty of unfilled energy levels (states). This makes it possible for the electrons move over these states with the external forces present.

Most of semiconductor materials do not allow for the electrons to move when the temperature is 0 K since they occupy the lower-energy valence band in which all states are filled with the electrons. When the temperature is increased, some valence electrons can be excited to the upper conduction band with plethora unfilled states and conducting feature of the material increases.

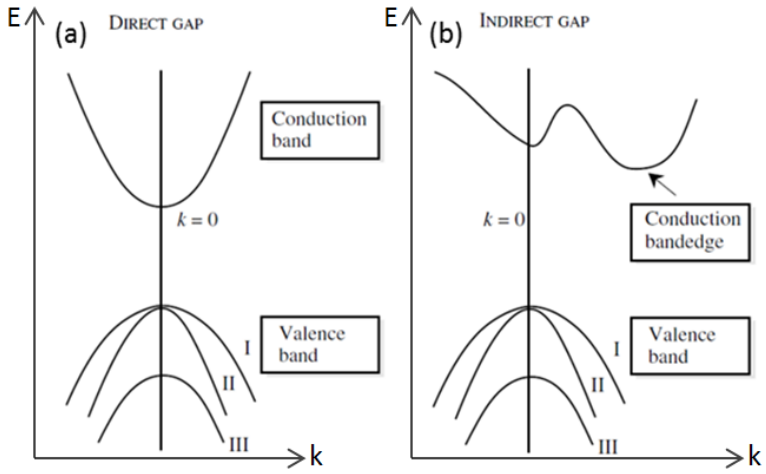

Fig. 3.4 (a) Direct and (b) indirect bandgap representations of semiconductors[148].

The semiconductors are generally classified by their bandgap structures. If the both the conduction band minimum edge and the valence band maximum edge of a semiconductor are located at the wave vector point k=0, such semiconductors are called the direct bandgap semiconductors, as is shown in Fig. 3.4.a. On the other hand, if these bandgap edges are on

different locations, like in Fig. 3.4.b, such semiconductors are called the indirect bandgap semiconductors. The different valence energy states shown in Fig. 3.4 with I, II and III are called the Heavy-Hole Band (I), Light-Hole Band (II), and Split-Off Band (III), respectively [149]. The direct bandgap semiconductors, such as Gallium Arsenide GaAs, Indium Phosphide InP, have strong light conversion by the electron transition between the valence and conduction energy bands due to the their direct bandgap structure. However, semiconductors like Si, Ge, and AlAs which have indirect bandgap structure, demonstrate weaker electron interaction with light. In Fig. 3.5 below, the valence-conduction band representations of some semiconductors with direct and indirect bandgap structures are shown.

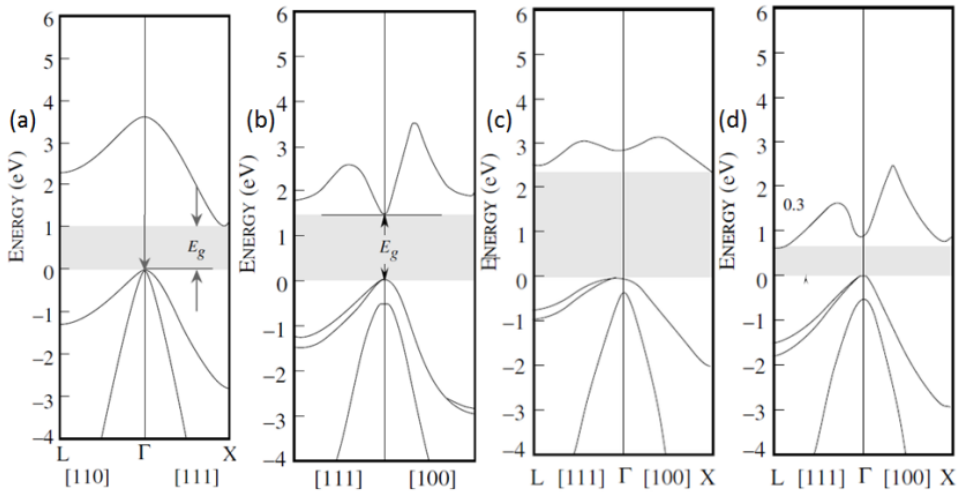

Fig. 3.5 Band structures of different semiconductor materials: (a) Silicon S (b) Gallium Arsenide GaAs (c) Aluminium Arsenide AlAs (d) Indium Phosphide InP [149].

Although Silicon has an indirect bandgap property, it is one of the most the popular semiconductor material used in electronics. The main reason of it comes from its natural purity for manufacturing. Its band structure is demonstrated in Fig. 3.5.a above. The bandgap from the bottom of conduction band to the top of the valence band is 1.1eV. Due to this natural drawback for the light emission by the electron transitions, Silicon cannot be used in such active devices as lasers. However, it is the most popular material for manufacturing various electronic devices,

such as diodes and transistors. Its oxide, like SiO_2, can be used as an isolator for high-field (more than 20kV/cm) electronic devices such as metal-oxide field-effect transistors.

On the other hand, GaAs has a direct bandgap structure as shown in Fig. 3.5.b, and this feature makes it useful for utilisation as an active material in laser production. Its bandgap structure makes the E-k conduction band energy dispersion relation quite simple (parabolic) within the effective mass approximation at reasonably small energy values (less than 0.1 – 0.3 eV) [149]:

$$E = \frac{\hbar^2 k^2}{2m^*} \tag{3.19}$$

The effective mass m^* of GaAs is 0.067 m_0, where m_0 is the free electron mass. (Note, that the valence band energy dispersion has generally more complex non-parabolic shape. The only drawback of GaAs semiconductor is more complex manufacturing compared with Si, although the technology is quite mature at present. Since it is a compound material, it is easy to have more structural imperfections. On the other hand, it has a larger bandgap (1.43 eV) compare to Si, and has good electrical and optical characteristics and temperature and radiation stability. The temperature change directly affects the bandgap of semiconductors. For GaAs the bandgap is 1.51eV for when temperature is 0K. If the temperature increases to 273K the bandgap reduces to 1.43eV due to increase of the interatomic distance under material expansion.

Other semiconductor material AlAs shown in Fig. 3.5.c has an indirect bandgap structure but since it has good lattice match with GaAs it is mostly used in making the heterostructure lasers with GaAs as active layer and AlGaAs as barriers (AlGaAs/GaAs/AlGaAs heterostructure). Another semiconductor material which has a direct bandgap is Indium phosphate InP. It is also very popular in manufacturing infrared lasers for telecommunication using compounds like InGaAsP as active layers (due appropriate bandgap values) and the lattice-matched InP as barrier in laser designs.

3.5 Holes in Semiconductors

In most semiconductors, valence band is entirely occupied by electrons when the temperature is 0 K. If the temperature increases, some electrons start making transitions to conduction band leaving the unfilled states in the valence band which are called the holes.

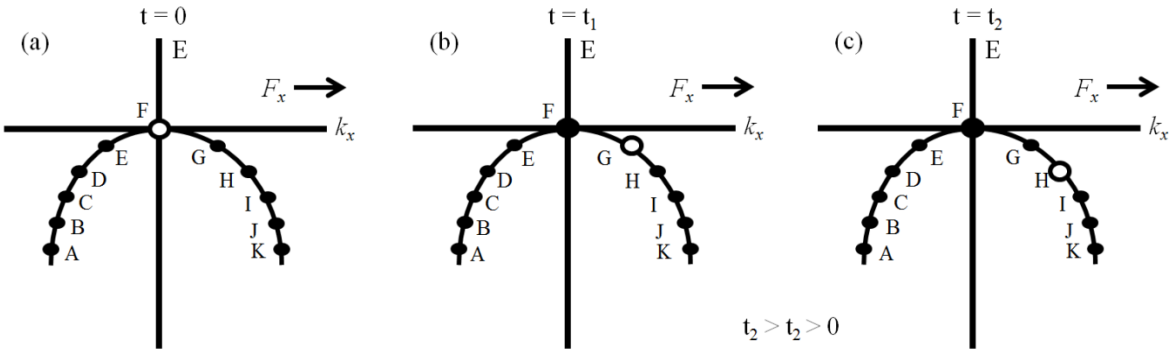

Fig. 3.6 Movement of holes in semiconductor lasers with external forces [149].

When the valence band is full with electrons, it is not possible to transport currents. To have an electron movement in valence band, it is essential to provide empty states - holes. The electron and the hole behaviour under the external force is illustrated in Fig. 3.6. The negative charged electrons move in the opposite direction to the electric field direction. In Fig 3.6.a, the empty state is initially located at k_x=0. When the electric field is applied to the semiconductor material, the electron on the right hand side of the hole fills the hole's position and the electron's previous position leaves another hole. As long as the electric field is applied, hole in valence band seems to move in the direction of the electric field. It is necessary to note that this is a very simplified picture and rigorous quantum-mechanical description of the electron/hole dynamics in the valence band is considerably more complex [151].

3.6 Doping of Semiconductors

As was already mentioned, in semiconductor materials the valence band is full of electrons when temperature is 0 K and there cannot be any current flow due to the lack of holes. With increase in temperature, electrons in the valence band start jumping to conduction band and leave holes in the valence band. As a result of this, it becomes possible for electrons to move. But this phenomenon requires the inter-band transitions of electrons which can only be achieved at very high temperatures due to large bandgap energy, often much higher than the melting point of the material. The concentration of free carries created by thermal excitation is temperature-dependent, it is not easy controllable, and it is not generally useful for the required operation of semiconductor devices which rely on high free carrier density. The carriers produced by the excitation from the valence into the conduction band are called the intrinsic carriers. In Fig. 3.7 the intrinsic carrier concentration in some semiconductors like Ge, Si, GaAs and GaN is shown as a function of temperature [148].

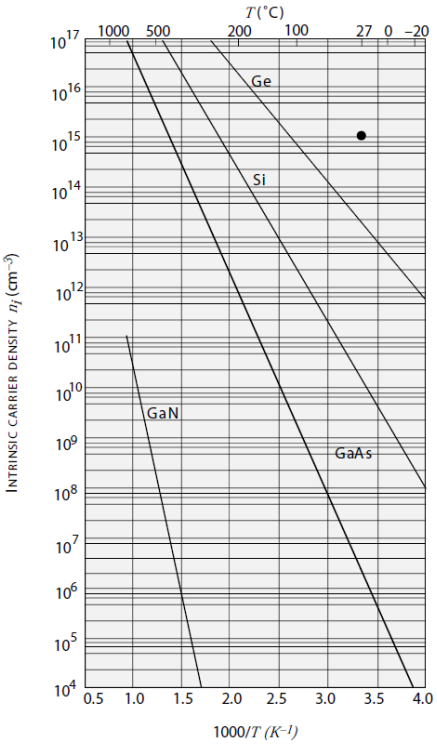

Fig. 3.7 Intrinsic carrier concentration of semiconductor materials versus temperature [148].

In Fig. 3.7, it is shown that the intrinsic carrier concentration of GaAs is below 10^7 cm^{-3} at room temperature. The conductivity of the semiconductor materials at room temperatures is much lower than metals due to low carrier densities. The main technique used in order to increase the number of carriers in semiconductors is the material doping by suitable chemical impurities. To generate free electrons in conduction band or holes in valence band, the semiconductor material is doped with donors or acceptors, respectively. To give an example to understand the mechanism behind doping, we can investigate doping of the group-IV semiconductor material Si. In Fig. 3.8.a it is shown that if a group-V donor atom (Arsenic) replaces one of the native atoms in Si material, one of the valence electrons of As becomes weaker bound and can easy be detached from it, thus the As impurity in Si becomes a positively charged donor. The additional electron is excited from the impurity level to the conduction band because this requires considerably less energy compared to the bandgap energy and can be achieved at room temperatures. The electron becomes free to move in the conduction band. This semiconductor doped with the donor impurities is called the n-type semiconductor. It is also possible to increase number of holes in Si by doping it by acceptor type impurities. To do this we can add a group-III acceptor atom (Boron) which has three valence electrons into the Si material. After Si atom complete the bond with this new impurity atom, there will be one electron from the valence band of Si to join the bond and leaving a hole behind. The required excitation energy for the valence electron to move into the acceptor level is considerably smaller than the bandgap energy and can be achieved at room temperatures. Consequently, the B impurity in Si becomes a negatively charged acceptor with an empty hole state created in the valence band, as shown in Fig. 3.8.b. This semiconductor doped with the acceptor impurities is called the p-type semiconductor.

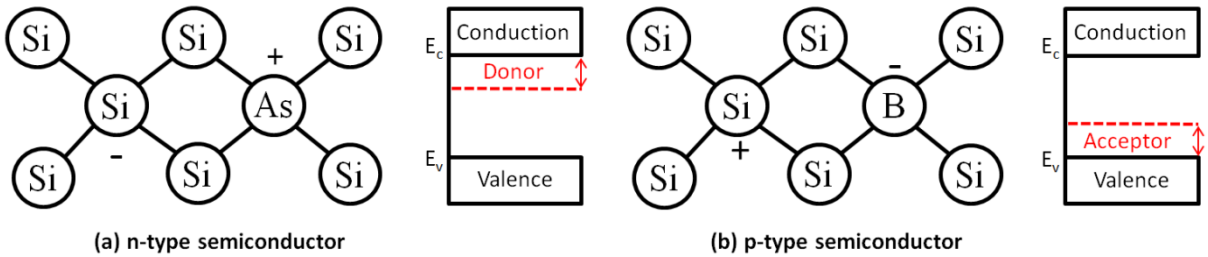

Fig. 3.6 (a) n-type and (b) p-type doped semiconductors produced with doping [148].

When doping is applied to a compound semiconductor like GaAs, the dopant atoms can also be either donor or acceptor type. If Si is used in GaAs, it can be a donor for Ga or acceptor for As atom. And also, some compound semiconductors can be doped by one of the atoms they already have. Like in HgCdTe, it is possible to provide doping with adding extra Te impurities instead of Hg.

3.7 Semiconductor Materials for Laser Diodes

To realise a well-designed semiconductor injection laser fabrication, it is crucial to select proper laser materials for both cladding layers and the active region. The key feature of semiconductor lasers is that they are designed using the double-heterostructures (DH) concept. A DH structure can be considered as a p-i-n diode structure where p- and n-cladding layers have higher bandgap energy than the sandwiched between them an active layer. As a result, generated in active layer photons are not absorbed in the cladding layers [152]. Heterostructure lasers can be provided by using more than two layers of different materials to improve both the electric and optical confinement taking into account that the refractive index profile is reversed to the energy bandgap profile. The refractive index is larger in a small-bandgap material and smaller in the large-bandgap material. Since the photons are better confined in the regions with larger refractive index (smaller bandgap), it is possible to simultaneously achieve a good carrier

confinement and photon confinement using multiple cladding layers. These materials should be chosen carefully since the crystal structures of them (lattice constants) must match to prevent any defection and have the necessary bandgap energy E_g to generate the photons of the required frequency ν (or wavelength λ), $h\nu \approx E_g$ (or $\lambda(\mu m) = 1.24 / E_g(eV)$). Any defection reduces the symmetrical structure of laser and it increases non-radiative recombination losses of the injected carriers. The diagram of the required bandgap energies and the corresponding lattice constants of various semiconductor compound materials are shown in Fig. 3.9. The solid lines correspond to the direct bandgap materials and dashed lines show the indirect bandgap materials.

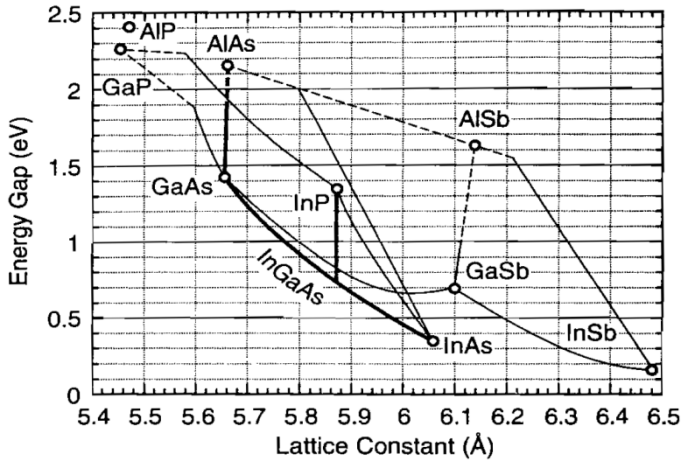

Fig. 3.9 Semiconductor materials with their energy bandgap vs lattice constant [152].

As an example, the InGaAsP/InP structure is one of the well-known structures for lasers operating at 1.55 μm wavelength because of it can provide the required bandgap energy and the lattice matching. The InP based structure can operate between 1-1.6 μm wavelength range. As is seen in Fig. 3.9 that when InGaAs layer is grown on InP there is a lattice matching too which is required to prevent structural defections.

3.8 Theoretical Analysis of Semiconductor Laser Operation

To understand how light is generated/ produced in the active laser cavity; the optical (electro-magnetic) wave propagation along cavity can be considered firstly. The general form of the wave equation for the electric field $\vec{E}(\vec{r},t)$ propagation is written as:

$$\nabla^2\vec{E}(r,t)-\frac{n^2}{c_0^2}\frac{\partial^2 E(\vec{r},t)}{\partial t^2}=0 \tag{3.20}$$

In Eq. (3.20), *n* represents the total refractive index, and c_0 is the speed of light in vacuum. The semiconductor medium in general could be either with or without gain and loss. If there is no gain or loss, the imaginary part of the refractive index n'' becomes zero. Assuming that the real part of the refractive index n' is constant in the cavity and considering one-dimensional wave propagation (along the z-axis), the solution of the wave equation can be written as:

$$E(z,t)=A_0e^{i(\omega t-kz)} \tag{3.21}$$

The propagation constant *k* in Eq. (3.21) is:

$$k=k_0n'=\frac{2\pi}{\lambda_0}n' \tag{3.22}$$

On the other hand, if the semiconductor medium includes gain, the imaginary part of the refractive index does is not zero anymore. The imaginary part will be either positive for gain, or negative for loss. The wave in Eq. (3.21) changes as (again assuming constant gain/loss):

$$E(z,t)=A_0e^{i(\omega t-\beta z)} \tag{3.23}$$

The propagation constant β in Eq. (3.23) includes real and imaginary part of the refractive index, as shown in Eq. (3.24). If the wave propagates along -z direction, the sign in front the term 'βz' becomes positive.

$$\beta = k_0 n = k_0 (n' + in'') = k_0 n' + i\frac{g}{2} = k + i\frac{g}{2} \tag{3.24}$$

If we substitute the term 'βz' in Eq. (3.23) with $k + i\frac{g}{2}$, the wave becomes:

$$E(z,t) = A_0 e^{\frac{g}{2}z} \cdot e^{i(\omega t - kz)} \tag{3.25}$$

If the calculation is carried out for –z direction, the wave in Eq. (3.25) changes as:

$$E(z,t) = A_0 e^{-\frac{g}{2}z} \cdot e^{i(\omega t + kz)} \tag{3.26}$$

For the backward- and forward-propagating waves, the general form of the wave equation is written as:

$$E^{+}(z,t) = A_0 e^{i(\omega t - \beta z)} = F^{+}(z) e^{i\omega t} \tag{3.27}$$

$$E^{-}(z,t) = A_0 e^{i(\omega t + \beta z)} = F^{-}(z) e^{i\omega t} \tag{3.28}$$

$$\frac{\partial F^{\pm}(z)}{\partial z} \pm i\beta F^{\pm}(z) = 0 \tag{3.29}$$

In Fig. 3.10 below, schematic of a travelling wave inside of the Fabry-Perot cavity is shown, with mirror reflections present (for simplicity, the reflectivity of both mirrors is assumed the same). When the light wave enters the cavity from z=0, as a result mirror reflectivity $r \cdot F_{in}$ amount of the light will be reflected back and only $t \cdot F_{in}$ amount of it will be transferred into cavity (r is the reflection coefficient and t is the transmission coefficient). The wave travels

along +z-direction and hits the end mirror at z=L. In this case only $r{\cdot}F^{+}$(L) amount of the light wave will be reflected back into cavity, and $t{\cdot}F^{+}$(L) will leave the cavity as the output wave. The reflected part of the light becomes F^{-}(L) and it travels along –z-direction until it reaches the z=0 interface. When this wave hits the mirror at z=0, only $r{\cdot}F^{-}$(0) of it will contribute to the wave inside the cavity and $r{\cdot}F^{-}$(0) of it will escape. This process will be repeated with several similar reflections and finally there will be a steady state condition for lasing established.

The gain inside the cavity will increase the wave field (the amount of power) each time when the light travels inside the cavity between mirrors. The cavity gain can be defined as:

$$G = \frac{\left|F_{out}\right|^2}{\left|F_{in}\right|^2} \tag{3.30}$$

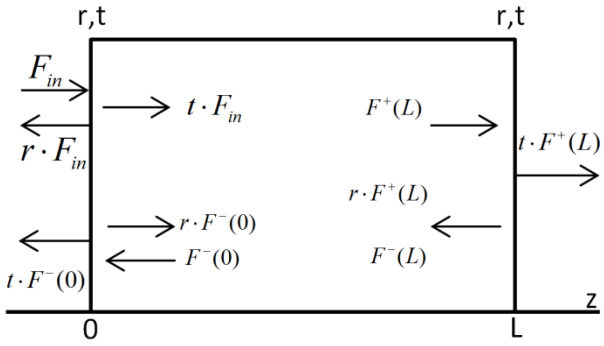

Fig. 3.10 Schematic demonstration of the travelling wave inside the laser cavity.

Fig. 3.10 shows how the travelling wave changes at the reflecting mirrors and the travelling forward and backward components along + and – z directions, respectively. The wave amplitudes F^{+}(0), F^{+}(L), F^{-}(0) and F^{-}(L) are specified as:

$$F^{+}(0) = A^{+}, \quad F^{-}(0) = A^{-} \tag{3.31}$$

$$F^{+}(L) = A^{+}e^{-i\beta L}, \quad F^{-}(L) = A^{-}e^{i\beta L} \tag{3.32}$$

In Fig. 3.10 it is shown that the wave amplitude at z=0 along +z direction includes both $t \cdot F_{in}$ and $r \cdot F^{-}(0)$ components. This gives: $F^{+}(0) = tF_{in} + rF^{-}(0)$ and $F^{-}(L) = rF^{+}(L)$. Using here Eqs. (3.31) and (3.32) gives the amplitudes $A^{\pm}$ in terms of the incident field F_{in}:

$$A^{+} = \frac{t}{1 - r^2 e^{-i2\beta L}} F_{in}, \qquad A^{-} = \frac{rte^{-2i\beta L}}{1 - r^2 e^{-2i\beta L}} F_{in} \tag{3.33}$$

Using Fig. 3.10 we can calculate the field F_{out}:

$$F_{out} = tF^{+}(L) = tA^{+}e^{-i\beta L} \tag{3.34}$$

Substitution of Eq. (3.33) into Eq. (3.34) allows finally to calculate the output field in terms of the input field:

$$F_{out} = \frac{t^2 e^{-i\beta L}}{1 - r^2 e^{-2i\beta L}} F_{in} \tag{3.35}$$

Then by substituting F_{out} from Eq. (3.35) into the Eq. (3.30), the total gain of the active cavity can be presented as:

$$G = \frac{|F_{out}|^2}{|F_{in}|^2} = \frac{\left| \frac{t^2 e^{-i\beta L}}{1 - r^2 e^{-2\beta L}} F_{in} \right|^2}{|F_{in}|^2} \tag{3.36}$$

$$\beta = k_0 n' + i\frac{g}{2}, \qquad \beta^{*} = k_0 n' - i\frac{g}{2}, \qquad \beta - \beta^{*} = ig \tag{3.37}$$

After some trivial algebra in Eq. (3.36) and taking into account Eqs. (3.36) – (3.37) the wavelength dependent gain can be written as:

$$G(\lambda_0) = \frac{(1-R)^2 e^{gL}}{(1 - \mathrm{Re}^{gL})^2 + 4\mathrm{Re}^{gL} \sin^2(k_0 n' L)} \tag{3.38}$$

Here $R = r^2$ is a power reflectivity of the mirror, and $t^2 = 1 - R$ is the power transmission through the mirror. In case of laser Fabry-Perot cavity there is no incident field, i.e. $F_{in} \to 0.$ In this case the (final) output power $|F_{out}|^2 = G|F_{in}|^2$ generated by the active cavity is only possible if one (formally) requires that the gain G is infinite. This in turn requires for the denominator in Eq. (3.38) to be equal zero. There are two conditions to provide that:

$$g(\lambda_M) = \frac{1}{L} \ln \frac{1}{R} \tag{3.39}$$

$$\lambda_M = \frac{2n'(\lambda_M)L}{M} \tag{3.40}$$

In Eq. (3.40), M is the mode number, and we also take into account wavelength dependence (dispersion) of the refractive index. The obtained Eqs. (3.39) and (3.40), which are called the gain condition and the phase condition, respectively, are the two fundamental conditions which must be both satisfied simultaneously by the lasing modes in the laser cavity. Note, that there are other approaches which can be used to derive the lasing conditions given by Eqs. (3.39) and (3.40), for example, using a round trip stationarity condition when the field at any point in the cavity repeats itself in both the amplitude and phase after every round trip. This again will result in the same lasing conditions.

To obtain lasing for a given mode number, it is essential to provide enough gain. In semiconductor lasers gain is provided in the active region but only a fraction of it is useful for producing stimulated emission since the volume of occupied by electromagnetic field (photons) in the cavity is higher than active layer volume occupied by the carriers because the photon field expands in transverse direction into the cladding layers of the cavity. Stimulated emission is only possible in the active layer region where both the photons and the electrons overlap. The ratio of the volume occupied by the electrons to the volume occupied by the photons is represented by

the confinement factor Γ (Γ<1). The reduced material gain due to the confinement factor is called the mode gain:

$$g_{\mathrm{mod}} = \Gamma g_m \tag{3.41}$$

The reduction of the material gain due to confinement factor is not only the sole reason for decreasing of the gain seen by the light propagating along the cavity. The generated photons are also lost due to various internal optical losses (absorption, scattering) in the active layer $\Gamma\alpha_a$ and in the cladding layers $(1-\Gamma)\alpha_c$. Thus, the net mode gain seeing by the cavity field is defined as $g_{net} = \Gamma g_m - \Gamma\alpha_a - (1-\Gamma)\alpha_c$. This gain should be used in the left hand side of Eq. (3.39). On the other side, the escape of the photons through the cavity mirrors can be interpreted as a mirror loss α_m. Inspection of Eq. (3.39) shows that the right hand side can be interpreted as these mirror losses, i.e. $\alpha_m = (1/L)\ln(1/R)$. To have enough gain to lase, the net gain must be equal to mirror losses, in agreement with Eq. (3.39):

$$g_{net} = \Gamma g_m - \Gamma\alpha_a - (1-\Gamma)\alpha_c = \alpha_m \tag{3.42}$$

The Eq. (3.42) can also be interpreted in a little different way if one introduces the cavity roundtrip gain g_c which includes all gain and loss contributions considered above: $g_c = g_{net} - \alpha_m = \Gamma g_m - \Gamma\alpha_a - (1-\Gamma)\alpha_c - \alpha_m$. Then the gain lasing condition in Eq. (3.42) stipulates that the cavity roundtrip gain must be equal zero at lasing: $g_c = g_{net} - \alpha_m = 0$, or $g_{net} = \alpha_m$ according to Eq. (3.42). The cavity roundtrip gain plays very important role in considering dynamics of lasers, and in particular in case of external optical injection, which will be studied in this thesis. In case when the cavity mirrors have different power reflectivity R_1 and R_2, the mirror losses of the cavity are given by the formula which generalises the right hand side of Eq. (3.39):

$$\alpha_m = \frac{1}{2L} \ln \frac{1}{R_1 R_2} \tag{3.43}$$

As is mentioned before, the carriers in semiconductor structures are created by current injection, but only some fraction of the injected current actually contributes to the carrier generation in the active region. This is generally the result of current leakage at electrical contacts and other carrier losses in the claddings of the laser structure which is quantitatively described by an empirical parameter η_i called the internal quantum efficiency. The leakage current can increase the temperature of the material (an undesirable effect in lasers). The total rate of the carrier injection into the active region is [152]:

$$G_{gen} = \frac{\eta_i I}{qV} \tag{3.44}$$

The injected electrical current at the contact is *I*, the volume of the active layer is *V*, and *q* represents the electron charge.

The injected carriers take part in various recombination processes, which in laser structures can be generally separated into two main contributions: (i) stimulated recombination rate $R_{st}(N, N_p)$ which depends on both the electron carrier density N in the active layer and the photon density N_p in the cavity; (ii) non-stimulated recombination rate which includes all possible non-radiative (without emission of a photon) mechanisms R_{nr} and radiative (with spontaneous emission of a photon) recombination mechanisms R_{sp}, and vertical and lateral carrier leakage out of the active layer at the rate R_l.These recombination mechanisms depend on a carrier density only (and do not depend on the photon density), and can generally be represented as $N/\tau_N(N)$, where $\tau_N(N)$ is the carrier lifetime which is a function of the carrier density. The total recombination rate $R(N, N_p)$ in the laser cavity is thus equal:

$$R(N, N_p) = R_{st}(N, N_p) + \frac{N}{\tau_N(N)} \tag{3.45}$$

The electronic transitions that include various mechanisms of recombination processes which we mentioned above are schematically illustrated in Fig. 3.11.

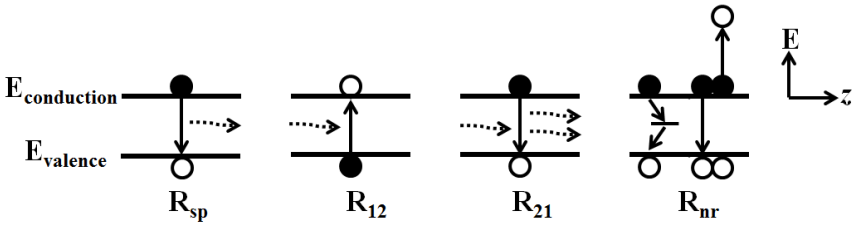

Fig. 3.11 Electronic transitions occur in active layer [152].

There are four recombination-generation processes shown in Fig. 3.11. The first mechanism which is denoted as R_{sp} is a spontaneous photon emission. It represents the randomly recombined electron-hole pairs due to transition between conduction and valence bands and the photons emitted as a result. The second and the third schemes correspond to stimulated emission R_{st}. For lasers which are lasing above threshold level, stimulated recombination is the dominant mechanism. They demonstrate how the electron from the valence band is stimulated by the photon absorption and leaves makes a transition to the conduction band at the rate R_{12}, and the reverse process, when the electron in the conduction band is stimulated by the present photon and makes a transition to the valence band (i.e. recombines with the hole) at the rate R_{21} with a new photon emitted. It is crucially important that the new emitted photon is a full replica of the photon which stimulated the R_{21} recombination transition. The stimulated recombination mechanism is responsible for coherent radiation in lasers when the emitted photons have the same frequency and phase. The last mechanism R_{nr} in Fig. 3.11 illustrates various the non-radiative recombination processes.

If we look for more details for the second term in Eq. (3.45), the carrier lifetime parameter $\tau_N(N)$ includes three important recombination mechanisms:

$$\tau_N^{-1}(N) = A_{nr} + BN + CN^2 \tag{3.46}$$

The first term on the right-hand side A_{nr} is for a non-radiative Shockley-Read-Hall recombination process, B is for bimolecular spontaneous photon emission recombination coefficient, and the last parameter C represents the non-radiativre Auger recombination process. By taking Eq. (3.44) and Eq. (3.45) into account, we can now write the final version of the carrier density change equation (the carrier rate equation):

$$\frac{dN}{dt} = \frac{\eta_i I}{qV} - \frac{N}{\tau_N} - R_{st} \tag{3.47}$$

The photon density N_p change in semiconductor laser mainly depends on the stimulated emission R_{st} and the photon loss in the cavity. The volume of occupied by the photons generated under the current injection is usually bigger than the volume of the active layer occupied by the electrons. Therefore, only the fraction (V_{el}/V_{ph}) of the generated photons overlaps with the electrons and can contribute to the stimulated emission recombination process. The parameter $\Gamma = V_{el}/V_{ph}$ is called the confinement factor, as was already discussed. For the photon generation rate calculation it is essential to take confinement factor into account, since only the Γ fraction of the photons will be affected by the stimulated and spontaneous recombination. The photon density change in semiconductor laser cavity is given as (the photon rate equation) [152]:

$$\frac{dN_p}{dt} = \Gamma R_{st} + \Gamma \beta_{sp} R_{sp} - \frac{N_p}{\tau_p} \tag{3.48}$$

The spontaneous emission R_{sp} occurs into all modes (either lasing or not) which have positive gain. Since the photon density in Eq. (3.48) represents only the photons which are in the lasing

modes, it is necessary to take into account only a small fraction of the spontaneously emitted photons which are emitted into the lasing modes. To decrease the represented effect of spontaneous emission for the modes which are not in the lasing spectrum, the factor β_{sp}, is used in the second term in Eq. (3.48). This parameter is called the spontaneous emission factor and it is equal to the inverse of the number of optical modes within the spontaneous emission bandwidth [4]. The last term in Eq. (3.48) takes into the photon loss in the cavity due to various mechanisms, such as light absorption by impurities or inter-valence band absorption, light scattering out of the lasing modes or out of the cavity, or light decoupling from the cavity through the mirrors. The stimulated emission which is represented by R_{st} in Eq. (3.48) is responsible for coherent net photon generation as the optical field propagates along the cavity's *z*-direction. The photon number increases due to the cavity gain (i.e. via the photon-stimulated recombination) , as is shown by Eq. (3.49). If the light wave propagates through a Δz long path in the active section, the initial photon number N_p increases by ΔN_p amount, which can be phenomenologically represented using the gain as:

$$N_p + \Delta N_P = N_p e^{g\Delta z} \tag{3.49}$$

Assuming that $g\Delta z << 1$ and using $\exp(g\Delta z) \approx 1 + g\Delta z$, the photon number increase ΔN_p due to the photon-stimulated recombination can be written as $\Delta N_p = N_p g\Delta z$. Since the light propagates through the cavity with group velocity v_g and $\Delta z = v_g \Delta t$, then $\Delta N_p = N_p v_g g\Delta t$. Therefore, the rate of the photon generation due to the photon-stimulated recombination can be represented as

$$R_{st} = \left(\frac{dN_p}{dt}\right)_{st} \approx \frac{\Delta N_p}{\Delta t} = v_g g N_p \tag{3.50}$$

As is seen from Eq. (3.50), the stimulated emission rate indeed depends on both the electron and the photon densities N and N_p since the material gain g is a function of the carrier

densityin the active layer. By taking Eq. (3.48) and (3.51) into account, finally the change in photon density (photon rate equation) is written as [152]:

$$\frac{dN_p}{dt} = \Gamma \nu_g gNp + \Gamma \beta_{sp} R_{sp} - \frac{N_p}{\tau_p} \tag{3.51}$$

3.9 Light-Current (L-I) Characteristics of the Laser

The output power P_{out} of the laser depends on the injected current I, and this relation constitutes the light-current (L-I) characteristics of the laser. Because of the non-radiative carrier losses present in the laser structure, the laser does not lase immediately if any current is injected into the active region. Before lasing begins, it is necessary first to compensate these carrier losses. The required for this electric injection current is called a threshold current I_{th}. In order to understand the physical meaning of threshold current and calculate the L-I characteristics, it is essential to consider two regimes which of the current injection – below the threshold ($I < I_{th}$) and above the threshold ($I < I_{th}$). If the injection current is lower than the threshold current (I_{th}), the laser does not provide feedback to produce stimulated emission and there is no lasing. Therefore, the change in the electron density only includes the non-stimulated recombination mechanisms, and the photon-stimulated recombination can be excluded from the carrier rate equation (3.47):

$$\frac{dN}{dt} = \frac{\eta_i I}{qV} - R(N) \tag{3.52}$$

The last term includes the spontaneous emission R_{sp}, non-radiative recombination R_{nrt} and carrier leakage R_l. Out of these parameters, only R_{sp} contributes to the (spontaneous!) output power P_{sp}, and therefore the other recombination mechanisms must be excluded from the power generation. To do this, we introduce the radiative efficiency η_r which is defined as:

$$\eta_r = \frac{R_{sp}}{R(N)} = \frac{R_{sp}}{R_{sp} + R_{nr} + R_l} \tag{3.53}$$

As is shown by Eq. (3.52) that the injected current I generates $\eta_i I/qV$ electrons and under the steady state conditions $(dN/dt = 0)$ this is equal to the carrier recombination rate $R(N)$. The density of photons produced in the cavity per unit time is given by the spontaneous recombination rate R_{sp}. The total number of photons produced in the cavity per unit time is $R_{sp}V$. Each emitted photon has energy $h\nu$. Thus, the total amount of energy produced in the cavity per unit time is $h\nu \times R_{sp}V$. By definition, the energy generated per unit time is called a power. Therefore, the output power from the cavity due to spontaneous emission is $P_{out(sp)} = h\nu V R_{sp}$. The output power below threshold is found using Eqs. (3.52) and (3.53) as:

$$P_{out(sp)} = h\nu V R_{sp} = \eta_i \eta_r \frac{h\nu}{q} I \tag{3.54}$$

As is seen from Eq. (3.54), spontaneous emission output power increases linearly with the injection current. Lasers are generally operated above the threshold current and the consideration of the operation below the threshold is mostly useful for understating light emitting diodes (LEDs) operations. In LEDs, there is only spontaneous emission taken into account to provide the output power, but only a small fraction (around 10%) of the produced power can be sent efficiently to the desired output point due to internal scatterings and multidirectional emission when the light escapes through claddings.

When the number of carriers produced in the active layer by the injected current increases, the carrier density depended gain also increases. As was discussed before, when the net gain g_{net} of the cavity compensates the mirror losses, the propagating electric field reproduces itself after each round trip at any point in the cavity. This situation corresponds to the lasing conditions of the laser. The electric current which at which these conditions are achieved is called a threshold

current I_{th}. Even though the injected current is increased to higher levels above the threshold current, the carrier density N and the material gain $g(N)$ of the laser stays at the threshold levels, $N = N_{th}$ and $g = g_{th} = g(N_{th})$, respectively (this situation is called the gain-clamping regime). This condition keeps also the carrier density dependent spontaneous emission rate at the same value as $R_{sp}(N_{th})$ and the power generated from the spontaneous emission becomes fixed at its threshold level for any current above the threshold. There are two fundamental physical reasons for keeping the fixed carrier density and the gain at their threshold values. First, is the gain condition given by Eq. (3.42). Because the mirror loss in the right hand side is constant, this condition can be satisfied only at a particular value of the material gain $g_m(N)$, which in turn can be achieved at a particular value of the carrier density N. Once this condition is achieved, the material gain must stay the same because only in this case the cavity roundtrip gain g_c is equal zero and the laser operates coherently. If the increase of the current would result in an increase of the carrier density, the material gain would also increase, the round trip gain would become positive, and the lasing field in the cavity would increase after each round trip without bound, i.e. the steady state laser operation would be impossible. Therefore, the gain lasing condition in Eq. (3.42) provides a fundamental requirement for the carrier density and the material gain to be fixed at their threshold levels. The second fundamental physical process which allows to maintain this state of the laser when the injection current further increases above the threshold, is the photon-stimulated recombination process. The stimulated recombination rate is proportional to the number of the photons in the cavity and this term dominates the recombination processes in the cavity above the threshold. An increase of the injection current results in an increase of the generated by stimulated emission photons which results in an increase of the stimulated recombination rate in the carrier rate equation (3.47). This increased recombination consumes all injected carriers (converting them into the photons) and does not allow any increase of the carrier density in the active layer (at steady state Eq. (3.47) gives $R_{st} = R_{st}(N_{th}, N_p) \approx \eta_i I / qV$, and

increase of the current leads only to increase of the photon density N_p). The threshold current I_{th} can be calculated from Eq. (3.52) at steady state (and neglecting the stimulated emission term) as:

$$\frac{\eta_i I_{th}}{qV} = R(N_{th}) \tag{3.55}$$

where the threshold currier density is obtained from the gain lasing condition of Eq. (3.42), assuming that the dependence $g_m(N)$ of the material gain on the carrier density is known.

Therefore, above the threshold the stimulated emission becomes the dominant recombination process and it defines the output power. The carrier rate equation (3.47) above the threshold can be presented as:

$$\frac{dN}{dt} = \frac{\eta_i I}{qV} - R(N_{th}) - R_{st}(N_{th}, N_p) \tag{3.56}$$

Here the second term can be substituted using Eq. (3.55), and the last term $R_{st}(N)$ representing the stimulated emission can also be modified using Eq. (3.50) as $R_{st}(N_{th}, N_p) = v_g g(N_{th}) N_p = v_g g_m^{th} N_p$, where $g_m^{th} = g(N_{th})$ is the material threshold gain. Thus, Eq. (3.56) becomes:

$$\frac{dN}{dt} = \eta_i \frac{I - I_{th}}{eV} - v_g g_m^{th} N_p V \tag{3.57}$$

At a steady state $(dN/dt = 0)$ the photon density N_p can be calculated as a function of the current as $N_p = \eta_i (I - Ith) / q v_g g_{th} V$. In order to obtain the output power at lasing, we first calculate the total energy of the generated photons as $E=h\nu N_p V_p$, where V_p is the volume occupied by the photon in the active section. Finally, the output power (through both mirrors) can be found by multiplying the total photon energy by the photon escape rate through the

mirrors, $1/\tau_m = v_g \alpha_m$, where α_m is the cavity mirror loss given by Eq. (3.42), and v_g is the photon group velocity in the cavity. This finally gives for the power output:

$$P_{out} = \frac{E}{\tau_m} = \frac{h\nu V_p N_p}{\tau_m} = \eta_i \frac{h\nu}{q} \frac{\alpha_m}{g_m^{th}} \frac{V_p}{V} (I - I_{th}) = \eta_i \frac{h\nu}{q} \frac{\alpha_m}{\Gamma g_m^{th}} (I - I_{th}) \tag{3.58}$$

And it is already shown in Eq. (3.42) that the net gain is equal to the sum of internal losses $\alpha_i = \Gamma \alpha_a + (1-\Gamma)\alpha_c$ and the mirror losses α_m:

$$\Gamma g_m^{th} = \alpha_i + \alpha_m \tag{3.59}$$

Using this in Eq. (3.58) and introducing the differential quantum efficiency $\eta_d = \eta_i \alpha_m / (\alpha_i + \alpha_m)$, the output power above the threshold can finally be presented as:

$$P_{out} = \eta_d \frac{h\nu}{q} (I - I_{th}) \tag{3.60}$$

The output power of the laser calculated above is the total power laser could emit from its both mirrors. As a result of this, if the laser has two mirrors for light emission, the amount of power emitted from each will be reflectivity depended. If the mirrors have same reflectivity, each mirror will emit half of the power. The power change with input current above threshold level is linear as is demonstrated in Fig. 3.12.

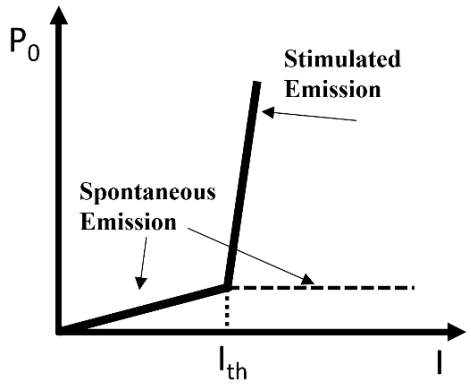

Fig. 3.12 Typical L-I characteristics of the laser for below and above threshold currents [152].

3.10 Distributed Bragg Reflector (DBR) Lasers

In Fabry-Perot lasers, there are usually many cavity lasing modes having enough gain to provide lasing due to relatively wide gain bandwidth. It is essential to obtain single mode operation lasers for optical fibre networks and the other various applications. To achieve a single mode operation there are different approaches and types of laser design. A distributed Bragg reflector (DBR) laser is one of the models which provides a wavelength depended mirror reflectivity spectrum and this allows select a single desired cavity mode which provides the laser output. DBR section provides the mirror power reflectivity $R_g(\lambda_0)$ for lasing wavelength λ_0 and the threshold (net) gain condition becomes (see Eq. (3.42)):

$$g_{net} = \alpha_{DBR} = \frac{1}{2L} \ln \frac{1}{R_1 R_g(\lambda_0)} \tag{3.61}$$

If power reflectivity of DBR R_g is small, the threshold gain becomes high. So in order to obtain lasing for a very low threshold gain, R_g should be closer to 1. As indicated before, the power reflectivity of DBR mirrors is a strong function of the incident light's wavelength. To have a single mode operation with DBR mirrors, it is essential to have the reflectivity bandwidth which is considerably smaller than the inter-mode distance $\Delta\lambda_m$ in the cavity (this can easy be calculated using the phase condition from Eq. (3.40) at lasing).

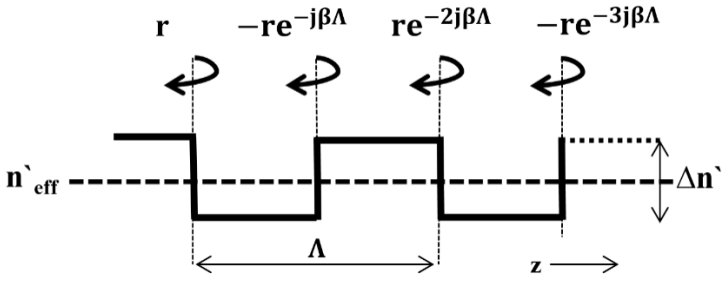

Fig. 3.13 Wave propagation inside DBR mirror [153].

The propagation of light inside the DBR section is schematically depicted in Fig. 3.13. The DBR structure consists of a periodic stack of layers with different refractive index and it is assumed that the refractive index of the DBR changes periodically around $n`_{eff}$. The period of the structure is Λ long. As an example, we consider the DBR structure in which the change of refractive index along the *z*-axis is analytically presented as:

$$n(z) = n'_{eff} + \frac{\Delta n}{2}\cos(2\beta_0 z) \tag{3.62}$$

The β_0 parameter in Eq. (3.62) is called the Bragg propagation constant which is related to the period of the structure Λ and can be presented as [153]:

$$\beta_0 = \frac{M\pi}{\Lambda} = \frac{2\pi}{\lambda_B} n'_{eff} = k_0(\lambda_B) n'_{eff} \tag{3.63}$$

Here λ_B is a free space Bragg wavelength and k_0 is a free space propagation constant. It is important that the propagation constant β_0 in DBR section is a function of the period Λ and thus it can be engineered via the suitable design of the structure. The parameter M defines the order of the grating and can take any integer value. We consider the first-order gratings with M=1. The Bragg period of the first-order structure is found as half Bragg wavelength:

$$\Lambda = \frac{\lambda_B}{2n'_{eff}} \tag{3.64}$$

When electromagnetic wave enters the DBR structure as is shown in Fig. 3.13, the forward wave is reflected back from the interfaces. As a result, there are coupled forward and backward propagating waves in the DBR structure. The wave equation inside the DBR structure is given as:

$$\frac{d^2E}{dz^2} + [n(z)k_0]^2 E = 0 \tag{3.65}$$

Some better physical insight into the propagation of the wave through the DBR structure can be obtained by considering the periodic structure with a step-wise periodic change of the refractive index. The field reflectivity *r* for each half period (Λ/2) is given by the Fresnel formula:

$$r = \pm \frac{\Delta n'}{2n'_{eff}} \tag{3.66}$$

Here the sign of *r* is plus for the reflections when we go from a high to a low refractive index at the interface, and is minus in the opposite case. The change in the refractive index and reflectivity in a step-wise periodic grating is illustrated in Fig. 3.13. While electromagnetic wave propagates along +z direction, the reflectivity changes due to the refractive index variation. If the light's wavelength λ_0 is equal to the Bragg λ_B wavelength, then the exponent in the propagation term $e^{-j\beta\Lambda}$ becomes:

$$\beta_0 \Lambda = \frac{2\pi n'_{eff}}{\lambda_0} \frac{\lambda_B}{2n'_{eff}} = \pi \tag{3.67}$$

This gives for the reflected wave at the second (from the left) interface $-r\exp(-i\beta\Lambda) = -r\exp(-i\pi) = +r$, i.e. the same reflectivity coefficient as at the first interface. This behaviour is repeated at all other interfaces. As a result, all reflections at all interfaces add up in phase. It is shown by Eq. (3.66) that, the reflectivity coefficient *r* has the same magnitude but it changes sign at every interface, i.e. every half period (Λ/2) of the structure. Therefore, the field reflectivity per unit length is:

$$\kappa' = \frac{r}{\Lambda/2} = \frac{\Delta n'}{n'_{eff}} \frac{2n'_{eff}}{\lambda_B} = \frac{2\Delta n'}{\lambda_B} \tag{3.68}$$

The parameter κ' is called the coupling coefficient. The wavelength dependent reflectivity of DBR section makes it possible to choose the single emission wavelength in the laser structure with the DBR reflector which reflects only this single wavelength and transmits all the other

wavelengths. The DBR acts as a wavelength-selective filter. If there is a difference between the Bragg wavelength and the corresponding wavelength of the light generated in the active section, the reflectivity will decrease at such wavelengths.

The reflectivity of DBR section of the length L (between z=0 and $z=L$) is obtained from the ratio between the reflected and the incident waves for the whole DBR section. In order to calculate the reflected field it is necessary to solve the wave equation (3.65). Substituting Eq. (3.62) into Eq. (3.65) and neglecting a term containing $(\Delta n)^2$ and using $\beta = n_{eff}^{'}(\lambda)k_0(\lambda)$ for the propagation constant of the wave with the wavelength λ, the wave equation becomes

$$\frac{\partial^2 E(z)}{\partial z^2} + [\beta^2 + 4\beta\kappa\cos(2\beta_0 z)]E(z) = 0 \tag{3.69}$$

Here the coupling constant is defined as $\kappa = \pi\Delta n / 2\lambda$ (which a little differs from κ' in Eq. (3.68) for a square grating). The deviation in the propagation constants with different wavelengths can be derived as:

$$\Delta\beta = \beta - \beta_0 = \frac{2\pi n'_{eff}(\lambda)}{\lambda} - \frac{2\pi n'_{eff}(\lambda_B)}{\lambda_B} \approx \frac{2\pi n_g}{\lambda_B^2}\Delta\lambda \tag{3.70}$$

Considering the wavelength very close to the Bragg wavelength, $\lambda \approx \lambda_B$, it is clear that in this case $\beta = \beta_0 + \Delta\beta$ and $\Delta\beta << \beta_0$. In this case the wave Eq. (6.69) can be solved analytically using for example, the perturbation technique. The solution is presented as two coupled forward R(z) and backward S(z) propagating waves. The field reflectivity is then obtained as a ratio of the amplitudes of these waves at z=0 interface of the structure, $r_{DBR} = S(0)/R(0)$ [5]:

$$r_{DBR} = \frac{S(0)}{R(0)} = \frac{-(i\kappa/\gamma)\sinh(\gamma L)}{\cosh(\gamma L) + (i\Delta\beta/\gamma)\sinh(\gamma L)} \tag{3.71}$$

The power reflectivity of the DBR grating is $R_g = |r_{DBR}|^2$ and is given as:

$$R_g(\lambda) = (\kappa L)^2 \frac{\frac{\tanh^2(\gamma L)}{(\gamma L)^2}}{1+(\Delta\beta L)^2 \frac{\tanh^2(\gamma L)}{(\gamma L)^2}} \tag{3.72}$$

Here for the wavelengths close to the Bragg wavelength γ is defined as:

$$\gamma^2 = \kappa^2 - \Delta\beta^2, \quad \kappa = \pi\Delta n / 2\lambda_B \tag{3.73}$$

The obtained power reflectivity R_g shows that if $\lambda = \lambda_B$, then $\Delta\beta = 0$ and $\gamma = \kappa$. As a result the magnitude of the peak power reflectivity R_g depends only on κL:

$$R_g(\lambda = \lambda_B) = \tanh^2(\kappa L) \tag{3.74}$$

The spectral dependence of the reflectivity in DBR section for a range of the wavelength can be depicted using Eq. (3.72), and is shown in Fig. 3.14 for various values of the κL parameter. It is demonstrated that maximum reflectivity for any κL value is always obtained when λ is equal to λ_B, and detuning from the Bragg wavelength decreases reflectivity.

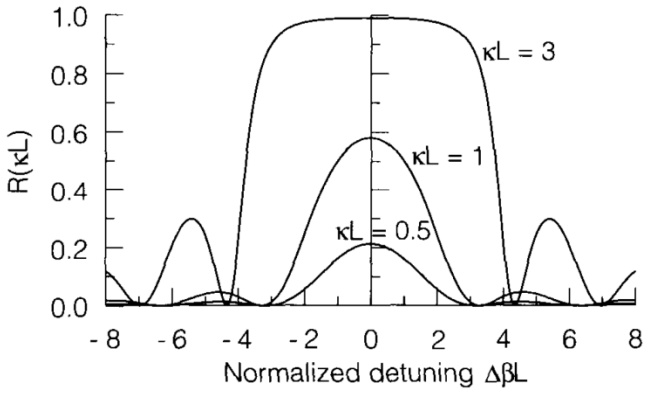

Fig. 3.14. Reflectivity spectrum of DBR section for different κL values [153].

In order to obtain a single mode operation, the reflectivity bandwidth of the DBR mirror must be smaller than the inter-mode distance. The bandwidth of the DBR reflectivity is:

$$\Delta\lambda_r = \frac{\lambda_B \Delta n}{2n_{g,eff}} \tag{3.75}$$

The mode distance in a laser with the total cavity of length L' is:

$$\Delta\lambda_m = \frac{\lambda^2}{2n_{g,eff}L'} \tag{3.76}$$

The distributed gratings are currently used in various types of lasers, such as the fixed wavelength DBR laser where the DBR reflector is simply replaces one of the mirrors in the Fabry-Perot laser, or a distributed feedback (DFB) lasers where the grating and the active region overlap, or in a vertical cavity surface emitting laser (VCSEL) where two highly-reflectivity DBRs provides both strong reflectivity and the mode selection. More advanced types of gratings are currently designed in novel wavelength tunable laser diodes (TLDs) which consist of a few sections in order to provide the necessary gain (active section) and continuous and discontinuous wavelength tuning (tuning sections). In a most popular and well-studied embodiment the TLD includes the active section (providing gain), the passive phase section (for a fine continuous tuning within the inter-mode separation range), and the DBR section (for a discontinuous tuning between different cavity modes). The wave in the TLD cavity penetrates some distance into the DBR section and is reflected by grating. If the detuning between the Bragg wavelength and the lasing mode wavelength is very small, then such reflection can be approximated with a discrete mirror which has the same reflectivity as the DBR reflectivity given by Eq. (3.72) but it placed a distance L_{eff} "inside" of the DBR reflector. The distance L_{eff} is called the effective length L_{eff} and is found as [4]:

$$L_{eff} = \frac{\tanh(\kappa L)}{2\kappa} \tag{3.77}$$

A schematic demonstration of three-section TLD is shown by Fig. 3.15. The fabrication of a TLD laser requires a complex processing since three integrated sections must be grown on the same wafer [152].

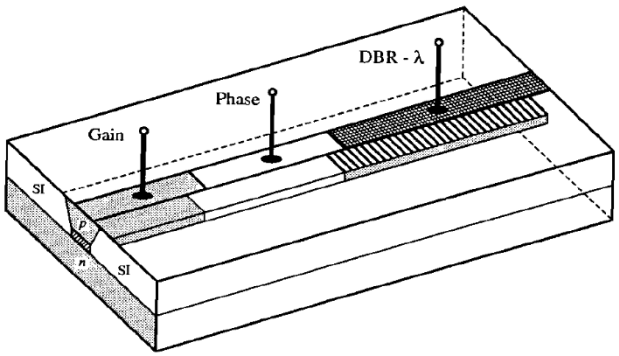

Fig. 3.15 Tunable laser diode schematic with three different contacts [152].

The lasing gain condition in this TLD is given by the equation similar to Eq. (3.61), but taking into account the composite structure of the cavity. The length of the laser now includes three sections of the laser and additionally the mirror reflectivity of DBR section is wavelength depended. This gives:

$$\Gamma g_{th} = \alpha_i + \frac{1}{2\left(L_a + L_p + L_{eff}\right)} \ln \frac{1}{R_1 R_g(\lambda_0)} \tag{3.78}$$

The confinement factor Γ and internal loss α_i which are shown in Eq. (3.78) are the averaged characteristics of the cavity [4]. The second term on right hand side represents the composite cavity mirror losses α_m. As is seen in Fig. 3.15, each TLD section has separate electrical contacts. The current injection into the active section controls the gain and the output power. The current injection into the phase section controls the phase of the wave and fine wavelength tuning via the change of the refractive index there (due to the free carrier contribution to the material dielectric constant), and finally the DBR current injection is changing the Bragg wavelength by changing the refractive index of the DBR section according to Eq. (3.63). The current injection results in a

decrease of the refractive index [5] and this shifts the Bragg wavelength λ_B (and thus the peck reflectivity of the DBR) to shorter wavelengths as can be obtained from Eq. (3.63) [152].

$$\frac{\Delta\lambda_B}{\lambda_{B0}} = \frac{\Delta\bar{n}_{eff\ DBR}}{\bar{n}_{geff\ DBR}} \tag{3.79}$$

In Eq. (3.79) $\Delta\bar{n}_{eff\ DBR}$ is decreasing (negative) under the current injection [5] and the wavelength is shifted by $\Delta\lambda_B < 0$ to a shorter wavelength with respect to the initial Bragg wavelength λ_{B0}. The refractive index $\bar{n}_{geff\ DBR}$ in the denominator od Eq. (3.79) is the average effective group index of the DBR section [5].

There are there different wavelength tuning regimes which can be achieved in TLDs: continuous tuning, discontinuous tuning, and quasi-continuous tuning. By applying currents to phase and DBR sections, the refractive index of these sections can be changed and different tuning mechanisms can be realised. The emission wavelength can be tuned continuously by applying current to the phase section only. This behaviour can be understood by inspecting the phase lasing condition in Eq. (3.40): current injection into the phase section results in decrease of the cavity average refractive index and the lasing mode M wavelength must shift accordingly to a shorter wavelength in order to keep this condition satisfied. Obviously, this can only provide the limited wavelength tuning, not bigger than the inter-mode separation, since at higher current injection the tuned lasing mode M is replaced by the previous mode (M-1), they simply interchange and the process is repeated. To achieve tuning over a larger range, the DBR section is to be tuned by the current injection. This will shift the Bragg wavelength, but the lasing wavelength of the cavity mode M will remain unchanged until the Bragg wavelength reaches the neighbouring mode (M-1). A this point the mode (M-1) has lower mirror loss and it wins the competition with the mode M and the laser switches to lasing at the shorter wavelength of the mode (M-1), i.e. mode hopping from M to (M-1) takes place with a sudden (discontinuous)

wavelength change. Further current injection will again result in a mode jump to the next cavity mode with yet shorter wavelength. The process is repeated with a discontinuous step-wise change of the lasing wavelength. So, this mechanism is called ‘discontinuous tuning’. The last mechanism of a quasi-continuous tuning is a hybrid mechanism which includes simultaneous current injection into the phase and the DBR section. With correct selection of the injected currents, it is possible to achieve a quasi-continuous wavelength change. This regime, however, requires a careful pre-calibration of the currents injected into each section in order to achieve lasing at the required wavelength.

3.11 Optical Injection Locked (OIL) Lasers

Application of semiconductor lasers as optical transmitters in modern optical-fibre systems requires enhancement of their dynamic properties, which means fast response of the laser to the current injection change. There are various approaches to improve speed of the directly modulated lasers, including special design of laser structures with low-dimensional active region (for example, quantum-well lasers), or utilising special regimes of the laser operation. One of such special regimes of the directly-modulated laser operation is the optical injection locking (OIL). This regime is of direct interest to the research undertaken in this thesis and will be briefly reviewed next.

OIL is a light injection technique which provides more stabilised laser operation and it has been shown in many studies that OIL improves dynamic properties of lasers and it also provides better spectral purity of the emitted light [125, 154]. The injection locking is achieved by injecting light from a master laser to a slave laser, as is schematically shown in Fig. 3.16

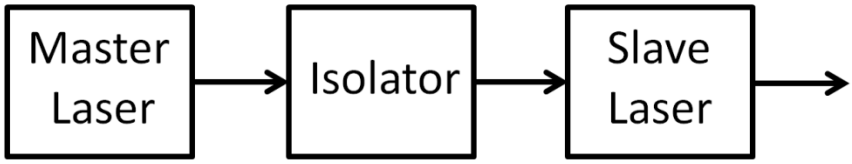

Fig 3.16 General demonstration of optical injection locking.

Injection locking is a unidirectional optical field application, and in order to prevent any light to flow back from the slave laser to the master laser, both lasers are separated by an optical isolator. A comprehensive theoretical analysis of OIL lasers was pioneered by Lang in 1982 [15]. He derived the set of key equations in the OIL. Here we will follow the later works of various authors in which the same results have been obtained using in some cases simpler approaches.

The rate equation for the electric field in the laser cavity without an external light injection is [23]:

$$\frac{dE(t)}{dt} = \frac{1}{2}(G-\gamma)E(t) + j\omega E(t) \tag{3.80}$$

Here E(t) is the electric field, G is the gain from the active material, γ is the total loss which includes the internal cavity loss and the cavity mirror loss, and ω is the cavity resonance frequency. The total cavity loss can be expressed in terms of the inverse photon lifetime τ_p [4]. The change in the carrier density (without light injection) is described by the carrier rate equation:

$$\frac{dN(t)}{dt} = \frac{I}{qV} - \frac{N}{\tau_N} - G\left|E(t)\right|^2 \tag{3.81}$$

The electric field change in the slave laser $dE_s(t)/dt$ under optical injection from the master laser can be derived by adding the injected field into the Eq. (3.82) as:

$$\frac{dE_s(t)}{dt} = \frac{1}{2}\left[G(N) - \frac{1}{\tau_p}\right]E_s(t) + j\omega(N)E_s(t) + \kappa E_{inj}(t) \tag{3.82}$$

Here κ is the coupling coefficient which takes into account the fraction of the injected field which is coupled into the cavity. The electric fields of slave E_s(t) and master E_{inj}(t) lasers include amplitudes, angle frequencies, and phases of each field. Substituting the complex forms of these fields, $E_s(t) = E(t)\exp i[\omega_{FR}t + \phi_s(t)]$ and $E_{inj}(t) = E_{inj}\exp i[\omega_{inj}t + \phi_{inj}]$, into Eq. (3.82) one obtains the rate equations for the amplitude $E(t)$ and the phase $\phi(t)$ of the cavity field [23]:

$$\frac{dE(t)}{dt} = \frac{1}{2} g v_g \left[N(t) - N_{th}\right] E(t) + \kappa E_{inj} \cos\phi(t) \tag{3.83}$$

$$\frac{d\phi(t)}{dt} = \frac{\alpha}{2} g v_g \left[N(t) - N_{th}\right] - \Delta\omega - \kappa \frac{E_{inj}}{E(t)} \sin\phi(t) \tag{3.84}$$

Here we used that $G(N) = g v_g (N(t) - N_{th})$, g is the differential gain, v_g is the field group velocity in the cavity, N_{th} is the threshold carrier population in the cavity, α is the Henry linewidth enhancement factor, $\Delta\omega = \omega_{inj} - \omega_{FR}$ is the frequency detuning, and the relative phase difference between the slave and the master laser fields is $\phi(t) = \phi_s(t) - \Delta\omega - \phi_{inj}$.

The rate equation (3.81) can be presented as:

$$\frac{dN(t)}{dt} = \frac{I}{qV} - \frac{N(t)}{\tau_N} - \left\{\frac{1}{\tau_p} + g v_g \left[N(t) - N_{th}\right]\right\} E^2(t) \tag{3.85}$$

Here in the last term we used that $1/\tau_p = g v_g (N_{th} - N_{tr})$, where N_{tr} is the cavity carrier population at transparency.

By providing stable locking by the optical injection, the slave laser will start lasing at the master laser's frequency. When the slave laser is locked by the master laser, the additional injected photons will reduce the carrier density in the slave laser's active region because of the

increased photon population. As a result of this decrease despite the fact that the emission frequency of the slave laser is locked to the master laser, its cavity resonance actually red shifts.

To find the change in carrier density after stable locking is established, it is possible to investigate Eq. (3.83) under steady state conditions ($dE/dt = 0$):

$$\frac{1}{2} g \nu_g \left[N - N_{th}\right] E = -\kappa E_{inj} \cos \phi_0 \tag{3.86}$$

This gives:

$$\Delta N = N - N_{th} = -\frac{2\kappa}{g \nu_g} \frac{E_{inj}}{E} \cos \phi_0 \tag{3.87}$$

Under optical injection the frequency difference between the injected laser frequency and the shifted slave laser cavity resonance frequency gives the new modulation bandwidth of the OIL laser [9]. This is the new fundamental feature of the laser dynamics under OIL conditions in comparison with a free-running laser where dynamic response of the laser is completely defined by internal parameters of the active region of the lasers, such as differential gain and the resonance oscillation frequency. With OIL the response characteristics of the slave laser can be tuned by selecting suitable characteristics of the injected light, such as frequency detuning and the injection power ratio. The most important outcome of the carrier density drop in the slave laser under optical injection is the increase in the modulation bandwidth of the slave laser [9]. This is because the slave laser's cavity resonance (lasing) frequency is shifted due to change (increase) in the refractive index of the cavity which in turn is the result of the decrease of the carrier density there. The bigger is the cavity resonance frequency shift, the bigger is the difference between the master laser frequency and this cavity shifted resonance frequency. This is the physical reason for enhancement of the modulation bandwidth. This feature can be qualitatively understood by considering the steady state limit of the OIL laser operation which

also allows deriving the limits of the locking bandwidth. Using $d\phi/dt = 0$ in Eq. (3.84) and using Eq. (3.87):

$$\frac{\alpha}{2} g v_g \left[-\frac{2\kappa}{g v_g} \frac{E_{inj}}{E_0} \cos\phi_0 \right] - \kappa \frac{E_{inj}}{E_0} \sin\phi_0 = \Delta\omega \tag{3.88}$$

$$\kappa \frac{E_{inj}}{E} (\alpha \cos\phi_0 + \sin\phi_0) = \Delta\omega \tag{3.89}$$

The limits of Eq. (3.89) can be found by investigating the minimum and maximum values of the expression $[\alpha\cos\phi_0+\sin\phi_0]$ as a function of ϕ_0. The minimum limit is calculated as -1 and the maximum is $\sqrt{1+\alpha^2}$. Therefore, the injection locking limit for a given injection ratio (E_{inj}/E) can be written as:

$$-\kappa \frac{E_{inj}}{E_0} \sqrt{1+\alpha^2} \le \Delta\omega \le \kappa \frac{E_{inj}}{E_0} \tag{3.90a}$$

$$-\frac{\kappa\lambda^2}{2\pi c} \sqrt{\frac{P_{inj}}{P_0}} \le \Delta\lambda \le \frac{\kappa\lambda^2}{2\pi c} \sqrt{\frac{P_{inj}}{P_0}} \sqrt{1+\alpha^2} \tag{3.90b}$$

Eq. (3.90b) is the Eq. (3.90a) re-written in the equivalent form using the wavelength detuning $\Delta\lambda$ versus the power ratio P_{inj}/P_0 with $\Delta\omega = (2\pi/c\lambda^2)\Delta\lambda$ and $E_{inj}/E_0 = \sqrt{P_{inj}/P_0}$.

As is seen from Eq. (3.90), the locking range of the OIL lasers is not symmetrical for positive and negative frequency detuning due to the $\sqrt{1+\alpha^2}$ factor. This asymmetry is increasing at higher values of the linewidth enhancement factor. The other important feature of the Eq. (3.90) shows that the higher injection ratio enhances the injection locking range. The OIL laser has unstable behaviour outside of the locking range. There can be in general different types of nonlinear regimes which occur in this region under the optical injection. These regimes have been widely studied in literature [16]. In this thesis we are mainly interested in the OIL regime

when the slave laser is locked to the master laser frequency and is in stable condition. In order to achieve enhance modulation dynamics of the slave laser under optical injection, it is essential to provide the stable locking regime.

In 1985, Henry [155] suggested a phasor diagram to demonstrate the relation between the photon field injected from master laser and the photon field produced in slave laser's active region. The phasor diagram provides very good physical insight into the optical injection locking.

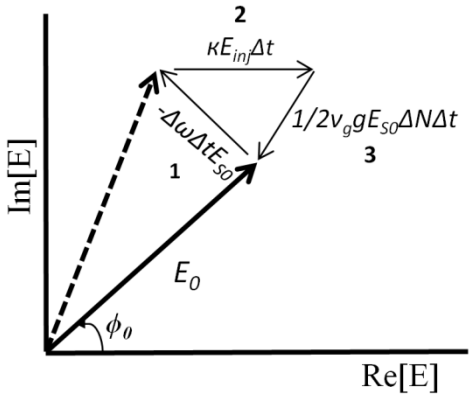

Fig. 3.17 Phasor diagram of OIL lasers [107].

The phasor diagram of a statically OIL laser is shown in Fig. 3.17 . The free-running slave laser has a field presented by E_0 and its phase difference with the master laser field is given by the angle ϕ_0. According to Eqs. (3.83) and (3.84), during Δt injection time, the field vector turns by -$\Delta\omega\Delta t$ amount, as shown by the vector 1 ($\Delta\omega$ here denotes the frequency detuning). If there is no frequency difference between the master and the slave laser fields, there will be no rotation, accordingly. The external field also contributes to the field by the amount denoted by the vector 2. Due to reduction of the carrier density under optical injection, the gain in the slave laser cavity is reduced, which in turn result in a reduction of the field amplitude, which is shown by the vector 3. As a result, the slave laser field phasor returns to its original position since under the

stable locking the sum of all above contribution is exactly zero. And finally the vector field stops rotating and stable locking is provided.

3.12 Small-Signal Analysis and Bandwidth Enhancement of OIL Lasers

The dynamic response of the directly modulated lasers can be analysed by small-signal analysis. This can be achieved by measuring the laser response to the variation of the injected current. The change in carriers and photons in the cavity according to the perturbation of the injected current can be formulated by modifying the rate equations. In this section, firstly the small signal response of the stand-alone laser is investigated by following the derivation briefly given by Coldren et al. [COLDREN]. Later, the similar investigation will be carried out for the optically-injection locked laser. The rate equations for carrier density and photon density are given as:

$$\frac{dN}{dt} = \frac{I(t)}{eV} - \frac{n}{\tau_0} - \upsilon_g a(n - n_0)N_p \tag{3.91}$$

$$\frac{dN_p}{dt} = \Gamma \upsilon_g a(n - n_0)N_p - \frac{N_p}{\tau_p} \tag{3.92}$$

In [152], it is explicitly demonstrated that the small signal response of the laser can be analysed by taking the derivatives of Eq. (3.91) and Eq. (3.92). The dynamic variables are presented as the carrier density N, current I, photon density N_P, and gain g. The change in gain depends on two parameters carrier density and photon density as:

$$dg = adN - a_p dN_p \tag{3.93}$$

The decrease in gain with increasing photon density is shown with the gain compression factor ε.

$$g(N,N_P)=\frac{g_0}{1+\varepsilon N_P}\ln\left(\frac{N+N_s}{N_{tr}+N_s}\right) \tag{3.94}$$

The carrier density dependent change in the gain:

$$a=\frac{\partial g}{\partial N}=\frac{a_0}{1+\varepsilon N_P} \tag{3.95}$$

The photon density dependent change in the gain:

$$a_P=-\frac{\partial g}{\partial N_P}=\frac{\varepsilon g}{1+\varepsilon N_P} \tag{3.96}$$

The derivation of the Eq. (3.91) and Eq. (3.92) are:

$$\frac{d}{dt}\left(dN\right)=\frac{\eta_i}{qV}dI-\gamma_{NN}dN-\gamma_{NP}dN_p \tag{3.97}$$

$$\frac{d}{dt}\left(dN_P\right)=\gamma_{PN}dN-\gamma_{PP}dN_p \tag{3.98}$$

In order to produce a matrix demonstration of the derivation, the changes in carrier densities and photon densities are given by the rate coefficients:

$$\gamma_{NN}=\frac{1}{\tau_{\Delta N}}+\upsilon_g aN_P \qquad \gamma_{NP}=\frac{1}{\Gamma\tau_P}-\frac{R'_{SP}}{N_P}-\upsilon_g a_P N_P \tag{3.99a}$$

$$\gamma_{PN}=\frac{\Gamma}{\tau'_{\Delta N}}+\Gamma\upsilon_g aN_P \qquad \gamma_{PP}=\frac{\Gamma R'_{SP}}{N_P}+\Gamma\upsilon_g a_P N_P \tag{3.99b}$$

The term $\tau_{\Delta N}$ shows the differential carrier lifetime. The differential carrier lifetime of the carriers which contribute the spontaneous emission is shown with $\tau'_{\Delta N}$. In order to test the change

in the input current, following matrix calculation is used for single mode lasers: Eq. (3.97) and Eq. (3.98) are demonstrated in matrix form as:

$$\frac{d}{dt}\begin{bmatrix} dN \\ dN_P \end{bmatrix} = \begin{bmatrix} -\gamma_{NN} & -\gamma_{NP} \\ \gamma_{PN} & -\gamma_{PP} \end{bmatrix}\begin{bmatrix} dN \\ dN_P \end{bmatrix} + \frac{\eta_i}{qV}\begin{bmatrix} dI \\ 0 \end{bmatrix} \tag{3.100}$$

In order to obtain the small signal response of the laser, the drive current is changed above threshold. The matrix form given in Eq. (3.100) includes the change in current *dI*. If the change in drive current is given as $dI(t) = Ie^{i\omega t}$, the change in carrier density and photon density is assumed to have a sinusoidal form. By taking this new form of the input current, the change in the photon and carrier density can be formulated in a matrix form as:

$$\begin{bmatrix} \gamma_{NN} + i\omega & \gamma_{NP} \\ -\gamma_{PN} & \gamma_{PP} + i\omega \end{bmatrix}\begin{bmatrix} N \\ N_P \end{bmatrix} = \frac{\eta_i I}{qV}\begin{bmatrix} 1 \\ 0 \end{bmatrix} \tag{3.101}$$

The carrier density and photon density change can be found by applying Cramer's rule to the matrix. If the matrix determinant is found as $\Delta = \gamma_{NP}\gamma_{PN} + \gamma_{NN}\gamma_{PP} - \omega^2 + i\omega(\gamma_{NN} + \gamma_{PP})$ then both densities can be calculated as:

$$N_1 = \frac{\eta_i I_1}{qV} \cdot \frac{\gamma_{PP} + i\omega}{\omega_R^2} H(\omega) \tag{3.102}$$

$$N_{P1} = \frac{\eta_i I_1}{qV} \cdot \frac{\gamma_{PN}}{\omega_R^2} H(\omega) \tag{3.103}$$

Here the parameter $H(\omega) = \frac{\omega_R^2}{\Delta}$ is used for defining the transfer function [152]. The resonance frequency is found as below.

$$\omega_R^2 = \gamma_{NP}\gamma_{PN} + \gamma_{NN}\gamma_{PP} \approx \frac{v_g a N_P}{\tau_P} \tag{3.104}$$

In order to define the relation between injection current and threshold current, the term $\frac{N_P}{\tau_P}$ in Eq. (3.104) can be written as $\frac{N_P}{\tau_P} = \frac{P_0}{\eta_0 h\nu V_P}$ and then the Eq. (3.104) becomes:

$$\omega_R^2 = v_g a \frac{P_0}{\eta_0 h\nu V_P} \tag{3.105}$$

And finally by using the definition of power given in Eq. (3.54), the final version of the resonance frequency definition becomes:

$$\omega_R^2 = v_g a \frac{\eta_i \eta_0 \frac{h\nu}{q}(I - I_{th})}{\eta_0 h\nu V_P} = \frac{v_g a}{q} \eta_i (I - I_{th}) \tag{3.106}$$

It has been shown by many investigations that the small signal response of lasers can be increased by injection locking. To demonstrate theoretical analysis of small signal response of OIL lasers, rate equations are modified and the change in amplitude ΔA $\left(E(t) = A(t)\exp(i\omega t)\right)$ corresponding to the sinusoidal input current $\Delta I(t)$ are presented as a transfer function for the linearized main equations (3.83) – (3.85) [156]. This relation is shown using the transfer matrix (TM) approach [156] which we will closely follow in this analysis:

$$TM \cdot \begin{bmatrix} \Delta A \\ \Delta \phi \\ \Delta N \end{bmatrix} = \begin{bmatrix} 0 \\ 0 \\ \Delta I \end{bmatrix} \tag{3.107}$$

The sinusoidal change in input current is shown as:

$$I(t) = I_0 \exp\left(i\omega t\right) \tag{3.108}$$

To obtain the small signal response of the OIL laser, it is necessary to use linearization of the rate equations (3.83) – (3.85). The TM in this case is given in Eq. (3.107) as was derived by Lau [156, 157]:

$$\begin{bmatrix} m_{AA+j\omega} & m_{A\phi} & m_{AN} \\ m_{\phi A} & m_{\phi\phi+j\omega} & m_{\phi N} \\ m_{NA} & m_{N\phi} & m_{NN+j\omega} \end{bmatrix} \begin{bmatrix} \Delta A \\ \Delta\phi \\ \Delta N \end{bmatrix} = \begin{bmatrix} 0 \\ 0 \\ \Delta I \end{bmatrix} \tag{3.109}$$

The matrix components are ($z = \kappa A_{inj}/A_0$):

$$m_{AA} = z\cos\phi_0 \qquad m_{A\phi} = zA_0\sin\phi_0 \qquad m_{NN} = -\frac{1}{2}gA_0 \qquad m_{\phi A} = \frac{-z\sin\phi_0}{A_0} \tag{3.110a}$$

$$m_{\phi\phi} = z\cos\phi_0 \qquad m_{\phi N} = -\frac{\alpha}{2}g \qquad m_{NA} = 2A_0\left(\gamma_P - 2z\cos\phi_0\right) \qquad m_{NN} = \gamma_N + gA_0^2 \tag{3.110b}$$

The small signal response function ($H(\omega)=\Delta A/\Delta I$) is then computed as:

$$H(\omega) = \frac{\Delta A}{\Delta I} = M\frac{i\omega + Z}{(i\omega)^3 + A(i\omega)^2 + B(i\omega) + C} \tag{3.111}$$

The corresponding terms in Eq. (3.111) are given as:

$$A = m_{AA} + m_{\phi\phi} + m_{NN}$$

$$B = m_{AA}m_{\phi\phi} + m_{AA}m_{NN} + m_{\phi\phi}m_{NN} - m_{A\phi}m_{\phi A} - m_{AN}m_{NA}$$

$$C = m_{AA}m_{\phi\phi}m_{NN} + m_{A\phi}m_{\phi N}m_{NA} - m_{A\phi}m_{\phi A}m_{NN} - m_{AN}m_{NA}m_{\phi\phi}$$

$$Z = \left(m_{A\phi}m_{\phi N} - m_{AN}m_{\phi\phi}\right)/m_{AN}$$

$$M = -m_{AN} \tag{3.112}$$

By using the Eq. (3.111), it is possible to find the resonance frequency. Lau has shown that the resonance frequency ω_R can be computed as [156]:

$$\omega_R^2 \approx -m_{AN} m_{NA} - m_{A\phi} m_{\phi A} \tag{3.113}$$

Mainly the first term in Eq. (3.113) dominates the second term. If we use the matrix components as shown above, the resonance frequency formula becomes:

$$\omega_R^2 \approx -m_{AN} m_{NA} = g\gamma_P A_0^2 \left(1 + \frac{g}{\gamma_P}\Delta N_0\right) = \omega_{RO}^2 \left(1 - \frac{\gamma_N}{\gamma_P}\frac{\Delta N_0}{A_{fr}^2}\right) \tag{3.114}$$

Eq. (3.114) includes two components of Eq. (3.113) and the resonance frequency enhancement is given by:

$$\omega_R^2 = \omega_{R0}^2 + \Delta\omega_R^2 \tag{3.115}$$

The second term in Eq. (3.113) shows the bandwidth enhancement and it is:

$$\Delta\omega_R = \sqrt{m_{A\phi} m_{\phi A}} = \left|\kappa \frac{A_{inj}}{A_0} \sin\phi_0\right| \tag{3.116}$$

By using Eq. (3.88) and Eq. (3.116), the bandwidth enhancement formula is finalised as:

$$\Delta\omega_R = \left|-\frac{\alpha}{2} g(N_0 - N_{th}) + \Delta\omega_{inj}\right| \tag{3.117}$$

It is also theoretically shown by Murakami [17] that the resonance frequency enhancement of OIL laser is equal to the difference between the cavity shifted frequency which is shown in the first term in Eq. (3.117), and the detuning frequency is given by the second term. The theoretical explanation of the modulation bandwidth enhancement is derived for a single mode lasers and neglecting the side modes. According to this theory it is possible to provide very high resonance frequency and thus the modulation bandwidth enhancement with higher detuning frequency.

3.13 Three-Section Tunable Laser Diode in Transmission Line Model

The Transmission Line Laser Model (TLLM) has been developed by Lowery [29] in 1987 in order to obtain an accurate laser modelling. It has been adapted to different types of lasers including Fabry-Perot lasers [158], distributed feedback lasers [159, 160] and multisection DBR lasers [161]. To achieve a realistic demonstration of laser modelling under direct modulation regime, TLLM solves rate equations for spatially separated cavity lengths rather than frequency. The cavity length 'L' is divided into ΔL subsections which is defined by light propagation during Δt time step ($v_g \Delta t$). It is also aimed to model the electronic parasitic effects of the laser by taking laser's equivalent electrical circuit into account [29]. Each TLLM subsection which has ΔL long length and the incident and reflected waves are processed by a 'scattering matrix'. The scattering matrices include the fundamental features of the cavity; gain, loss, noise and grating parameters. After processing the electromagnetic waves in the scattering matrix, the reflected wave is transmitted to next node by a transmission line. Each transmission line has Δt time delay. The waves are connected between nodes by a 'connection matrix.

The scattering matrix is applied to the incident wave with spontaneous emission factors for the section (n) and time step (k) as below [160]:

$$ {}_k A(n)^r = S \cdot {}_k A(n)^i + {}_k A(n)^s \tag{3.118} $$

Where the term ${}_k A(n)^i$ represents the incident wave inside the node, and scattering matrix 'S' is applied to it to introduce the cavity effects. The last term on the right hand side of the equation ${}_k A(n)^s$ is showing the spontaneous emission. The reflected wave is denoted by ${}_k A(n)^r$. In Fig. 3.18.a representation of the scattering matrix with incident and reflected waves propagating

forward and backward along the cavity is demonstrated. Scattering matrices which are connected by transmission line are also illustrated by Fig. 3.18.b.

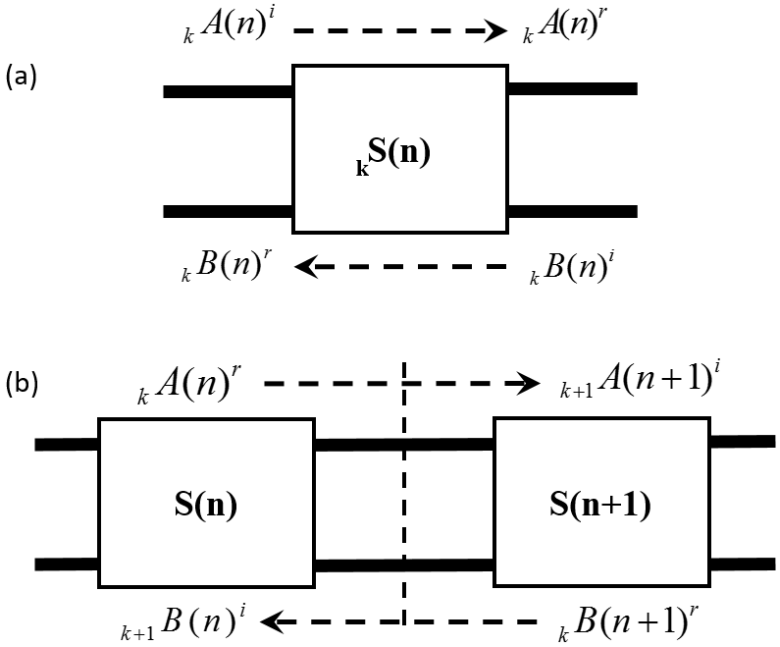

Fig. 3.18 Representation of the scattering matrix and connections of the adjacent nodes [161].

In Fig. 3.18.b, the scattering matrices of adjacent nodes are presented by S(n) and S(n+1). The forward wave is symbolized by letter 'A' and the backward wave is by letter 'B'. The first scattering matrix produces a reflected wave with scattering matrix S, and the transmission line model converts it as the incident wave of the following node. In TLLM, each section of the three section TLD is modelled separately.

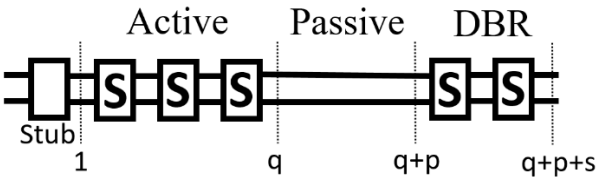

Fig. 3.19 Demonstration of three section TLD in TLLM [161].

The active section of the three-section TLD in TLM includes gain, noise and losses. The wavelength selection is achieved by DBR section, so that there is no filtering in active section as

it is applied in Fabry-Perot TLM [29]. The scattering matrix for active section which is derived by Lowery [161] is:

$$\begin{bmatrix} A(n) \\ B(n) \end{bmatrix}_k^r = \begin{bmatrix} g'(n)t(n) & 0 \\ 0 & g'(n)t(n) \end{bmatrix}_k \begin{bmatrix} A(n) \\ B(n) \end{bmatrix}_k^i + \begin{bmatrix} I_s Z_p t(n)/2 \\ I_s Z_p t(n)/2 \end{bmatrix} \tag{3.119}$$

A(n) and B(n) denote the forward and backward waves. The first term on the right hand side shows the effect of gain g'(n) and loss t(n) on the incident wave. The last term represents the spontaneous emission noise of the model section. I_s is the injected current to the section, Z_p is the cavity impedance. In TLM the active section cavity is divided into q equal sections as it is shown in Fig. N, and the calculation is achieved from n=1 to n=q-1. The first matrix on the right hand side includes gain and attenuation. The gain term 'g' can be shown as in [29]:

$$g'(n) = \exp\{a\Delta L\Gamma[N - N_0]/2\} \tag{3.120}$$

Where a represents the differential gain, Γ is confinement factor and N_0 is the carrier density at transparency. The loss which is shown with t(n) can be given similarly as Eq. (3.120) in Eq. (3.121) below:

$$t(n) = \exp[-\alpha_{sc}\Delta L/2] \tag{3.121}$$

The last term represents the white noise sources, and it can be shown as:

$$\left\langle I_S^2 \right\rangle = 2\beta L_q hfB[N(n)]^2 m^2 / Z_p \tag{3.122}$$

N(n) shows the carrier density for the model section 'n' and it is calculated with conventional rate equation.

$$\frac{dN(n)}{dt} = \frac{I(n)}{wdL_g q} - AN(n) - B[N(n)]^2 - C[N(n)]^3 - \frac{a\Gamma}{n_e}[N(n) - N_0]S(n) \tag{3.123}$$

Where *I*(n) is the injected current, A is for monomolecular, B bimolecular, and C is for Auger recombination, w×d is the area of active section, q is for electron charge and Γ is for confinement factor. The photon number S(n) for each section can be given as:

$$S(n) = ([A^i(n)]^2 + [B^i(n)]^2) n_e / (hfcZ_p m^2) \tag{3.124}$$

After calculating the scattering matrix for given section 'n', the connection matrix is produced to generate the next section's forward and backward waves by using the previous section's reflected wave. This process can continue until the end of the active section. The connection matrix is presented as below by Lowery [161]:

$$\begin{bmatrix} A(n+1) \\ B(n) \end{bmatrix}_{k+1}^{i} = \begin{bmatrix} 1 & 0 \\ 0 & 1 \end{bmatrix}_k \begin{bmatrix} A(n) \\ B(n+1) \end{bmatrix}^{r} \tag{3.125}$$

The connection matrix of the adjacent nodes in active section which is demonstrated in Eq. (3.125) shows the bidirectional behaviour of the TLLM. The forward reflected wave from the scattering matrix 'n' becomes the incident wave of the next node. Additionally, the backward wave reflected from the scattering matrix (n+1) is transferred to previous node. The letter 'k' here shows the number of the iteration of the numerical analysis. As is depicted in Fig. 3.18, the output of the active section is connected to the node called 'Stub'. This node is added to system to represent the phase delay due to the carrier density variations in the cavity. This is applied by inserting a matrix which is shown in Eq. (3.126).

$$\begin{bmatrix} A(1) \\ B_e \\ A_s \end{bmatrix}_k^i = \frac{1}{Z_p + Z_s} x \begin{bmatrix} \rho_{cc}(Z_s - Z_p) & 2\rho_{cc} Z_p \\ \tau_{ca}(Z_p - Z_s) & 2\tau_{ca} Z_p \\ 2Z_s & (Z_p - Z_s) \end{bmatrix}_k \begin{bmatrix} B(1) \\ A_s \end{bmatrix}^i \tag{3.126}$$

Where the stub impedance is Z_s, the reflectivity is ρ (either from cavity to cavity ρ_{cc} or air to cavity τ_{ca}), transmission is τ, B_e is output power, A_s^i and A_s^r are the incident and reflected waves of the stub. The stub impedance equation which is derived by Lowery [161] is:

$$Z_s = Z_p \cot[-0.5\alpha a \Gamma L_a [N(ave) - N_3] \tag{3.127}$$

The stub impedance is calculated as a variation of cavity impedance corresponding to the linewidth factor α and the change in carrier density. To model the phase section, the scattering and the connection matrices have similar structure like active section. The only important difference between two sections is that the passive section does not have any stimulated emission. Only loss mechanism is taken into account to calculate the scattering matrix.

The mode selectivity is achieved in DBR section and there is no gain mechanism similar to phase section. So that the scattering matrix will be like in Eq. (3.128) but without gain:

$$\begin{bmatrix} A(n) \\ B(n) \end{bmatrix}_k^r = \begin{bmatrix} t(n) & 0 \\ 0 & t(n) \end{bmatrix}_k \begin{bmatrix} A(n) \\ B(n) \end{bmatrix}_k^i \tag{3.128}$$

As it is given in fig. 3.20 that the scattering matrices are connected via high and low impedance transmission lines. The forward and backward waves are passing through these lines and they are coupling. For each section, the coupling coefficient κ is multiplied by the section length ΔL.

The transfer matrix for low-high impedance boundary is [161]:

$$\begin{bmatrix} A(n+1) \\ B(n) \end{bmatrix}_{k+1}^i = \begin{bmatrix} 1+\kappa\Delta L & -\kappa\Delta L \\ \kappa\Delta L & 1-\kappa\Delta L \end{bmatrix}_k \begin{bmatrix} A(n) \\ B(n+1) \end{bmatrix}^r \tag{3.129}$$

The transfer matrix for high-low impedance boundary:

$$\begin{bmatrix} A(n+2) \\ B(n+1) \end{bmatrix}_{k+1}^i = \begin{bmatrix} 1-\kappa\Delta L & \kappa\Delta L \\ -\kappa\Delta L & 1+\kappa\Delta L \end{bmatrix}_k \begin{bmatrix} A(n+1) \\ B(n+2) \end{bmatrix}^r \tag{3.130}$$

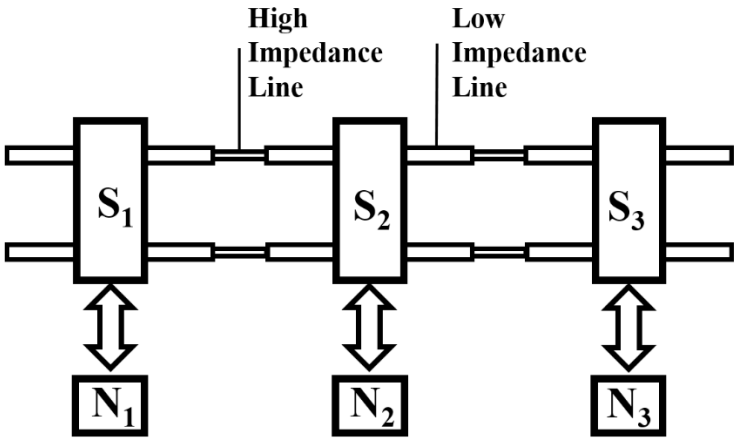

Fig. 3.20 The demonstration of the DBR section representation in TLLM [162]

The length of each node ΔL is an important parameter to obtain a modelling with a good accuracy. The time duration of light propagating along node length Δt is related to the simulation bandwidth. It has been presented by different studies that by having enough time-steps, the modelling of different type of lasers can be carried out. Firstly, Lowery showed that the three section TLD can be modelled by TLLM and later in 2011 the modelling of SGDBR laser is demonstrated by Tan and Yonglin [162]. Both results include consistent spectral and dynamics response demonstration of TLD with TLLMs

CHAPTER 4

OVERVIEW OF TCAD SOFTWARE FOR LASER MODELLING - THE VPI TOOL

4.1 Specifications of the TCAD Tool

Transmission Line Modelling (TLM) is an effective technique to model different types of semiconductor lasers and it was developed by Lowery in 1987 [29]. VPIphotonics is a TLM based Technology Computer-Aided Design (TCAD) tool and it is developed to obtain accurate simulation of photonics components, optical networks [27]. More than 170 universities and industrial companies have been using VPI to improve the quality of their research [163]. Since 1999, more than 1000 scientific publications have been released with original results that were obtained by using VPI tools.

The decision of signal representation plays a crucial role in the accuracy of the simulation. In VPI there are two main signal modes: Sample Mode and Block Mode. If the photonics module is run with TLM, it is necessary to use sample mode. In sample mode, the signal is iterated bidirectionality and the data is packed sample by sample [27]. On the other hand, Block Mode iterates data as a block and unidirectional during the time window as is shown in Fig. 4.1. In VPI, these modes can be converted from either sample mode to block mode (SampleToBlock) or block mode to sample mode (BlockToSample) by using necessary simulation tool.

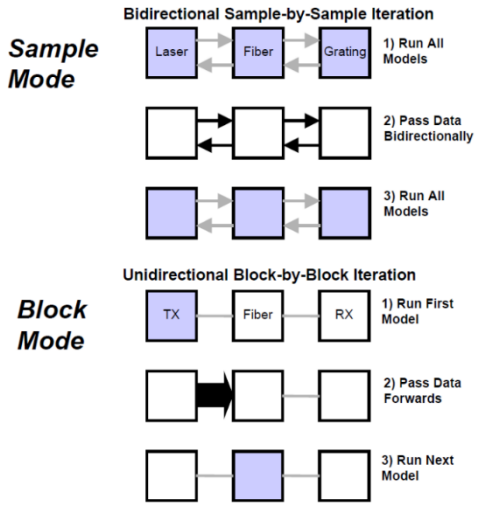

Fig. 4.1 Data iteration in sample and block mode [27].

In VPI, the global parameters of the simulation which are same for every component must be chosen correctly. The parameter window can be modified as is given in Fig. 4.2. The first parameter TimeWindow sets the duration of one run and the reverse of it gives the frequency resolution of Fourier transform. SampleModeBandwidth defines the optical bandwidth of the spectrum. The center frequency of the spectrum is set by the other global parameter SampleModeCenterFrequency.

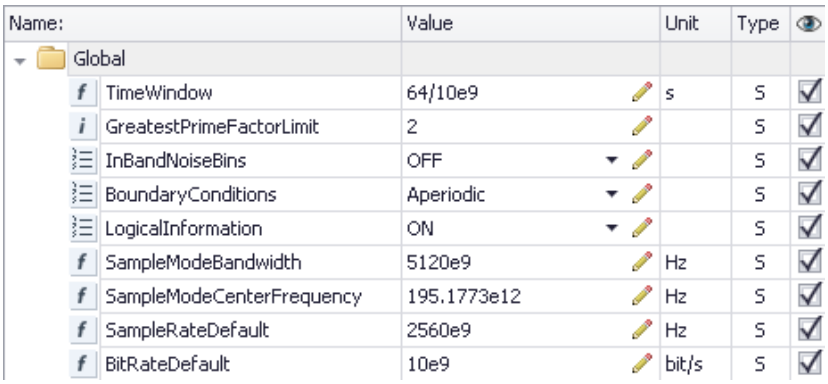

Fig. 4.2 Global parameters window on VPI.

Each TLM component is divided into subsections and the number of them is an important factor which is directly related to the accuracy of the simulation. In TLM, the number of sections is calculated:

$$S = round(L \times SampleModeBandwidth \times \frac{n_g}{c}) \tag{4.1}$$

Where L is device length, n_g is group velocity, and c is speed of light in vacuum. The difference between the length of total number of sections (S*Section length) and original device length (L) will give the amount of unrolled part. Section length is the length which light propagates during each iteration time and it is computed as in Eq. 4.2. This amount must be as small as possible to increase the accuracy.

The computation time of the program is defined by the global parameter SampleModeBandwidth. The inverse of the SampleModeBandwidth is also called “sample

interval". This value also defines the number of sections which cavity is divided during the simulation. The electromagnetic wave that propagates along the cavity passes Δz length during the sample interval Δt is calculated:

$$\Delta z = \nu_g \Delta t \tag{4.2}$$

Where, ν_g is the group velocity. It is clearly seen that by increasing the SampleModeBandwidth, the number of cavity subsections increases and this causes longer computational time. To find optimal value of the SampleModeBandwidth, it is important to cover the number of modes to be simulated, and gain peak inside simulation window.

4.2 Photonics Circuits Demonstration in VPI

In this part, the implementation of the TLM in VPI to simulate photonics circuits will be discussed. In VPI, simulation of multisection lasers can be carried out successfully for different type of active section structures Bulk or Multi-Quantum Well (MQW). It is possible to investigate different characteristics of them such as modulation responses, CW operations, spectral properties, different noise characteristics, linewidth, light injection responses etc.

The relation between time and space is given as in Eq. 4.2. Each divided subsection is connected to the adjacent ones with sampling interval Δt delay. After completing the necessary calculations, these waves are sent to next nodes. The time delay Δt is defined by the inverse of 'SampleModeBandwidth'. All this scattering process in VPI is graphically demonstrated in Fig. 4.3 below. If the semiconductor laser has more than one section, each of the device section is represented with the letter 'k' and they also have their own contact to provide electrical injection. The device sections are divided into the TLM sections which have Δz long length and each of them has gain, loss, recombination, and grating processes.

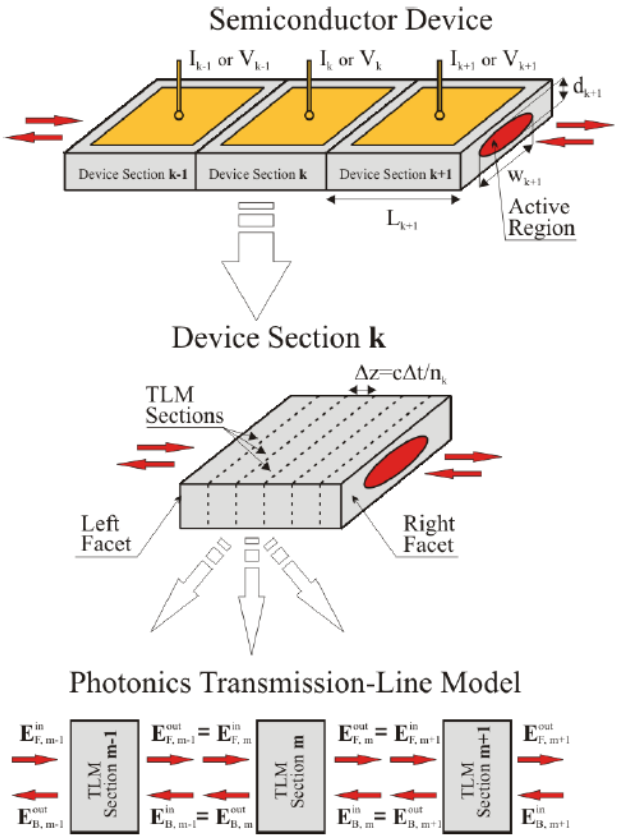

Fig. 4.3 The TLM demonstration of the semiconductor laser in VPI. The scattering nodes are connected with lossless transmission lines [27].

The TLM sections in each component are connected by lossless transmission lines and they are denoted by 'm'. The scattering waves between TLM sections are represented for given TLM section m as $E_{F,m}^{in}$, $E_{F,m}^{out}$ for forward waves and $E_{B,m}^{in}$ $E_{B,m}^{out}$ for backward waves. The output wave of the TLM section m-1 is transformed to the input wave of the adjacent TLM section m by using connection matrix in TLM. Every semiconductor laser which is modelled with TLM has electrical input and output ports for each device section. The change in carrier dynamics can be controlled by the electrical input, and the carrier density of the section can be plotted by using the electrical output port. The optical process consists of the carrier generation, absorption and propagation. There are different device sections defined according to their optical and electronic

designs. In our study, a three section tunable laser diode (TLD) is modelled with three different type of device sections in Fig.4.4:

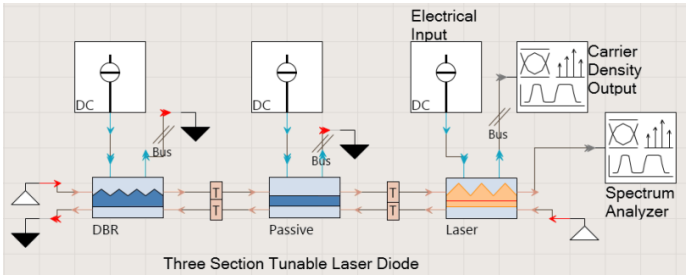

Fig. 4.4 Three-Section Tunable Laser Diode representation in VPI.

The three-section TLD must be established by using active and passive device components in VPI. The scattering mechanisms of passive and active section in VPI are shown in Fig. 4.5 and Fig. 4.6. The main difference between two scattering mechanisms is that the spontaneous and stimulated emission mechanisms do not exist in passive sections.

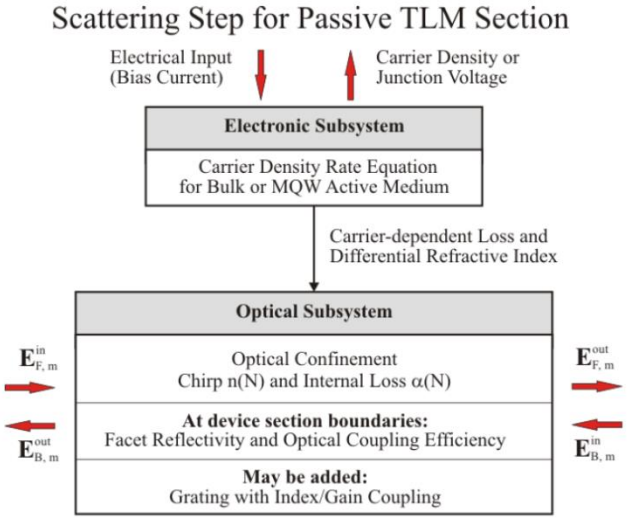

Fig. 4.5 The scattering scheme of the passive section modelling in VPI [27].

Electronic and optical subsystems in the cavity; carrier density calculations, the available gain definitions, grating and chirping modelling are explained with details in following sections.

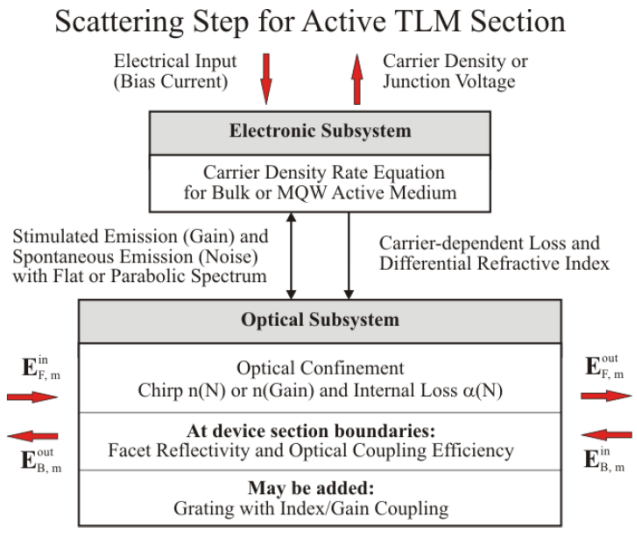

Fig. 4.6 The scattering scheme of the active section modelling in VPI [27].

4.3 The calculation of the carrier dynamics with rate equation

The carrier density dynamics of the laser is controlled by the electrical input, and are calculated via rate equations. The derivation depends on the material structure. If the laser is modelled with bulk material, the change in carrier density is calculated as in Eq. 4.3 below:

$$\frac{dN_m}{dt} = \frac{\eta_k I_k}{qV_k} - R(N_m) - v_{g,k}\widehat{G}(N_m, S_m)\cdot S_m + \frac{\beta_{TPA,k}}{2E_{ph}}\frac{\left\langle |E|^4 \right\rangle}{A_{eff,k}^2} \tag{4.3}$$

The calculation is carried out for given device section's (k) TLM section (m). The calculated carrier density is accepted uniform during the TLM section Δz (m) but it varies for whole cavity (k). This is one of the most important differences between TLM and conventional rate equations. This result also shows the way of improving the accuracy of the calculation. It is necessary to divide the cavity in smaller sections to obtain more consistent simulation results. This can be achieved by increasing the SampleModeBandwidth of the simulation.

The first right hand side of the Eq. 4.3 shows the generated carrier density. The electric current which is applied to the device section (k) is shown with I_k. The current efficiency of the device section which can be controlled by the parameter CurrentInjectionEfficiency and it is denoted with "η_k". Due to the impairments of the electrical contacts, only a fraction of the injected current can contribute to the carrier generation. The volume of the section is shown with V_k and q represents the electron charge. The three dimensions of the component can be specified by using the parameters under the section "Device Structure".

The second term on the right hand side of Eq. 4.4 includes three recombination rates which cause spontaneous emission and nonradiative loss in the cavity. This relation can be given as:

$$R(N_m) = A_k N_m + B_k N_m^2 + C_k N_m^3 \tag{4.4}$$

The parameters which are shown in Eq. 4.4 are that A is for the linear recombination, B is the bimolecular recombination, and C represents the Auger recombination. These parameters can be modified for any laser sections directly under the Carrier Dynamics section.

The third parameter is responsible for the change in photon density due to the gain exist in the cavity. The available gain definitions in VPI are explained in section 4.5. The fourth term in Eq. 4.3 includes the parameters to insert the two-photon absorption (TPA) effect. The parameters $\beta_{TPA,k}$ and $A_{eff,k}$ can be defined by the parameters "TwoPhotonAbsorption" and "EffectiveModeArea".

If the active section is defined with MQWs, the change in the carrier density is calculated with two rate equations: one for conduction band $N_m(t)$ and one for undoped SCH region $N_{SCH,m}(t)$ [27].

$$\frac{dN_{SCH,m}}{dt} = \frac{\eta_k I_k}{qV_{SCH,K}} - \frac{N_{SCH,m}}{\tau_{cap,k}} + \frac{N_m}{\tau_{esc,k}} \cdot \frac{d_{MQW,k}}{d_{SCH,k}} + \frac{\beta_{TPA,k}}{2E_{ph}} \cdot \frac{\left\langle |E|^4 \right\rangle}{A_{eff,k}^2} \tag{4.5}$$

$$\frac{dN_m}{dt} = \frac{N_{SCH,m}}{\tau_{cap,k}} \cdot \frac{d_{SCH,k}}{d_{MQW,k}} - \frac{N_m}{\tau_{esc,k}} - R(N_m) - \nu_{g,k}\widehat{G}(N_m, S_m) \cdot Sm + \frac{\beta_{TPA,k}}{2E_{ph}} \cdot \frac{\left\langle |E|^4 \right\rangle}{A_{eff,k}^2} \tag{4.6}$$

Where, terms $\tau_{cap,\,k}$ and $\tau_{esc,k}$ denote the capture and escape times of the carriers between SCH and MQW regions, $V_{SCH,k}$ represents the volume of SCH region, $d_{SCH,k}$ and $d_{MQW,k}$ are the thicknesses of SCH and MQW regions. To specify $\tau_{cap,k}$ and $\tau_{esc,k}$ terms, CarrierCaptureTimeconstant and CarrierEscapeTimeconstant parameters are modified in VPI. In [27], it has been shown that these terms have significant effect on modulation bandwidth of the lasers. The carrier density modelling of MQW active sections is carried out according to the effective MQW model explained in [164] and [165]. In these studies, an effective MQW demonstration is carried out with a MQW section and two SCH on both sides. The capture and escape times show the carrier change between MQW and SCHs. In Eq. 4.5, the change of the carrier density in SCH region is given as a sum of the generated carriers by injected current in the SCH region, captured carriers by MQW, escaped carriers from MQW, and the carriers created by two photon absorption (TPA) mechanism. In Eq. 4.6, the computation of the change in carrier density in MQW region is given. The captured and escaped carriers, the carriers generated by spontaneous and stimulated emissions and finally the effect on TPA in MQW region are taken into account.

4.4 The Travelling Wave Equations and Photon Density

The electric field in TLM is represented as in Eq. 4.7:

$$\vec{E}(\vec{r},t) = \exp(j2\pi f_c t)\left[\vec{F}(\vec{r}_\perp, f_c)A(z,t) + \vec{F}^*(\vec{r}_\perp, f_c)B(z,t)\right] + c.c. \tag{4.7}$$

The forward and backward fields in the cavity are given with A(z,t) and B(z,t). The SampleModeCenterFrequency is denoted with f_c. The variations of the complex propagating fields are shown as:

$$a(z,t) = e^{i(\beta_0 - \delta_{grating})z} \cdot A(z,t) \tag{4.8}$$

$$b(z,t) = e^{-i(\beta_0 - \delta_{grating})z} \cdot B(z,t) \tag{4.9}$$

Where the propagation constant is shown with β_0, and the detuning due to the grating parameter is given with $\delta_{grating}$. The propagation constant is:

$$\beta_0 = \frac{2\pi f_0}{c} n_{eff}(f_0) \tag{4.10}$$

Where f_0 is the nominal frequency, n_{eff} is the effective refractive index. Finally the travelling wave equations are derived [27] as:

$$\left[\frac{1}{v_{g,k}}\frac{\partial}{\partial t} + \frac{\partial}{\partial z}\right]a = \left[\frac{1}{2}\hat{G}(N_m, S_m) - \frac{1}{2}\alpha_a - i\delta_a\right]a - i\kappa_{ab}b + Q_a \tag{4.11}$$

$$\left[\frac{1}{v_{g,k}}\frac{\partial}{\partial t} + \frac{\partial}{\partial z}\right]b = \left[\frac{1}{2}\hat{G}(N_m, S_m) - \frac{1}{2}\alpha_b - i\delta_b\right]b - i\kappa_{ba}a + Q_b \tag{4.12}$$

The material gain which is depended on the carrier density N_m is given by $\hat{G}(N_m, S_m)$, the optical loss is shown with α, the grating detuning is presented by δ, the coupling coefficient of waves is denoted by κ. There are also noise terms for both waves shown with Q. The photon density of each TLM subsection is shown with S_m. In TLM, the photon density is calculated as:

$$S_m(t) = \frac{\Gamma_k}{E_{ph} v_{g,k}} \frac{1}{w_k d_k \Delta z} \int_{z_m - \Delta z/2}^{z_m + \Delta z/2} \left|A(z,t) + B(z,t)\right|^2 dz \tag{4.13}$$

In Eq. (4.13), confinement factor for each device section is given with Γ_k, photon energy is E_{ph}, the width and the thickness of each section are shown by w_k and d_k. It is shown in [27] that all these computations are achieved in VPI by using the approach defined in [166].

4.5 Gain models in VPI

In VPI, the spectral dependence of the gain can be specified by three different models. The common definition of the gain operator with confinement factor Γ_k, and nonlinear gain saturation ε is given as [27]:

$$\hat{G}(N_m, S_m) = \Gamma_k \cdot \frac{\hat{g}(N_m)}{1 + \varepsilon \cdot S_{R,m}} \tag{4.14}$$

The frequency dependent gain coefficient $\hat{g}(f, N_m)$ can be modelled for one of the following shapes: parabolic, flat or measured (defined by user) shape. The gain shape can be changed inside the active section's parameter window. The parameter GainShapeModel in this section includes these three models to be chosen by users.

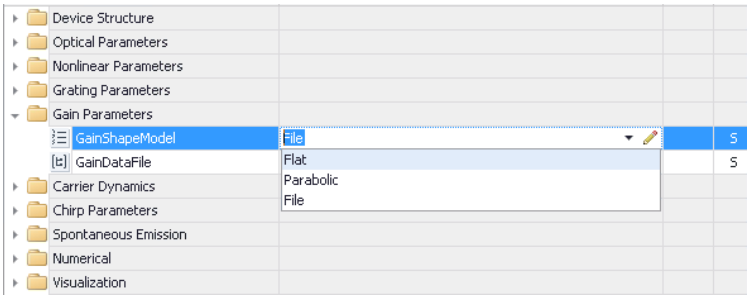

Fig. 4.7 Gain Shape Model definition in VPI.

4.5.1 Flat Gain Shape

If the gain shape model is defined with a flat shape, the gain value for given carrier density N_m becomes constant along the spectrum, and the change of the gain peak value $g_{peak}(N_m)$ for corresponding carrier density can be modelled with either linear or logarithmic dependency. This can be specified by choosing one of the options offered by GainModel section. In Fig. 4.8 the gain model is defined as linear. The change in the gain peak value for different N_m is calculated by Eq. (4.15).

$$g_{peak}(N_m) = a_{lin,k} \cdot (N_m - N_{0,k}) \tag{4.15}$$

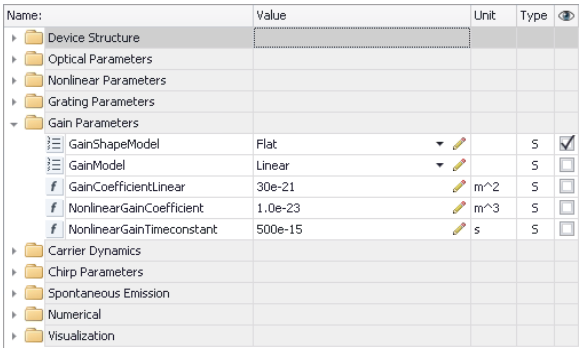

Fig. 4.8 Gain definition for flat shape in VPI.

The parameter GainCoefficientLinear defines the differential gain value $a_{lin,k}$ of the device section k. The gain peak value of the laser changes according to the linear difference between carrier density and transparency carrier density $N_{0,k}$ of the TLM section. The transparency carrier density is defined by the parameter CarrierDensityTransparency in active section.

If the gain model of the laser is defined as Logarithmic, the change of the gain peak value with carrier density becomes logarithmic. For this case the gain peak value for different carrier density N_m:

$$g_{peak}(N_m) = a_{\log,k} \cdot \log\left(\frac{N_m}{N_{0,k}}\right) \tag{4.16}$$

4.5.2 Parabolic Gain Shape

The flat gain shape model is not adequate for laser modelling and the spectrum dependent change in gain value must be taken into account to carry out a realistic analysis. There are two types of gain spectrum shapes for Bulk and MQW cavity lasers. The shape which is offered by VPI is a parabolic spectrum. In this model, the increase of the gain peak value for different carrier densities is calculated by either linear or logarithmic increase. The frequency range which is given in Fig. 4.9 is defined by a global parameter SampleModeBandwidth.

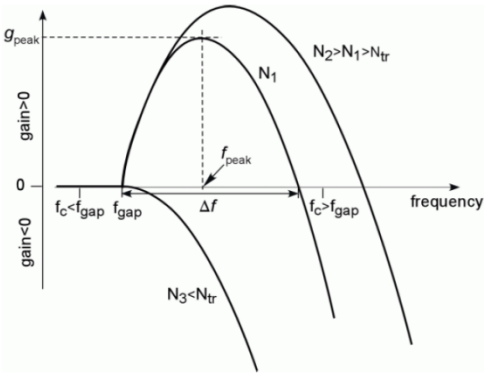

Fig. 4.9 Parabolic gain shape demonstration in VPI [27].

If the carrier density N_m is more than transparency carrier density, for frequencies higher than bandgap frequency gain value becomes positive until the end of gain bandwidth. Otherwise for the carrier densities which are less than the transparency carrier density, the gain is negative. The gain value for given carrier density and frequency is calculated as in Eq. 4.17 below:

$$g(f, N_m) = g_{peak}(N_m) \cdot \left\{ 1 - \left[\frac{f - f_{peak}(N_m)}{\Delta f(N_m)/2} \right]^2 \right\} \tag{4.17}$$

The peak gain value $g_{peak}(N_m)$ can be specified as a either like in Eq. 4.15 or in Eq. 4.16. To model a reference parabolic gain spectrum, the gain parameters in active section are specified as in Fig. 4.10. The gain coefficient $a_{lin,k}$ in Eq. 4.15 is specified by the parameter GainCoefficientLinear to produce a linear gain model. The peak frequency of the reference gain spectrum is defined with an offset value to the centre frequency of the simulation setup by GainPeakFrequency. The centre frequency of the simulation is the global parameter SampleModeCenterFrequency. The bandwidth of the reference gain spectrum is presented by the parameter GainBandwidth. Finally, this reference gain spectrum shape is designed for the carrier density CarrierDensityRefGainShape.

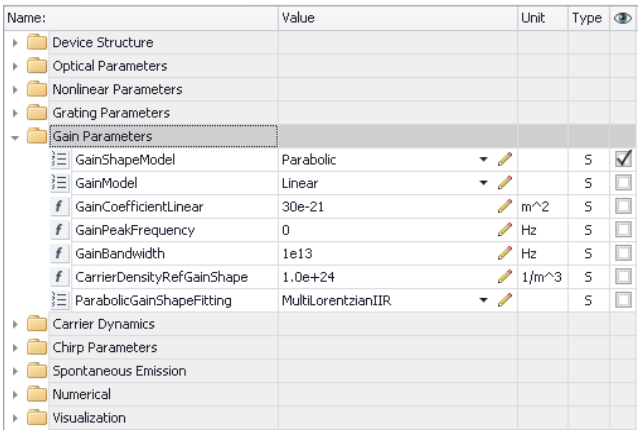

Fig. 4.10 Definition of the parabolic gain shape parameters.

After designing the reference gain spectrum as it is shown in the Fig. 4.10, carrier density depended gain spectrum is calculated according to the reference curve. The gain bandwidth $\Delta f(N_m)$, and the gain peak frequency $f_{peak}(N_m)$ for the carrier density N_m is calculated by:

$$\Delta f(N_m) = \Delta f(N_{ref,k}) \cdot \sqrt{\frac{g_{peak}(N_m)}{g_{peak}(N_{ref,k})}} \tag{4.18}$$

$$f_{peak}(N_m) = f_{peak}(N_{ref,k}) + \frac{\Delta f(N_{ref,k})}{2} \cdot \left[\sqrt{\frac{g_{peak}(N_m)}{g_{peak}(N_{ref,k})}} - 1 \right] \tag{4.19}$$

If the carrier density is lower than the transparency, there will be only absorption after the bandgap frequency f_{gap}. The negative gain value (loss) can be calculated as:

$$g(f) = -g_{peak}(N_{ref,k}) \cdot \left[\frac{f - f_{gap}}{\Delta f(N_{ref,k})/2} \right]^2 \tag{4.20}$$

In our setup, the three section laser is modelled with transmission laser modelling (TLM) and to obtain realistic gain curve in time domain, there are two types of filters can be applied to the gain spectrum: First Order IIR, and Multi Lorentzian IIR. One of these models can be chosen by changing the parameter ParabolicGainShapeFitting inside the gain parameters window in active section of the laser.

4.5.3 Measured Gain model

Apart from parabolic and flat gain models, it is also possible to upload a data file includes the gain spectrum for given carrier densities. This file can be obtained either from experimental results or extracted from an advanced laser physics simulator. To activate this model, the 'GainShapeModel' parameter has to be set to 'File'. The loaded file includes the gain in different units for frequencies inside the simulation window. It is essential to provide data for given SampleModeBandwidth range which is centred at SampleModeCenterFrequency. The data file must include the frequency and gain data for corresponding carrier densities as is show in Fig. 4.11. The comment lines in data file start with double slashes //. The header lines which include the information about the spectrum start with the number sign #. The data which is required to define the spectrum is entered as below in Fig. 4.11.

```
// Material Gain for N=[0.8-1.5]e24 m^(-3)
# CarrierDensity = 0.8e24 (1/m^3)
# Wavelength    Gain
# (um)          (1/cm)
  0.151500E+001 -0.189896E+003
  0.151504E+001 -0.189480E+003
  0.151508E+001 -0.189064E+003
  0.151511E+001 -0.188648E+003
  0.151515E+001 -0.188232E+003
```

Fig. 4.11 Gain data file format in VPI.

To compute the gain values for undefined wavelengths (or frequencies), VPI uses Multilorentzian filters for interpolation. It is vital to define the value of Multilorentzian filter in order to complete the setup. It is clear that higher order filter provides more accuracy. The Multilorentzian fitting is successfully applied to 80% of the gain bandwidth. On the other hand, 10% of the both end of the bandwidth is not fit correctly. As a result of this, it is important to be careful about the definition of bandwidth of the spectrum. There could be a computational mistake if the emission frequency coincide the edge of the spectrum.

4.5.4 First Order IIR and Multi Lorentzian IIR

A filter is applied to the gain spectrum defined in the active section to obtain accurate results in TLM. The difference between these two types of the filters is given for different carrier densities in Fig. 4.12. Black curve represents the original gain spectrum, blue curve is the result of the first order IIR filtering, and green and red curves are derived by using Multilorentzian filtering for different fitting orders. In Fig. 4.12.a, the gain spectrum is plotted for N=1.5e24 $1/m^3$ which is equal to the transparency carrier density. In this spectrum, gain becomes negative for the frequencies above the bandgap frequency. The reference gain spectrum is plotted for the carrier density N=2.0e24 $1/m^3$ in Fig. 4.12.b. Gain peak frequency and gain bandwidth is defined in active section by users. The First Order IIR filter provides accurate gain value for only peak gain frequency and 2-3 adjacent frequencies.

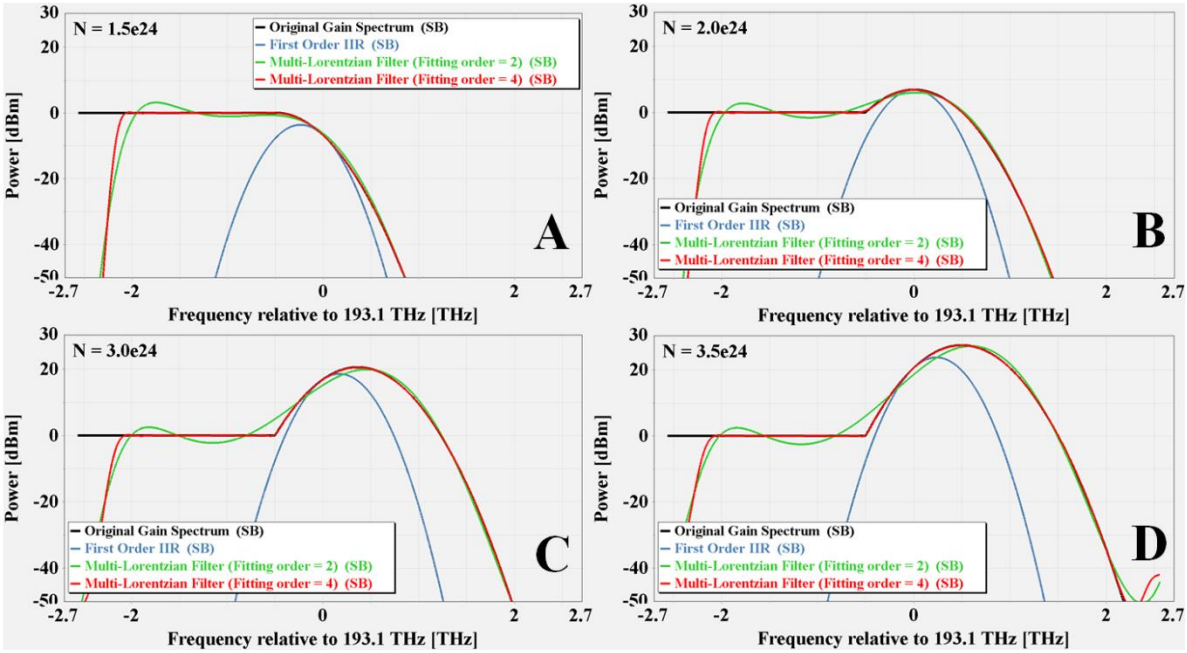

Fig. 4.12 First Order IIR and Multilorentzian IIR filter representations for different carrier densities.

On the other hand, Multilorentzian IIR filter provides more accurate gain spectrum interpolation. It is clearly demonstrated in Fig. 4.12.c and 4.12.d that the filter accuracy is directly related to the fitting order. The order of the Multilorentzian filter is defined in the active section under the subsection Numerical in active section. In this section accuracy and the time duration of the simulation are specified by the parameters GainFilterOrder, MinimumStepScalling and StepAdjustmentFactor.

4.6 Chirping Modelling in VPI

The TLM equations which are given by Eq. 4.11 and 4.12 include the detuning factors δ_a and δ_b. The variation of refractive index causes a change in the phase and the detuning related to this change is presented by δ_a. On the other hand, the second term δ_b shows the frequency change due to the Bragg condition. This could be activated only if there is any grating model defined. To model the refractive index change Δn_{eff} for forward and backward waves, two models are offered by VPI: "Differential Index Model for Free-Carrier Dispersion" and "Linewidth Factor Model of Free Carrier Dispersion" [27]. There is only plasma effect taken into account to model this free carrier dispersion. In Chapter 5, we demonstrate an integrated model to show both plasma effect and Kramer's Kronig effect on refractive index change.

$$\delta_a = \frac{2\pi f_0}{c} \cdot \Delta n_{eff,m,a} + \delta_{grating} \tag{4.21}$$

$$\delta_b = \frac{2\pi f_0}{c} \cdot \Delta n_{eff,m,b} + \delta_{grating} \tag{4.22}$$

In Eq. (4.21) and Eq. (4.22), f_0 denotes the nominal frequency which is specified by the parameter "NominalFrequency" in active section. This value can be changed according to the desired frequency to improve accuracy.

4.6.1 Chirping Modelling with Differential Index Parameter

In VPI, the change in the refractive index parameter can be specified by the chirping parameters of every device section. In the first model the differential index parameter can be specified directly and the corresponding change of the refractive index can be calculated for Bulk region as:

$$\Delta n_{FCD}(N_m) = \Gamma_k \cdot \frac{dn}{dN_m}(N_m - N_{ch,k}) \tag{4.23}$$

Or for MQW region:

$$\Delta n_{FCD}(N_m) = \Gamma_k \cdot \frac{dn}{dN_m}(N_m - N_{ch,k}) + \Gamma_{SCH,k} \cdot \frac{dn_{SCH}}{dN_{SCH,m}}(N_{SCH,m} - N_{ch,k}) \tag{4.24}$$

To model the chirping of the laser with differential index model, following parameters must be defined: Γ_k denotes confinement factor, dn/dN represents differential index, and $N_{ch,k}$ shows the reference carrier density. The refractive index change is calculated according to the difference between reference carrier density $N_{ch,k}$ and the carrier density of the laser N_m.

4.6.2 Chirping Modelling with Linewidth Enhancement Factor

If the chirping model in active section is set to “LinewidthFactor”, the differential index is derived through the linewidth enhancement factor. As it is shown in Eq. (4.25) below, the differential index of the laser depends on the change in differential gain value.

$$\frac{dn}{dN_m} = -\frac{\lambda \alpha_{lw}}{4\pi} \cdot \frac{dg_{peak}}{dN_m} \tag{4.25}$$

The differential gain value and reference carrier density are defined by users in VPI if the gain spectrum is selected as parabolic or flat shape in VPI. On the other hand, if the gain spectrum is specified by a data file which is installed by user, α factor cannot be defined and the linewidth enhancement factor cannot be used to model the chirping. To define the chirping modelling for the user defined gain spectrum, it is essential to use differential index parameter model.

4.7 Grating Models in VPI

In VPI, DBR gratings can be added to any type of laser section which is modelled with TLM. The parameter editing window for grating definition is shown in Fig. 4.13. The following text will include the grating models and corresponding equations explained in [27].

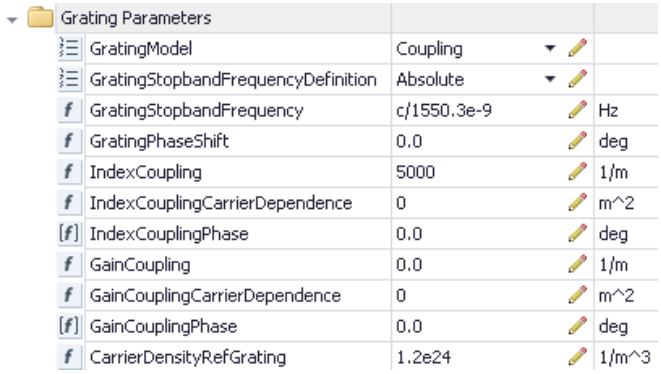

Fig. 4.13 Grating parameter editing window in VPI.

As is given in Eq. 4.11 and Eq. 4.12, TLM equations include grating terms $\delta_{grating}$, κ_{ab} and κ_{ba}. The detuning term $\delta_{grating}$ is formulated as below:

$$\delta_{grating} = \frac{2\pi\Delta f_{Bragg}}{c} \cdot n_{eff,k} \tag{4.26}$$

There are three ways to define the position of grating stopband center frequency by using one of the parameter under 'GratingStopbandFrequencyDefinition' section. If the parameter 'Absolute' is chosen, the stopband f_{res} in eq. N becomes equivalent to the parameter 'GratingStopbandFrequency'. To have a relative value to the center frequency of the simulation, the parameter 'Relative' can be chosen and f_{res} becomes GratingStopbandFrequency + SampleModeCenterFrequency. If the user wants to use the formula which is given in Eq. 4.26 the parameter 'GratingPeriod' is chosen, and the grating period parameter is defined manually.

The detuning parameters κ_{ab} and κ_{ba} give the coupling backward and forward waves. These coefficients are defined by the parameter 'GratingModel'. There are three options to do this

selection: NoGrating, Coupling, Parameters. ‘NoGrating’ model switches the grating modelling off and there is no grating parameter becomes activated.

The other models ‘Coupling’ and ‘Parameters’ are working as follows. The equations which define the coupling parameters are given as below:

$$\kappa_{ab} = \kappa_i \exp(i\Psi_i) + i\kappa_g \cdot \exp(i\psi_g) \tag{4.27}$$

$$\kappa_{ba} = \kappa_i \exp(i\Psi_i) + i\kappa_g \cdot \exp(i\psi_g) \tag{4.28}$$

The second coupling term κ_g in Eq. (4.27) and Eq. (4.28) is a carrier density depended value and it could be either gain or loss coupling according to its sign. If the GratingDetailed parameter is set as Coupling, the effect of carrier density change is accepted as linear as it is shown in Eq. (4.29) and Eq. (4.30) below.

$$\kappa_i(N_m) = \kappa_i(N_{gr,k}) + \frac{d\kappa_i}{dN_m} \cdot (N_m - N_{gr,k}) \tag{4.29}$$

$$\kappa_g(N_m) = \kappa_g(N_{gr,k}) + \frac{d\kappa_g}{dN_m} \cdot (N_m - N_{gr,k}) \tag{4.30}$$

In both formula, the reference carrier density is given as $N_{gr,k}$ and it is defined by the parameter ‘CarrierDensityRefGrating’. The index coupling κ_i and gain coupling κ_g parameters are specified by the parameters IndexCoupling and GainCoupling. The derivatives in both equations are set with parameters ‘IndexCouplingCarrierDependence’ and ‘GainCouplingCarrierDependence’.

If the grating model is defined with ‘Parameters’, the coupling coefficient $\kappa_i(N_m)$ given in Eq. (4.29) above will be calculated as below for Bulk and MQW materials:

For bulk material:

$$\kappa_i(N_m) = \frac{2\mu_k \Delta\Gamma_k}{\lambda}\left[\Delta n_k + \frac{dn}{dN_m} \cdot (N_m - N_{gr,k})\right] \tag{4.31}$$

For MQW:

$$\kappa_i(N_m) = \frac{2\mu_k \Delta\Gamma_k}{\lambda}\left[\Delta n_k + \frac{dn}{dN_m}\cdot(N_m - N_{gr,k})\right] + \frac{2\mu_k \Delta\Gamma_{SCH,k}}{\lambda}\left[\Delta n_k + \frac{dn_{SCH}}{dN_{SCH,m}}\cdot(N_{SCH,m} - N_{gr,k})\right] \quad (4.32)$$

The coefficients given above are defined in the parameter window as is seen in Fig. 4.14 below. GratingShapeFactor is for gain shape coefficient μ_k (1 for rectangular shape), CarrierDensityRefGrating is for reference carrier density $N_{gr,k}$, EffectiveIndexStep is for Δn_k, ConfinementFactorStep is for the difference in confinement factor for Bulk material $\Delta\Gamma_k$. On the other hand, if the grating is defined for MQW lasers confinement factor difference in MQW region is defined with ConfinementFactorStepMQW, ConfinementFactorSCH for SCH region. The refractive index change of the laser with carrier density (dn/dN and dn_{SCH}/dN) is defined in ChirpModel section.

Grating Parameters		
GratingModel	Parameters	
GratingStopbandFrequencyDefinition	Absolute	
GratingStopbandFrequency	c/1550.3e-9	Hz
GratingPhaseShift	0.0	deg
EffectiveIndexStep	0.04	
InternalLossStep	0.0	1/m
CarrierDensityRefGrating	1.2e24	1/m^3
ConfinementFactorStepMQW	0.03	
ConfinementFactorStepSCH	0.1	
GratingShapeFactor	1.0	

Fig. 4.14 Grating parameters definition in the 'Parameters Model'

Additionally, the gain coupling coefficient is calculated as:

$$\kappa_g(N_m) = \frac{\mu_k}{2\pi}\left\{G(N_m, S_m)\frac{\Delta\Gamma_k}{\Gamma_k} - \left(\Delta\Gamma_k + \Delta\Gamma_{SCH,k}\right)\left(\Delta\alpha_k + \alpha_{iN}\frac{\Delta\Gamma_k}{\Gamma_k}N_m\right)\right\} \quad (4.33)$$

Where $G(N_m,S_m)$ denotes the gain of the section and $\Delta\alpha_\kappa$ and $\Delta\alpha_{iN}$ are the loss parameters. $\Delta\alpha_\kappa$ is defined by the parameter InternalLossStep, and $\Delta\alpha_{iN\ defines}$ the carrier density depended loss which is modified by the parameter InternalLossCarrierDependence.

4.8 Typical methods for laser characterization on VPI

4.8.1 Small signal analysis in VPI

Although there is a single component to make it easier to measure in the recent version of VPI, we have used the method as is shown in Fig. 4.15 below for small signal analysis of the semiconductor laser. The figure includes three components and a 2D analyser to plot the intensity modulation (IM) response in Watt/Ampere (W/A). To drive the laser with a sinusoidal input current, the component 'FuncSinEl' is connected to the active section of the laser. This component produces a sinusoidal electrical signal of which properties such as frequency, bias current, drive current, and phase can be directly defined by users. The output of the laser is connected to the module is shown in fig. N. The output signal of the laser which is in the optical form firstly passes through the component 'TimeResolved_Freq_Power' and its amplitude and frequency is detected and the signal is converted to electrical form. This output signal is sent to the second component 'TwoPortAnalyzer' to detect frequency, phase and amplitude of the electrical input. Before plotting the output to drop the transient effects it 'Chop' is added to remove the first runs (even if it is only one run per modulation frequency, the number of run will be duplicated automatically).

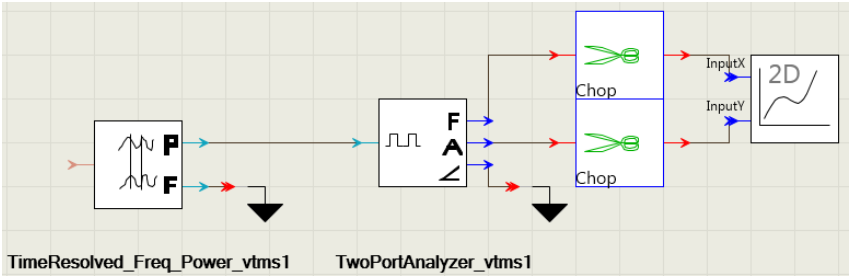

Fig. 4.15 Small signal IM response module in VPI.

Finally, the response of instantaneous frequency vs detected power by modulation depth is plotted on a 2D analyser. To change the frequency modulation in a range, the sweep function is

added. It allows users any parameter in simulation to be swept in user defined range. It should be also noted here that the frequency modulation (FM) response of the laser can be also plotted by measuring the frequency output of the TimeResolved_Freq_Power module. An example of the small signal IM response of laser is given in fig. N below.

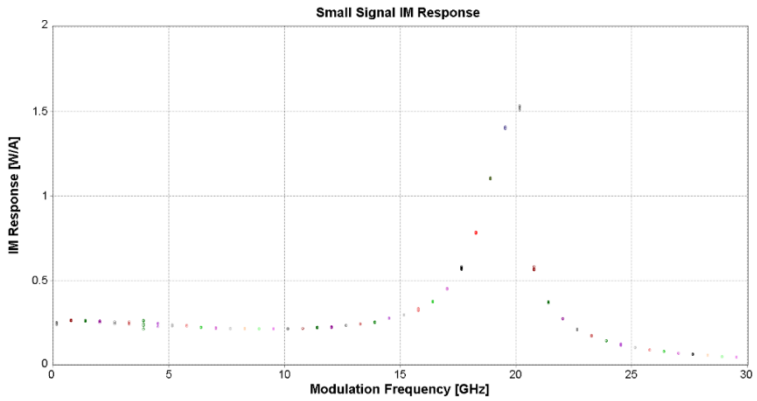

Fig. 4.16 Small Signal IM Response of TLD with multiple run.

4.8.2 Chirping estimation in VPI

In VPI it is also possible to demonstrate the frequency deviation of the lasers. As is seen in fig. N, the optical output of the laser can be analysed and the frequency deviation can be plotted versus time by using the component 'TimeResolved_Freq_Power'.

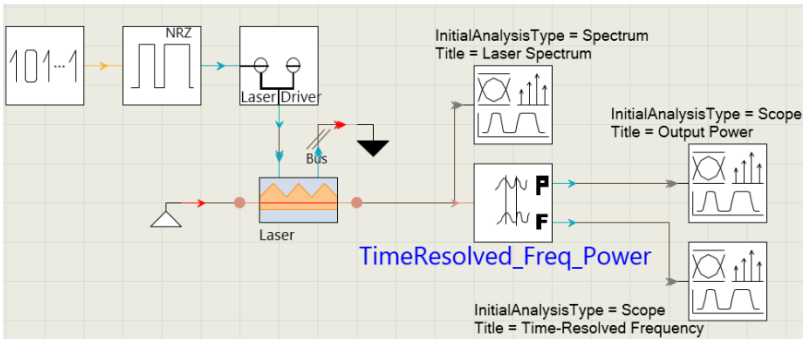

Fig. 4.17 Chirping estimation model in VPI.

To have a correct estimation of chirping, it is essential to calibrate the component 'TimeResolved_Freq_Power' correctly. There are parameters to do this. The frequency

difference between the emission frequency and SampleModeCenterFrequency of the global parameter should be assigned in the parameter FrequencyOffset. If the FrequencyScallingFactor is left as zero, the frequency output is plotted in Hertz. By changing the scale, it is possible to plot in different unit (1e-9 for Gigahertz). It is also possible to show the deviation in power. The same parameters scale and offset can be adjusted by changing the parameters for power.

CHAPTER 5

TRAVELLING-WAVE MODELLING OF THE MODULATION DYNAMIC PERFORMANCE OF WAVELENGTH-TUNABLE LASER DIODES USING THE INTEGRATED VPI AND PICS3D MODEL

5.1 Introduction

Directly intensity (or amplitude) modulated (DIM or DAM) wavelength-tunable laser diodes (TLDs) with a wide tuning range have many practical applications in modern optical communications and beyond [79, 153, 167]. Large TLD tuning ranges have been reported in literature by experimental works (13.88 nm) [168] and simulation models (32 nm) [105]. On the other hand, the continuing demand for higher transmission bit rates has also led to ways of enhancing the modulation bandwidth of directly modulated TLDs, which in a small signal approximation (SSA) analysis is directly related to the relaxation oscillation frequency (ROF) of the laser.

Many papers in the published literature deal with ways to enhance as much as possible the ROF of various single-mode modulated semiconductor lasers such as distributed feedback (DFB) and distributed Bragg reflector (DBR) lasers with the reported values of the 3-dB bandwidth being at and above 14 GHz [169-175]. The most common method which is used to enhance the ROF of these lasers is by increasing the injection current in the active region (AR). This method is also followed in the case of two-section and four-section TLDs [168], [176], [177] with reported 3-dB bandwidth values of 16 GHz, 5 GHz, and 6 GHz, respectively. However, the TLDs described there operated at a single fixed wavelength continuous wave (CW) lasing and no wavelength tuning had been considered. The dynamics of TLD performance under the DIM regime during wavelength tuning and the effect of tuning on the ROF and the modulation bandwidth have not been investigated in published literature so far, in spite of the physical interest of the problem and its practical importance.

In this chapter, the main focus of the investigation concerns the dynamic response of DIM TLDs during discontinuous wavelength tuning in a SSA analysis. We show that the ROF can significantly be increased not by simply increasing the pump current in the AR as is usually

suggested in literature for single wavelength lasers, but by taking advantage of the increase of the wavelength dependent differential gain during discontinuous wavelength tuning of the TLD.

Most of the works on the SSA response of semiconductor lasers are based on the rate equation model (REM) because of its physical transparency and computational simplicity. These advantages of the REM are not obvious or easily justifiable in the case of multi-section semiconductor lasers, like TLDs, in which different sections operate at fundamentally different physical conditions providing different functionality elements to the overall laser operation. The essence of the REM is that all spatial dependences of the laser field (power) and carrier densities are replaced by the corresponding averaged over the cavity values. The only important variable on which these parameters depend is time. In the case of multi-section TLDs, it is difficult to introduce or physically justify the cavity average optical fields or carrier densities which can be assigned to the whole device. Investigation of dynamic responses in such devices requires the use of spatio-temporal dependences of the above parameters, and the most appropriate formalism in this case is the travelling wave equation (TWE) model.

In the simulation modelling of a three-section bulk InGaAsP/InP TLD we use the VPI software tool [27]. The TLD design and device parameters are identical to those used in our previous work [105]. An important advantage of the VPI simulator in the context of our work is that it incorporates spatio-temporal cavity effects using a traveling-wave approach based on the transmission line laser model (TLLM). This allows us to overcome the key difficulties of using the REM approach in the case of multi-section devices like TLDs. At the same time, VPI has very serious limitations such as that it uses a simplistic (parabolic) built-in gain spectra model. For widely-tunable lasers the shape of gain spectra plays an important role for both the wavelength selectivity and tuning performance, and the output power stability [105]. In addition, as will be demonstrated later, the differential gain of a TLD strongly depends on the lasing wavelength. Because of this, the use of a parabolic gain spectra shape is not suitable for widely-

tunable TLDs. In order to overcome this drawback, we have developed an integrated dynamic simulation model which incorporates the gain spectrum calculated by the physics-based software tool PICS3D [28]. The upgrade of the recent version of the VPI software enables to use the interface tool in order to upload the measured or calculated frequency- and carrier-dependent gain curves into the VPI's laser model. The uploaded gain spectra curves are then fitted with multi-Lorentzian infinite-impulse response (IIR) filters for different values of the carrier density. In our case the optical gain spectra were calculated self-consistently by PICS3D from the local carrier densities at each bias point and then imported into VPI (VPI+PICS3D model). As a by-product of our consideration, we also show how for widely-tunable laser diode modelling in VPI one still can use the built-in simplified parabolic-shape gain spectrum model in order to obtain adequate results. This, however, requires careful fitting of the parabolic gain shape to the PICS3D-calculated spectrum within the required tuning range. It is demonstrated that both the integrated (VPI+PICS3D) model and the VPI's fitted parabolic model produce results which are in good agreement in terms of tuning and modulation performance of the TLD studied within the SSA approach, including the effect of a significant increase of the wavelength dependent differential gain under the blue wavelength shift with tuning.

In Section 2, the basic theory and physical model equations are briefly outlined. Section 3 describes the simulated device structure and all the relevant parameters used in the modelling. The obtained results from all investigations are described and explained in a comprehensive way in Section 4. All the conclusions that were made from the results of the investigation are presented in Section 5.

5.2 Theoretical background and physical and computational models

5.2.1 Travelling-wave equations for optical fields

VPI uses the travelling-wave equations for the propagation of the electro-magnetic field in the composite optical cavity within the TLLM approximation. The TLD cavity in a longitudinal z-direction is divided into small sections of length ΔL where the travelling wave fields are calculated at small time steps Δt for each section. The propagating electric field $\vec{E}(\vec{r},t)$ in each TLLM section is represented as a superposition of the forward and backward travelling waves with a complex envelope amplitude $A(z,t)$ and $B(z,t)$, respectively, [27]:

$$\vec{E}(\vec{r},t) = e^{i2\pi c f_0 t}\left[\vec{F}(\vec{r}_\perp, f_0)A(z,t) + \vec{F}^*(\vec{r}_\perp, f_0)B(z,t)\right] \quad + \quad c.c. \tag{5.1}$$

where f_0 is the frequency of the propagating wave and $\vec{F}(\vec{r}_\perp, f_0)$ is the profile of the electric field in the cross-section area normal to the propagation directions ($\vec{F}^*(\vec{r}_\perp, f_0)$ here represents the electric field travelling backward direction).

Amplitudes $A(z,t)$ and $B(z,t)$ are varying slowly in time, but are still rapidly oscillating along the propagation direction *z*, so it is useful to introduce in the calculations the amplitudes $a(z,t)$ and $b(z,t)$ which are slowly varying in both time *t* and *z* coordinates, and are defined as:

$$a(z,t) = e^{i(\beta_0 - \delta_{grating})z} A(z,t) \tag{5.2}$$

$$b(z,t) = e^{-i(\beta_0 - \delta_{grating})z} B(z,t) \tag{5.3}$$

where $\beta_0 = (2\pi f_0 / c) n_{eff}(f_0)$ is the complex propagation constant at the propagation frequency f_0, where *c* is the speed of light in vacuum and $n_{eff}(f_0)$ is the frequency-dependent complex

effective refractive index, and $\delta_{grating} = \beta_0 - \beta_{Bragg} = (2\pi\Delta f_{grating}/c) n_{eff}(f_0)$ is the deviation of the propagation constant β_0 from the Bragg propagation constant $\beta_{Bragg} = (2\pi f_{Bragg}/c) n_{eff}(f_0)$ in the presence of grating inside the optical cavity, where $\Delta f_{grating} = f_0 - f_{Bragg}$ is the deviation of the propagation frequency f_0 from the Bragg frequency f_{Bragg} of the grating (central stopband frequency of the Bragg reflectivity spectrum). In device sections where no grating exists $\delta_{grating} = 0$.

Forward a(z,t) and backward b(z,t) propagating amplitudes are presented by the travelling wave equations as [27]:

$$\left(\frac{1}{v_g}\frac{\partial}{\partial t} + \frac{\partial}{\partial z}\right)a = \left(\frac{1}{2}g(N) - \frac{1}{2}\alpha_{i,FC} - i\delta_a\right)a - i\kappa_{ab}b + Q_a \tag{5.4}$$

$$\left(\frac{1}{v_g}\frac{\partial}{\partial t} - \frac{\partial}{\partial z}\right)b = \left(\frac{1}{2}g(N) - \frac{1}{2}\alpha_{i,FC} - i\delta_b\right)b - i\kappa_{ba}a + Q_b \tag{5.5}$$

where $v_g = c/n_g$ is the group velocity, where n_g is the group refractive index, $g(N)$ is the optical gain in the AR which depends on the carrier density N (which varies in time according to the rate equations as will be described in Section 5.2.2), $\alpha_{i,FC}$ accounts for the optical losses in the cavity, $\delta_{a(b)} = (2\pi f_0/c)\Delta n_{eff,a(b)} + \delta_{grating}$ denotes the deviation of the propagation constant due to the phase shift caused by the change $\Delta n_{eff,a(b)}$ of the effective refractive index due to free-carrier effects, $\kappa_{ab(ba)}$ is the grating (if present) coupling coefficient, and $Q_{a(b)}$ describes the spontaneous emission into the forward (backward) propagating optical waves, respectively. The optical losses $\alpha_{i,FC}$ include the internal background losses α_i of the cavity, the free-carrier (FC) absorption in the conduction band, and the inter-valence band absorption within the valence bands. In VPI the latter two contributions are lumped together since both depend linearly on the carrier density N. This gives $\alpha_{i,FC} = \alpha_i + \alpha_{FC}N$, where α_{FC} is the total FC absorption

coefficient. Note, that in the case of TLDs the FC absorption is present in active and passive sections that are under current injection.

The average photon density $S(t)$ in the AR of the TLLM device for a small amount of length Δz in time t can be determined by the amplitudes $A(z,t)$ and $B(z,t)$ of the forward and backward propagating optical fields, respectively, and in VPI is defined as [27]:

$$S(t) = \frac{\Gamma}{E_{ph} v_g} \frac{1}{wd\Delta z} = \int_{z-\Delta z/2}^{z+\Delta z/2} |A(z,t) + B(z,t)|^2 \, dz \tag{5.6}$$

where E_{ph} is the energy of a photon with frequency f_0, and Γ, w, and d are the optical confinement factor, width and thickness of the waveguide region, respectively.

5.2.2 Rate equations for carrier density dynamics

The processes of generation and recombination of electron-hole pairs in the AR of a TLLM device are governed in VPI by the rate equation responsible for the variation in time t of the carrier density N. The current injection is described by the injection efficiency parameter. No spatial drift-diffusion effects are included in VPI, which is a drawback of the model. In the case of bulk active or passive regions the carrier dynamics are defined by the simple rate equation:

$$\frac{dN}{dt} = \frac{\eta I}{eV} - R(N) - v_g g(N) S(t) \tag{5.7}$$

where I is the injection current into the corresponding section, η is the current injection efficiency, e is the electron charge, V is the volume of the corresponding region, and $R(N) = AN + BN^2 + CN^3$ is the carrier density dependent recombination rate, where A is the non-radiative Shockley-Read-Hall (SRH) recombination coefficient, B is the radiative

bimolecular recombination coefficient, and *C* is the non-radiative Auger recombination coefficient.

Although, as was mentioned, VPI does not simulate spatial carrier distributions, we did manage to take into account these effects implicitly by calibrating the CW operation of the same TLD in the VPI and PICS3D models. In PICS3D a 3D embodiment of the TLD is simulated which takes into account 3D spatial distributions of both the optical fields and carrier densities. We have calibrated the VPI model of the TLD against the PICS3D output data in such a way that all key performance parameters, like the output power and wavelength tuning, were either the same or very close in both models for given injection currents in all sections. Unfortunately, the superior physical models of PICS3D only allow to simulate the steady state CW laser operation, and do not extend to studying laser dynamics, which is of main interest here and which can be modelled with VPI.

5.2.3 Stimulated emission (gain) models

In this work we use two VPI models to describe stimulated emission or gain: (i) a parabolic gain model, and (ii) an imported gain data file (obtained either from experiment or direct calculations). In the parabolic gain model, the gain depends on both the wavelength λ and the carrier density *N*:

$$g(\lambda, N) = g_p(N) - b_p\left(\lambda - \lambda_p(N)\right)^2 \tag{5.8}$$

where $g_p(N) = a_p(N - N_{tr})$ is the gain peak which has a linear dependence on the carrier density, where $a_p = dg_p(N)/dN$ is the differential gain with typical values of $a_p = (3 \div 5) \times 10^{-16}$ cm^2 for InGaAsP materials lasing at the 1300÷1550-nm wavelength at the gain peak [178] and

N_{tr} is the transparency carrier density, $b_p = g_p(N)/(\Delta\lambda(N)/2)^2$ defines the width of the parabola and has a typical value of $b_p = 0.15$ cm^{-1}/nm^2 for InGaAsP at 1550-nm [178], where $\Delta\lambda(N)$ is the gain bandwidth, and $\lambda_p(N) = \lambda_g - \Delta\lambda(N)/2$ is the carrier density dependent gain peak wavelength, where λ_g is the bandgap wavelength.

Because the TLLM is a time-domain model represented by Eq. 5.4 and Eq. 5.5, the frequency-dependent gain shape cannot be exactly modelled as would be possible in the frequency domain [27]. For this reason the TLLM approximates the actual gain shapes by a first order IIR filter or a multi-Lorentzian IIR filter. The IIR filter approximation procedure is the same for a parabolic gain spectrum and for uploaded from file gain data.

5.3 Device structure and parameters

The model which is used in all the investigations of this chapter is a three-section TLD with a bulk $In_{0.61}Ga_{0.39}As_{0.84}P_{0.16}$ AR operating at 1550-nm CW which is designed with VPI and is similar to the bulk TLD designed with PICS3D and reported in [105]. The structure and material parameters of the TLD designed in VPI are shown in Table 5.1. The small-signal analysis setup is shown in Fig. 5.1.

Symbol	Parameter Name	Value	Units
R_a	Left facet reflectivity	0.3 (z=0)	-
R_r	Right facet reflectivity	10^{-4} (z=800 μm)	-
w	TLD width	1.5	μm
L_a	Active section length	400	μm
L_p	Phase section length	100	μm

L_{DBR}	DBR section length	300	μm
d_a	AR thickness	0.18	μm
d_p	Waveguide (WG) thickness of the passive sections	0.38	μm
λ_{ga}	AR bandgap wavelength	1553	nm
λ_{gp}	WG bandgap of passive sections	1460	nm
α_{ia}	AR Internal losses	15	cm^{-1}
α_{ip}	WG internal losses of the passive sections	5	cm^{-1}
α_{FC}	Free-carrier absorption coefficient	2.2×10^{-18}	cm^2
Γ_a	AR confinement factor	0.3	-
Γ_p	WG confinement factor of the passive sections	0.8	-
κ	Coupling coefficient	50	cm^{-1}
n_{ga}	AR group refractive index	3.2	-
n_{gp}	WG group refractive index of the phase section	3.2	-
$n_{g\mathrm{DBR}}$	WG group refractive index of the DBR section	3.4	-
A	SRH recombination	1×10^{8}	s^{-1}
B	Bimolecular recombination	2×10^{-10}	$cm^3\ s^{-1}$
C	Auger recombination	3.5×10^{-29}	$cm^6\ s^{-1}$

Table 5.1 Structure and material parameters [105].

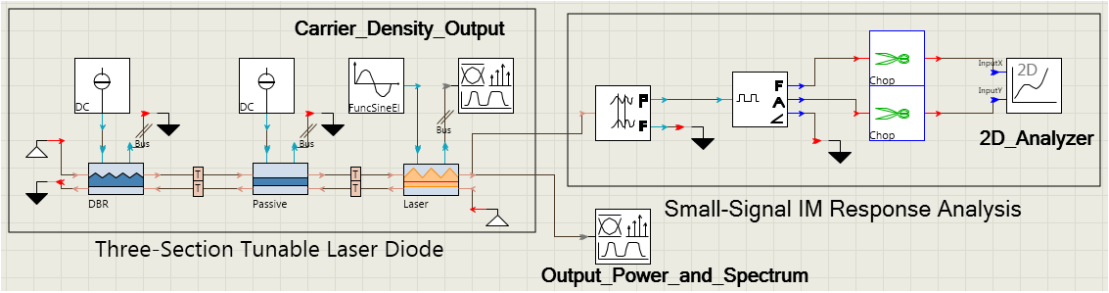

Fig. 5.1 VPI setup for a small-signal modulation analysis of the three-section bulk TLD.

The TLD setup consists of three sections with an active section (labelled 'Laser'), a phase section which acts as a passive waveguide (WG) (labelled 'Passive'), and a DBR section which includes the Bragg grating (labelled 'DBR'). The active section is injected with an AC current on top of a DC current bias, while the phase and DBR sections are injected with the DC tuning currents.

The small-signal DIM response function of the TLD is obtained by injecting a small (~1 mA, 12.5% of the threshold current I_{th} = 8 mA) modulation AC current $I_{AC} = 0.125I_{th}$ on top of the AR DC current I_a = 18.9 mA and by sweeping an adequate frequency range [0, 10 GHz] with a tiny frequency step (0.1 GHz). The frequency sweep and the calculation of the transfer function (in W/A vs GHz) of the DIM response of the TLD at each frequency is processed by the '2D_Analyzer' shown on the right side of Fig. 5.1.

5.4 Simulations and results

5.4.1 Gain spectra and wavelength-dependent differential gain

As was discussed earlier, the simplistic built-in parabolic shape gain spectra that are simulated in VPI are not suitable for widely-tunable TLDs due to the importance of using the correct dependence of the differential gain on the lasing wavelength λ. Fig. 5.2(a) shows a great difference between the VPI's built-in parabolic gain (red dashed line) and PICS3D's calculated gain (black solid line) spectra for the injected AR carrier density $N = 1.2\times10^{18}$ cm^{-3} (which is the threshold carrier density in our TLD lasing at the initial λ_0 = 1550-nm wavelength). The parabolic curve was obtained using typical values of the fitting parameters in Eq.5.8 $a_p = 5\times10^{-16}$ cm^2, $b_p = 0.15$ cm^{-1}/nm^2, reported for InGaAsP in [178], and $N_{tr} \approx 0.82\times10^{18}$ cm^{-3}.

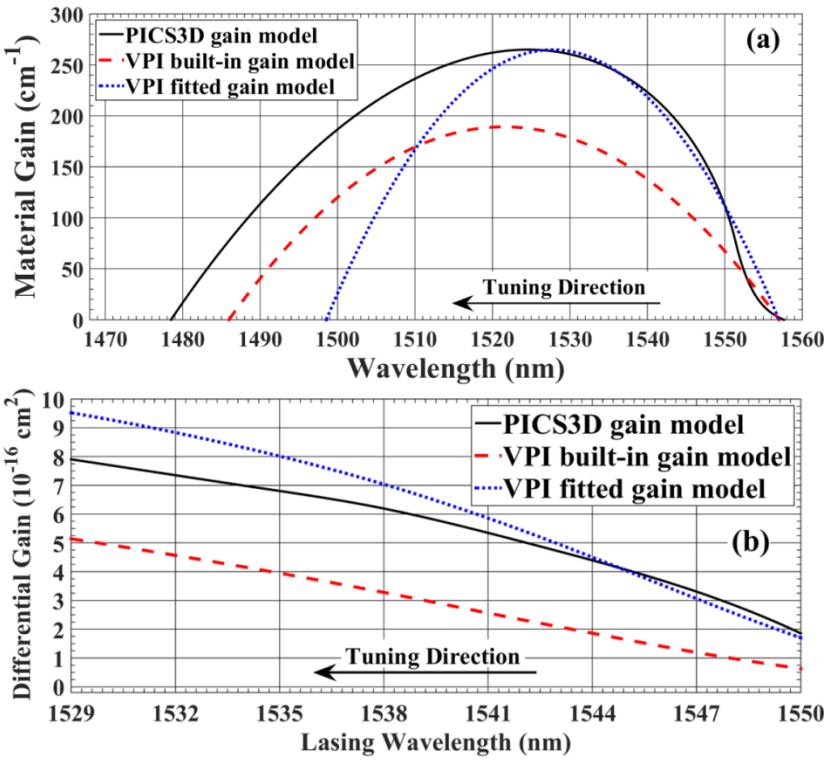

Fig. 5.2 Various gain spectra models (a) and their differential gains (b) used in the simulation: the PICS3D's model (black solid line), the parabolic fitted model (blue dotted line), and the built-in VPI's model (red dashed line).

One of the consequences of the difference between the actual gain shape spectrum and its parabolic approximation is the very big difference (about 100%) between the corresponding differential gains, which are shown in Fig. 5.2(b) Dependence of differential gain on the lasing wavelength was first reported in [179] for DFB bulk lasers using parabolic gain shape approximation. Our result in Fig. 5.2(b) for the case of a parabolic gain approximation (red dashed line) qualitatively agrees with [179]. (Recently, the dependence of differential gain on the wavelength detuning was utilized in multi-quantum-well distributed reflector laser arrays [180] to experimentally demonstrate its high-speed direct modulation). Here we show that the gain spectra shape plays very important role in calculating the correct value of differential gain. Note, that the differential gain coefficients in Fig. 5.2(b) are calculated self-consistently at each lasing wavelength of the TLD taking into account the variation of the threshold carrier density with tuning [105], i.e. taking into account that each lasing wavelength corresponds to a different gain spectrum curve.

As a byproduct of our comparative analysis of the gain spectra effect on the TLD response, we have also investigated the possibility of using the VPI's simplified parabolic shape model which, however, is carefully fitted to the experimental or simulated realistic gain curve. In the case of TLDs, this approach is possible only if the wavelength tuning range is small compared to the gain bandwidth (at least less than half of the gain bandwidth). The blue dotted line in Fig. 5.2(a) corresponds to the parabolic gain shape fitted to the PICS3D real gain (black solid line) for the investigated TLD with a 21-nm tuning range (from λ = 1550 nm to λ = 1529 nm) which is obtained during discontinuous wavelength tuning.

The parameters that were used to fit the parabolic gain spectrum were $a_p = 7\times10^{-16}$ cm^2, $b_p = 0.31$ cm^{-1}/nm^2, and the PICS3D measured transparency carrier density $N_{tr} \approx 0.82\times10^{18}$ cm^{-3}. (Note that the values of the fitting parameters a_p and b_p which are used in the fitted parabolic gain model differ considerably from the typical values reported in literature). As is seen, the

fitted parabolic gain model agrees well with the calculated gain spectrum within the considered wavelength interval between λ = 1550 nm and λ = 1525 nm. It is, however, impossible to get satisfactory fitting of the real gain with a parabolic shape over the whole gain bandwidth. The calculated differential gain obtained from the fitted parabolic gain spectrum is shown in Fig. 2(b) (blue dotted line). Although, it differs from the real differential gain (black solid line), the maximum deviation is less than 20%, which is considerably better than the result obtained from the VPI's built-in parabolic model (red dashed line).

Since the gain spectrum shape and the differential gain play a crucial role in TLD wavelength tuning and its modulation dynamics, the results of Fig. 5.2(a) and Fig. 5.2(b) clearly demonstrate the importance of using correct gain spectra in order to obtain a correct laser response function. To address this, we have developed an integrated dynamic simulation model (VPI+PICS3D) which directly incorporates realistic gain spectra obtained in PICS3D and imported into VPI. The importance of the developed integrated model goes beyond the SSA analysis carried out in this chapter. One of the advantages of the VPI software is that it allows to simulate both the small- and large-signal DIM response of advanced lasers and photonic integrated circuits, including optical fibre transmission links fed by a pseudo-random bit sequence (PRBS). The suggested integrated model can directly be utilized in these cases as well.

5.4.2 Wavelength tuning of the TLD

Wavelength tuning in most TLDs is achieved by free-carrier (FC) injection into the passive tuning sections which changes the electronic contribution to the material dielectric function (refractive index). Two most important physical mechanisms have been identified as the main contributors to the refractive index change – the FC plasma effect and the band filling effect [100, 101]. It was shown in [105] that, contrary to usual assumption, the band filling effect dominates over the plasma effect at all injected levels. However, the ratio between these two

contributions varies with the injection current (it increases with the current increase). For this reason it is necessary to consider both mechanisms and take into account their variation with tuning. Both mechanisms are included in PICS3D laser models.

The band filling effect is implemented via the standard Kramers-Kronig (KK) relations. Note, that due to strong dispersion of the KK relations this contribution to the refractive index change also affects the spectral dependence of tuning (contrary to the weakly-dispersive plasma effect contribution). Unfortunately, VPI uses a simplified refractive index model in which only the FC plasma effect contribution to the real part of the refractive index change $\Delta n'_{pl}$ is included via a simplified plasma coefficient β_{pl} as $\Delta n'_{pl} = \beta_{pl} N_{DBR}$ [27, 178]. We have investigated the differential refractive index dn'/dN (real part) obtained from PICS3D simulation of the TLD under DBR injection tuning. To quantitatively evaluate all contributions to the differential refractive index change, we have simulated in PICS3D the TLD tuning performance separately for each mechanism. The results are shown in Fig. 5.3.

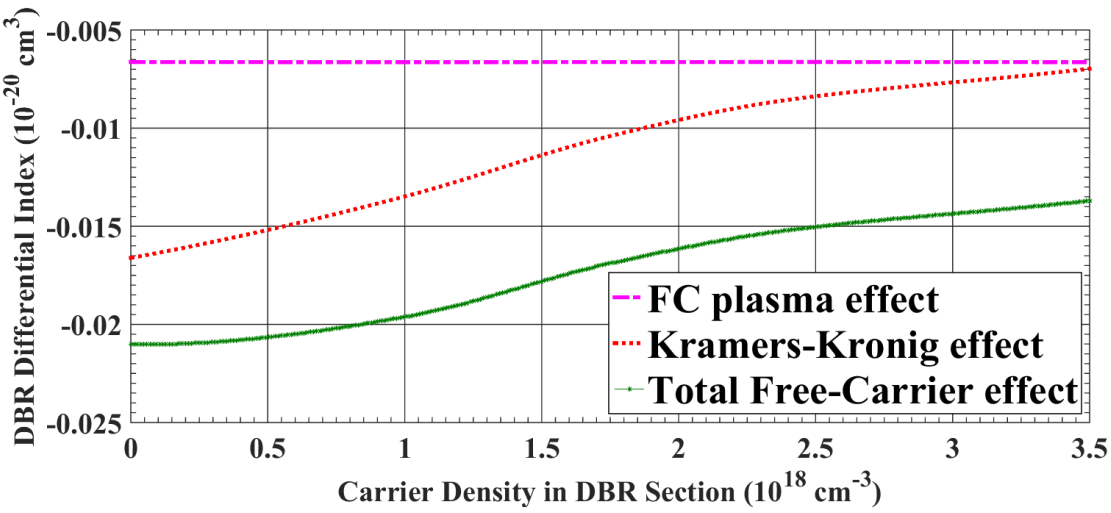

Fig. 5.3 Differential index of the TLD as a function of the injected DBR carrier density for different FC contributions.

We then tuned the DBR section by injecting current I_{DBR} which varied from a 0 A to a maximum I_{DBR} = 75 mA. The DBR carrier density N_{DBR} at the maximum current was around

3.33×10^{18} cm^{-3}. As is seen from Fig. 5.3, due to the dominating contribution from the KK effect, the total differential refractive index differs substantially from its value given by the plasma effect only. This shows that the VPI's built-in TLD model will demonstrate a seriously undervalued tuning performance. In order to match the actual values obtained by PICS3D in Fig. 5.3, we change the β_{pl} coefficient in VPI accordingly during tuning. The wavelength tuning performance of the TLD is shown in Fig. 5.4.

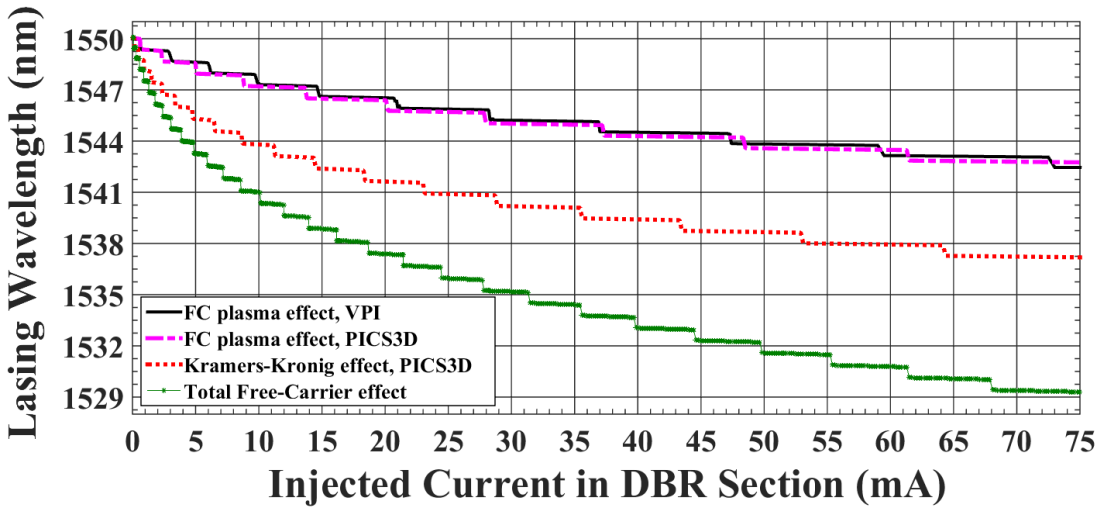

Fig. 5.4 DBR wavelength tuning performance of the TLD for different FC contributions and their combined effect.

When only the plasma effect is activated with β_{pl} = -0.0066x10^{-20} cm^3, both the VPI and the PICS3D models show very similar tuning performance (black solid line and pink dashed-dotted line, respectively). However, the actual tuning in the TLD, which includes the FC plasma effect and the KK effect (red dotted line), is considerably bigger (green line with asterisks). In order to incorporate the required tuning performance into the VPI model, we use for the β_{pl} coefficient the values of the total differential refractive index dn'/dN from Fig. 5.3. Note, that this value is not constant and is changed with the carrier injection. With this modification, the obtained tuning curves from PICS3D and VPI TLD modelling are practically the same (green line with asterisks).

The CW output power performance under DBR tuning is also very similar in both models, as is shown in Fig. 5.5. The more advanced PICS3D model of the TLD is also capable to demonstrate the power oscillations [105] during each tuning step (pink dashed-dotted line). Although, the VPI's models do not show these oscillations, the power variation with the DBR current injection is reasonably close to the PICS3D model.

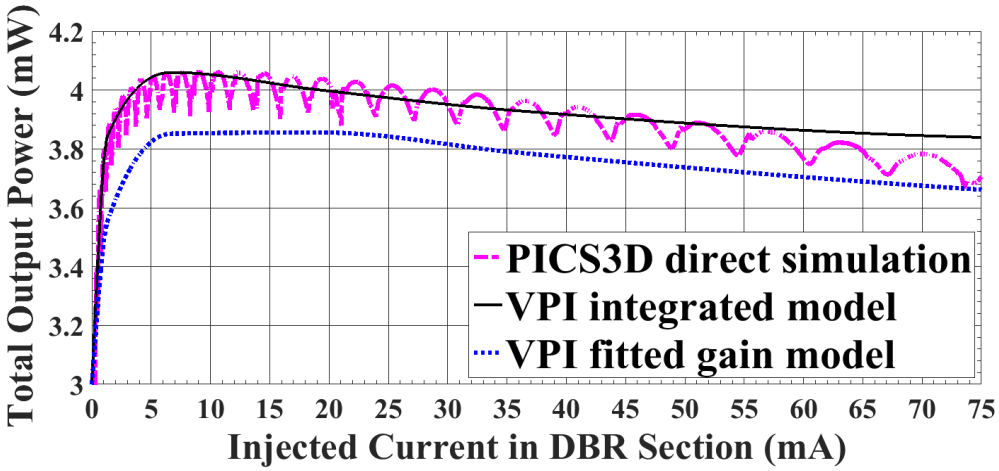

Fig. 5.5 Output power of the TLD as a function of the DBR current for two different models.

5.4.3 Modulation responses of the TLD under wavelength tuning using VPI+PICS3D integrated model

We start investigations using the VPI+PICS3D integrated model of the TLD which operates at the initial lasing wavelength λ_0 = 1550 nm in CW mode under I_a = 18.9 mA AR current injection ($I_{th} \approx 8$ mA). In order to study the effect of wavelength discontinuous tuning on the modulation response, we tune the DBR section by injecting the DBR current varied between 0 and 75 mA. In this simulation the phase section remained unbiased. At a maximum DBR current the total refractive index change is $\Delta n' \approx -0.056$, which results in a large blue wavelength tuning range of $\Delta\lambda$ = 21 nm, from λ_0 = 1550 nm to λ = 1529 nm. The inter-mode distance $\Delta\lambda_m$ here was $\Delta\lambda_m$ = 0.63 nm. The VPI's TLD DIM responses are shown in Fig. 5.6. In Fig. 5.6(a), the small signal analysis is carried out for fixed AR injection current. As is shown in Fig. 5.5 that the output

power of the TLD varies with tuning and in order to eliminate this effect on resonance frequency enhancement, the same investigation is repeated for constant output power and the results are given in Fig. 5.6(b).

The obtained ROF f_R from the DIM investigation at λ_0 = 1550 nm was $f_R \approx 2.24$ GHz. The CW output power was P_o = 3 mW. We compare the obtained ROF value with the theoretical value of f_{Rt} which can be calculated from the SSA analysis of lasers based on the REM as defined in [152]:

$$f_{Rt} = \frac{1}{2\pi}\sqrt{\frac{\Gamma_a\left(\langle\alpha_i\rangle + \alpha_m\right)}{hVn_{ga}\alpha_m} aP_o\lambda} \tag{5.9}$$

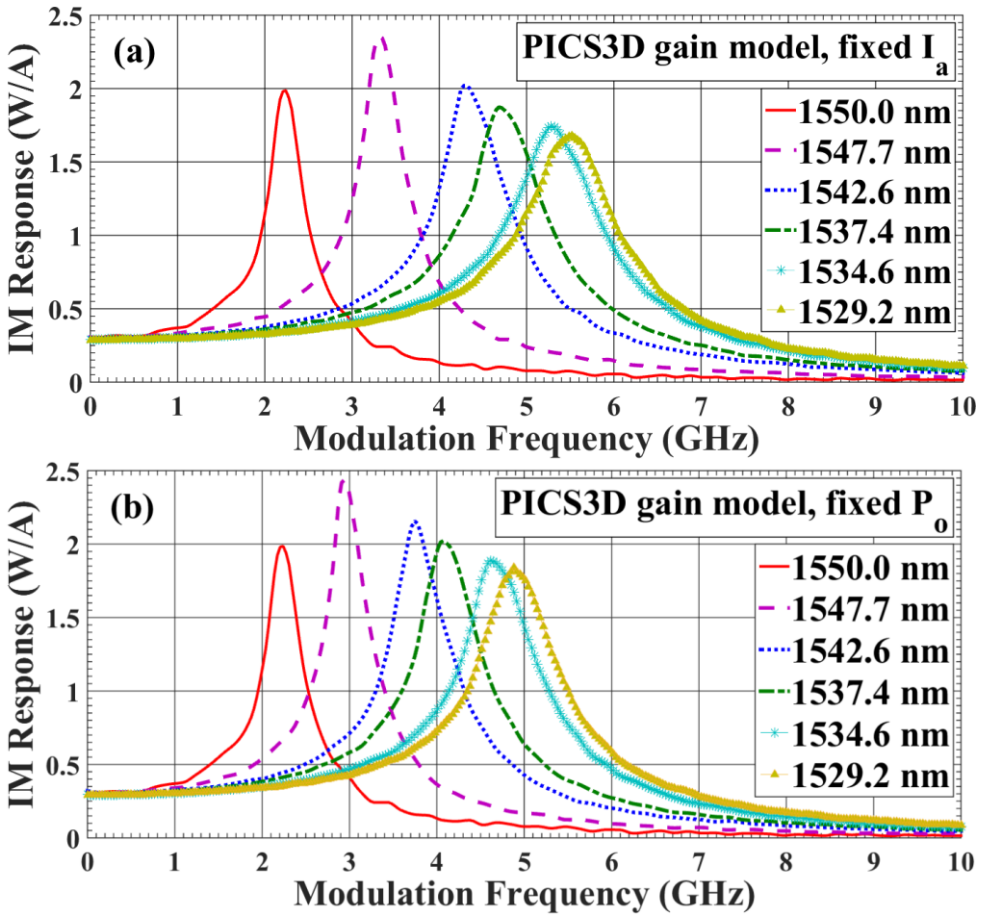

Fig. 5.6. Small-signal response of the TLD using the PICS3D gain model for different lasing wavelengths at a fixed AR current I_a (a) and at a fixed output power P_o (b).

Where $\Gamma_a = 0.3$ is the confinement factor of the AR, $\langle \alpha_i \rangle = \left(\alpha_{ia} L_a + \alpha_{ip}\left(L_p + L_{eff}\right)\right) / L_{eff,TLD}$ are the average internal losses, where $L_{eff} = \tanh(\kappa L_{DBR}) / 2\kappa = 90.5\,\mu\text{m}$ is the DBR penetration depth and $L_{eff,TLD} = L_a + L_p + L_{eff}$ is the effective length of the composite TLD cavity, $\alpha_m = \left(1/2L_{eff,TLD}\right)\ln\left(1/R_a R_g(\lambda)\right)$ are the mirror losses, where R_a = 0.3 is the left facet reflectivity of the TLD and $R_g(\lambda)$ is the Bragg reflectivity spectrum defined in [105] with $R_g(\lambda_B) \approx 0.8$ at the Bragg wavelength λ_B, h is the Planck constant, $V = L_a w d_a$ is the volume of the AR, $n_{ga} = 3.2$ is the group refractive index of the AR, $a = dg/dN$ is the differential gain, and P_o is the CW output power at the lasing wavelength λ. The definition of f_{Rt} refers to the dominant lasing mode of the laser, so in principle it can be applied to both multi-mode and single-mode lasers, such as the TLD in our case.

The term $\left(\Gamma_a\left(\langle \alpha_i \rangle + \alpha_m\right)\right) / hVn_{ga}\alpha_m$ in Eq. (5.9) is constant, so the only variables that affect the ROF during tuning are a, P_o and λ. The differential gain was measured numerically from the PICS3D imported gain spectrum as $a = dg/dN = 1.86 \times 10^{-16}$ cm^2, where the value of the gain difference dg was taken at λ_0 = 1550 nm for a very small carrier density step $dN = 0.01 \times 10^{18}$ cm^{-3} around the threshold carrier density $N_{th} \approx 1.2 \times 10^{18}$ cm^{-3}. Eq. (5.9) now gives $f_{Rt} \approx 2.33$ GHz which is in an excellent 96% agreement with the ROF obtained from the VPI simulation.

We then keep a fixed AR current I_a = 18.9 mA, and tune the TLD to five different lasing wavelengths: λ=1547.7 nm, λ=1542.6 nm, λ=1537.4 nm, λ=1534.6 nm and λ=1529.2 nm. The corresponding response functions are shown in Fig. 5.6(a). The obtained ROFs were $f_R \approx 3.31$ GHz, $f_R \approx 4.31$ GHz, $f_R \approx 4.72$ GHz, $f_R \approx 5.28$ GHz and $f_R \approx 5.52$ GHz for each wavelength, respectively. All of the obtained ROFs f_R were in very good ~90% agreement with theoretical estimations as is given in Eq. (5.9).

As is seen in Fig. 5.6(a), the ROF is increased by $\Delta f_R / f_R \approx 146\%$ (from $f_R \approx 2.24$ GHz to $f_R \approx 5.52$ GHz) during DBR tuning. As was mentioned earlier, the ROF is mainly affected by the differential gain a, the output power P_o and the lasing wavelength λ during tuning. In the simulated TLD the increase of ROF is due to the $\Delta a / a \approx 325\%$ increase of a (from $a = 1.86 \times 10^{-16}$ cm^2 to $a = 7.9 \times 10^{-16}$ cm^2, see Fig. 5.2(b), black solid line) and the variation of P_o (see Fig. 5.5, black solid line) during tuning. The decrease of λ during tuning is very small compared to the change in a and P_o. It can also be observed in Fig. 5.6(a) that the rate of increase of ROF is faster between λ=1550 nm and λ=1542.6 nm and slower between λ=1542.6 nm and λ=1529.2 nm during tuning. The reason for this effect is the variation of P_o during tuning since the differential gain always increases throughout the tuning range.

By examining Fig. 5.4 (green line with asterisks) and Fig. 5.5 (black solid line), it can be observed that the output power increases by $\Delta P_o / P_o \approx 37\%$ from P_o = 3 mW to $P_o \approx 4.1$ mW during tuning between λ=1550 nm and λ=1542.6 nm. This together with the increase of a results in a faster increase of the ROF in Fig. 5.6(a). The opposite situation takes place during tuning between λ=1542.6 nm and λ=1529.2 nm. The output power in Fig. 5.5 (black solid line) decreases by $\Delta P_o / P_o \approx 8\%$ from $P_o \approx 4.1$ mW to $P_o \approx 3.8$ mW and causes a slower rate of increase of the ROF in Fig. 6(a) for this tuning range. In order to eliminate the effect of the power variation during tuning we carried out the same analysis for a fixed output power P_o = 3 mW. The DIM responses are plotted in Fig. 5.6(b). Again, all of the obtained ROFs f_R were in very good agreement with the theoretical ROFs f_{Rt}.

It is seen in Fig. 5.6(b) that the increase of the differential gain is the main factor for the increase of the ROF during tuning. The obtained ROFs are slightly smaller than those in Fig. 5.6(a) for the same lasing wavelengths due to the fact that the output power P_o = 3 mW is now smaller than in the previous case.

5.4.4 Modulation responses of the TLD under wavelength tuning using the fitted parabolic gain model

We have carried out exactly the same as above small-signal analysis of the TLD using the VPI's fitted parabolic gain model. The obtained DIM responses of the TLD at different lasing wavelengths during discontinuous tuning for the cases of a fixed AR current I_a = 18 mA ($I_{th} \approx 7$ mA) and a fixed output power P_o = 3 mW are plotted in Fig. 5.7(a) and Fig. 5.7(b), respectively. As in the case of the TLD using the PICS3D integrated gain model, all of the obtained ROFs f_R were in very good agreement with the theoretical ROFs f_{Rt}. The total output power P_o performance of the TLD during tuning is shown in Fig. 5.5 (blue dotted line). The main advantage of the fitted parabolic gain model is that the values of the differential gain $a(\lambda, N)$ of the fitted parabolic gain spectrum $g(\lambda, N)$ at each lasing wavelength λ and corresponding carrier density N can be calculated analytically from Eq. (5.8) which gives $a(\lambda, N) = dg(\lambda, N)/dN = (\lambda_g - \lambda)\sqrt{a_p b_p/(N - N_{tr})}$.

As can be observed, the obtained response functions from the VPI fitted gain model slightly differ from the results in Fig. 5.6(a) and Fig. 5.6(b) for the integrated gain model for the same lasing wavelengths. The main reason for this difference is that the fitted parabolic shape follows closely the real gain spectra only for a chosen carrier density in the AR. Here we suggested to carry out the fitting procedure at the threshold carrier density of the TLD lasing at the initial wavelength λ_0=1550 nm. Once the best fitting parameters a_p and b_p have been calculated, they are kept unchanged during the TLD tuning process.

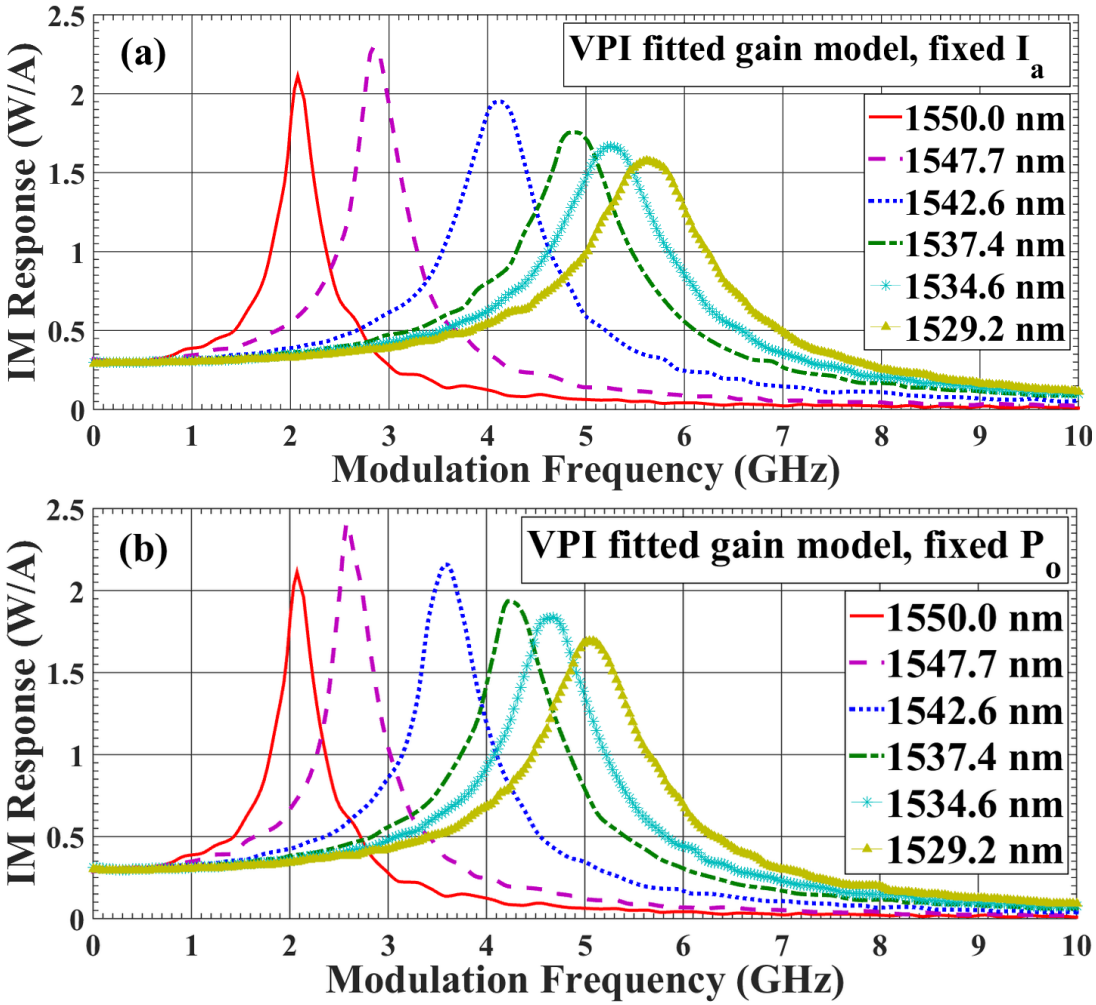

Fig. 5.7 Small-signal response of the TLD using the VPI fitted gain model for different lasing wavelengths at a fixed AR current I_a (a) and at a fixed output power P_o (b).

However, when the DBR section is tuned, the threshold current and the threshold carrier density change. (This is because of the change of the gain at different lasing wavelengths. The value of the net threshold gain (defined by the internal and mirror losses) remains practically constant). As a result of the variations in the threshold carrier density the actual gain spectra will also change with tuning [105] [181]. Rigorously, this would require to carry out a new fitting procedure, since the fitting only worked well at or close to the initial lasing wavelength λ_0 = 1550 nm, but this would go beyond the assumed approximations here.

As a result, the differential gain and the output power of the TLD simulated with the fitted parabolic gain model will deviate from the real values (see Fig. 5.2(b) and Fig. 5.5). This in turn will affect the obtained ROFs for the same lasing wavelengths. The dependences of ROFs on the tuned lasing wavelength are plotted in Fig. 5.8 for the cases of a fixed AR current I_a and a fixed output optical power P_o using different simulation models. As can be observed from Fig. 5.2(b) and Fig. 5.8, the increase of the differential gain dominates the performance of the TLD under direct intensity modulation for both models and is the main reason for the increase of the ROF during discontinuous wavelength tuning.

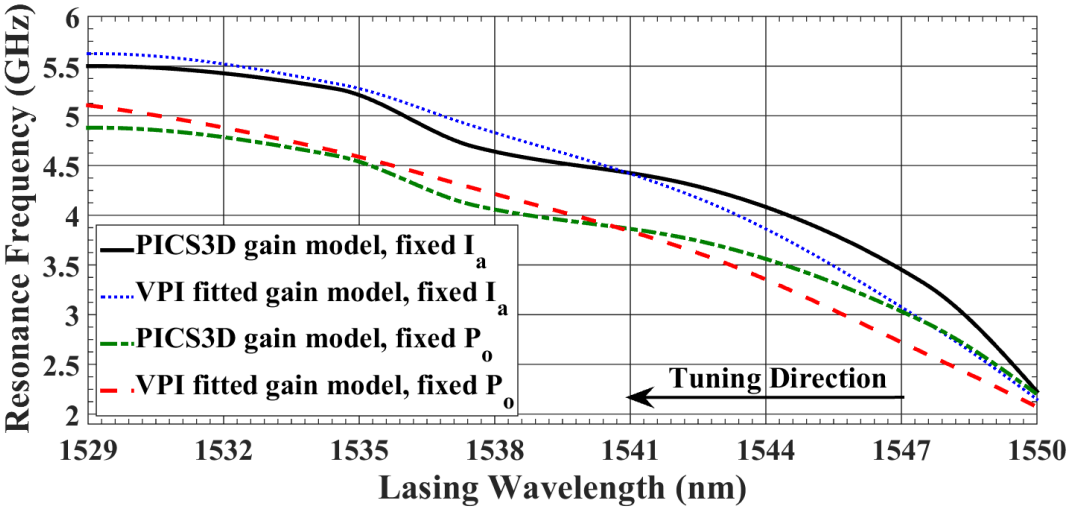

Fig. 5.8 Resonance frequency vs lasing wavelength for a fixed AR current I_a and fixed output power P_o using different models.

5.5 Conclusions

The modulation dynamic performance of a three-section bulk InGaAsP/InP TLD operating at 1550-nm CW under direct intensity modulation during discontinuous wavelength tuning has been investigated. The modelling of the TLD's dynamics was carried out using the travelling-wave approach with the use of commercial software simulation tools VPI and PICS3D. We demonstrate a strong effect of the gain spectra shape on the modulation response of the TLDs. The VPI's built-in parabolic shape model can successfully be utilised for simulation of lasers operating at a fixed wavelength, but it gives a large (more than 100%) error for simulation of the TLD's modulation response under wide wavelength tuning. Two models of a small-signal modulation response have been developed for simulation in VPI which correctly incorporates real gain spectra of TLDs obtained either from experimental measurements or ab-initio calculations: (i) the VPI+PICS3D integrated model, and (ii) the fitted parabolic shape gain model. The first model uses physics-based realistic gain spectra calculated by PICS3D and imported into VPI. The second model relies on a careful fitting procedure of the VPI's built-in gain model to the real gain spectrum within the required wavelength tuning range and it allows analytical calculation of the TLD's ROF. The results of both models are in good agreement.

We show that a significant increase (~3 times) of the ROF and the corresponding modulation bandwidth takes place under blue wavelength tuning of the TLD over a 21-nm range from the initial 1550-nm lasing wavelength. The main physical reason for this increase is a dispersion of the differential gain which increases about 4-5 times when the lasing wavelength decreases over the above tuning range. The reported enhancement of the modulation response of TLDs is important for their practical applications

CHAPTER 6

INVESTIGATION OF MODULATION RESPONSE OF OPTICAL-INJECTION-LOCKED WAVELENGTH-TUNABLE SEMICONDUCTOR LASER DIODES

6.1 Introduction

Wavelength tunable laser diodes (TLD) are essential system components to provide advanced solutions for current wavelength/frequency-division-multiplexed (WDM/FDM) fibre optic networks [182]. Direct modulation of semiconductor laser transmitters is also an important modulation technique in order to achieve a cost-effective transmission. Due to fundamental limitations of internal semiconductor laser dynamics, the maximum modulation bit rate of directly modulated lasers is considerably less than the externally modulated ones. As a result, there has been much research on the investigation of the ways of enhancement of the dynamic characteristics of semiconductor lasers. Optical injection locking (OIL) is a robust technique which can improve the dynamic response of directly modulated semiconductor lasers [16]. By locking the slave laser (SL) (free-running TLD) emission frequency to the master laser (ML) frequency, it is possible to enhance the modulation bandwidth and reduce frequency chirping. Locking can be provided by injecting light from the ML into the SL via an isolator in order to avoid optical reflection feedback on the ML.

In general, research on laser dynamics under external optical injection covers a vast field which includes a few different directions, such as studies of various instabilities in optically-injected lasers, laser stabilisation, chaos and its control, chaotic communications, laser response characteristics enhancement, etc. The overview of these research activities and a reasonably detailed corresponding bibliography can be found e.g. in [16]. Here, our main interest is the modulation response of TLDs under optical injection. There were several related theoretical and experimental studies on different types of OIL lasers, such as distributed feedback (DFB) lasers [183], TLDs [184], vertical-cavity surface-emitting lasers (VCSELs) [185], and Fabry-Perot lasers [186]. The first experimental study on the optically-injected AlGaAs laser was reported by Kobayashi and Kimura in 1980 [187]. The investigations on OIL lasers demonstrated the emission frequency stabilisation and considerable side mode suppression. The multimode Fabry-

Perot laser was turned to a single mode lasing by supressing the side modes with injection locking [154]. This eventually led to development and utilisation of the injection-locked Fabry-Perot lasers as efficient single-mode optical transmitters for WDM passive optical networks [188-190]. Lang [15] has developed the first theoretical formalism on OIL lasers by modifying the conventional rate equations describing semiconductor lasers. The important effect of injection locking on the frequency chirp reduction in directly modulated semiconductor lasers was demonstrated in [191], [138]. The resonance frequency enhancement of optical- injection locked lasers was reported in [17, 127, 130, 156, 157, 192].

There are two different approaches to investigating nonlinear dynamics of OIL lasers. The first approach, which takes the carrier density and the optical field as an average over the cavity, is based on the rate equation model [26, 193, 194]. Here the complex time-dependent laser electric field is considered at the SL's cavity interface with the external optical signal field which couples into the cavity with the corresponding coupling round-trip feed-in rate [16], [195]. (A kind of a modified version of the rate equation model is the Fabry-Perot model suggested in [25]. In this model the time is in essence a discrete quantity which is measured in units of a round-trip time of the cavity. Comparative analysis of the rate equation and the Fabry-Perot model under optical injection is given in [24]). The other approach is the travelling wave model which considers spatio-temporal effects inside of the SL cavity. The travelling wave model is considerably more advanced in comparison with the rate equation model. Furthermore, in a context of lasers with composite cavity structures, like multi-section TLDs, it is not straightforward to even introduce or physically justify the cavity average electric field or carrier density which are assigned to the whole device because different sections play very different roles in the laser operation. Thus, the travelling wave model for investigation of TLD dynamics under optical injection seems to be the adequate approach. Due to the presence of both spatial and time derivatives in field equations and, in addition, due to the non-linearity of the problem,

only numerical solutions are possible. The cavity is divided into small subsection elements which are connected to each other with nodes. The carrier density and the field of the travelling wave are calculated for each subsection rather than averaging them like in the rate equation model [184], [24, 25, 196]. This advanced analysis allows us to obtain accurate dynamic response characterisation of the OIL lasers.

In this study, we demonstrate a significant enhancement of the relaxation oscillation frequency and modulation bandwidth of a three-section TLD under optical injection by using the travelling wave model, and show how these parameters depend on the TLD tuning. Although, there are various studies on the demonstration of nonlinear dynamics of multi-section lasers under optical injection, there seems to be no systematic investigation of the modulation dynamic performance of OIL TLDs under wavelength tuning which is addressed here. In Section 2, we briefly discuss the theoretical framework of the model, Section 3 describes the simulation setup of OIL TLDs in VPI with a transmission line model. In Section 4, we present the obtained results on the small-signal intensity modulation (IM) response of the OIL TLD. The effect of the injection parameters such as the detuning frequency and power injection ratio on the IM response of the OIL TLD for different tuning regimes are investigated in detail. The final Section 5 summarizes the results with the conclusions.

6.2 Theory and Models

Most of the theoretical research on semiconductor injection locked laser diodes have been carried out with the modified rate equations [17], [156]. Due to the complexity of the multi-section TLD with composite cavities, we have to use here the travelling wave approach based on the transmission line laser model (TLLM) implemented in the VPI simulation software [27]. The advantage of VPI is that it allows to simulate in the time domain quite complex optical

components including TLDs, photonic integrated circuits, and optical fibre transmission links. This, however, comes on the expense of using simplified physics in describing some important characteristics of the simulated devices. For example, for simulation of lasers in the VPI built-in model of gain spectra only a parabolic shape dependence is available. This approximation is in principle acceptable for the modelling of fixed wavelength lasers. Contrary to this, in the case of TLDs it was demonstrated in [105] that details of gain spectra play a very important role for adequate description of both the output power and the wavelength tuning performance of the lasers. For this reason we will use here the integrated VPI+PICS3D model that has recently been developed in [197] which uses the advanced physics-based calculation of the gain spectra from PICS3D [28]. In the recently upgraded version of VPI [27], a new functionality has been added which allows to upload data files containing a set of gain spectra obtained either from experiment or from ab initio calculations for a range of carrier densities.

The TLLM model of the TLD takes into account inhomogeneous spatial effects along the laser cavity. The model was developed by A. J. Lowery in 1987 [29]. The TLLM-based simulation of TLDs has demonstrated good agreement of the obtained results with the experimental results [162]. In the TLLM, the laser composite cavity which may consist of *k* sections (e.g. an active section, grating sections, passive sections, etc.) is divided into a set of *m* small TLLM elements of Δz length each. The time delay due to the propagation of the wave in the cavity is calculated as $\Delta t = \Delta z / v_g$ (v_g is the group velocity). The complex propagating electric field in each TLLM section in the cavity is presented as:

$$\vec{E}(\vec{r},t) = e^{j2\pi f_c t}\left[\vec{F}(\vec{r}_\perp, f_c)A(z,t) + \vec{F}^*(\vec{r}_\perp, f_c)B(z,t)\right] \quad + \quad c.c. \tag{6.1}$$

This field equation includes the forward and backward propagating waves *A(z,t)* and *B(z,t)*, respectively, and $\vec{F}(\vec{r}_\perp, f_c)$ is the profile of the electric field in the cross-section area normal to the propagation directions. The travelling wave equations are derived as *:*

$$\left(\frac{1}{v_{g,k}}\frac{\partial}{\partial t}+\frac{\partial}{\partial z}\right)a=\left(\frac{1}{2}g(N_m,S_m)-\frac{1}{2}\alpha_a-i\delta_a\right)a-i\kappa_{ab}b+Q_a \tag{6.2}$$

$$\left(\frac{1}{v_{g,k}}\frac{\partial}{\partial t}-\frac{\partial}{\partial z}\right)b=\left(\frac{1}{2}g(N_m,S_m)-\frac{1}{2}\alpha_b-i\delta_b\right)b-i\kappa_{ba}a+Q_b \tag{6.3}$$

In general, each laser section may contain gain, loss, grating, filter, and noise parameters. In Eq. 6.2 and 6.3, the gain modelled TLLM element m is denoted by $g(N_m, S_m)$ as a function of the carrier density N_m and the photon density S_m, α_a and α_b represent the cavity losses, δ_a *and* δ_b show the deviation of the propagation constants of the forward and backward waves, respectively, due to the refractive index change, κ_{ab} and κ_{ba} are the grating (if present) coupling coefficients, and Q_a and Q_b describe the spontaneous emission into the forward and backward propagating waves, respectively.

The injected light is coupled into the cavity at the corresponding interface of the laser. In case of the rate equation approach the injected external optical field is considered as a source in the field rate equation with the corresponding feed-in rate [195]. For the travelling wave approach the injected external optical field is used as a boundary condition to the equations 6.1 – 6.2 at the injection interface taking into account its time dependence and frequency detuning Δf and phase shift between the SL and the ML fields.

Irrespective of a particular approach used for the description of the OIL dynamics, the key physical effects responsible for a non-linear interaction between the injected ML and the SL fields are the same. The injected field increases the stimulated emission rate in the active region of a composite cavity and reduces the carrier density, which in turn affects both the gain and the refractive index (In VPI the coupling between the gain and refractive index change is described by the $\alpha-$factor). The resulting state of the SL strongly depends on the frequency detuning $\Delta f = f_{ML} - f_{FR}$ between the ML and the FR SL, and the power injection ratio $R_{inj} = P_{ML} / P_{FR}$ of the two lasers.

The carrier dynamics in VPI in each TLLM element *m* of the laser section *k* is described by a simple rate equation which assumes that the injected current is homogeneously distributed in section *k*

$$\frac{dN_m}{dt} = \frac{\eta I_k}{eV_k} - R(N_m) - v_{g,k} g_k (N_m, S_m) S_m(t) \tag{6.4}$$

where I_k is the injection current into the corresponding section, η is the current injection efficiency, e is the electron charge, V_k is the volume of the corresponding section, and $R(N_m) = AN_m + BN_m^2 + CN_m^3$ is the carrier density dependent recombination rate, where A is the non-radiative Shockley-Read-Hall (SRH) recombination coefficient, B is the radiative bimolecular recombination coefficient, and C is the non-radiative Auger recombination coefficient. The gain is present only in the active section of the TLD. Although, Eq. 6.4 does not explicitly include the dependence of the carrier density on the longitudinal coordinate *z*, the densities N_m may still differ in different TLLM sections *m* due to coupling between N_m and the optical field (photon density) which does depend on *z*. Because of this, for example, such effects as spatial hole burning are included in the VPI model. Spatial hole burning is a physical phenomenon which mainly affects laser operation when laser is driven above threshold. By increasing the injection current, the stimulated emission in the active section increases and thus this causes the drop in carriers. As a result of this the real part of the refractive index increases and the imaginary part (gain) decreases. This causes the gain compression and it is implemented in VPI analytically.

In case of multi-section TLDs, the carrier density also differs in different sections of the device due to the different role played in each section in the TLD operation. These explicit longitudinal dependences of the carrier densities on coordinate *z* along the cavity is an important novel element in modelling the dynamics of OILs with the travelling wave approach in comparison with the rate equation approach.

With the TLLM method [27] each devise section k is divided into a set of small m elements with size $\Delta z = v_{g,k}\Delta t$. This is also the relationship between the time and space discretisation steps. Each TLLM section contains a scattering node representing gain, loss, and reflection from the grating (if present). The nodes generate scattered forward and backward propagating fields. The scattering matrix which is required for self-consistent calculation of these fields is obtained from discretization of Eq. 6.2 and 6.3 as well as the rate equations for the carrier densities in Eq. (6.4).

6.3 Setup of Optically-Injected TLD in VPI

The VPI's TLLM based setup for the IM response of the TLD under optical injection is shown in Fig. 6.1.

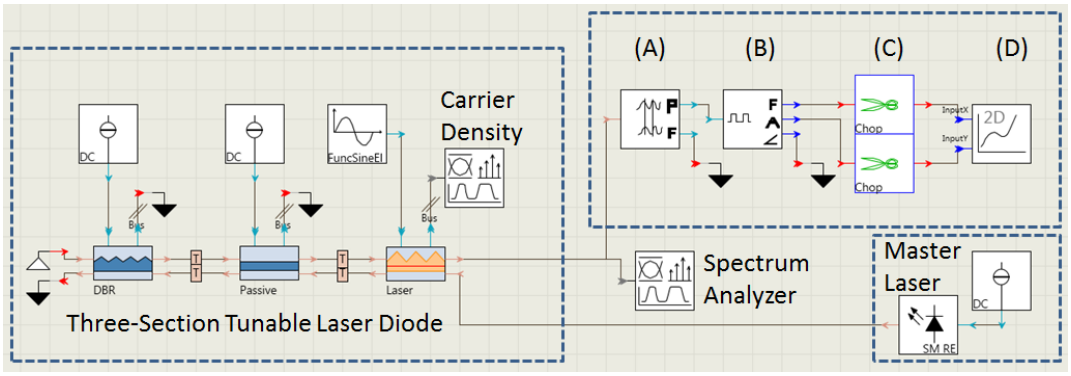

Fig. 6.1 VPI setup for small signal intensity modulation modelling of the optically-injected TLD

The simulation model includes a 3-section TLD SL, a single-mode ML, and the output signal processing unit which includes a "TimeResolved_Freq_Power" module (A), a "TwoPort_Analyser" (B), a "Chop" module (C), and a "Numerical Analyzer2D" module (D).

To calculate the IM response of the TLDs in a small-signal approximation (SSA) analysis, the modulation frequency of a sinusoidal electrical signal current in the active region is swept over a

specified frequency range, and the instantaneous output power of the TLD is detected and scaled with the modulation current. The VPI's "TimeResolved_Freq_Power" module detects the instantaneous frequency and power of the optical output of the laser and converts it to an electric signal. This electrical output is analysed by the "TwoPort_Analyser" component which estimates the frequency, the phase, and the amplitude of the signal. Before plotting the results, it may be necessary to remove the transient effects in the output signal, and the "Chop" modules are included to carry out this task. The final results are plotted by the "Numerical Analyzer2D" module.

The parameters of the TLD are the same as in [197]. The three-section TLD, consisting of the active section, passive phase section, and passive DBR section, is modelled with the TLLM version of the travelling wave approach. Although, the TLD is a monolithic device structure, its implementation in VPI is designed as a set of three separate sections. This is simply due to computational flexibility of VPI in order to model complex photonic integrated circuits with various combinations of active and passive sections. This approach may affect an adequate description of the electronic carrier transport problem (since, in principle, the carriers injected into different sections can propagate via drift-diffusion between the adjacent sections). However, prior to simulating the TLD with the VPI software, we have carried out an auxiliary CW simulation of the same device with the three-dimensional physics-based simulator PICS3D and have calibrated the VPI model as necessary in order to obtain similar performance of the TLD in both cases.

The optical problem for the propagating fields in VPI is solved rigorously, although within a one-dimensional approximation (along the cavity's *z*-direction). In this model the laser cavity is divided into small TLLM elements and the optical wave travels back and forth in the composite cavity. The gain spectrum of the laser in VPI can be designed either by defining gain parameters and creating respective gain spectra with the built-in flat or parabolic shapes, or by importing a

gain spectra data. Here we use an integrated model that we have developed in [197] which has a realistic gain spectrum calculated in PICS3D and imported into VPI. The DBR tuning is achieved by injecting free carrier density *N* into the DBR section which modifies its refractive index $\Delta n = -\beta N$ [178]. As was shown in [105], various physical mechanisms contribute to the free carrier refractive index change. Since VPI takes only plasma effect into account to calculate Δn, we have calibrated the VPI refractive index model with the refractive index change data obtained from PICS3D. In the TLD simulation we use the calculated total differential index dn/dN instead of β, which in addition varies with the DBR current injection (wavelength tuning).

The linewidth enhancement factor model (alpha coefficient) is not available for the calculation of the interrelation between the gain and refractive index change in the active section if the real gain spectra are imported from a data file. The VPI requires users to directly specify the differential refractive index dn/dN parameter instead of the α-factor. Due to the great importance of the α-factor for OIL simulation [16], [198], we kept here the α-factor constant at around $\alpha \approx 4.4$, and have calculated the corresponding value of the differential index dn/dN using the obtained from PICS3D differential gain dg/dN at each lasing wavelength. This was repeated for every tuning regime. The dispersive change of the differential gain dn/dN with wavelength tuning was explained in [197].

The ML which injects light into the TLD is supposed to be connected via an isolator to prevent any feedback, however in our setup the input and the output ports are computationally separated, so there is no need to use an isolator [27].

There are two main modes in VPI for the description and computation of the optical wave propagation in the modelled devices – the Block Mode (to pass signals unidirectionally) and the Sample Mode (to pass signals bidirectionally). Due to the physical nature of laser cavities, at each point there are in general two (forward and backward) propagating and interacting waves.

The wave interaction at the scattering nodes in each TLLM element requires to calculate and pass information about the amplitude and phase of each wave from one node to another. In addition, the external optical injection of the field into the laser cavity also requires careful consideration of asymmetric coupling between the SL and the ML fields at the cavity's boundary. Thus, it is vital to use the Sample Mode in the TLD modelling. For the sake of simplicity, the ML here is described by a simplified single-mode rate equation model. We specify its emission frequency f_{ML} and the injection current which defines the output power P_{ML}. VPI uses the Sample Mode and simulates self-consistently in the time domain the integrated two-laser setup shown in Fig. 1, and produces the output signal of the SL as well as the longitudinal cavity distributions of its various parameters.

6.4 Modulation Dynamics of OIL TLD

Nonlinear dynamics of optically-injected lasers is very rich [16]. Before investigating the modulation response of the TLD, we first produce the stable locking boundary map for our device which separates the stable locking region from chaotic or quasi-chaotic regions. There have already been several studies devoted to the investigation of various regimes of nonlinear dynamics of optically-injected TLDs [184], [24]. Here we are not interested in producing a detailed stability map, for our purpose we just need to reliably identify the region of stable locking. In Fig. 2 we demonstrate the stable locking boundary (red solid line) plotted as the frequency detuning $\Delta f = f_{ML} - f_{FR}$ against the injection power ratio $R_{inj} = P_{ML} / P_{FR}$ for the front mirror OIL TLD when it emits at the tuned wavelength λ = 1542.6 nm. The initial lasing wavelength for a non-tuned TLD is λ_0 = 1550 nm. Note that the stability map varies with wavelength tuning.

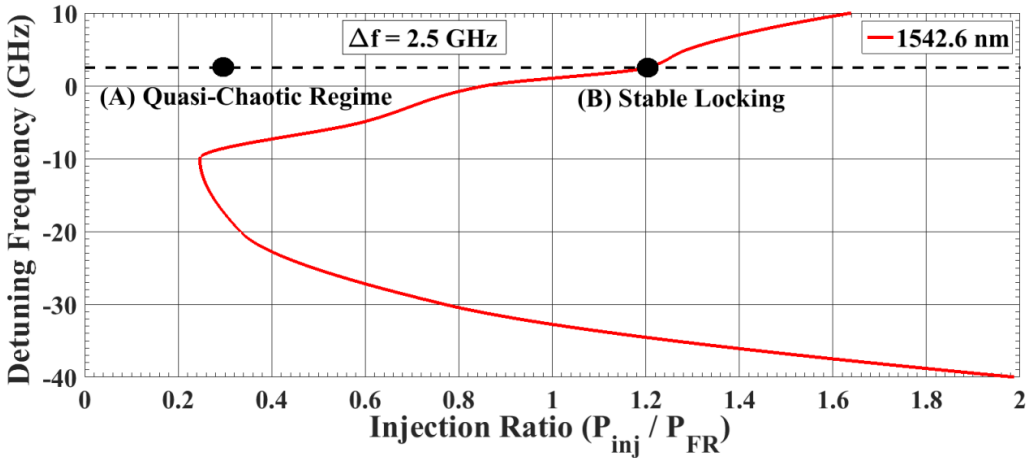

Fig. 6.2 Stable locking boundary map of the optically-injected TLD tuned to the FR lasing wavelength λ_{FR} = 1542.6 nm.

To demonstrate dramatic changes in the laser dynamics by optical injection, we compare two points which show quasi-chaotic (A) and stable locking (B) regimes when Δf = 2.5 GHz. The FR TLD power output was P_{FR} = 3.93 mW. In case (A), the injected light power is P_{inj} = 1.31 mW which gives the injection ratio R_{inj} = 0.33. In case (B), the stable locking takes place for R_{inj} = 1.2 (P_{inj} = 4.74 mW).

Fig. 6.3(a) shows the corresponding lasing spectra of the TLD under optical injection for both cases (A) (red solid line) and (B) (blue solid line). It is clearly seen that the frequency spectrum for case (A) shows a quasi-chaotic behaviour as was explained in [4]. In addition to the emission modes of the FR SL and ML, there is a set of side modes which are clearly separated and there is no dominant mode because of the poor side mode suppression ratio (SMSR) (below 20 dB). On the other hand, the spectrum in case (B) shows stable lasing of the OIL TLD at the ML frequency with large SMSR (above 40 dB).

Fig. 6.3(b) shows a striking difference between the large-signal transient responses (turn-on relaxation oscillations [152]) of the optically-injected TLDs in quasi-chaotic regime (red solid line), in stable-locked regime (blue solid line), and the FR TLD (black solid line) to a step-like

current injection into the active section of the SL lasing at the tuned wavelength λ = 1542.6 nm. A few important features can be observed in Fig. 6.3(b).

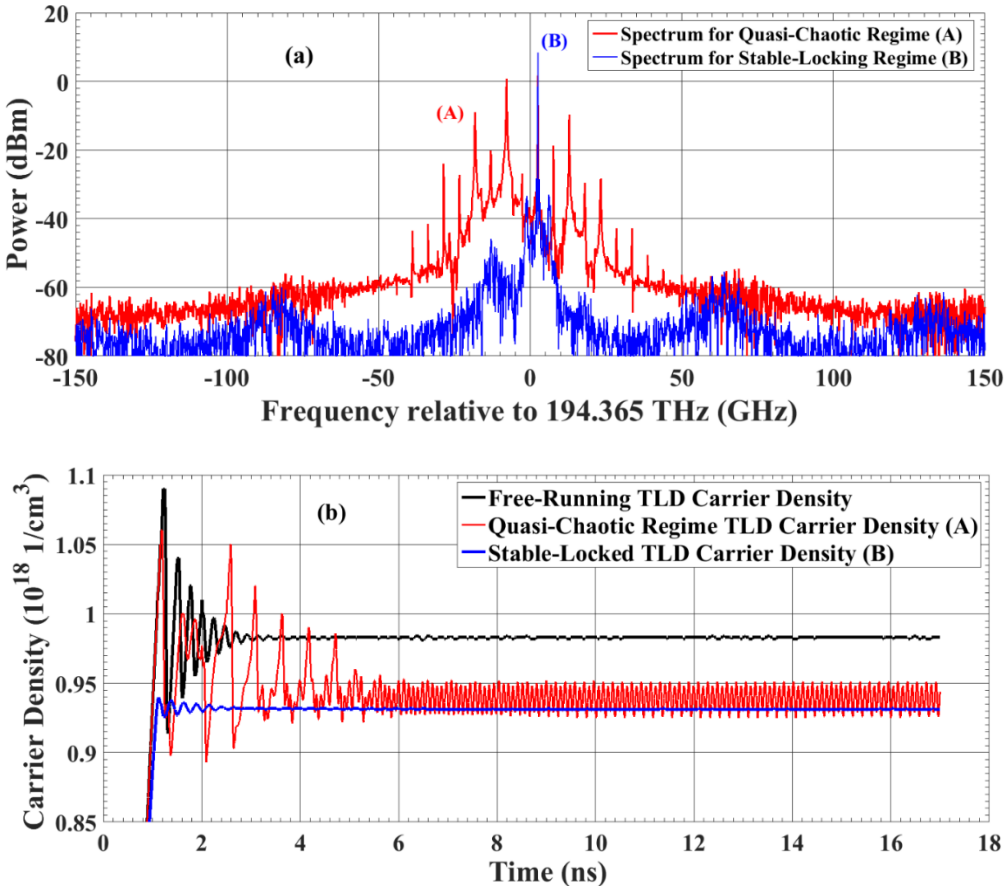

Fig. 6.3 Frequency spectra of the optically-injected TLD for different lasing regimes (a), and carrier density response to large-signal current injection of OIL TLD for the same regimes and the FR TLD (b)

Firstly, there is a very fast response time (below 1 ns) to the large-signal input in case (B) of the OIL TLD in comparison with the FR TLD (about 3-4 ns). Secondly, there is a very small relaxation oscillation amplitude of the carrier density response. Thirdly, there is a sharp drop in the clamped carrier density value [17]. Although, in this Chapter we do not consider large-signal TLD modulation (e.g. under digital pseudo-random sequence input), the above features clearly indicate the modulation enhancement potential of OIL TLDs in terms of the response time to the modulating signal. A sharp drop in the carrier density oscillations will also improve the spectral purity of the output emission from the OIL TLD in comparison with the FR TLD due to the

reduction in the frequency chirping. This can even be observed from a comparison of the CW spectra of the OIL TLD and the FR TLD, as is shown in Fig. 6.4. In both cases the TLD was tuned to emit at λ = 1542.6 nm (*f* = 194.365 THz). As is seen, the lasing spectrum of the OIL TLD (red solid line) is considerably narrower and it has a better SMSR in comparison with the FR TLD (black solid line).

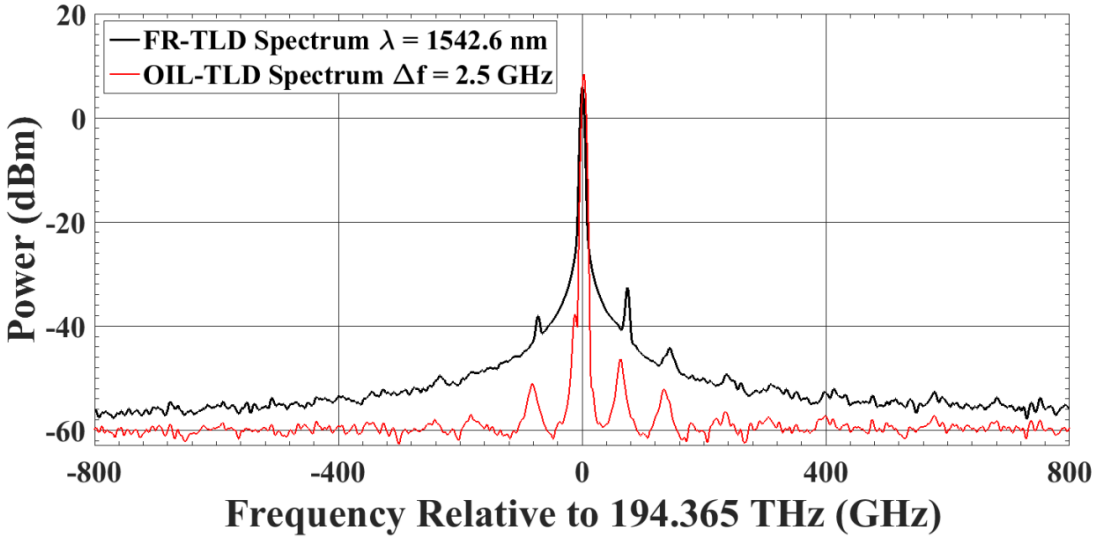

Fig. 6.4. CW spectra of the FR TLD (black solid line) and the OIL TLD (red solid line).

The IM SSA response of the FR TLD for a wide tuning range (Δλ = 21 nm) has been investigated in [197] and a nearly 3-time increase in the relaxation oscillation frequency (ROF) has been demonstrated. Here we investigate the effect of optical injection on the TLD modulation performance and how it varies with wavelength tuning. Both cases of the front and the rear (DBR) mirror injection are considered. A specific feature of the TLD is that the output power varies with tuning, as is shown in Fig. 6.5. The range of the considered DBR injection current allows to blue-tune the TLD over a 21-nm wavelength range from the initial lasing wavelength λ_0 = 1550 nm.

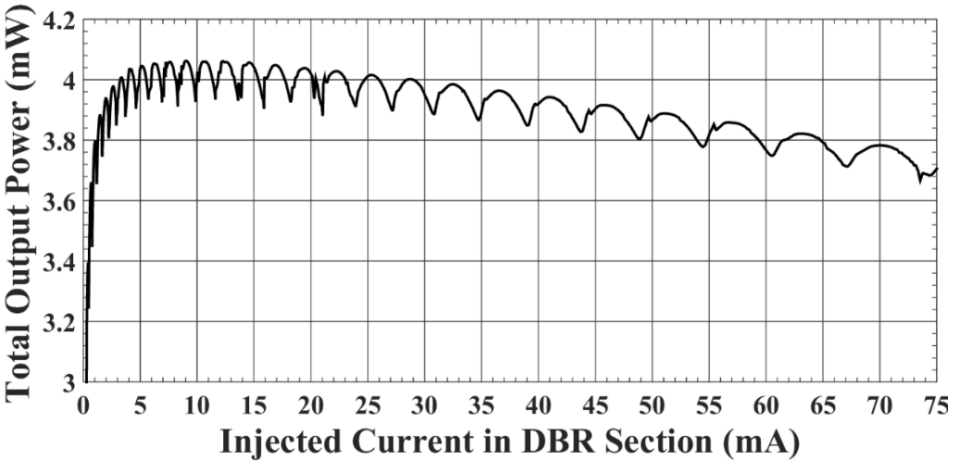

Fig. 6.5 The output power variation of the FR TLD as a function of the DBR tuning current.

In all presented simulations we kept the active section current fixed at the same value ($I_a \approx 18.9$ mA, with the threshold current $I_{th} \approx 8$ mA) which gives a 3-mW optical output power for the FR TLD at the initial lasing wavelength. The variation of the FR TLD output power with tuning is taken into account in order to correctly calculate the injection ratio. In the case of the rear DBR mirror optical injection, the required ML power to obtain stable locking is considerably higher in comparison with the front mirror injection due to the strong reflectivity of the DBR. As a result, the required injection power ratio becomes $R_{inj} = 5.9$ (rear mirror injection) compared to $R_{inj} = 1.2$ (front mirror injection) in order to achieve stable locking at the tuned lasing wavelength $\lambda = 1542.6$ nm and $\Delta f = 2.5$ GHz frequency detuning. Due to the narrow stopband of the DBR reflectivity spectrum (~2 nm), the change in the reflected power can be significant even for small detuning frequency differences.

The results of the SSA IM response are shown in Fig. 6 for the case of optical injection through the front mirror (a) and the rear mirror (b) for the TLD tuned to four different FR wavelengths λ_{FR} from 1550 nm to 1529.2 nm at the frequency detuning $\Delta f = 2.5$ GHz. For consistency of comparison of different cases, the SSA IM analysis for each case has been carried just after the stable locking regime is achieved.

The results for the front mirror injection in Fig 6.6(a) show that the ROF enhances between 8 GHz and 23 GHz, depending on the depth of the wavelength tuning. The bigger is the blue-shift of the tuned wavelength, the higher is the ROF in the OIL TLD. We explain this behaviour of the ROF by the increase in the differential gain of the TLD under wavelength tuning [197]. The injection ratio R_{inj} necessary to achieve stable locking is also increasing with wavelength tuning.

The injection locking from the rear mirror, Fig. 6.6(b), also demonstrates the ROF enhancement which is understandably achieved at higher R_{inj} due to the DBR reflectivity (although, the actual amount of the optical power injected into the active region is approximately the same for both cases).

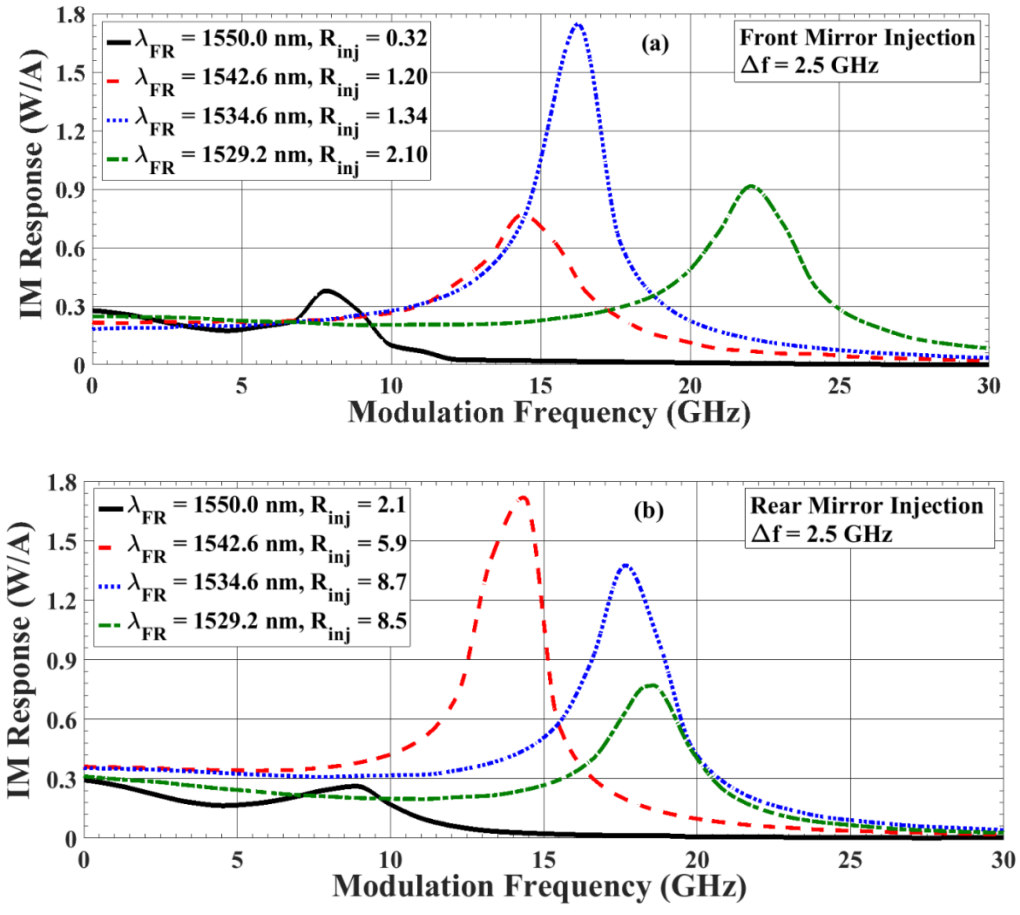

Fig. 6.6 IM response of the OIL TLD tuned to four wavelengths λ_{FR} under injection through the front (a) and the rear (b) mirrors.

In Fig. 6.7 the ROF enhancement of the OIL TLD is plotted for the whole wavelength tuning range for both optical injection directions. The ROF of the FR TLD versus the lasing wavelength [197] (black solid line) is also shown. The figure clearly demonstrates the contributions to the ROF enhancement due to the differential gain dispersion [197] (black solid line) and due to the OIL effect [17] (blue dotted line and red dashed line). A stronger effect of the OIL on the ROF enhancement observed for the front mirror injection (blue dotted line) can probably be explained by the different feed-in rate at the laser interfaces for the two injection directions [199], although at present there is no investigation of this issue for TLDs.

The effect of the front-mirror injection locking parameters, R_{inj} and Δf, on the OIL TLD's modulation response is demonstrated in Fig. 6.8(a) and Fig. 6.8(b), respectively. The FR TLD's output power is P_{FR} = 3.95 mW and the ROF was 4.3 GHz at λ = 1542.6 nm lasing wavelength. In the presence of optical injection from the front mirror, the stable locking is obtained when P_{inj} = 4.74 mW, which gives R_{inj} = 1.2 at Δf = 2.5 GHz. To demonstrate the effect of injection ratio on the IM response, we keep Δf = 2.5 GHz constant, Fig. 6.8(a) and increase the injected power after the stable locking is achieved.

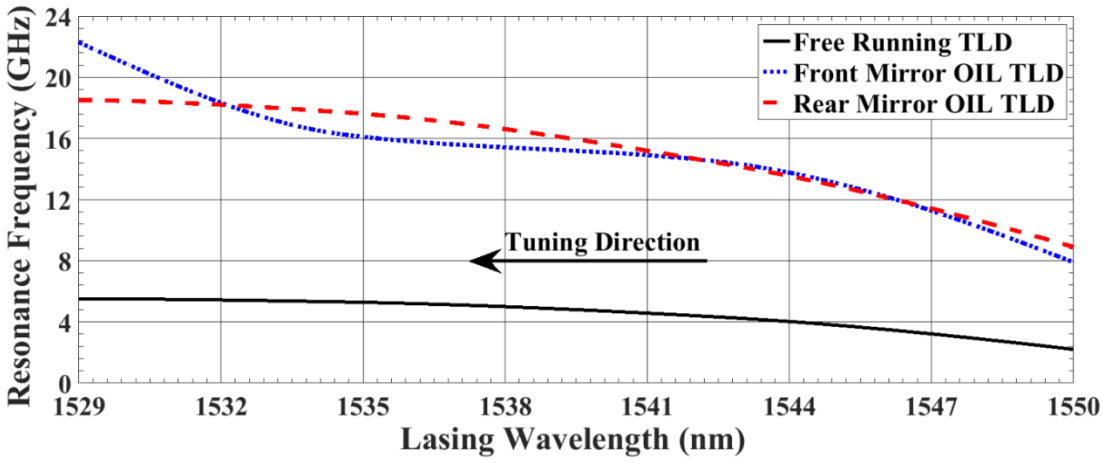

Fig. 6.7 ROF versus lasing wavelength of the FR TLD and OIL TLD with front and rear mirror injection.

The modulation frequency is swept from 0.15 GHz to 30 GHz and the instantaneous output power is taken for ever modulation frequency. The results in Fig. 6.8(a) (black solid line) show

that the ROF of the OIL TLD is increased more than 3 times (from 4.3 GHz to 14.4 GHz). By increasing the injection ratio to 1.6, the resonance frequency is further increased to 16.6 GHz. The physical reason for the ROF increase when R_{inj} increases is the carrier density drop in the active region under the optical injection [17]. The carrier density drop results in the cavity resonance frequency shift due to the refractive index change. According to Murakami [17] the ROF in the OIL lasers is defined by the difference between the shifted cavity resonance frequency and the FR laser emission frequency. Thus the bigger is this difference, the bigger is the ROF, in agreement with the results in Fig. 6.8(a).

The dependence of the ROF on the detuning frequency Δf is also an important feature of OIL lasers. To compare the effect of detuning frequency it is vital to keep the injection ratio constant. In this case we keep the injection ratio constant at $R_{inj} = 1.2$ with the ML power $P_{inj} = 4.74$ mW. The detuning frequency Δf was varied from -5 GHz to 5 GHz. The IM response of the OIL TLD for different detuning frequencies is shown in Fig. 6.8 (b). The results demonstrate that the positive detuning frequencies provide a higher resonance frequency than the negative detuning frequencies.

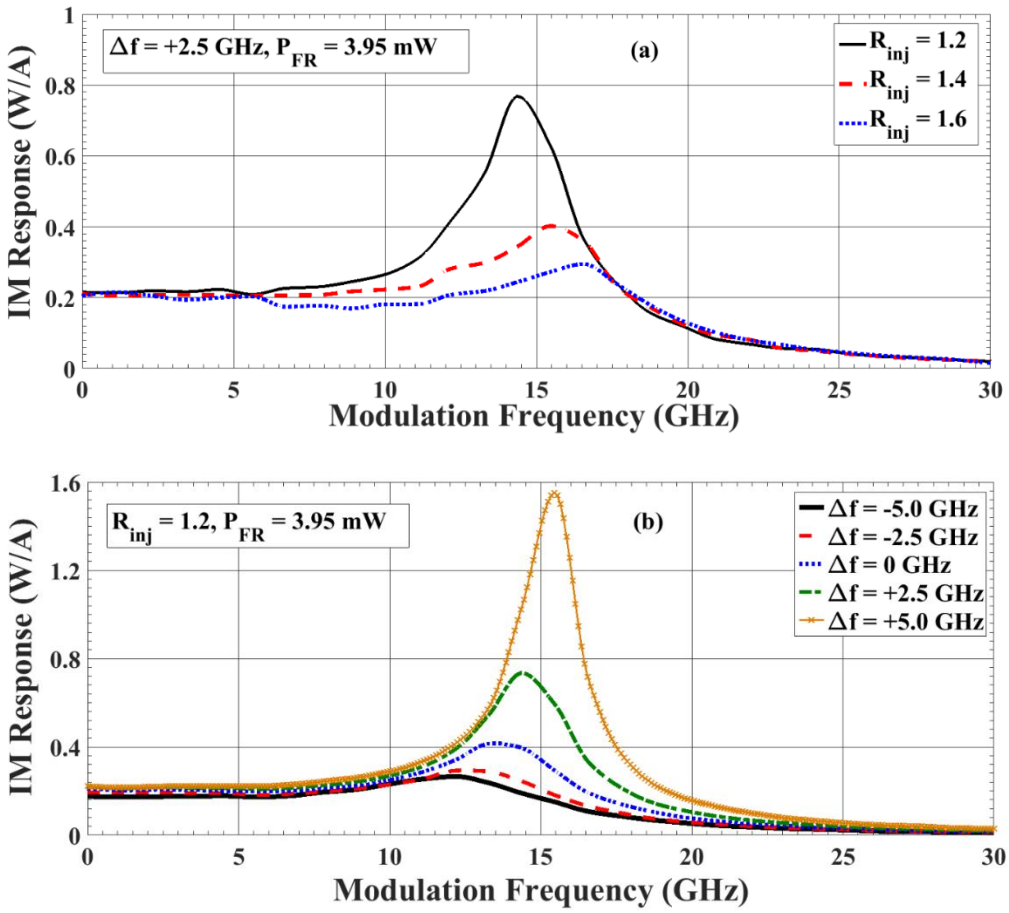

Fig. 6.8 IM response of the front-mirror optically-injected TLD for a fixed detuning frequency (a) and a fixed injection ratio (b).

In addition, it is also visible that the transfer function peak of the IM response is also increased with the positive detuning frequency. The difference between the ML emission frequency and the new cavity resonance frequency of the SL becomes less with negative detuning and, as a result, the ROF enhancement is smaller than the one in the positive detuning case.

Similar analysis can be carried out for each lasing wavelength of the TLD, which is important from a practical point of view in order to find the best modulation performance of the OIL TLD. The novel feature of the modulation response of the OIL TLD compared to the usual single-mode lasers emitting at a fixed wavelength is due to the frequency dispersion of the differential gain in TLDs. Since the ROF under the OIL is proportional to the differential gain which

increases with wavelength tuning, this allows to further optimise the modulation response and achieve further ROF enhancement in the OIL TLD.

6.5 Conclusions

A small-signal intensity modulation response of an optically-injected TLD is investigated for different wavelength tuning regimes. The three-section TLD is modelled in TLLM based VPI software using the travelling wave model. To adequately simulate spatio-temporal dynamics of a TLD we have integrated the VPI's time-domain model with the advanced physics-based software PICS3D. The realistic gain spectra are calculated in PICS3D and imported into the VPI simulation setup. In addition to this, the refractive index change in the DBR tuning section under the free carrier injection is also calculated in PICS3D by taking into account all physically important contributions. The differential refractive index in the active section is calculated through the specified linewidth enhancement alpha-factor using the calculated differential gain.

We have calculated the stable locking boundary map of the OIL TLD which depends on the tuned lasing wavelength and have carried out investigation of the TLD response in different injection states. The results show a dramatic change in the emission spectra and the relaxation oscillation frequency and huge improvement of these characteristics under stable injection locking.

The effect of the optical injection parameters, such as the frequency detuning and the power ratio of the SL and the ML outputs, on the OIL TLD was studied for different tuned lasing wavelengths. We show that forward optical injection and positive frequency detuning together with blue wavelength tuning are preferable regimes for obtaining enhanced modulation performance of OIL TLDs.

We demonstrate a large increase of the relaxation oscillation frequency (above 20 GHz) and the modulation bandwidth (above 25 GHz) of the OIL TLD. Both these parameters strongly depend on the tuned lasing wavelength. The novel feature of the modulation response of the OIL TLD compared to usual single-mode lasers emitting at a fixed wavelength is due to the frequency dispersion of the differential gain in TLDs which increases with blue-shifted wavelength tuning. It is shown that both the differential gain increase with wavelength tuning and the optical injection effect on the cavity resonance frequency shift contribute to the substantial enhancement of the modulation response of the OIL TLD. This allows to further optimise the modulation response and achieve a substantial relaxation oscillation frequency enhancement in multi-section wavelength tunable laser diodes.

CHAPTER 7

MODULATION RESPONSE OF OPTICALLY INJECTION-LOCKED TUNABLE LASER DIDES WITH SIDE-MODE INJECTION AND LARGE SIGNAL ANALYSIS

7.1 Introduction

High-speed widely tunable semiconductor lasers diodes (TLDs) are key components for ultra-fast fibre optic networks. Recently, a 3-section TLD with more than 30-nm tuning range was presented in experiment [200] and simulation [105]. Moreover, optical injection locking (OIL) is an effective technique which increases the modulation response and spectral purity of the lasers. Consequently, there has been a great interest in OIL lasers and it is a promising technique to improve the laser dynamics.

The small signal analysis of OIL lasers has been carried out by different studies and the conventional rate equations RE are modified to explain the mechanism behind the bandwidth enhancement [17, 125]. There have been also experimental observations of bandwidth enhancement for different type of lasers [183, 185]. Murakami et al. [17] devised a theoretical explanation for bandwidth enhancement of OIL lasers, and proved that the difference between the locked (master laser) frequency and the shifted cavity resonance frequency of the slave laser defines the enhanced relaxation oscillation frequency (ROF). This analysis was carried by utilizing the rate equation-based theoretical approach.

The cavity resonance frequency is related to the carrier-density-depended refractive index of the laser cavity. The refractive index of the laser is inversely correlated with the carrier density. The carrier density in the slave laser active region of the OIL laser always drops as a result of enhanced stimulated emission due to externally-injected light from the slave laser. The relation between the *m*th cavity's resonance mode and the refractive index is:

$$\nu_0 = \frac{c}{2\mu l} \times m \tag{7.1}$$

Here c is speed of light, μ is the refractive index, *l* is the cavity length, and *m* is the mode number. After providing stable locking, the carrier density of the laser drops as:

$$\Delta N = N - N_{th} = -\frac{2\kappa}{g v_g}\frac{E_{inj}}{E}\cos\phi_0 \tag{7.2}$$

Here κ is coupling coefficient, g is differential gain, v_g is group velocity, E_{inj} and E are the injected and solitary laser fields, respectively, and ϕ_0 is the phase difference between these two fields. As a result of the drop in carrier density, the refractive index increases and the cavity resonance frequency red-shifts, and the amount of the shift at steady-state is derived as:

$$\Delta\omega(N) = \frac{\alpha}{2} g\Delta N \tag{7.3}$$

Here α is the linewidth enhancement factor. The shift in the cavity resonance and the position of the modes in the OIL laser are schematically shown in Fig 7.1.

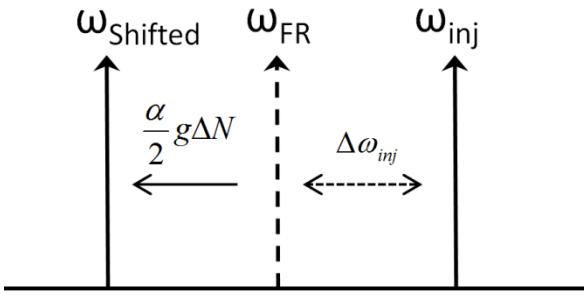

Fig. 7.1 Cavity resonance shift in OIL lasers.

The OIL laser at steady-state conditions starts always lasing at locking frequency, but the actual cavity resonance frequency stays in the shifted mode. As we have found and this will be shown later, this shifted cavity mode can also be observed in optical spectrum while laser is operating at CW regime. Physically this mode (which is not the lasing mode!, as the OIL laser emits at the master laser frequency), has been interpreted in literature [201] as the 'amplified

spontaneous emission' (ASE) mode. Finally, the ROF of the directly-modulated OIL laser under small-signal modulation is given as:

$$\omega_{res} = \Delta\omega_{inj} - \frac{\alpha}{2} g\Delta N \tag{7.4}$$

Frequency chirping of the directly modulated laser is an important parameter which affects the long haul fibre optic transmission due to dispersive effect in the fibre cables. Because of this, it is important to provide laser operation with increased spectral purity. The refractive index parameter and gain of the laser varies with direct modulation because of the change in the carrier density of the OIL slave laser. As a result of this, the lasing frequency of the laser fluctuates and increases its instability. In [191] the reduction of chirping of OIL laser was confirmed in experiment.

The effect of injection locking on the frequency chirping is formulated as follows [23]:

$$\frac{d\phi}{dt} = \frac{\alpha}{2}\frac{\varepsilon S}{\tau_p} + \frac{\alpha}{2}\frac{1}{S}\frac{dS}{dt} + k_c\sqrt{\frac{S_{inj}}{S}}\left[\sin\phi(t) - \alpha\cos\phi(t)\right] - \Delta\omega \tag{7.5}$$

Here ε is gain compression, τ_p is photon lifetime k_c is the coupling rate coefficient of the injected light into the slave laser, S_{inj} and S are the injected photon number and the photon number inside the slave laser, respectively. The first term in Eq. (7.5) represents the adiabatic chirp which is the result of the change in the carrier density. The transient chirp is presented by the second term which becomes dominant when the laser drive current during the modulation cycles changes from the off (a zero) to the on (a one) level, or vice versa. To carry out a successful direct modulation operation of the lasers, it is essential to reduce the transient chirping. It has been experimentally demonstrated that the reduction in frequency chirping is increasing the maximum transmission distance in optical fibre links [202, 203].

In this Chapter, we firstly investigate the ROF enhancement of OIL TLD and how it is affected by different tuned wavelengths in order to demonstrate the effect of tuning on ROF. Such investigation on OIL TLDs to best our knowledge has not been undertaken before. Secondly, we will analyse the effect of large detuning frequencies and to show possible modulation speed enhancement limits. Additionally, we have carried out analysis of side-mode locking, when the master laser light is injected in the vicinity of the side mode rather than near the main lasing mode. We demonstrate that large ROF and modulation bandwidth enhancement is achievable for the side-mode injection and that the increase in ROF is defined by the cavity side-mode shift. The side-mode OIL of semiconductor lasers have been first suggested in [204]. Although, there were some further publications on side-mode OIL lasers and their applications in optical fibre systems [205], these works are mainly focussed on fixed wavelength lasers. To the best of our knowledge, this regime was not previously studied in TLDs. Finally, we have investigated the large signal response of OIL TLD for high modulation bit rates including and demonstrate simultaneous increase of the modulation speed and decrease of the frequency chirping. These findings are of great importance for utilisation of TLDs as optical transmitters for high-speed optical communication applications.

7.2 Bandwidth Enhancement of OIL TLD and Cavity Resonance Shift

In previous chapter, the injection locking is carried out for both rear and front mirror injection, and it was observed that the differential gain has a substantial effect on modulation bandwidth enhancement. In this section we will first investigate the cavity resonance shift of the OIL TLDS with front mirror injection for different tuning regime. Before investigating the bandwidth enhancement of the OIL TLD, we first expand the stability boundary map to a wider range of parameters and obtain the maps for three different lasing wavelength. The results are shown in Fig. 7.2.

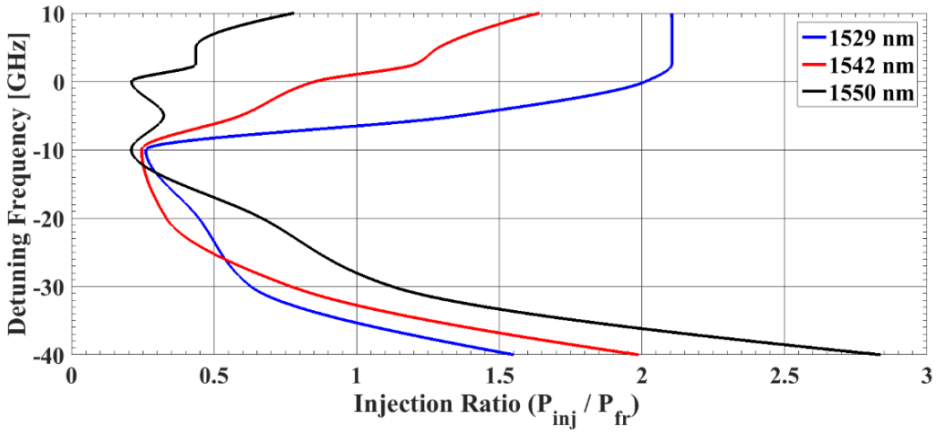

Fig. 7.2 Stable locking boundary map of OIL TLD for different tuning regimes.

It is necessary to indicate that the boundary lines are separating the stable locking regime from other nonlinear dynamics (chaotic, quasi-chaotic, and period-one regimes). It is seen in Fig. 7.2 that the stable locking boundary map exhibits different injection characteristics for different tuning regimes. This could be explained by the change in the differential gain coefficient under the wavelength tuning [179, 197]. The variation in differential gain with tuning is shown in Fig. 7.3. It is clearly seen that a4-times increase in differential gain coefficient is obtained by tuning

the laser over a wide range (21 nm). The comparison of two different gain models (imported gain model produced in PICS3D and parabolic gain model) shows that the parabolic gain spectrum considerably underestimates the actual increase in differential gain. To obtain a realistic analysis of the ROF increase of OIL TLDs, we have imported into the VPI the gain spectrum which was produced using the physics-based software PICS3D according to our integrated model [197].

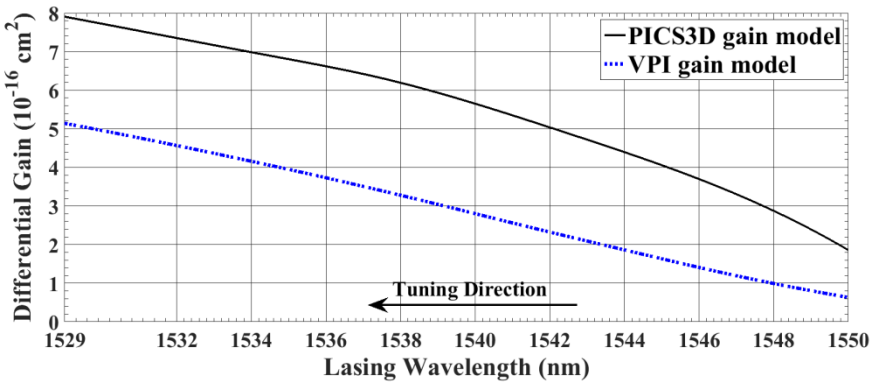

Fig. 7.3 Variation of differential gain with the wavelength tuning using different gain models.

To compare the small signal IM response of OIL TLD for different tuning regimes, we investigate three different tuned lasing wavelengths: 1550 nm, 1542.6 nm and 1529.2 nm. For each tuning regime, the light injection is applied with the same fixed detuning frequency Δf which is equal to 2.5 GHz. By using the stable locking boundary map in Fig. 7.2, the minimum required injection ratios (P_{inj}/P_0) have been determined for each case.

The CW free running (FR) TLD which operating at 1550 nm is injection locked to a master laser and the frequency spectrum of OIL TLD is plotted in Fig. 7.4 for detuning frequency Δf = +2.5 GHz and power injection ratio (P_{inj}/P_0) of 0.23.

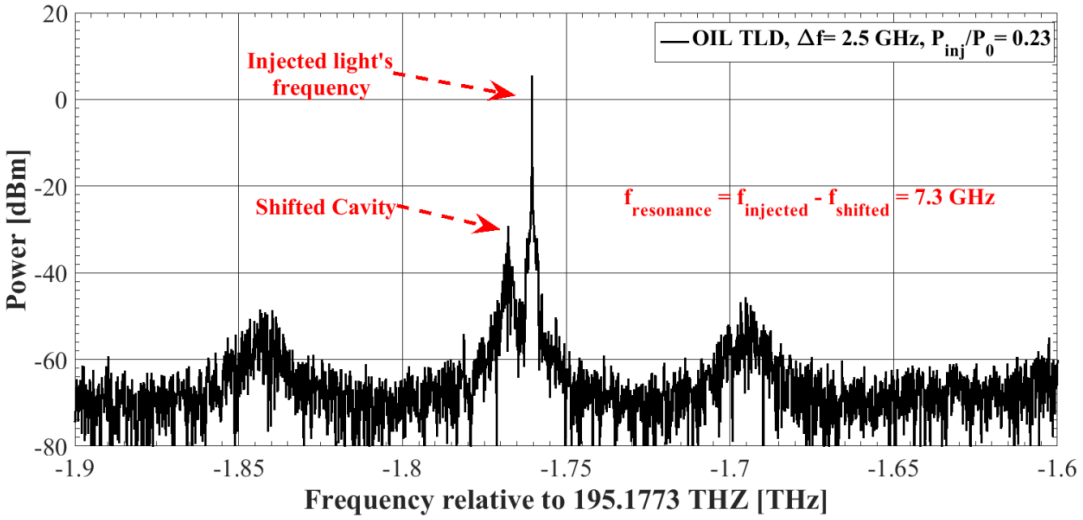

Fig. 7.4 Frequency spectra of OIL TLD λ_{FR} = 1550 nm.

The most important result in this figure is that our model is capable to identify not only the main lasing mode (which is at the maser laser frequency), but it also clearly identify the new (non-lasing!) cavity shifted mode. This is a remarkable result because this is not one of the lasing mode in the OIL slave TLD, but the mode which according to [201] physically corresponds to the ASE process. The cavity resonance frequency of the TLD is red-shifted due to the drop in carrier density from 1.2×10^{18} cm^{-3} to 1.16×10^{18} cm^{-3}. Although, the new cavity resonance frequency is different, the TLD is lasing at the injected light's frequency as a result of the locking. The frequency difference between the locked frequency and the cavity resonance frequency is measured as 7.3 GHz. This means that the drop in the carrier density causes a 4.8 GHz red shifting in the cavity resonance frequency.

In Fig. 7.5, the small-signal of IM responses of FR and OIL TLD are plotted for λ_0=1550 nm. The dashed brown curve represents the modulation response of FR TLD. The ROF of the FR TLD is about 2.25 GHz. According to [152] it depends on the lasing power and is completely defined by a single laser parameter – its differential gain. Our estimation using formula for ROF from [152], differential gain from Fig. 7.3, and the obtained output power gives the same value.

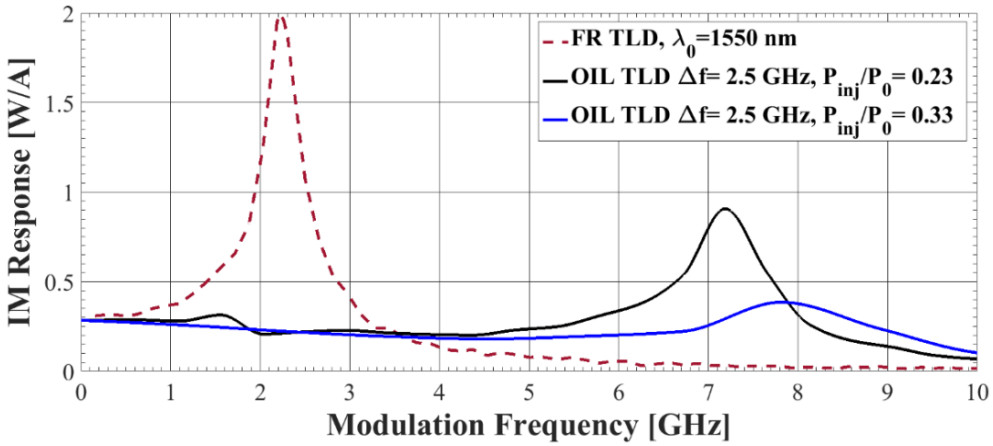

Fig. 7.5 Small-signal response of OIL TLD lasing at λ_0= 1550 nm for Δf= 2.5 GHz.

As it is seen from the black curve, the ROF of OIL TLD is exactly at 7.3 GHz for the power injection ratio of 0.23. It was demonstrated in [17] for case of the main-mode optical injection, that the ROF of the OIL is defined by the difference between the injected master frequency and the cavity shifted mode frequency. The obtained result in Figs. 7.4 and 7.5 directly validate the above assumption regarding the relation between the spectral characteristics under CW regime and the ROF of the directly-modulated OIL TLD. Finally, the blue curve represents the IM response of OIL TLD for higher injection ratio (0.33) which further increases the cavity resonance shift and the ROF of the OIL TLD which is obtained around 8 GHz. This is a very important result which demonstrates advantage of optical injection for enhancement of modulation response of semiconductor lasers. This is because the modulation characteristics of the OIL laser do not depend anymore on the laser cavity parameters only, but to large extent they are defined by the parameters of the injected light such as the power ratio and the frequency de-tuning. For example, ROF is completely defined the above frequency difference. Of course, the FR laser parameters are still important in defining the shape of the response function in Fig. 7.5.

After observing the small signal IM characteristics of the OIL TLD for λ_0 = 1550 nm, the TLD has been tuned to 1542.6 nm and 1529.2 nm lasing wavelengths. The investigation of the IM response of the OIL TLD was then carried out for these wavelengths. The wavelength tuning is

achieved by injecting additional electrical current into the DBR section, and the differential index parameter in DBR section is modified according to the data obtained from PICS3D, as was explained in Chapter 5. To keep the α-factor constant for each tuning regime, the differential index coefficient in the active section is also modified by taking the change of the differential gain into account. For each tuning regime, the injected current into the active section was kept constant (18.9 mA), which gives 3 mW output power for λ_0= 1550 nm. When the lasing wavelength is tuned to 1542.6 nm, the output power of FR TLD increases to 3.93 mW due to the change in the gain value, as was discussed in Chapter 5.

After obtaining a 7.4-nm wavelength tuning to the 1542.6 nm in the FR TLD, the injection locking was achieved for Δf = 2.5 GHz for minimum necessary injection power ratio (to get the stable locking) which was observed as 1.2 from the stable locking boundary map in Fig. 7.2. The threshold carrier density of FR TLD is measured as 9.83×10^{18} cm^{-3}. As a result of increased stimulated emission due to the externally injected light, the carrier density drops to a lower value of 9.26×10^{18} cm^{-3}. Fig. 7.6 shows the IM response of FR and OIL TLD for different values of the injected power ratio.

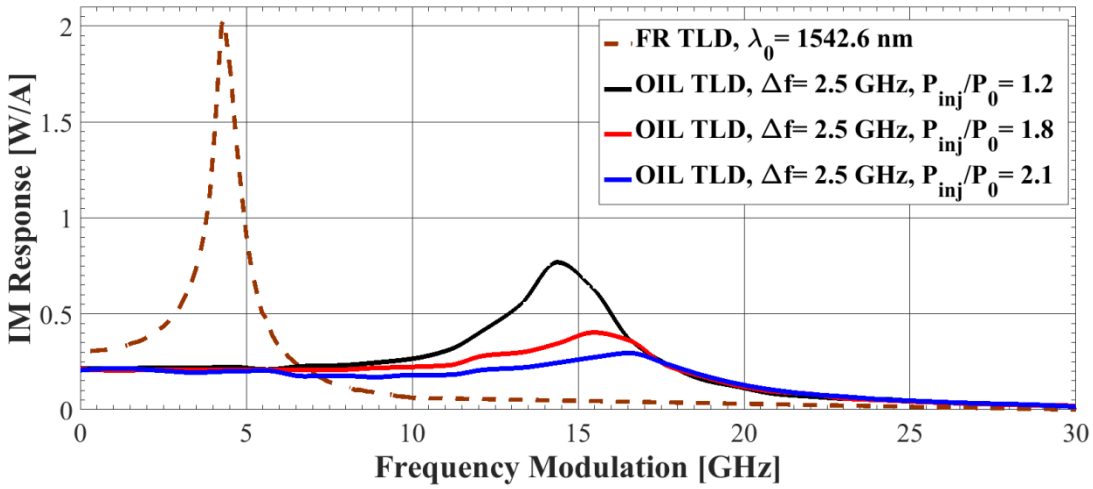

Fig. 7.6 Small-signal response of OIL TLD lasing at λ_0= 1542.6 nm for Δf= 2.5 GHz.

As a result of carrier density drops, the cavity resonance frequency shifts, and the difference between the locked (master laser) frequency and the cavity resonance frequency results in the ROF enhancement from 4.29 GHz to 14.4 GHz. Consequently, the shift in cavity frequency is observed as 11.9 GHz, which was also observed in the CW spectra similar to shown in Fig. 7.4.

The last investigation of the observation of the ROF enhancement is carried out for a near 21-nm tuned lasing wavelength λ_0= 1529.2 nm. The IM response of FR TLD is plotted in Fig. 7.7.

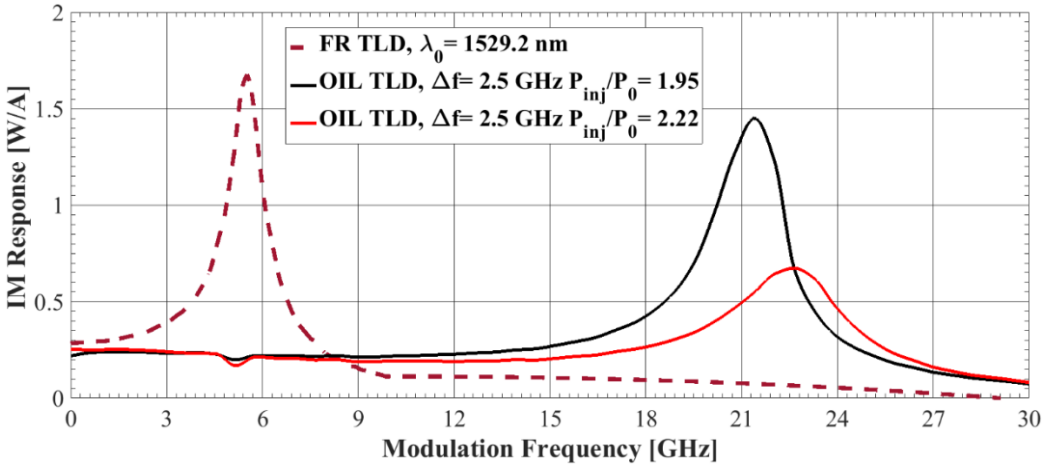

Fig. 7.7 Small-signal response of OIL TLD lasing at λ_0= 1529.2 nm for Δf= 2.5 GHz.

The ROF of the FR TLD in this case is found as 5.5 GHz. Under the OIL regime the power injection ratio is found 1.95 in stability map to obtain stable locking for Δf= 2.5 GHz. The carrier density drops from the threshold value of $9.93\times\cdot10^{18}$ cm^{-3} to 9.68×10^{18} cm^{-3}. The ROF of the OIL tuned TLD is found as 21.4 GHz. Hence, the resonance cavity shifted mode is measured as 18.9 GHz, which was also confirmed by the CW spectra analysis.

After completing investigation of the bandwidth enhancement for different tuned wavelengths, the summary of the corresponding change in the carrier density (ΔN) with the emission wavelength for the four considered cases is shown in Fig. 7.8.

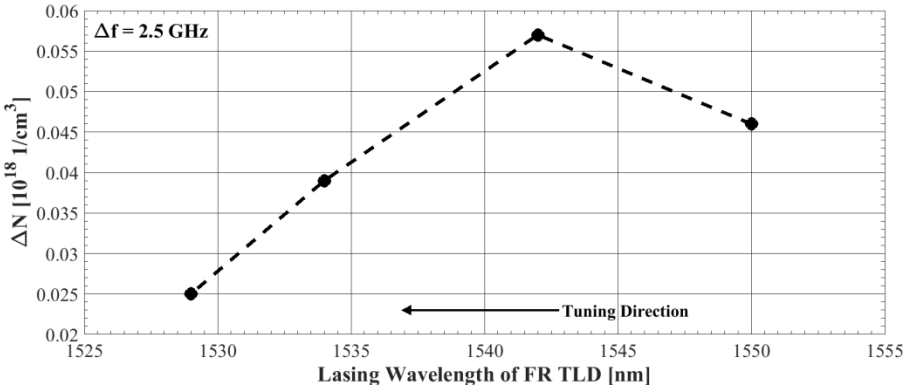

Fig. 7.8 Change in carrier density of the OIL TLD for different tuned wavelength.

It is observed that change in the carrier density in OIL TLD is wavelength-depended. The main physical reason behind such behaviour is not completely clear. This may be investigated in a future work.

7.3 Investigation of IM Response of OIL TLD at High Detuning Frequencies

The IM response of OIL TLD can be further enhanced for higher detuning frequencies to test the limits of possible extreme enhancement. Theoretical investigations of modulation bandwidth enhancement suggest that a substantial amount of bandwidth enhancement can be obtained by increasing the detuning frequency, but the achievable limit is not very clear. It is also mentioned by Murakami [17] and Lau [156] that a positive frequency detuning can provide higher bandwidth enhancement than a negative detuning. In case of negative detuning, the injected light's frequency will be on the left hand side of the FR slave laser's main mode; consequently the difference between the shifted cavity resonance frequency and the locked emission frequency will be smaller than for the positive detuning. As a result of this asymmetry, the investigation of the effect of the frequency detuning on ROF enhancement is carried out here only for a positive detuning to achieve higher possible bandwidth enhancement.

Before investigating the IM response of OIL TLD for higher detuning frequencies, the stable locking boundary map is extended to higher detuning frequencies in order to correctly identify the minimum required injection power to achieve stable locking. As is seen from Fig. 7.9, the required injection ratio increases for the frequency detuning which reaches almost half of the inter-mode distance (74 GHz), and it starts increasing until the detuning reaches the first side-mode.

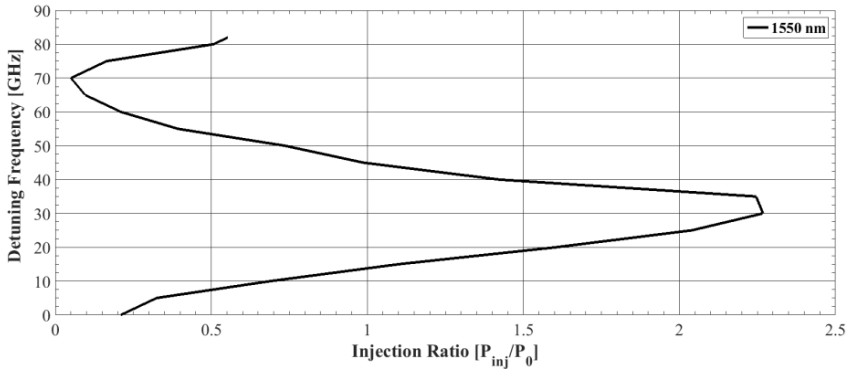

Fig. 7.9 Stable locking boundary map for higher positive detuning frequencies (λ_0= 1550 nm).

As can be observed from Fig. 7.3, a substantial increase in differential gain is obtained by tuning the TLD from 1550 nm to 1529.2 nm. Thus, the investigation of the effect of detuning frequency on bandwidth enhancement was carried out for these two lasing wavelengths. In both cases, the injection locking is provided for 3 different detuning frequencies; 10, 15, and 20 GHz.

In Fig. 7.10, a small signal IM response of FR and OIL TLD is plotted for λ_0= 1550 nm. In order to provide stable locking for Δf = 10 GHz, the required injected power ratio is obtained as 0.69 from the boundary map in Fig. 7.9. As a result of injection locking, the carrier density of TLD drops from 1.26×10^{18} cm^{-3} to 1.178×10^{18} cm^{-3}.

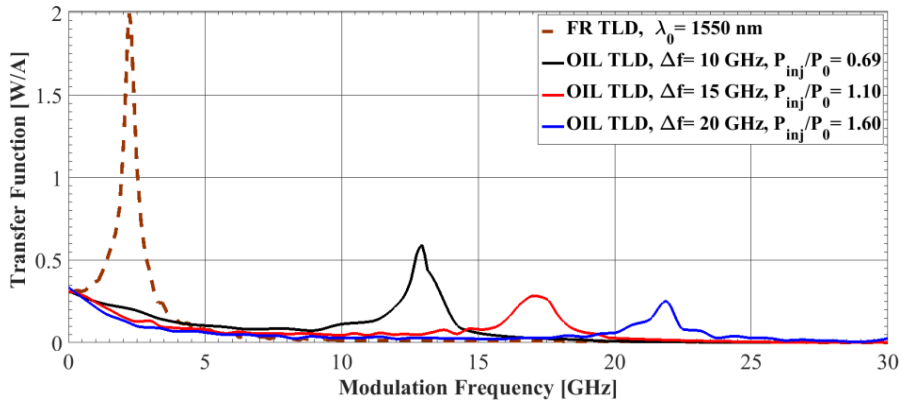

Fig. 7.10 IM response of OIL TLD for large detuning frequencies (λ_0= 1550 nm).

The corresponding IM response functions are shown in Fig. 7.10 with the blue curve corresponding to 20-GHz detuning when a ROF of 13 GHz is achieved. The same investigation

is repeated for 15 GHz and 20 GHz detuning frequencies. To provide stable locking in both cases, the required injected power ratios were obtained as 1.10 for 15 GHz detuning, and 1.6 for 20 GHz detuning. The change in carrier density for both cases was also observed. The carrier density drops to 1.186×10^{18} cm^{-3} for Δf = 15 GHz, and to 1.187×10^{18} cm^{-3} for Δf = 20 GHz. It should be noted that the change in carrier density for higher detuning frequencies becomes smaller and this reduces the shift in cavity resonance frequency for each case. A substantial increase in the ROF of OIL TLD was 17 GHz for Δf = 15 GHz, and 21.9 GHz for Δf = 20 GHz.

Similar analysis of the ROF enhancement is carried out for λ_0= 1529.2 nm. The required power ratio for corresponding detuning frequency is obtained and the TLD is locked for three different detuning frequencies. The stable locking boundary map for λ_0= 1529.2 nm is given in Fig. 7.11.

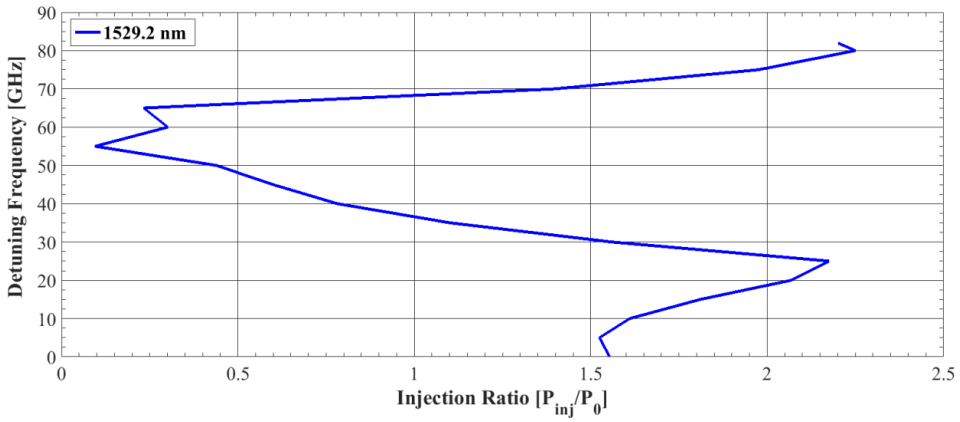

Fig. 7.11 A table locking boundary map for λ_0= 1529.2 nm lasing frequency.

In order to have a meaningful comparison between two lasing wavelengths, the stable injection locking is provided for the same detuning frequencies. In Fig. 7.12 below, the IM response of OIL TLD is plotted for corresponding detuning frequencies.

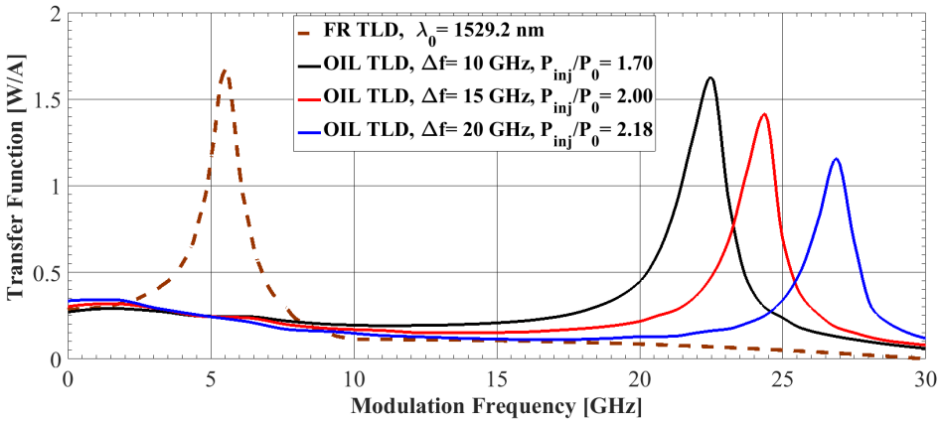

Fig. 7.12 IM response of OIL TLD for different detuning frequencies (λ_0= 1529.2 nm).

Although the required injected power ratio increases for each detuning frequency, the drop in the carrier density is decreasing. To obtain the stable locking for Δf = 10 GHz, the power injection ratio should be 1.7. This reduces the carrier density from 0.981×10^{18} cm^{-3} to 0.978×10^{18} cm^{-3}. For 15 GHz and 20 GHz detuning frequencies, the minimum required power ratio increases to 2 and 2.18, respectively. The decreased carrier densities are measured as 0.981×10^{18} cm^{-3} and 0.984×10^{18} cm^{-3}, respectively. As a result of high differential gain coefficients at 1529.2 nm lasing wavelength, the observed ROF enhancement is higher than at λ_0= 1550 nm.

The carrier density of the OIL TLD decreased sharply after 20 GHz detuning frequency, as is shown in Fig. 7.13.

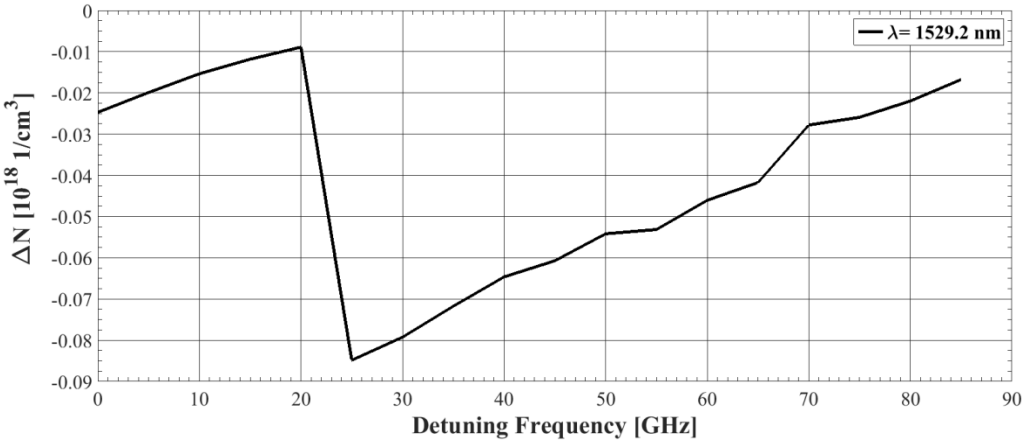

Fig. 7.13 Carrier density change of OIL TLD for high detuning frequencies λ_0= 1529.2 nm.

We also observed that the cavity shifted ASE mode became not visible on the CW spectrum. It should be mentioned that this change was observed for both emission wavelengths.

7.4 Investigation of IM Response of OIL TLD at Side-Mode Injection

The analysis of injection locking was also carried out for detuning frequencies near positive side-mode of FR TLD. The IM response of OIL TLD was investigated for two different lasing wavelength; λ_0 = 1550 nm and λ = 1529 nm. The inter-mode-distance was 74 GHz, and the locking was provided for Δf = 75, 80, and 82 GHz. The CW spectra of FR (λ_0=1550 nm) and OIL TLDs for the side-mode injection and different detuning Δf are shown in Figs. 7.14 - 7.16.

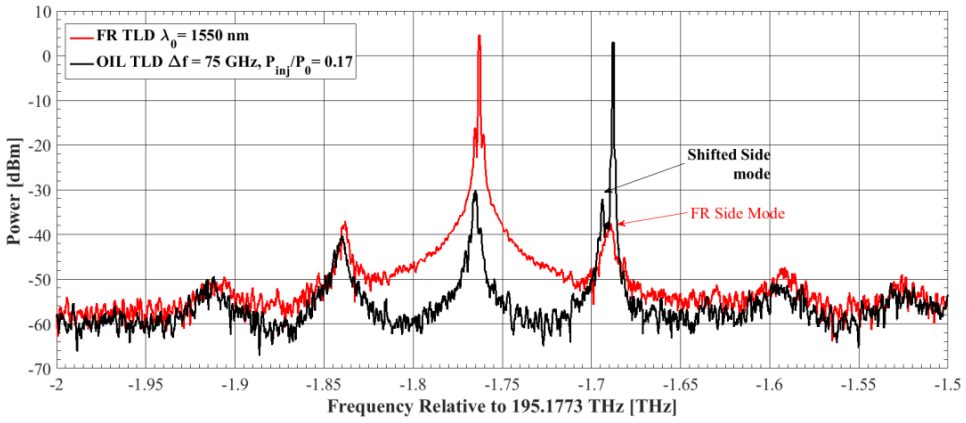

Fig. 7.14 Optical spectra of FR and OIL TLD at λ_0= 1550 nm for Δf= 75 GHz.

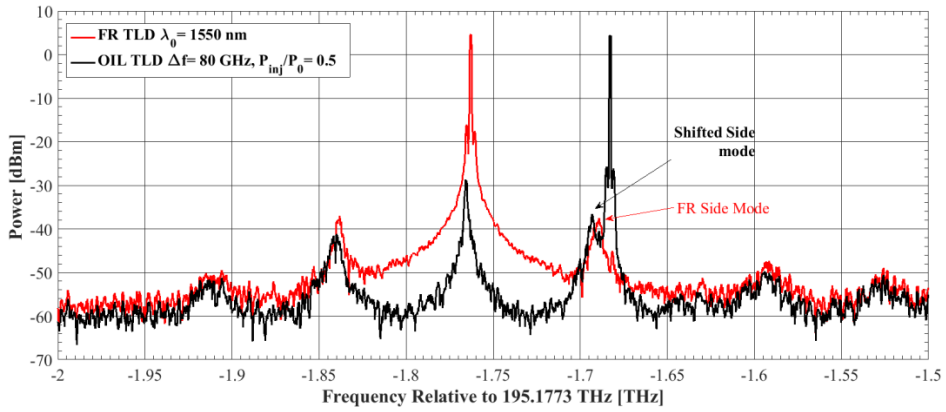

Fig. 7.15 Optical spectra of FR and OIL TLD at λ_0= 1550 nm for Δf= 80 GHz.

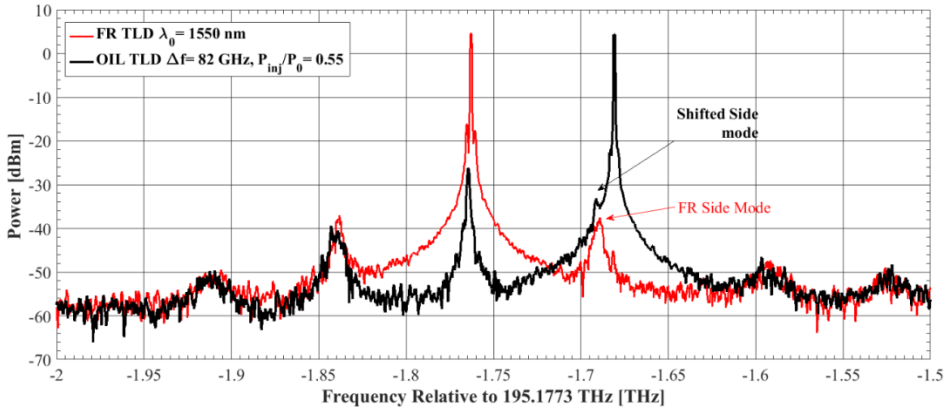

Fig. 7.16 Optical spectra of FR and OIL TLD at λ_0= 1550 nm for Δf= 82 GHz.

The side-mode OIL was achieved for Δf = 75 GHz and the required power injection ratio was found as 0.17 from the stable locking map in Fig. 7.9. The carrier density of TLD dropped to from 1.206×10^{18} cm^{-3} to 0.978×10^{18} cm^{-3} which caused the corresponding shift in the main and the side-mode cavity frequencies. The CW optical spectra of the FR and OIL TLD for this case are plotted in Fig. 7.14. The shift in cavity frequency is clearly observed not only for the main mode, but also for the first side-mode.

When we increased the detuning frequency to 80 and 82 GHz, the shift in cavity modes and the frequency difference between the shifted first positive side-mode and the locking (master laser) frequency were still well visible on the CW optical spectra. The stable locking was provided for

both cases by increasing the injected power ratio to 0.5 and 0.55, respectively. By increasing the detuning frequency, the change in the carrier density became smaller, similar as was observed before. It was measured that the carrier density dropped to 1.18×10^{18} cm^{-3} by locking the TLD with 80 GHz detuning frequency, and to 1.194×10^{18} cm^{-3} with 82 GHz detuning frequency.

The IM response for each investigated case is plotted in Fig. 7.17.

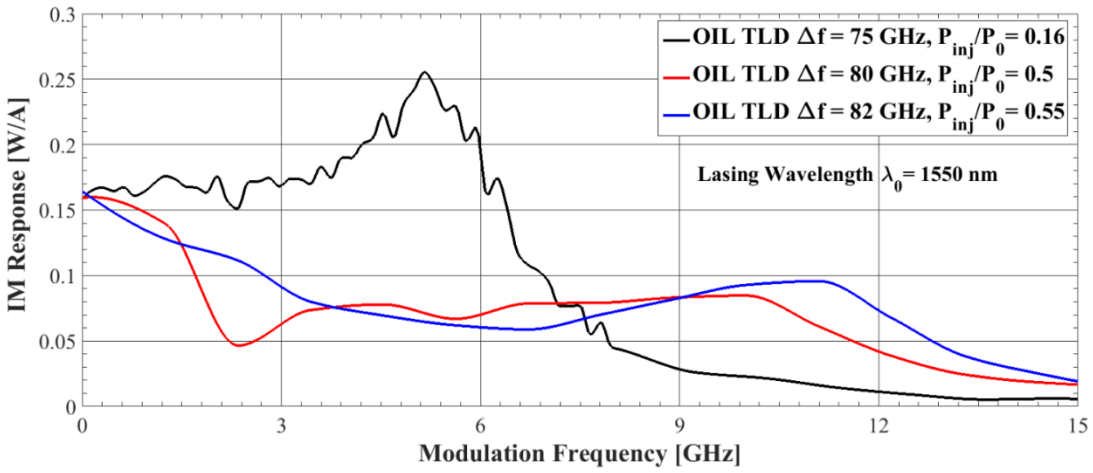

Fig. 7.17 The IM response of OIL TLD for side-mode locking (λ_0= 1550 nm).

Although, as was found, the ROF was increasing for higher detuning frequencies, the amount of cavity shift drops due to smaller change in the carrier density. Most importantly, it was observed that the shifted cavity side-mode can also contribute to the ROF and bandwidth enhancement if the laser is locked near this mode.

The side-mode injection locking was further investigated for lasing wavelength λ_0 = 1529.2 nm. The detuning frequencies were kept the same as in the previous case, and the minimum required power injection ratio was obtained from the stability map in Fig. 7.11.

The optical spectra for each case are shown in Figs. 7.18-7.20. The stable locking was observed with visible shifted cavity modes. For each locking regime, the SMSR between lasing wavelength and cavity modes was at least 30 dBm.

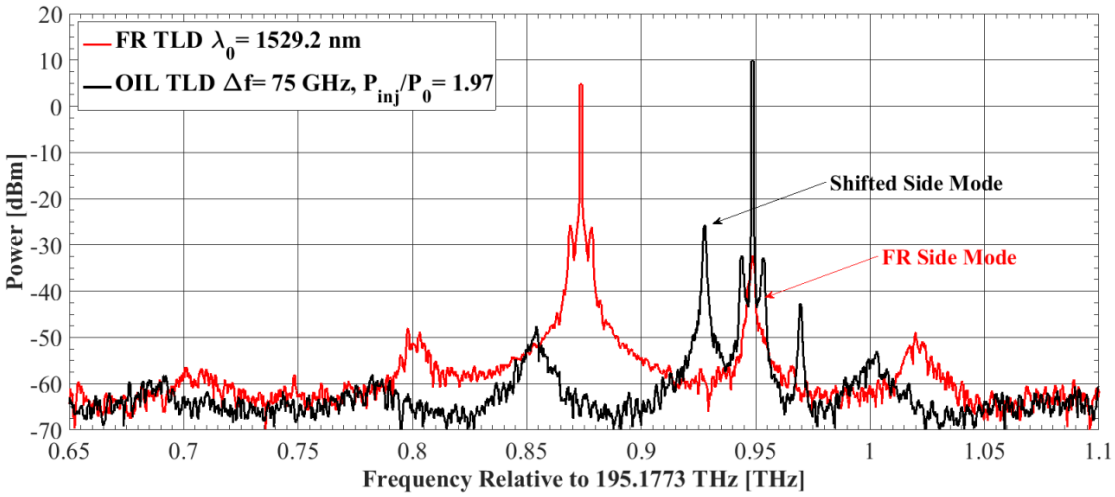

Fig. 7.18 Optical spectra of FR and OIL TLD at λ_0= 1529.2 nm for Δf = 75 GHz.

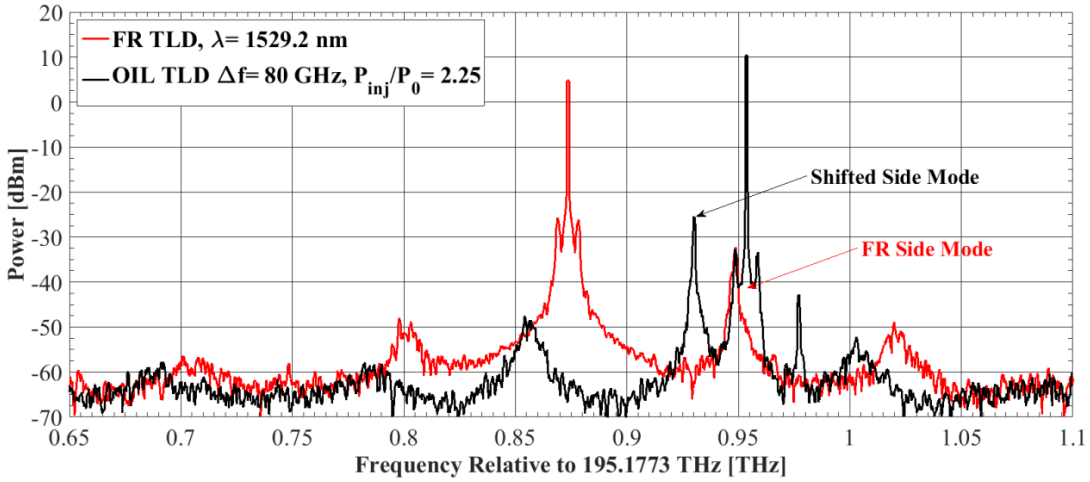

Fig. 7.19 Optical spectra of FR and OIL TLD at λ_0= 1529.2 nm for Δf = 80 GHz.

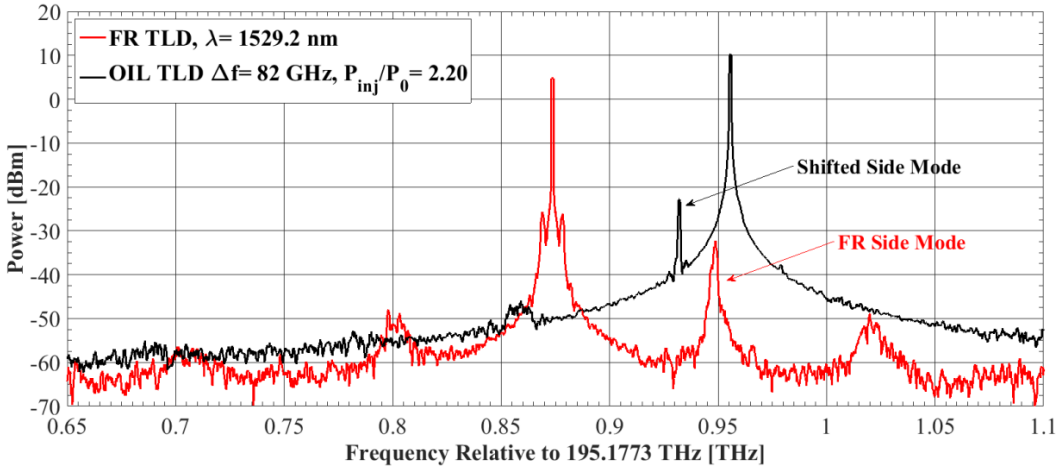

Fig. 7.20 Optical spectra of FR and OIL TLD at λ_0= 1529.2 nm for Δf= 82 GHz.

After tuning the TLD to the lasing wavelength 1529.2 nm, the injection locking was firstly applied with Δf = 75 GHz and the required power ratio was found 1.97 from the stability map. It should be mentioned that the injected current into the active section of TLD was kept 18.9 mA which results in 3.72 mW output power. The carrier density dropped from 0.993×10^{18} cm^{-3} to 0.967×10^{18} cm^{-3}, and the cavity resonance frequencies of the main mode and side-mode were shifted. The first most important outcome of the investigation was that the shifts in cavity resonance frequencies were higher than the previous case. This could be explained by the dramatic increase in differential gain due to wavelength tuning.

As a result of the side-mode locking, the ROF of the OIL TLD was enhanced to 21 GHz, and this is shown by the black curve in Fig. 7.21. The same investigation has been carried out for frequency detuning of Δf = 80 GHz and 82 GHz. As is directly observed from the stability map, the required injected power ratio is increased for 80 GHz detuning frequency, but it than drops for 82 GHz detuning. On the other hand, the drop in the carrier density is decreasing with higher detuning frequencies, as in the previous cases. For 80 GHz detuning frequency, stable locking is achieved with the power injection ratio of 2.25, and the carrier density of TLD drops to 0.968×10^{18} cm^{-3}. On the other hand, the power injection ratio decreased to 2.2 when the detuning frequency changes only slightly to 82 GHz. The carrier density of the OIL TLD becomes 0.97×10^{18} cm^{-3}. The ROF of OIL TLD enhances for both cases due to the increase in detuning frequency and the side-mode cavity resonance shift, but the amount of the shift drops with higher detuning frequencies. As is seen from Fig. 7.21, the ROF of OIL TLD is 23 GHz for 80 GHz detuning frequency, and it becomes 23.6 GHz for 82 GHz detuning frequency.

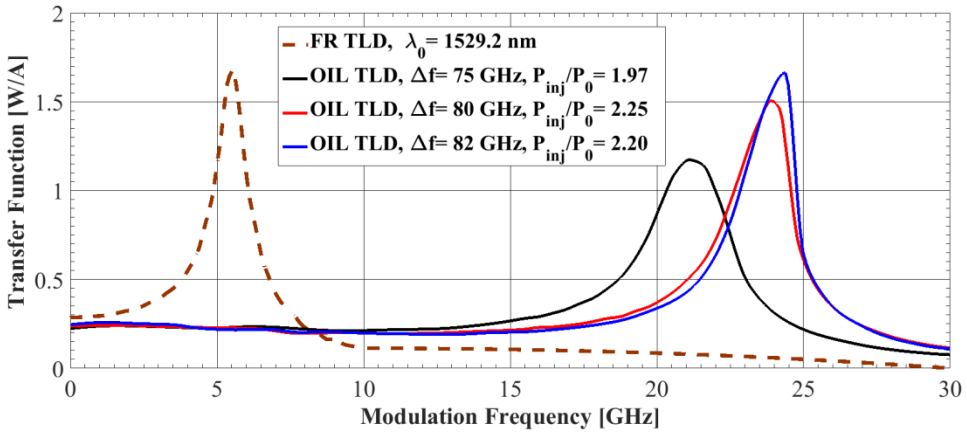

Fig. 7.21 The IM responses of FR and OIL TLD for side-mode injection for λ_0= 1529.2 nm.

Another important funding of the side-mode injection case is that the ROF is now defined by the difference between the injected (master laser) light's frequency and the cavity shifted side-mode frequency. This is rigorously confirmed by the CW spectra for all investigated cases with the side-mode injection. To the best of our knowledge this the first observation of the modulation performance enhancement of the OIL TLD under the side-mode injection and first quantitative definition of the ROF increase due to the cavity shifted side-mode which generalises the results of [17] for the main mode injection to the case of the side-mode injection.

In addition, we also found that there is a limitation on the ROF and bandwidth enhancement in OIL lasers when the detuning frequency increases and reaches the point located approximately between the half inter-mode distance between the main and the first side-mode. In this case, a sharp decrease in carrier density was observed and the OIL TLD ceased to respond to a small signal modulation. The shifted cavity resonance frequency was not visible on the CW optical spectra. Most likely physical reason of such behaviour is a large decrease of the gain at the cavity shifted side-mode frequency because the observed drop in the carrier density was too large in this case. As a result of a small gain, the shifted side-mode, which we believe physically correspond to the ASE process, is not visible in the CW spectra.

To test further the behaviour of modulation dynamics in OIL TLD under the side-mode optical injection, we have further increased the detuning frequency to be higher than the first side mode of the FR TLD. The ROF and bandwidth enhancement behaviour has been restored again. In this case, the shifted side-mode was providing the necessary cavity resonance condition for the ROF and bandwidth enhancement.

7.5 Large Signal Analysis of OIL TLD

Up to this stage we have completed a detailed small-signal analysis of the ROF enhancement of TLD subject to optical injection locking. We have showed that there could be a substantial amount of ROF bandwidth enhancement achieved for different tuning regimes. As a result of bandwidth enhancement, we expected to obtain a better large signal operation with OIL than in the FR TLD. In order to test such possibility we investigate the large-signal performance of the OIL TLD for higher (in comparison with achievable in the FR TLD) modulation bit rates to confirm the enhancement in modulation bandwidth. In addition to this, we also demonstrate a substantial improved of the chirping performance of the OIL TLD. Preliminary results of this Chapter were reported in [206].

It was previously shown by Chang et al. [202], experimentally as well as theoretically, that OIL reduces substantially the transient and the adiabatic chirping of VCSEL. We have investigated the chirp reduction of TLD with OIL and we observed a dramatic reduction in TLD's chirping.

The simulation setup which was created to carry out large signal analysis with injection locking is demonstrated in Fig. 7.21. The chirping analysis was carried out in the VPI by using the component TimeResolved_Freq_Power which allows calculating the instantaneous change in the

frequency and power of the output optical signals. The pulse shape and the eye diagram of the generated signal was analysed by adding a receiver photodiode.

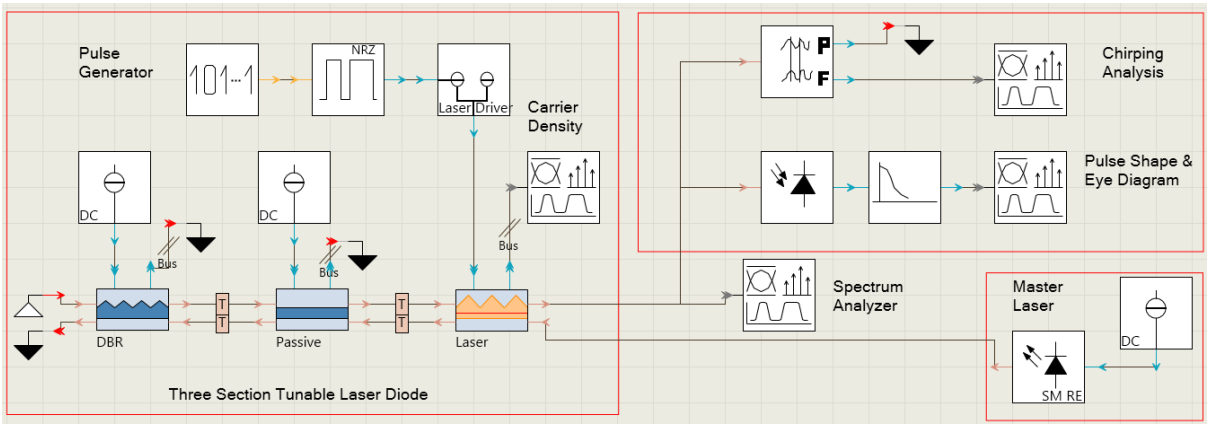

Fig. 7.22 VPI setup for large signal analysis of the OIL TLD.

In order to study the effect of bandwidth enhancement of OIL TLD, we monitored the response of TLD to high speed direct modulation. The FR TLD was firstly tuned to 1529.2 nm to obtain the highest differential gain. Then TLD was stable locked to the master laser with 2.5 GHz detuning frequency and 1.97 power injection ratio. The FR TLD had ROF of 5.5 GHz which was enhanced to 21.4 GHz as a result of stable optical injection locking.

The FR TLD shows a limited modulation bandwidth compare to the OIL TLD and it has no reliable response to bit rates higher than 5 Gbps. In Fig. 7.23, the optical spectra of directly modulated FR and OIL TLD are shown for the bit rate of 10 Gbps using pseudo-random bit sequence (PRBS) as a a modulating signal. It is clearly demonstrated that the FR TLD spectrum has large amount spread and the main mode is almost not visible. On the other hand, the spectrum of OIL TLD has good spectral purity and the main mode is clearly visible.

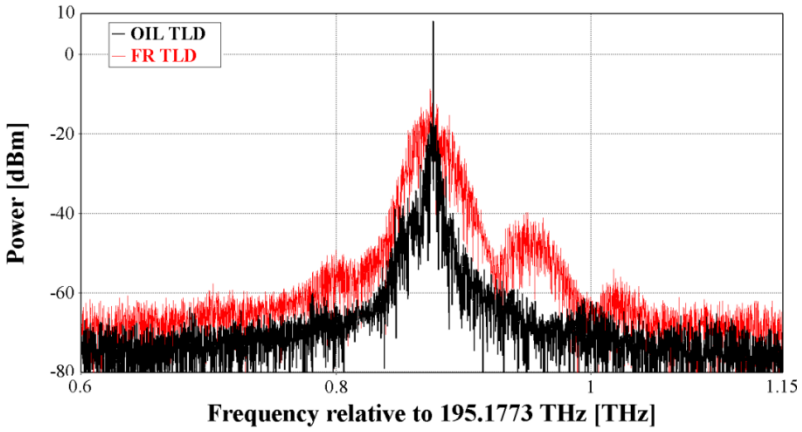

Fig. 7.23 Dynamic optical spectra of directly modulated FR and OIL TLD.

The direct modulation response of OIL TLD was plotted for 10- and 20-Gbps modulation bit rates in Fig. 7.24. For both cases, the TLD was DC-biased above threshold at I_{dc}=9.5 mA, with the threshold current I_{th}= 7.5 mA. The zero-bit modulation current was I_0= 9.5 mA, and the one-bit modulation current was I_1= 19 mA. The output time-dependent power and the eye diagram of the output signal of TLD was obtained by using a PIN photodiode because it was necessary to convert the output signal of TLD from optical to electrical to produce the eye diagram. The responsivity of photodiode was assigned as 1 and all other noise parameters were ignored to remove the irrelevant effects of the receiving photodiode.

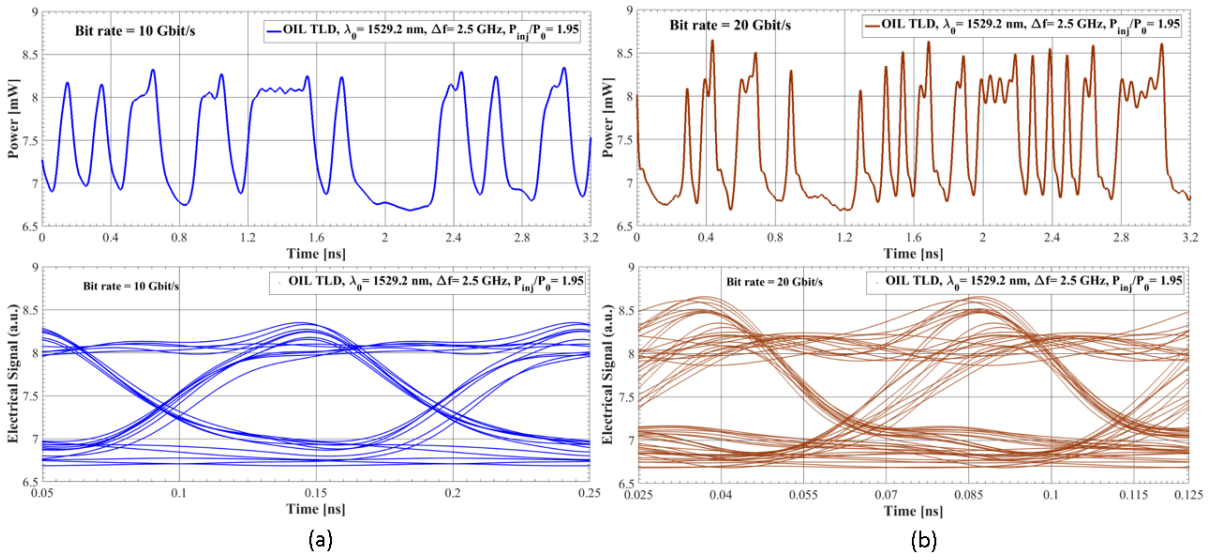

Fig. 7.24 Output power and eye diagram of IM OIL TLD for bit rates (a) 10 Gbps (b) 20 Gbps.

In Fig. 7.24 (a), the power output of the directly modulated TLD with 10 Gbps bit rate has a good pulse shape which reproduces well the PRBS signal in order to achieve a reliable transmission. The zero-bits and the one-bits are staying at almost the same constant levels, respectively, and the perturbations are not essential in terms of the effect on the eye opening. On the other hand, if the bit rate is increased to 20 Gbps, Fig. 7.24 (b), which is closer to the ROF, the zero-bit and the one-bit levels become unstable, and the perturbations of power output are visible in eye diagram, which is still acceptable. These results clearly demonstrate that it is possible to obtain high modulation speed TLD operation by providing stable optical injection locking.

Another important effect of the OIL on the TLD performance is the increased stability of lasing frequency and reduced frequency chirping. To perform a qualitative frequency chirping decrease demonstration in the VPI, it is necessary to analyse the output signal of TLD with TimeResolved_Freq_Power component. This component is calculating the instantaneous change in frequency and power of the optical signals. By modifying its parameters, it is possible to change the frequency scale and to shift the offset level.

In Fig. 7.25, the frequency chirping performance of the FR and OIL TLD is demonstrated under large signal modulation.

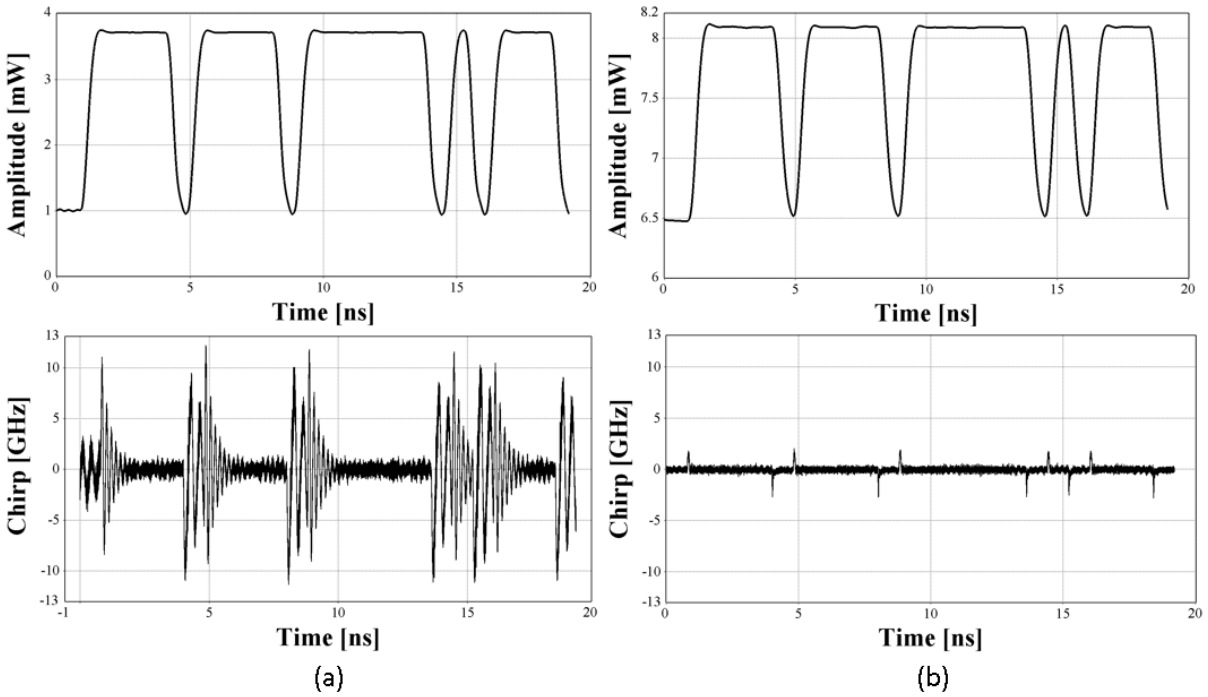

Fig. 7.25 Output power and chirping demonstration of (a) FR TLD (b) OIL TLD.

The emission wavelength of the FR TLD was selected at 1529.2 nm because of its highest differential gain characteristics. The bit rate of the drive pulses was defined as 1.25 Gbps. (This relatively low modulation bit rate was chosen because at higher speeds the FR running TLD fails to reliably respond to the PRBS). The pulse shape and chirping performance of directly modified FR TLD is shown in Fig. 7.25 (a). The peak to peak deviation in frequency was measured as 20 GHz and this is mainly the result of the transient chirping. On the other hand, the chirping performance with OIL TLD is demonstrated in Fig. 7.25(b). By locking the TLD with 2.5 GHz detuning frequency, the transient chirping was reduced to less than 4 GHz. The obtained results on the chirping performance improvement in the OIL TLDs are quantitatively close to the results reported in [23] for VCSELs.

7.6 Conclusion

In this Chapter the OIL TLD was first investigated for different tuning regimes and the ROF and bandwidth enhancement was demonstrated for a given detuning frequency. To find the minimum required power injection ratio, a stabile locking boundary maps were plotted for each tuning regime Lasing wavelength). After providing the stable locking for each case, the shifted cavity resonance frequency and locking frequency were observed in optical spectrum in CW regime. After measuring the IM response of the OIL TLD, it was obtained that the difference between the shifted cavity resonance frequency and the locked (master laser) frequency defines the ROF of OIL TLD. The change in carrier density was highlighted by Murakami et al. [17] as one of the reason of cavity resonance frequency shift. The change in carrier density of OIL TLD was found different for each tuning regime, and the main reason for this difference is still not clear. On the other hand, the dramatic change in differential gain became dominant part of the Eq. 7.3 and the effect of the variation in carrier density was minimal.

The second analysis was carried out for high detuning frequencies to demonstrate the limits of the bandwidth enhancement. The carrier density of the OIL TLD dropped dramatically for Δf = 25 GHz, and the laser stopped responding to the small signal modulation. Additionally, the shifted cavity resonance frequency was also not visible in CW optical spectra. For detuning frequencies higher than the inter-mode distance, it was observed that the side-mode of the TLD contributed to the bandwidth enhancement and substantial amount of ROF and bandwidth enhancement is achieved.

The final analysis was focussed on the large signal modulation response of OIL TLD. As a result of the bandwidth enhancement, the OIL TLD had better response to direct modulation for higher bit rates. The FR TLD had poor response to modulation bit rates above 1.25 GHz and had no response at modulation bit rate of 5 Gbps. The OIL TLD operation under large signal

modulation was extended to considerably higher bit rates. Finally, the frequency chirping of the directly modulated TLD was drastically reduced by OIL. The transient chirping which is the dominant part of frequency deviation was suppressed to 4 GHz from 20 GHz. The obtained in this Chapter results are of great practical importance for utilisation of TLDs as high-speed transmitters for optical-fibre communication applications.

CHAPTER 8

CONCLUSIONS AND FUTURE WORKS

8.1 Conclusions

In this study we have investigated dynamic operation of TLDs, focusing on the modulation response of the device with and without external light injection into the TLD. The conclusions of this thesis are discussed separately for each chapter in the following paragraphs.

The first four Chapters 1–4 of the thesis are devoted to general introduction into the subject of the undertaken research, review of the related published works, and in depth discussion of underlying theoretical basics of physics of semiconductor laser materials and devices, their operation at various external conditions, including CW operation, direct modulation response, and external optical injection locking, and in detail description of the used computational software tools and the models. These chapters provide necessary support for better understanding the original problems and their solutions which are presented in Chapter 5–7.

In Chapter 5, we examine the dynamic modulation response of a three-section bulk-based TLDs and present the developed integrated computational simulation model. In order to achieve an adequate and accurate description of multi-section composite cavity TLD, the laser simulation was carried out using the travelling wave approach which is implemented in VPI using the transmission link laser model (TLLM). Our integrated model includes two advanced physics-based simulation tools - the VPI and PICS3D. We first used PICS3D to calculate the gain spectra and the change in the refractive index of the DBR section of TLD by taking different FC contributions into account. The obtained results were used to modify the VPI setup accordingly.

We analysed the effect of gain spectra shape on the dynamic response of TLD and we observed that it directly affects qualitatively and quantitatively the simulation outputs over a wide tuning range. The parabolic gain shape model which is offered within the VPI has a good performance in case of a fixed frequency laser modelling. On the other hand, we have noticed that it has a very low reliability in case of modelling the dynamic modulation response of TLDs. We

observed that the parabolic gain spectrum exhibited very limited accuracy of modelling the small signal response of TLD under wide blue wavelength tuning. The parabolic gain shape did not follow the real material gain spectrum and this resulted in an extensive difference in the simulation accuracy. For this reasons we carried out the analysis of the small-signal response of TLD using the physics-based realistic gain spectrum which was calculated in PICS3D and imported into the VPI using special interface. As a by-product of such approach, we have also developed a modified model which allows to use the VPI's parabolic gain shape spectra which are fitted to the realistic gain spectra using special fitting procedure, and proved that such model gives reliable results.

The simulation results showed that the ROF of TLD is a strong function of wavelength tuning – it is increasing approximately 3-4 times with the wavelength tuning. Physically this behaviour was explained due to the dramatic change in the differential gain coefficient with tuning. We believe that this finding is very important for real TLD applications in WDM systems.

In Chapter 6, we investigated the small-signal modulation response of the OIL TLD under different tuning regimes. The analysis was carried out in the traveling wave-based model which is defined in Chapter 5. Since we previously observed that the realistic gain spectrum (which is produced using PICS3D) improves the accuracy of the results, all simulations in the thesis are based on the use of these spectra which were imported into the VPI to model the laser.

Firstly, a stable locking boundary maps of OIL TLD were produced, and different nonlinear dynamic regimes were identified for different injection parameters (frequency detuning and injection power ratio). The change in the carrier density and optical spectra for corresponding regimes were also demonstrated. We showed that the stably locked TLD in CW operation had improved spectral purity and the carrier density oscillations became less pronounced than in a

FR TLD. Reduced oscillations were good indicator of improved small and large signal responses of the OIL TLD in comparison with the FR TLD.

The IM response of the OIL TLD was investigated for different tuning regimes. For each regime, the detuning frequency of the injected light was kept constant (2.5 GHz) and dynamic modulation response of OIL TLD was obtained. It should be mentioned here that the injected power for each case was different because the minimum necessary power injection ratio also changes with tuning. As a result of tuning, the injected power ratio for each tuning regime was found to be different. The IM response of the OIL TLD for fixed detuning frequency showed that a substantial enhancement of ROF and modulation bandwidth can be achieved by OIL and wavelength tuning. In particular, higher levels of the ROF and bandwidth enhancement of OIL TLD were obtained due to a notable increase in differential gain obtained by wavelength tuning.

Finally, the effects of injection locking parameters, the power injection ratio and the detuning frequency on the ROF and modulation bandwidth enhancement were investigated for a fixed emission wavelength. To do this, we kept the detuning frequency of the injected light constant and monitored the small signal modulation response of OIL TLD for different power injection ratios. Our results show that high levels of the injected power ratio enhance the ROF and modulation bandwidth, while on the other hand, the magnitude of the transfer function of the modulation response was decreasing. Keeping the injected power fixed, we analysed the effect of the frequency detuning on bandwidth enhancement. We found that higher bandwidth enhancement with better transfer function response could be obtained under positive detuning.

In Chapter 7, a detailed analysis of OIL TLD was carried out for high detuning frequencies and the improvement of the large signal modulation response was demonstrated. The stable locking boundary map which was presented in Chapter 6 was extended for two more lasing wavelengths. It was shown that the stable locking map exhibits different characteristics for each tuning regime.

The IM response enhancement of OIL TLD was measured for different lasing wavelengths for fixed detuning frequencies. The required power injection ratio for each tuning regime was obtained from the stable locking boundary maps. The ROF of OIL TLD was measured higher with wavelength tuning due to the sharp increase in differential gain, as was explained in Chapter 6. It was shown using the emission spectra under the CW regime that the enhancement in bandwidth is related to the difference between the locked frequency and the shifted cavity resonance frequency. This result is in agreement with the model proposed by Murakami et al. [17]. The cavity resonance shift occurs as a result of the change in refractive index which is inversely proportional to the carrier density. Hence, the change in the carrier density due to additional stimulated emission generated by the injected light is an important parameter which should be used to explain the ROF and modulation bandwidth enhancement. We have observed that the change in the carrier density of OIL TLD changes for different tuning regime. The physical reason of this feature is still unclear for us, and it may be the topic of the future work.

The ROF and modulation bandwidth enhancement investigation was next shifted to high detuning frequencies to investigate the possible limits of the achievable modulation speed. It was found that the carrier density of the OIL TLD drops sharply and the laser stopped responding to the current modulation at around half of the side-mode distance from the main mode (25 GHz). The maximum ROF of OIL TLD was found to be around 23 GHz for 1529.2 nm lasing wavelength. This could be increased to 26 GHz with higher injected power.

We found out that the bandwidth enhancement could be obtained if the detuning frequency was increased more than side mode distance (the side-mode injection regime). We tested this case for two different lasing wavelength and we found that the side-mode of the FR TLD was shifting and the difference between the injected light's frequency and the shifted side mode was exactly equal to the ROF.

The last investigated problem was focussed on the large signal modulation response and the frequency chirping improvement of the OIL TLD. The FR laser was not able to respond the modulation response higher than 5 Gbps. The OIL TLD was directly modulated with 10 Gbps and 20 Gbps rates, and considerable improvement of modulation output characteristics was clearly observed in terms of the output pulse shapes and the eye opening diagram. Additionally, we compared the frequency chirping performance of the FR and OIL TLD. In both cases the TLD was driven above threshold. We have seen the transient chirp (which is directly affects the fibre transmission performance due to fibre cable's dispersive characteristics) has been reduced from 20 GHz to less than 4 GHz.

8.2 Future Work

The following future original research problems and directions can be recommended as a continuation and extension of the work undertaken in this thesis:

1. The dynamic modulation response of FR TLD can be investigated with MQW active region structure. It is known, that modulation dynamic properties of FR laser diodes with bulk and MQW regions are very different, thus it is interesting to see how these lasers will comparatively perform under the OIL conditions.
2. Investigation of the effect of the DBR mirror reflectivity spectra on stable locking conditions is also interesting problem since it is still unclear how the laser finds the stable locking condition. The sharpness of the reflectivity spectrum can easily affect the locking conditions for different detuning parameters.
3. The dramatic change in the carrier density under external optical injection for detuning frequencies around the half of the distance between the main mode and the side-mode is a strong limiting factor of the modulation bandwidth enhancement. To the best of our knowledge there is no clear explanation of this result. Due to practical importance of

evaluating the maximum achievable modulation enhancement and identification of all factors which define such enhancement, detail investigation of the OIL TLDs and the above detuning levels is an interesting and important problem.

4. We demonstrated in Chapter 7 that the large signal response of the TLD was improved as a result of enhanced modulation bandwidth. The investigation was completed for the bias currents higher than the threshold. A further investigation can be carried out by considering different injection locking and tuning conditions. Additionally, different types of bit coding formats (such as NRZ and RZ) can be tested with OIL TLD.
5. We have shown that the dramatic decrease in frequency chirping was achieved with the OIL. This analysis can be extended to different tuning regimes and injection locking conditions. In addition to this, the performance of OIL TLD in an optical fibre links can be investigated and optimum conditions for high and reliable transmission can be defined.

The problems formulated above are of interest from both pure physical and applied points of view and their solutions can be important for future theoretical and experimental research on enhanced modulation dynamic performance of TLDs in various optical fibre applications.

REFERENCES

[1] G. P. Agrawal, *Fiber-Optic Communication Systems*: Wiley, 2012.

[2] B. A. Graham, "Improvement in telegraphy," ed: Google Patents, 1876.

[3] T. H. Maiman, "Stimulated Optical Radiation in Ruby," *Nature,* vol. 187, pp. 493-494, 08/06/print 1960.

[4] K. C. Kao and G. A. Hockham, "Dielectric-fibre surface waveguides for optical frequencies," *Electrical Engineers, Proceedings of the Institution of,* vol. 113, pp. 1151-1158, 1966.

[5] F. P. Kapron, D. B. Keck, and R. D. Maurer, "RADIATION LOSSES IN GLASS OPTICAL WAVEGUIDES," *Applied Physics Letters,* vol. 17, pp. 423-425, 1970.

[6] T. Miya, Y. Terunuma, T. Hosaka, and T. Miyashita, "Ultimate low-loss single-mode fibre at 1.55 μm," *Electronics Letters,* vol. 15, pp. 106-108, 1979.

[7] R. Ramaswami, K. Sivarajan, and G. Sasaki, *Optical networks: a practical perspective*: Morgan Kaufmann, 2009.

[8] R. J. Sanferrare, "Terrestrial lightwave systems," *AT&T Technical Journal,* vol. 66, pp. 95-107, 1987.

[9] D. Gloge, A. Albanese, C. A. Burrus, E. L. Chinnock, J. A. Copeland, A. G. Dentai, *et al.*, "High-speed digital lightwave communication using LEDs and PIN photodiodes at 1.3 um," *The Bell System Technical Journal,* vol. 59, pp. 1365-1382, 1980.

[10] N. S. Bergano, J. Aspell, C. R. Davidson, P. R. Trischitta, B. M. Nyman, and F. W. Kerfoot, "Bit error rate measurements of 14000 km 5 Gbit/s fibre-amplifier transmission system using circulating loop," *Electronics Letters,* vol. 27, pp. 1889-1890, 1991.

[11] T. Otani, K. Goto, H. Abe, M. Tanaka, H. Yamamoto, and H. Wakabayashi, "5.3 Gbit/s 11300 km data transmission using actual submarine cables and repeaters," *Electronics Letters,* vol. 31, pp. 380-381, 1995.

[12] I. Hayashi, M. B. Panish, P. W. Foy, and S. Sumski, "JUNCTION LASERS WHICH OPERATE CONTINUOUSLY AT ROOM TEMPERATURE," *Applied Physics Letters,* vol. 17, pp. 109-111, 1970.

[13] P. S. Zory, *Quantum well lasers*: Academic Press, 1993.

[14] R. Lang and K. Kobayashi, "Suppression of the relaxation oscillation in the modulated output of semiconductor lasers," *IEEE Journal of Quantum Electronics,* vol. 12, pp. 194-199, 1976.

[15] R. Lang, "Injection locking properties of a semiconductor laser," *IEEE Journal of Quantum Electronics,* vol. 18, pp. 976-983, 1982.

[16] J. Ohtsubo, *Semiconductor lasers: stability, instability and chaos* vol. 111: Springer, 2012.

[17] A. Murakami, K. Kawashima, and K. Atsuki, "Cavity resonance shift and bandwidth enhancement in semiconductor lasers with strong light injection," *IEEE Journal of Quantum Electronics,* vol. 39, pp. 1196-1204, 2003.

[18] C. Lin, J. K. Andersen, and F. Mengel, "Frequency chirp reduction in a 2.2 Gbit/s directly modulated InGaAsP semiconductor laser by CW injection," *Electronics Letters,* vol. 21, pp. 80-81, 1985.

[19] L. Chrostowski, C. H. Chang, and C. Chang-Hasnain, "Reduction of relative intensity noise and improvement of spur-free dynamic range of an injection locked VCSEL," in *Lasers and Electro-Optics Society, 2003. LEOS 2003. The 16th Annual Meeting of the IEEE*, 2003, pp. 706-707 vol.2.

[20] V. Annovazzi-Lodi, A. Scire, M. Sorel, and S. Donati, "Dynamic behavior and locking of a semiconductor laser subjected to external injection," *IEEE Journal of Quantum Electronics,* vol. 34, pp. 2350-2357, 1998.

[21] D. Labukhin, C. A. Stolz, N. Zakhleniuk, R. Loudon, and M. J. Adams, "Nonlinear spatio-temporal dynamics of optically-injected three-section tunable DBR lasers," in *Lasers and Electro-Optics (CLEO) and Quantum Electronics and Laser Science Conference (QELS), 2010 Conference on*, 2010, pp. 1-2.

[22] S. Kobayashi and T. Kimura, "Coherence of injection phase-locked AlGaAs semiconductor laser," *Electronics Letters,* vol. 16, pp. 668-670, 1980.

[23] C. J. Chang-Hasnain and X. Zhao, "6 - Ultrahigh-speed laser modulation by injection locking," in *Optical Fiber Telecommunications V A (Fifth Edition)*, ed Burlington: Academic Press, 2008, pp. 145-182.

[24] C. A. Stolz, D. Labukhin, N. Zakhleniuk, and M. J. Adams, "Locking bandwidth of optically injected Fabry-Perot semiconductor lasers for high injection strengths," *IET Optoelectronics,* vol. 2, pp. 223-230, 2008.

[25] R. Gordon, "Fabry-Perot semiconductor laser injection locking," *IEEE Journal of Quantum Electronics,* vol. 42, pp. 353-356, 2006.

[26] F. Mogensen, H. Olesen, and G. Jacobsen, "Locking conditions and stability properties for a semiconductor laser with external light injection," *IEEE Journal of Quantum Electronics,* vol. 21, pp. 784-793, 1985.

[27] (2015). *VPIcomponentMaker Photonic Circuits*.

[28] C. Software, "PICS3D," ed. Burnaby, BC, Canada, 2010.

[29] A. J. Lowery, "New dynamic semiconductor laser model based on the transmission-line modelling method," *IEE Proceedings J - Optoelectronics,* vol. 134, pp. 281-289, 1987.

[30] A. Einstein, "Zur Quantentheorie der Strahlung " *Physika Zeitschrift,* vol. 18, p. 7, 1917.

[31] J. P. Gordon, H. J. Zeiger, and C. H. Townes, "Molecular Microwave Oscillator and New Hyperfine Structure in the Microwave Spectrum of NH3," *Physical Review,* vol. 95, pp. 282-284, 1954.

[32] J. P. Gordon, H. J. Zeiger, and C. H. Townes, "The maser—new type of microwave amplifier, frequency standard, and spectrometer," *Physical Review,* vol. 99, pp. 1264-1274, 08/15/ 1955.

[33] A. L. Schawlow and C. H. Townes, "Infrared and Optical Masers," *Physical Review,* vol. 112, pp. 1940-1949, 12/15/ 1958.

[34] A. Javan, W. R. Bennett, and D. R. Herriott, "Population Inversion and Continuous Optical Maser Oscillation in a Gas Discharge Containing a He-Ne Mixture," *Physical Review Letters,* vol. 6, pp. 106-110, 02/01/ 1961.

[35] R. N. Hall, G. E. Fenner, J. D. Kingsley, T. J. Soltys, and R. O. Carlson, "Coherent Light Emission From GaAs Junctions," *Physical Review Letters,* vol. 9, pp. 366-368, 11/01/ 1962.

[36] M. I. Nathan, W. P. Dumke, G. Burns, F. H. Dill, and G. Lasher, "STIMULATED EMISSION OF RADIATION FROM GaAs p-n JUNCTIONS," *Applied Physics Letters*, vol. 1, pp. 62-64, 1962.

[37] N. Holonyak and S. F. Bevacqua, "COHERENT (VISIBLE) LIGHT EMISSION FROM Ga(As1−xPx) JUNCTIONS," *Applied Physics Letters,* vol. 1, pp. 82-83, 1962.

[38] R. H. R. T. M. Quist, R. J. Keyes, W. E. Krag, B. Lax, "SEMICONDUCTOR MASER OF GaAs," *Applied Physics Letters,* vol. 1, 1962.

[39] H. Kroemer, "A proposed class of hetero-junction injection lasers," *Proceedings of the IEEE,* vol. 51, pp. 1782-1783, 1963.

[40] Y. Suematsu and S. Arai, "Single-mode semiconductor lasers for long-wavelength optical fiber communications and dynamics of semiconductor lasers," *IEEE Journal of Selected Topics in Quantum Electronics,* vol. 6, pp. 1436-1449, 2000.

[41] Z. I. Alferov, V. Andreev, D. Garbuzov, Y. V. Zhilyaev, E. Morozov, E. Portnoi, *et al.*, "Investigation of the influence of the AlAs-GaAs heterostructure parameters on the laser

threshold current and the realization of continuous emission at room temperature," *Sov. Phys. Semicond,* vol. 4, pp. 1573-1575, 1971.

[42] D. B. Keck, R. D. Maurer, and P. C. Schultz, "On the ultimate lower limit of attenuation in glass optical waveguides," *Applied Physics Letters,* vol. 22, pp. 307-309, 1973.

[43] M. Horiguchi and H. Osanai, "Spectral losses of low-OH-content optical fibres," *Electronics Letters,* vol. 12, pp. 310-312, 1976.

[44] T. Ikegami and Y. Suematsu, "Resonance-like characteristics of the direct modulation of a junction laser," *Proceedings of the IEEE,* vol. 55, pp. 122-123, 1967.

[45] Y. Suematsu, "Long-wavelength optical fiber communication," *Proceedings of the IEEE,* vol. 71, pp. 692-721, 1983.

[46] Y. Suematsu and M. Yamada, "Transverse mode control in semiconductor lasers," *IEEE Journal of Quantum Electronics,* vol. 9, pp. 305-311, 1973.

[47] M. A. Shigehisa Arai, Yasuharu Suematsu and Yoshio Itaya, "Room Temperature CW Operation of GaInAsP/InP DH Laser Emitting at 1.51 μm," *Japanese Journal of Applied Physics,* vol. 18, pp. 2333-2334, 1979.

[48] H. Kawaguchi, K. Takahei, Y. Toyoshima, H. Nagai, and G. Iwane, "Room-temperature c.w. operation of InP/InGaAsP/InP double heterostructure diode lasers emitting at 1.55 microns," *Electronics Letters,* vol. 15, pp. 669-670, 1979.

[49] I. P. Kaminow, R. E. Nahory, M. A. Pollack, L. W. Stulz, and J. C. Dewinter, "Single-mode c.w. ridge-waveguide laser emitting at 1.55 μm," *Electronics Letters,* vol. 15, pp. 763-765, 1979.

[50] H. Kogelnik and C. V. Shank, "Coupled-Wave Theory of Distributed Feedback Lasers," *Journal of Applied Physics,* vol. 43, pp. 2327-2335, 1972.

[51] K. Utaka, S. Akiba, K. Sakai, and Y. Matsushima, "ROOM-TEMPERATURE cw OPERATION OF DISTRIBUTED-FEEDBACK BURIED-HETEROSTRUCTURE InGaAsP/InP LASERS EMITTING AT 1. 57 mu m.," *Electronics Letters,* vol. 17, pp. 961-963, 1981.

[52] K. Sekartedjo, N. Eda, K. Furuya, Y. Suematsu, F. Koyama, and T. Tanbun-Ek, "1.5 μm phase-shifted DFB lasers for single-mode operation," *Electronics Letters,* vol. 20, pp. 80-81, 1984.

[53] F. Koyama, Y. Suematsu, K. Kojima, and K. Furuya, "1.5 μm phase adjusted active distributed reflector laser for complete dynamic single-mode operation," *Electronics Letters,* vol. 20, pp. 391-393, 1984.

[54] G. P. Agrawal, J. E. Geusic, and P. J. Anthony, "Distributed feedback lasers with multiple phase-shift regions," *Applied Physics Letters,* vol. 53, pp. 178-179, 1988.

[55] M. Okai, T. Tsuchiya, K. Uomi, N. Chinone, and T. Harada, "Corrugation-pitch modulated MQW-DFB lasers with narrow spectral linewidth," *IEEE Journal of Quantum Electronics,* vol. 27, pp. 1767-1772, 1991.

[56] M. Okai, M. Suzuki, and T. Taniwatari, "Strained multiquantum-well corrugation-pitch-modulated distributed feedback laser with ultranarrow (3.6 kHz) spectral linewidth," *Electronics Letters,* vol. 29, pp. 1696-1697, 1993.

[57] M. Theurer, H. Zhang, Y. Wang, W. Chen, L. Zeng, U. Troppenz, *et al.*, "2 x 56 GB/s from a Double Side Electroabsorption Modulated DFB Laser and Application in Novel Optical PAM4 Generation," *Journal of Lightwave Technology,* vol. PP, pp. 1-1, 2016.

[58] J. Hauck, M. Schrammen, S. Romero-Garcia, J. Mueller, B. Shen, J. Richter, *et al.*, "Stabilization and frequency control of a DFB laser with a tunable optical reflector integrated in a Silicon Photonics PIC," *Journal of Lightwave Technology,* vol. PP, pp. 1-1, 2016.

[59] S. Dhoore, L. Li, A. Abbasi, G. Roelkens, and G. Morthier, "Demonstration of a Discretely Tunable III-V-on-Silicon Sampled Grating DFB Laser," *IEEE Photonics Technology Letters,* vol. 28, pp. 2343-2346, 2016.

[60] Q. Deng, J. Xu, L. Guo, S. Liang, L. Hou, and H. Zhu, "A Dual-Grating InGaAsP/InP DFB Laser Integrated With an SOA for THz Generation," *IEEE Photonics Technology Letters,* vol. 28, pp. 2307-2310, 2016.

[61] S. H. Bae, H. Kim, and Y. C. Chung, "Transmission of 51.56-Gb/s OOK signal over 15 km of SSMF using directly-modulated 1.5 μm DFB laser," in *2016 Optical Fiber Communications Conference and Exhibition (OFC)*, 2016, pp. 1-3.

[62] G. Morthier, A. Abbasi, M. Shahin, J. Verbist, X. Yin, J. Bauwelinck, *et al.*, "High speed modulation of InP membrane DFB laser diodes," in *2016 18th International Conference on Transparent Optical Networks (ICTON)*, 2016, pp. 1-4.

[63] G. Roelkens, L. Liu, D. Liang, R. Jones, A. Fang, B. Koch, *et al.*, "III-V/silicon photonics for on-chip and intra-chip optical interconnects," *Laser & Photonics Reviews,* vol. 4, pp. 751-779, 2010.

[64] P. Bardella and I. Montrosset, "A New Design Procedure for DBR Lasers Exploiting the Photon-Photon Resonance to Achieve Extended Modulation Bandwidth," *IEEE Journal of Selected Topics in Quantum Electronics,* vol. 19, pp. 1502408-1502408, 2013.

[65] M. Radziunas, A. Glitzky, U. Bandelow, M. Wolfrum, U. Troppenz, J. Kreissl, *et al.*, "Improving the Modulation Bandwidth in Semiconductor Lasers by Passive Feedback," *IEEE Journal of Selected Topics in Quantum Electronics,* vol. 13, pp. 136-142, 2007.

[66] M. Dumitrescu, A. Laakso, J. Viheriala, T. Uusitalo, M. Kamp, and P. Uusimaa, "Distributed feedback lasers with photon-photon-resonance-enhanced modulation bandwidth," in *CAS 2012 (International Semiconductor Conference)*, 2012, pp. 123-126.

[67] K.-i. I. Haruhisa Soda, Chiyuki Kitahara and Yasuharu Suematsu, "GaInAsP/InP Surface Emitting Injection Lasers," *Japanese Journal of Applied Physics,* vol. 18, pp. 2329-2330, 1979.

[68] Y. Suematsu and K. Iga, "Semiconductor Lasers in Photonics," *Journal of Lightwave Technology,* vol. 26, pp. 1132-1144, 2008.

[69] K. Iga, S. Kinoshita, and F. Koyama. (1987, Microcavity GalaAs/GaAs surface-emitting laser with Ith= 6 mA. *Electronics Letters 23(3),* 134-136. Available: http://digital-library.theiet.org/content/journals/10.1049/el_19870095

[70] F. Koyama, S. Kinoshita, and K. Iga, "Room-temperature continuous wave lasing characteristics of a GaAs vertical cavity surface-emitting laser," *Applied Physics Letters,* vol. 55, pp. 221-222, 1989.

[71] Y. H. Lee, J. L. Jewell, A. Scherer, S. L. McCall, J. P. Harbison, and L. T. Florez, "Room-temperature continuous-wave vertical-cavity single-quantum-well microlaser diodes," *Electronics Letters,* vol. 25, pp. 1377-1378, 1989.

[72] R. S. Geels and L. A. Coldren, "Submilliamp threshold vertical-cavity laser diodes," *Applied Physics Letters,* vol. 57, pp. 1605-1607, 1990.

[73] N. Nishiyama, C. Caneau, A. Kobyakov, J. D. Downie, M. Sauer, and C. Zah, "1.3 and 1.55 μm InP-based VCSELs for digital and radio signal transmission," in *Optical Fiber Communication and the National Fiber Optic Engineers Conference, 2007. OFC/NFOEC 2007. Conference on,* 2007, pp. 1-3.

[74] K. Iga, "Surface-emitting laser-its birth and generation of new optoelectronics field," *IEEE Journal of Selected Topics in Quantum Electronics,* vol. 6, pp. 1201-1215, 2000.

[75] J. P. van der Ziel, R. Dingle, R. C. Miller, W. Wiegmann, and W. A. Nordland, "Laser oscillation from quantum states in very thin GaAs−Al0.2Ga0.8As multilayer structures," *Applied Physics Letters,* vol. 26, pp. 463-465, 1975.

[76] R. Dupuis, P. Dapkus, R. Chin, N. Holonyak Jr, and S. Kirchoefer, "Continuous 300° K laser operation of single-quantum-well AlxGa1− xAs-GaAs heterostructure diodes grown

by metalorganic chemical vapor deposition," *Applied Physics Letters,* vol. 34, pp. 265-267, 1979.

[77] R. Dupuis, P. Dapkus, N. Holonyak Jr, and R. Kolbas, "Continuous room-temperature multiple-quantum-well AlxGa1− xAs-GaAs injection lasers grown by metalorganic chemical vapor deposition," *Applied Physics Letters,* vol. 35, pp. 487-489, 1979.

[78] E. A. Rezek, N. Holonyak, B. A. Vojak, G. E. Stillman, J. A. Rossi, D. L. Keune, *et al.*, "LPE In1−xGaxP1−zAsz (x∼0.12, z∼0.26) DH laser with multiple thin-layer (<500 Å) active region," *Applied Physics Letters,* vol. 31, pp. 288-290, 1977.

[79] Y. Suematsu, "Dynamic Single-Mode Lasers," *Journal of Lightwave Technology,* vol. 32, pp. 1144-1158, 2014.

[80] Y. Arakawa and H. Sakaki, "Multidimensional quantum well laser and temperature dependence of its threshold current," *Applied Physics Letters,* vol. 40, pp. 939-941, 1982.

[81] Y. Abe, K. Kishino, Y. Suematsu, and S. Arai, "GaInAsP/InP integrated laser with butt-jointed built-in distributed-Bragg-reflection waveguide," *Electronics Letters,* vol. 17, pp. 945-947, 1981.

[82] K. Utaka, K. Kobayashi, K. Kishino, and Y. Suematsu, "1.5-1.6 μm GaInAsP/InP Integrated twin-guide lasers with first-order distributed Bragg reflectors," *Electronics Letters,* vol. 16, pp. 455-456, 1980.

[83] Y. Tohmori, Y. Suematsu, H. Tsushima, and S. Arai, "Wavelength tuning of GaInAsP/InP integrated laser with butt-jointed built-in distributed Bragg reflector," *Electronics Letters,* vol. 19, pp. 656-657, 1983.

[84] Y. Tohmori, H. Oohashi, T. Kato, S. Arai, K. Komori, and Y. Suematsu, "Wavelength stabilisation of 1.5 μm GaInAsP/InP bundle-integrated-guide distributed-Bragg-reflector (BIG-DBR) lasers integrated with wavelength tuning region," *Electronics Letters,* vol. 22, pp. 138-140, 1986.

[85] L. Coldren, K. Furuya, B. Miller, and J. Rentschler, "Etched mirror and groove-coupled GaInAsP/InP laser devices for integrated optics," *IEEE Journal of Quantum Electronics,* vol. 18, pp. 1679-1688, 1982.

[86] K. J. Ebeling, L. A. Coldren, B. I. Miller, and J. A. Rentschler, "Generation of single-longitudinal-mode subnanosecond light pulses by high-speed current modulation of monolithic two-section semiconductor lasers," *Electronics Letters,* vol. 18, pp. 901-902, 1982.

[87] L. A. Coldren, "Monolithic tunable diode lasers," *IEEE Journal of Selected Topics in Quantum Electronics,* vol. 6, pp. 988-999, 2000.

[88] S. Murata, I. Mito, and K. Kobayashi, "Over 720 Ghz (5.8nm) frequency tuning by a 1.5 μm DBR laser with phase and Bragg wavelength control regions," *Electronics Letters,* vol. 23, pp. 403-405, 1987.

[89] Y. Kotaki, M. Matsuda, H. Ishikawa, and H. Imai, "Tunable DBR laser with wide tuning range," *Electronics Letters,* vol. 24, pp. 503-505, 1988.

[90] B. Broberg and S. Nilsson, "Widely tunable active Bragg reflector integrated lasers in InGaAsP-InP," *Applied Physics Letters,* vol. 52, pp. 1285-1287, 1988.

[91] E. Desurvire, "Study of the complex atomic susceptibility of erbium-doped fiber amplifiers," *Journal of Lightwave Technology,* vol. 8, pp. 1517-1527, 1990.

[92] A. Lidgard, T. Tanbun-Ek, R. A. Logan, H. Temkin, K. W. Wecht, and N. A. Olsson, "External-cavity InGaAs/InP graded index multiquantum well laser with a 200 nm tuning range," *Applied Physics Letters,* vol. 56, pp. 816-817, 1990.

[93] V. Jayaraman, D. A. Cohen, and L. A. Coldren, "Demonstration of broadband tunability in a semiconductor laser using sampled gratings," *Applied Physics Letters,* vol. 60, pp. 2321-2323, 1992.

[94] V. Jayaraman, Z. M. Chuang, and L. A. Coldren, "Theory, design, and performance of extended tuning range semiconductor lasers with sampled gratings," *IEEE Journal of Quantum Electronics,* vol. 29, pp. 1824-1834, 1993.

[95] W. Idler, M. Schilling, D. Baums, G. Laube, K. Wunstel, and O. Hildebrand, "Y laser with 38 nm tuning range," *Electronics Letters,* vol. 27, pp. 2268-2270, 1991.

[96] V. Jayaraman, A. Mathur, L. A. Coldren, and P. D. Dapkus, "Extended tuning range in sampled grating DBR lasers," *IEEE Photonics Technology Letters,* vol. 5, pp. 489-491, 1993.

[97] Y. Tohmori, Y. Yoshikuni, T. Tamamura, M. Yamamoto, Y. Kondo, and H. Ishii, "Ultrawide wavelength tuning with single longitudinal mode by Super Structure Grating (SSG) DBR Lasers," in *Semiconductor Laser Conference , 1992. Conference Digest. 13th IEEE International*, 1992, pp. 268-269.

[98] M. O. a. K. Onaka, "Tunability of Distributed Bragg-Reflector Laser by Modulating Refractive Index in Corrugated Waveguide," *Japanese Journal of Applied Physics,* vol. 16, pp. 1501-1502, 1979.

[99] C. H. Henry, R. A. Logan, and K. A. Bertness, "Spectral dependence of the change in refractive index due to carrier injection in GaAs lasers," *Journal of Applied Physics,* vol. 52, pp. 4457-4461, 1981.

[100] B. R. Bennett, R. A. Soref, and J. A. D. Alamo, "Carrier-induced change in refractive index of InP, GaAs and InGaAsP," *IEEE Journal of Quantum Electronics,* vol. 26, pp. 113-122, 1990.

[101] J. P. Weber, "Optimization of the carrier-induced effective index change in InGaAsP waveguides-application to tunable Bragg filters," *IEEE Journal of Quantum Electronics,* vol. 30, pp. 1801-1816, 1994.

[102] J. Manning, R. Olshansky, and S. Chin, "The carrier-induced index change in AlGaAs and 1.3 µm InGaAsP diode lasers," *IEEE Journal of Quantum Electronics,* vol. 19, pp. 1525-1530, 1983.

[103] L. Dong, R. Zhang, D. Wang, S. Zhao, S. Jiang, Y. Yu, *et al.*, "Modeling Widely Tunable Sampled-Grating DBR Lasers Using Traveling-Wave Model With Digital Filter Approach," *Journal of Lightwave Technology,* vol. 27, pp. 3181-3188, 2009.

[104] L. Schneider, M. Pfeiffer, J. Piprek, A. Witzig, and B. Witzigmann, "Sampled-grating DBR lasers: calibrated 3D simulation of tuning characteristics," 2005, pp. 95-106.

[105] G. Kyritsis and N. Zakhleniuk, "Self-Consistent Simulation Model and Enhancement of Wavelength Tuning of InGaAsP/InP Multisection DBR Laser Diodes," *IEEE Journal of Selected Topics in Quantum Electronics,* vol. 19, pp. 1-11, 2013.

[106] O. D. Georgios Kyritsis, and Nick Zakhleniuk, "Power and Wavelength Tuning Performance of Multi-Quantum-Well and Bulk Tunable Laser Diodes and Main Limiting Factors," presented at the The 25th International Semiconductor Laser Conference, Kobe, 2016.

[107] E. K. Lau, W. Liang Jie, and M. C. Wu, "Enhanced Modulation Characteristics of Optical Injection-Locked Lasers: A Tutorial," *IEEE Journal of Selected Topics in Quantum Electronics,* vol. 15, pp. 618-633, 2009.

[108] R. Adler, "A Study of Locking Phenomena in Oscillators," *Proceedings of the IRE,* vol. 34, pp. 351-357, 1946.

[109] H. L. Stover and W. H. Steier, "LOCKING OF LASER OSCILLATORS BY LIGHT INJECTION," *Applied Physics Letters,* vol. 8, pp. 91-93, 1966.

[110] C. Buczek and R. Freiberg, "Hybrid injection locking of higher power CO2lasers," *IEEE Journal of Quantum Electronics,* vol. 8, pp. 641-650, 1972.

[111] S. Kobayashi and T. Kimura, "Injection locking in AlGaAs semiconductor laser," *IEEE Journal of Quantum Electronics,* vol. 17, pp. 681-689, 1981.

[112] S. Kobayashi and T. Kimura, "Optical phase modulation in an injection locked AlGaAs semiconductor laser," *IEEE Journal of Quantum Electronics,* vol. 18, pp. 1662-1669, 1982.

[113] L. Goldberg, H. F. Taylor, and J. F. Weller, "FM sideband injection locking of diode lasers," *Electronics Letters,* vol. 18, pp. 1019-1020, 1982.

[114] D. Labukhin, C. A. Stolz, N. A. Zakhleniuk, R. Loudon, and M. J. Adams, "Modified Fabry-Perot and Rate Equation Methods for the Nonlinear Dynamics of an Optically Injected Semiconductor Laser," *IEEE Journal of Quantum Electronics,* vol. 45, pp. 864-872, 2009.

[115] I. Petitbon, P. Gallion, G. Debarge, and C. Chabran, "Locking bandwidth and relaxation oscillations of an injection-locked semiconductor laser," *Electronics Letters,* vol. 22, pp. 889-890, 1986.

[116] T. B. Simpson, "Mapping the nonlinear dynamics of a distributed feedback semiconductor laser subject to external optical injection," *Optics Communications,* vol. 215, pp. 135-151, 1/1/ 2003.

[117] R. Hui, A. D. Ottavi, A. Mecozzi, and P. Spano, "Injection locking in distributed feedback semiconductor lasers," *IEEE Journal of Quantum Electronics,* vol. 27, pp. 1688-1695, 1991.

[118] H. Sheng-Kwang, L. Jia-Ming, and J. K. White, "Characteristics of period-one oscillations in semiconductor lasers subject to optical injection," *IEEE Journal of Selected Topics in Quantum Electronics,* vol. 10, pp. 974-981, 2004.

[119] C. A. Stolz, D. Labukhin, N. Zakhleniuk, R. Loudon, and M. J. Adams, "Power fluctuations of a weakly optically-injected semiconductor laser in a period-one state," *Optics Communications,* vol. 282, pp. 2074-2080, 5/15/ 2009.

[120] A. Mecozzi, A. D. Ottavi, and R. Hui, "Nearly degenerate four-wave mixing in distributed feedback semiconductor lasers operating above threshold," *IEEE Journal of Quantum Electronics,* vol. 29, pp. 1477-1487, 1993.

[121] J. M. Tang and K. A. Shore, "Analysis of nearly degenerate four-wave mixing in multisection laser diodes," *IEEE Journal of Selected Topics in Quantum Electronics,* vol. 5, pp. 866-872, 1999.

[122] E.-K. Lee, H.-S. Pang, J.-D. Park, and H. Lee, "Bistability and chaos in an injection-locked semiconductor laser," *Physical Review A,* vol. 47, pp. 736-739, 01/01/ 1993.

[123] V. Kovanis, "Instabilities and chaos in semiconductor lasers with optical injection," in *Lasers and Electro-Optics Society Annual Meeting, 1995. 8th Annual Meeting Conference Proceedings, Volume 1., IEEE*, 1995, pp. 166-167 vol.1.

[124] S. Piazzolla, P. Spano, and M. Tamburrini, "Small signal analysis of frequency chirping in injection-locked semiconductor lasers," *IEEE Journal of Quantum Electronics*, vol. 22, pp. 2219-2223, 1986.

[125] T. B. Simpson, J. M. Liu, and A. Gavrielides, "Bandwidth enhancement and broadband noise reduction in injection-locked semiconductor lasers," *IEEE Photonics Technology Letters*, vol. 7, pp. 709-711, 1995.

[126] J. Wang, M. K. Haldar, L. Li, and F. V. C. Mendis, "Enhancement of modulation bandwidth of laser diodes by injection locking," *IEEE Photonics Technology Letters*, vol. 8, pp. 34-36, 1996.

[127] G. Yabre, "Effect of relatively strong light injection on the chirp-to-power ratio and the 3 dB bandwidth of directly modulated semiconductor lasers," *Journal of Lightwave Technology*, vol. 14, pp. 2367-2373, 1996.

[128] T. B. Simpson and J. M. Liu, "Enhanced modulation bandwidth in injection-locked semiconductor lasers," *IEEE Photonics Technology Letters*, vol. 9, pp. 1322-1324, 1997.

[129] J. M. Liu, H. F. Chen, X. J. Meng, and T. B. Simpson, "Modulation bandwidth, noise, and stability of a semiconductor laser subject to strong injection locking," *IEEE Photonics Technology Letters*, vol. 9, pp. 1325-1327, 1997.

[130] T. B. Simpson, J. M. Liu, and A. Gavrielides, "Small-signal analysis of modulation characteristics in a semiconductor laser subject to strong optical injection," *IEEE Journal of Quantum Electronics*, vol. 32, pp. 1456-1468, 1996.

[131] H. K. Sung, E. K. Lau, and M. C. Wu, "Optical Properties and Modulation Characteristics of Ultra-Strong Injection-Locked Distributed Feedback Lasers," *IEEE Journal of Selected Topics in Quantum Electronics*, vol. 13, pp. 1215-1221, 2007.

[132] E. K. Lau, X. Zhao, H.-K. Sung, D. Parekh, C. Chang-Hasnain, and M. C. Wu, "Strong optical injection-locked semiconductor lasers demonstrating >100-GHz resonance frequencies and 80-GHz intrinsic bandwidths," *Optics Express*, vol. 16, pp. 6609-6618, 2008/04/28 2008.

[133] E. K. Lau, H.-K. Sung, and M. C. Wu, "Scaling of resonance frequency for strong injection-locked lasers," *Optics Letters*, vol. 32, pp. 3373-3375, 2007/12/01 2007.

[134] M. I. Memon, B. Li, G. Mezosi, Z. Wang, M. Sorel, and S. Yu, "Modulation Bandwidth Enhancement in Optical Injection-Locked Semiconductor Ring Laser," *IEEE Photonics Technology Letters,* vol. 21, pp. 1792-1794, 2009.

[135] G. A. Smolyakov and M. Osinski, "High-Speed Modulation Analysis of Strongly Injection-Locked Semiconductor Ring Lasers," *IEEE Journal of Quantum Electronics,* vol. 47, pp. 1463-1471, 2011.

[136] H. Kalagara, G. A. Smolyakov, M. Osi, x, and ski, "Rate Equation Analysis of Q-Modulated Strongly Injection-Locked Whistle-Geometry Ring Lasers," *IEEE Journal of Selected Topics in Quantum Electronics,* vol. 21, pp. 619-627, 2015.

[137] H. Toba, Y. Kobayashi, K. Yanagimoto, H. Nagai, and M. Nakahara, "Injection-locking technique applied to a 170 km transmission experiment at 445.8 Mbit/s," *Electronics Letters,* vol. 20, pp. 370-371, 1984.

[138] N. Olsson, H. Temkin, R. Logan, L. Johnson, G. Dolan, J. v. d. Ziel, *et al.*, "Chirp-free transmission over 82.5 km of single mode fibers at 2 Gbit/s with injection locked DFB semiconductor lasers," *Journal of Lightwave Technology,* vol. 3, pp. 63-67, 1985.

[139] S. Mohrdiek, H. Burkhard, and H. Walter, "Chirp reduction of directly modulated semiconductor lasers at 10 Gb/s by strong CW light injection," *Journal of Lightwave Technology,* vol. 12, pp. 418-424, 1994.

[140] C. Sun, D. Liu, B. Xiong, Y. Luo, J. Wang, Z. Hao, *et al.*, "Modulation Characteristics Enhancement of Monolithically Integrated Laser Diodes Under Mutual Injection Locking," *IEEE Journal of Selected Topics in Quantum Electronics,* vol. 21, pp. 628-635, 2015.

[141] N. Schunk and K. Petermann, "Noise analysis of injection-locked semiconductor injection lasers," *IEEE Journal of Quantum Electronics,* vol. 22, pp. 642-650, 1986.

[142] M. C. Espana-Boquera and A. Puerta-Notario, "Noise effects in injection locked laser simulation: phase jumps and associated spectral components," *Electronics Letters,* vol. 32, pp. 818-819, 1996.

[143] G. Yabre, H. D. Waardt, H. P. A. v. d. Boom, and G. D. Khoe, "Noise characteristics of single-mode semiconductor lasers under external light injection," *IEEE Journal of Quantum Electronics,* vol. 36, pp. 385-393, 2000.

[144] M. Teshima, "Frequency stabilization of tunable DBR laser using multiwavelength light injection locking technique," *Journal of Lightwave Technology,* vol. 14, pp. 2749-2756, 1996.

[145] H. L. T. Lee, R. J. Ram, O. Kjebon, and R. Schatz, "Bandwidth enhancement and chirp reduction in DBR lasers by strong optical injection," in *Lasers and Electro-Optics, 2000. (CLEO 2000). Conference on*, 2000, pp. 99-100.

[146] A. Bhardwaj, S. Ristic, L. A. Johansson, C. Althouse, and L. A. Coldren, "Direct modulation bandwidth enhancement of strongly injection-locked SG-DBR laser," *Electronics Letters*, vol. 46, p. 362, 2010.

[147] O. Duzgol, G. Kyritsis, and N. Zakhleniuk. (2016, Modulation Dynamic Response of Optical-Injection-Locked Wavelength-Tunable Semiconductor Laser Diodes. *IET Optoelectronics*. Available: http://digital-library.theiet.org/content/journals/10.1049/iet-opt.2016.0075

[148] U. Mishra and J. Singh, *Semiconductor Device Physics and Design*: Springer Netherlands, 2007.

[149] J. Singh, *Semiconductor Devices: An Introduction*: McGraw-Hill, 1994.

[150] J.Piprek, *Semiconductor Optoelectronic Devices: Introduction to Physics and Simulation*: Academic Press, 2003.

[151] C. Kittel, "Introduction to Solid State Physics., ed. por John Wiley and Sons," *New York*, 2005.

[152] L. A. Coldren and S. W. Corzine, *Diode Lasers and Photonic Integrated Circuits*. New York USA: John Wiley & Sons Inc., 2012.

[153] J. Buus and E. J. Murphy, "Tunable lasers in optical networks," *Journal of Lightwave Technology*, vol. 24, pp. 5-11, 2006.

[154] K. Iwashita and K. Nakagawa, "Suppression of Mode Partition Noise by Laser Diode Light Injection," *IEEE Transactions on Microwave Theory and Techniques*, vol. 30, pp. 1657-1662, 1982.

[155] C. Henry, N. Olsson, and N. Dutta, "Locking range and stability of injection locked 1.54 μm InGaAsp semiconductor lasers," *IEEE Journal of Quantum Electronics*, vol. 21, pp. 1152-1156, 1985.

[156] E. K. Lau, H. K. Sung, and M. C. Wu, "Frequency Response Enhancement of Optical Injection-Locked Lasers," *IEEE Journal of Quantum Electronics*, vol. 44, pp. 90-99, 2008.

[157] E. K. Lau, L. J. Wong, X. Zhao, Y.-K. Chen, C. J. Chang-Hasnain, and M. C. Wu, "Bandwidth Enhancement by Master Modulation of Optical Injection-Locked Lasers," *Journal of Lightwave Technology*, vol. 26, pp. 2584-2593, 2008.

[158] L. V. T. Nguyen, A. J. Lowery, P. C. R. Gurney, and D. Novak, "Spectral study of a 1.55 μm multimode FP semiconductor laser using the transmission-line laser model," *Optical and Quantum Electronics,* vol. 27, pp. 663-678, 1995.

[159] A. J. Lowery, "Dynamic modelling of distributed-feedback lasers using scattering matrices," *Electronics Letters,* vol. 25, pp. 1307-1308, 1989.

[160] A. J. Lowery, "New dynamic model for multimode chirp in DFB semiconductor lasers," *IEE Proceedings J - Optoelectronics,* vol. 137, pp. 293-300, 1990.

[161] A. J. Lowery, "Integrated mode-locked laser design with a distributed-Bragg reflector," *IEE Proceedings J - Optoelectronics,* vol. 138, pp. 39-46, 1991.

[162] S. Tan and Y. Yonglin, "Modeling of Tunable DBRs Lasers Based on Transmission-Line Laser Model," *Journal of Physics: Conference Series,* vol. 276, p. 012088, 2011.

[163] *VPIphotonics University Program*. Available: http://www.vpiphotonics.com/Community/

[164] R. Nagarajan, T. Fukushima, M. Ishikawa, J. E. Bowers, R. S. Geels, and L. A. Coldren, "Transport limits in high-speed quantum-well lasers: experiment and theory," *IEEE Photonics Technology Letters,* vol. 4, pp. 121-123, 1992.

[165] R. Nagarajan, M. Ishikawa, T. Fukushima, R. S. Geels, and J. E. Bowers, "High speed quantum-well lasers and carrier transport effects," *IEEE Journal of Quantum Electronics,* vol. 28, pp. 1990-2008, 1992.

[166] Y. P. Xi, W. P. Huang, and X. Li, "High-Order Split-Step Schemes for Time-Dependent Coupled-Wave Equations," *IEEE Journal of Quantum Electronics,* vol. 43, pp. 419-425, 2007.

[167] L. A. Coldren, G. A. Fish, Y. Akulova, J. S. Barton, L. Johansson, and C. W. Coldren, "Tunable Semiconductor Lasers: A Tutorial," *Journal of Lightwave Technology,* vol. 22, pp. 193-202, 2004.

[168] L. Yu, H. Wang, D. Lu, S. Liang, C. Zhang, B. Pan, *et al.*, "A widely tunable directly modulated dbr laser with high linearity," *IEEE Photonics Journal,* vol. 6, pp. 1-8, 2014.

[169] O. K. Kwon, H. S. Cho, C. W. Lee, S. H. Oh, Y. A. Leem, and E. S. Nam, "10-Gb/s 1.59-DFB-LD Transmission Over 20 km SMF With No Compensation," *IEEE Photonics Technology Letters,* vol. 28, pp. 509-512, 2016.

[170] K. Nakahara, Y. Wakayama, T. Kitatani, T. Taniguchi, T. Fukamachi, Y. Sakuma, *et al.*, "Direct Modulation at 56 and 50 Gb/s of 1.3-m InGaAlAs Ridge-Shaped-BH DFB Lasers," *IEEE Photonics Technology Letters,* vol. 27, pp. 534-536, 2015.

[171] W. Kobayashi, T. Ito, T. Yamanaka, T. Fujisawa, Y. Shibata, T. Kurosaki, *et al.*, "50-Gb/s direct modulation of a 1.3-μm InGaAlAs-based DFB laser with a ridge waveguide

structure," *IEEE Journal of Selected Topics in Quantum Electronics,* vol. 19, pp. 1500908-1500908, 2013.

[172] W. Kobayashi, T. Fujisawa, K. Tsuzuki, Y. Ohiso, T. Ito, S. Kanazawa, *et al.*, "Design and fabrication of wide wavelength range 25.8-Gb/s, 1.3-μm, push-pull-driven DMLs," *Journal of Lightwave Technology,* vol. 32, pp. 3-9, 2014.

[173] T. Tadokoro, W. Kobayashi, T. Fujisawa, T. Yamanaka, and F. Kano, "43 Gb/s 1.3 μm DFB laser for 40 km transmission," *Journal of Lightwave Technology,* vol. 30, pp. 2520-2524, 2012.

[174] T. Fukamachi, K. Adachi, K. Shinoda, T. Kitatani, S. Tanaka, M. Aoki, *et al.*, "Wide temperature range operation of 25-Gb/s 1.3-μm InGaAlAs directly modulated lasers," *IEEE Journal of Selected Topics in Quantum Electronics,* vol. 17, pp. 1138-1145, 2011.

[175] L. Bach, W. Kaiser, J. Reithmeier, A. Forchel, M. Gioannini, V. I. Feies, *et al.*, "22-GHz modulation bandwidth of long cavity DBR laser by using a weakly laterally coupled grating fabricated by focused ion beam lithography," *IEEE Photonics Technology Letters,* vol. 16, pp. 18-20, 2004.

[176] J. Klamkin, J. M. Hutchinson, J. T. Getty, L. A. Johansson, E. J. Skogen, and L. A. Coldren, "High efficiency widely tunable SGDBR lasers for improved direct modulation performance," *IEEE Journal of selected topics in quantum electronics,* vol. 11, pp. 931-938, 2005.

[177] M. Majewski, J. Barton, L. Coldren, Y. Akulova, and M. Larson, "Direct intensity modulation in sampled-grating DBR lasers," *IEEE Photonics Technology Letters,* vol. 14, pp. 747-749, 2002.

[178] J. Buus, M.-C. Amann, and D. J. Blumenthal, *Tunable laser diodes and related optical sources*: Wiley-Interscience New York, 2005.

[179] H. Nishimoto, M. Yamaguchi, I. Mito, and K. Kobayashi, "High-frequency response for DFB LD due to a wavelength detuning effect," *Journal of lightwave technology,* vol. 5, pp. 1399-1402, 1987.

[180] M. Matsuda, A. Uetake, T. Simoyama, S. Okumura, K. Takabayashi, M. Ekawa, *et al.*, "1.3-μm-wavelength AlGaInAs multiple-quantum-well semi-insulating buried-heterostructure distributed-reflector laser arrays on semi-insulating InP substrate," *IEEE Journal of Selected Topics in Quantum Electronics,* vol. 21, pp. 241-247, 2015.

[181] R. Todt, T. Jacke, R. Meyer, R. Laroy, G. Morthier, and M.-C. Amann, "Widely tunable twin-guide laser diodes with sampled gratings: Design and performance," *IEEE Journal of Selected Topics in Quantum Electronics,* vol. 13, pp. 1095-1103, 2007.

[182] B.-S. Kim, J.-K. Kim, Y. Chung, and S.-H. Kim, "Time-domain large-signal analysis of widely tunable DBR laser diodes with periodically sampled and chirped gratings," *IEEE Photonics Technology Letters*, vol. 10, pp. 39-41, 1998.

[183] H.-K. Sung, T. Jung, M. C. Wu, D. Tishinin, T. Tanbun-Ek, K. Liou, *et al.*, "Modulation bandwidth enhancement and nonlinear distortion suppression in directly modulated monolithic injection-locked DFB lasers," in *Microwave Photonics, 2003. MWP 2003 Proceedings. International Topical Meeting on*, 2003, pp. 27-30.

[184] D. Labukhin, C. A. Stolz, N. A. Zakhleniuk, R. Loudon, and M. J. Adams, "Nonlinear dynamics of multi-section tunable lasers," *IEEE Journal of Quantum Electronics*, vol. 46, pp. 689-699, 2010.

[185] L. Chrostowski, B. Faraji, W. Hofmann, M.-C. Amann, S. Wieczorek, and W. W. Chow, "40 GHz bandwidth and 64 GHz resonance frequency in injection-locked 1.55 μm VCSELs," *IEEE Journal of Selected Topics in Quantum Electronics*, vol. 13, pp. 1200-1208, 2007.

[186] V. Erzen, M. Mikulic, and B. Batagelj, "Frequency-response measurements of an injection-locked Fabry-Perot laser diode in a colorless WDM-PON," in *Fiber Optics in Access Network (FOAN), 2015 International Workshop on*, 2015, pp. 26-30.

[187] S. Kobayashi and T. Kimura, "Injection locking characteristics of an AlGaAs semiconductor laser," *IEEE Journal of Quantum Electronics*, vol. 16, pp. 915-917, 1980.

[188] Z. Xu, Y. J. Wen, W.-D. Zhong, C.-J. Chae, X.-F. Cheng, Y. Wang, *et al.*, "High-speed WDM-PON using CW injection-locked Fabry-Perot laser diodes," *Optics express*, vol. 15, pp. 2953-2962, 2007.

[189] G.-R. Lin, Y.-S. Liao, Y.-C. Chi, H.-C. Kuo, G.-C. Lin, H.-L. Wang, *et al.*, "Long-cavity Fabry–Perot laser amplifier transmitter with enhanced injection-locking bandwidth for WDM-PON application," *Journal of Lightwave Technology*, vol. 28, pp. 2925-2932, 2010.

[190] C. Yeh, C. Chow, H. Chen, J. Sung, and Y. Liu, "Demonstration of using injection-locked Fabry-Perot laser diode for 10 Gbit/s 16-QAM OFDM WDM-PON," *Electronics letters*, vol. 48, pp. 940-942, 2012.

[191] C. Lin and F. Mengel, "Reduction of frequency chirping and dynamic linewidth in high-speed directly modulated semiconductor lasers by injection locking," *Electronics Letters*, vol. 20, pp. 1073-1075, 1984.

[192] E. K. Lau, L. J. Wong, and M. C. Wu, "Enhanced Modulation Characteristics of Optical Injection-Locked Lasers: A Tutorial," *IEEE Journal of Selected Topics in Quantum Electronics,* vol. 15, pp. 618-633, 2009.

[193] V. Annovazzi-Lodi, S. Donati, and M. Manna, "Chaos and locking in a semiconductor laser due to external injection," *IEEE Journal of Quantum Electronics,* vol. 30, pp. 1537-1541, 1994.

[194] C. Cui and S.-C. Chan, "Performance analysis on using period-one oscillation of optically injected semiconductor lasers for radio-over-fiber uplinks," *IEEE Journal of Quantum Electronics,* vol. 48, pp. 490-499, 2012.

[195] G. Van Tartwijk and D. Lenstra, "Semiconductor lasers with optical injection and feedback," *Quantum and Semiclassical Optics: Journal of the European Optical Society Part B,* vol. 7, p. 87, 1995.

[196] G. Hadley, "Injection locking of diode lasers," *IEEE journal of quantum electronics,* vol. 22, pp. 419-426, 1986.

[197] O. Duzgol, G. Kyritsis, and N. Zakhleniuk, "Travelling-wave modelling of the dynamic performance of wavelength-tunable laser diodes using the integrated VPI and PICS3D software," *IET Optoelectron,* vol. 11, 2017.

[198] C. Masoller, "Implications of how the linewidth enhancement factor is introduced on the Lang and Kobayashi model," *IEEE journal of quantum electronics,* vol. 33, pp. 796-803, 1997.

[199] F. Kéfélian and P. Gallion, "Locking and noise properties of multisection semiconductor lasers with optical injection. Application to Fabry–Pérot and DFB cavities," *IEEE Journal of Quantum Electronics,* vol. 44, pp. 547-560, 2008.

[200] L. Yu, D. Lu, B. Pan, L. Zhang, L. Guo, Z. Li, *et al.*, "Widely tunable narrow-linewidth lasers using self-injection DBR lasers," *IEEE Photonics Technology Letters,* vol. 1, pp. 50-53, 2015.

[201] X. Zhao and C. J. Chang-Hasnain, "A new amplifier model for resonance enhancement of optically injection-locked lasers," *IEEE Photonics Technology Letters,* vol. 20, p. 395, 2008.

[202] C. H. Chang, L. Chrostowski, and C. Chang-Hasnain, "Enhanced VCSEL performance by optical injection locking for analog and digital applications," in *The 16th Annual Meeting of the IEEE Lasers and Electro-Optics Society, 2003. LEOS 2003.*, 2003, pp. 704-705 vol.2.

[203] C. Chih-Hao, L. Chrostowski, C. J. Chang-Hasnain, and W. W. Chow, "Study of long-wavelength VCSEL-VCSEL injection locking for 2.5-Gb/s transmission," *IEEE Photonics Technology Letters*, vol. 14, pp. 1635-1637, 2002.

[204] J.-M. Luo, M. Osinski, and J. McInerney, "Side-mode injection locking of semiconductor lasers," *IEE Proceedings J-Optoelectronics*, vol. 136, pp. 33-37, 1989.

[205] A. Kuramoto and S. Yamashita, "All-optical regeneration using a side-mode injection-locked semiconductor laser," *IEEE Journal of Selected Topics in Quantum Electronics*, vol. 9, pp. 1283-1287, 2003.

[206] O. Duzgol, G. Kyritsis, and N. Zakhleniuk, "Enhanced dynamic response and spectral characteristics improvement of optically-injected widely-tunable laser diodes," in *2016 International Semiconductor Laser Conference (ISLC)*, 2016, pp. 1-2.